

Vanadium recovery in the ferrovanadium production process

By

Marnu CJ van der Merwe

In fulfilment of the requirements for the degree

MEng(Metallurgical Engineering)

Department of Material Science and Metallurgical Engineering

University of Pretoria

Supervisors: Prof. A.M. Garbers-Craig and Dr. R.D. Cromarty

August 2020

Abstract

Ferrovandium can be produced in a DC arc furnace by reducing V_2O_3 by means of an aluminothermic reaction. Vanadium recovery is decreased by the formation of vanadium oxides within the slag, along with ferrovandium droplet entrainment in the slag. High refractory wear rates increase the operational cost of the process, which is mainly a result of the high operating temperature (slag temperature of 2100°C) and incompatibility between the slag and the refractory.

The effect of slag composition on the extent of refractory wear was investigated by heating slags of different MgO contents to 1800°C in the contact with magnesia refractory. The chemical interaction between the slag and refractory was investigated, along with the dimensional change of a piece of refractory which was reacted with slag to determine the extent of slag-refractory interaction.

Changing the slag composition to favour an increase in vanadium recovery and implementing a two stage melting process were both investigated. The (CaO+MgO): Al_2O_3 ratio was varied to alter the amount of spinel ($MgAl_2O_4$) that forms in the slag in order to establish the effect of spinel formation on vanadium recovery. The two stage process included adding excess aluminium to the first stage to increase V_2O_3 reduction and adding Fe_2O_3 to the second stage to produce a ferrovandium product with an aluminium content below 1.5 wt%.

The slag-refractory test results indicated that the extent of refractory wear can be decreased by increasing the MgO content of the slag in contact with the MgO refractory. The results also indicated that refractory wear was driven by the formation of $MgAl_2O_4$, which is the product of a chemical reaction between the slag and the refractory.

The amount of spinel formed with a change in (CaO+MgO): Al_2O_3 ratio did not influence the vanadium recovery. The change in (CaO+MgO): Al_2O_3 ratio of the slag did influence the vanadium recovery due to the effect it has on the activity coefficient of V_2O_3 . The vanadium recovery decreased linearly from 75 wt% to 25 wt% as the (CaO+MgO): Al_2O_3 ratio increased from 0.30 to 1.43. The vanadium recovery was also strongly influenced by the calculated slag volume, with the metal recovery decreasing with an increase in slag volume.

A two stage process was simulated whereby excess aluminium was added in the first stage to increase vanadium recovery and hematite was added in the second stage to decrease the aluminium content of the ferrovandium. The two stage process tests done on a laboratory scale indicated that it is possible to increase the overall vanadium recovery by increasing the aluminium used to reduce the V_2O_3 , followed by the addition of Fe_2O_3 to produce a metal product with an aluminium content below 1.5 wt%. The optimum aluminium addition for the first stage was determined to be 3.5 wt% excess, which resulted in a vanadium recovery of 73.9 wt%. The vanadium recovery of the two stage process was 72.6 wt%, which is higher than the 71.4 wt% obtained for the single stage process. The use of Fe_2O_3 did however decrease the vanadium content of the metal from 68.6 wt% to 63.5 wt%.

Keywords: Ferrovandium, vanadium recovery, MgO refractory wear, spinel formation, $MgAl_2O_4$, $Ca_2(Al,V)_2O_5$

Acknowledgements

I would like to thank and express my sincere appreciation to the following people:

- Prof A.M. Garbers-Craig and Dr. R.D. Cromarty, my supervisors, for the opportunity and continuous guidance.
- A. Brugman for the opportunity and identifying the project.
- Glencore Rhovan for financial support.
- The Department of Material Science and Metallurgical Engineering, University of Pretoria, for the use of their facilities.
- D. Odendaal for his technical assistance and O. Rivera Li Kao for his assistance with sample analyses.
- My parents, sister and friends for their support.

Table of content

Chapter 1: Introduction	1
1.1 Introduction	1
1.2 Process background	1
1.3 Project background	2
1.4 Project aim	3
1.5 Hypothesis.....	4
Chapter 2: Literature review	5
2.1 Sources of vanadium.....	5
2.2 Iron-vanadium phase diagram	5
2.3 Oxidation states of vanadium	6
2.4 Factors influencing the equilibrium loss of vanadium to the slag	6
2.5 Activity coefficient of V_2O_3	7
2.5.1 Effect of basicity on vanadium losses to the slag	7
2.6 Metal droplet entrainment.....	10
2.6.1 Metal droplet attachment to spinel phase	12
2.6.2 Viscosity	13
2.7 Refractory lining.....	16
2.8 Interpretation of literature	16
2.9 Conclusions	19
Chapter 3: Project aim and experimental design	20
3.1 Design of experiments	20
3.1.1 Response, factors and levels.....	20
3.1.2 Test types	20
3.1.3 Factors for each test type	20
3.1.4 Levels for each test type	20
3.1.5 Response	22
3.1.6 Measurement of responses	22
3.1.7 Randomisation	23
3.1.8 Blocking and controlling.....	24
3.2. Experimental setup	24
3.2.1 Furnace setup.....	24
3.2.2 Test setup.....	26
3.2.3 Raw materials.....	27
3.2.4 Experimental procedure	28
3.3 Sampling.....	28

3.3.1 Slag samples from a ferrovanadium smelter	28
3.3.2 Post-mortem refractories samples from a ferrovanadium smelter	28
3.4. Sample analysis	29
3.4.1 XRF analysis	29
3.4.2 XRD analysis	29
3.4.3 SEM-EDS analysis	30
3.4.4 Metal recovery	30
Chapter 4: Post mortem analysis of industrial slag and refractory samples	31
4.1 Post-mortem slag analysis	31
4.1.1 Analysis using a CaO-Al ₂ O ₃ -MgO ternary phase diagram	31
4.1.2 XRD-analysis	33
4.1.3 SEM-EDS analysis	33
4.2 Post-mortem refractory analysis	36
4.2.1 XRF results	36
4.2.2 XRD results	41
4.2.3 SEM-EDS analysis	42
4.3 Conclusions	52
Chapter 5: Experimental results	54
5.1 Slag-refractory interaction	54
5.1.1 Background	54
5.1.2 Sample A	55
5.1.3 Sample B	60
5.2 Metal and vanadium recovery	65
5.2.1 Metal and vanadium recovery as a function of slag composition	65
5.2.2 Metal recovery as a function of spinel phase formation	72
5.2.3 XRD results versus SEM-EDS results	78
5.3 The effect of adding excess aluminium to the recovery of vanadium	79
5.3.1 Background	79
5.3.2 XRD results	79
5.3.3 Sample C1 (1.5 wt% Al) SEM-EDS analysis	80
5.3.4 Comparison between samples C1, C2 and C3	90
5.4 Two stage process	95
5.4.1 Metal and vanadium recovery as a function of aluminium (first stage)	95
5.4.2 First stage summary	99
5.4.3 Second stage	99
5.4.4 Vanadium recovery for the second stage	103

Chapter 6: Summary and discussion.....	105
6.1 Slag-refractory interaction tests	105
6.2 Metal recovery as a function of slag composition	105
6.2.1 The effect of slag volume and viscosity	105
6.2.2 The effect of the (CaO+MgO): Al ₂ O ₃ ratio.....	107
6.3 Two stage smelting process	109
6.3.1 Phases formed in stage 1	109
6.3.2 Comparison between samples C1, C2 and C3 of stage 1.....	109
6.3.3 Second stage of the smelting process.....	110
6.4 Comparison of the industrial slag and the laboratory scale slag.....	110
6.5 Comparison of the post mortem refractory analysis and slag-refractory interaction tests.....	111
6.6 Metal droplet interaction with spinel phase	112
6.7 Equilibrium tests	113
Chapter 7: Conclusions	116
Chapter 8: Recommendations	118
Chapter 9: Recommendations for future work.....	119
References	120
Appendix	122
1 Post-mortem slag analysis	122
2 Post-mortem refractory analysis	125
2.1 SEM-EDS results	126
3. Slag-refractory interaction	137
4 Metal-slag interaction.....	146
4.1 Vanadium recovery as a function of aluminium content	146
4.2 Sample C1.....	155
4.3 Sample C3.....	156
5 Vanadium recovery as a function of amount of spinel phases formed	157
5.1 Sample E.....	157
5.2 Sample F.....	158
5.3 Sample G	159
6 Second stage tests	160
7 Equilibrium tests	161
7.1 Sample D	161
7.2 Sample E.....	162
7.3 Sample F.....	163
7.4 Sample G	165

Chapter 1: Introduction

1.1 Introduction

The extraction of vanadium has become increasingly important in recent years, due to its increased use in high strength low-alloy steel (HSLA) (Katsumata et al., 1991) as well as the advances made in vanadium flow battery technology (Joerissen et al., 2004). Vanadium is mostly added to HSLA steel in the form of ferrovanadium, which can be produced through the aluminothermic reduction of V_2O_3 . The reduction process occurs in the presence of iron which then alloys with the vanadium to form ferrovanadium. Several challenges exist surrounding the ferrovanadium production process, partly due to the extremely high operating temperature (around 2100°C).

The high operating temperature complicates replicating the process at lab scale and therefore very little research has been done to enhance the understanding of the different technical aspects of the system. Relatively high vanadium recoveries are obtained in industry, but with increasing operating costs, methods of further increasing the vanadium recovery are being investigated. The high operating temperature also results in a limited number of refractory materials being suitable for use in the furnace. Typically magnesia based refractories are used, but extremely high wear rates are currently observed, adding to the operating cost of ferrovanadium production.

1.2 Process background

The process description that follows is a popular method of producing ferrovanadium from titaniferous magnetite. Other processing methods do exist, but the processing method explained is the method used by the plant concerned with this project. Vanadium is present in titaniferous magnetite due to the substitution of iron(III) by vanadium(III) in the spinel structure (Sandford and Breitenstein, 1951). The ore is crushed and separated using magnetic separation. The concentrate is roasted in a kiln, together with sodium carbonate and sodium sulphate, resulting in the formation of water soluble sodium metavanadate. The product is leached using water, producing an impure pregnant solution. The pregnant solution is brought into contact with ammonium sulphate to form ammonium metavanadate. The ammonium metavanadate is reduced to V_2O_3 and ammonia by means of calcination within a reactor (Sandford and Breitenstein, 1951).

Metallic vanadium is produced by aluminothermic reduction of the V_2O_3 in a direct current arc furnace. The raw materials that are fed to the furnace are V_2O_3 , aluminium, CaO and iron. The aluminium acts as a reductant to reduce the V_2O_3 and in turn is oxidised to Al_2O_3 . CaO is added as a fluxing agent to assist in slag formation. The slag consists of Al_2O_3 and CaO and reaches a temperature of 2100 °C just before the metal and slag are tapped. The iron alloys with the produced vanadium and therewith reduces the melting point of the vanadium from 1910 °C to 1730 °C (which is in the form of ferrovanadium). Typical commercial ferrovanadium grades are shown in Table 1.1, of which the 80% ferrovanadium product is the typical end product of the described process.

Table 1.1: Commercial ferrovanadium grades typically produced (Gupta, 1992).

Product type	Composition (Mass %)							
	V	C	N	Al	Si	P	S	Mn
50-60% ferrovanadium	50-60	0.2 max		2 max	1 max	0.05 max	0.05 max	
70-80% ferrovanadium	70-80			1 max	2.5 max	0.05 max	0.10 max	
80% ferrovanadium	77-83	0.5 max		0.5 max	1.25 max	0.05 max	0.05 max	0.05 max
Carvan	82-86	10.5-14.5		0.1 max	0.1 max	0.05 max	0.10 max	
Ferrovanadium carbide	70-73	10-12			0.5 max	0.05 max	0.05 max	0.05 max
Ferrovan	42 min	0.85 max			7 max			4.5 max
Nitrovan	78-82	10-12	6 min	0.1 max	0.1 max	0.05 max	0.05 max	0.05 max

The metal and slag are tapped into a ladle and allowed to cool in the ladle for 13 hours, after which the ladle is tilted over, to remove both the solid metal and slag. Upon removal from the ladle the slag separates from the metal (the force during removal results in a crack forming between the metal and the slag). The metal is moved to a cooling bay, where it is quenched and a sample taken for analysis once the metal has cooled to room temperature. The slag goes to the slag crushing section, where it is crushed, packed in bags and sold. Slag containing a high concentration of ferrovanadium is also crushed and then recycled by adding it to the bags containing steel scrap, which is fed to the furnace for the following melt.

The refractories inside the furnace consist of MgO brick below the tap hole, MgO-carbon brick above the tap hole, while the roof of the furnace is lined with alumina silicate bricks. MgO-based fettling material is used to increase the lifespan of the refractories by adding it to sections of the refractory lining where severe wear is evident. A monolithic alumina silicate refractory is used to line the ladle.

1.3 Project background

In order to obtain a high vanadium recovery in the ferrovanadium production process, the equilibrium for the reaction $V_2O_3 + 2Al \rightleftharpoons 2V + Al_2O_3$ must be manipulated to favour vanadium formation. Increasing the aluminium concentration will result in vanadium formation being more favourable, thus increasing the vanadium recovery. Increasing the aluminium content does however increase the aluminium content of the metal, resulting in a ferrovanadium composition which does not meet the specification requirements (aluminium content less than 1.5 wt%).

A two stage process whereby excess aluminium is added in the first stage to increase vanadium recovery and hematite addition in the second stage to decrease the aluminium content of the ferrovanadium can possibly increase the overall vanadium recovery of the process. The two stage process can therefore increase the overall vanadium recovery, but still produce a ferrovanadium product with an aluminium content below 1.5 wt%.

Spinel ($MgAl_2O_4$) formation in the slag is a source of vanadium losses to the slag as described in the literature (Vermaak and Pistorius, 2000). Aluminium (III) is replaced by vanadium(III), resulting in vanadium residing in the slag rather than reacting with aluminium and separating to the metal. Reducing the amount of spinel that forms in the slag will reduce the ability of the slag to host vanadium(III), resulting in an increase in vanadium recovery. Changing the spinel content of the slag entails changing the slag composition,

which will result in slag volume changes. The amount of Al_2O_3 in the slag cannot be altered, due to the aluminium requirement of the reduction reaction. The slag volume will therefore be dependent on the amount of MgO and CaO added when altering the $(\text{MgO}+\text{CaO}): \text{Al}_2\text{O}_3$ ratio of the slag. The change in slag composition will also result in a change of the phases that are present in the slag.

Refractory wear is a major concern in industry, as aggressive refractory wear results in high operating costs. Refractory wear in this instance is due to a combination of the high operating temperature (2100°C) and the slag not being compatible with the refractories used (mainly MgO bricks). Saturating the slag with the main component of the refractory (MgO in this instance) can significantly reduce the rate of refractory wear and therefore reduce the operating costs of the process.

1.4 Project aim

The project aim is divided into three parts:

1. Highlight the importance of having a MgO saturated slag for this process.
2. Determine if there is a relation between vanadium recovery and the amount of spinel phase present in the slag.
3. Determine the feasibility of a two stage process (in terms of vanadium recovery).

The points of interest that were identified as the scope of the investigation were the high refractory wear rate of the MgO refractories in industry, the effect of spinel formation on the vanadium recovery and the possibility of increasing the vanadium recovery by implementing a two stage melting process.

The rate of refractory wear in industry is excessive, which increases the operational cost of producing ferrovanadium. A refractory lining is chosen based on the operating temperature of a furnace, as well as considering the compatibility between the refractory and the slag. Due to the high operating temperature (around 2100°C), magnesia based refractories are the only viable option. The use of MgO refractories require that the slag contains a certain amount of MgO in order to achieve slag-refractory compatibility. The effect of MgO addition to the slag on the refractory wear rate will therefore be investigated.

Previous work done by Vermaak and Pistorius (2000) indicated that vanadium is lost to the slag in the form of V_2O_3 , due to the ability of V^{3+} to substitute Al^{3+} in the spinel (MgAl_2O_4) structure. The amount of spinel phase which is present in the slag will therefore affect the vanadium recovery. It might therefore be beneficial to design the slag composition in such a way as to limit the amount of spinel phase which forms. The investigation therefore aims to determine if there is a relation between the vanadium recovery and the amount of spinel phase which forms during the ferrovanadium production process.

Vanadium is recovered in the ferrovanadium by reacting V_2O_3 with aluminium in order to produce vanadium and Al_2O_3 . The vanadium recovery is therefore affected by the amount of aluminium added to the reaction according to Le Chatelier's principle (applied to the equation $\text{V}_2\text{O}_3 + 2\text{Al} \rightleftharpoons 2\text{V} + \text{Al}_2\text{O}_3$). Increasing the $\text{Al}: \text{V}_2\text{O}_3$ ratio in the reaction will only affect the vanadium recovery up to the point where V_2O_3 becomes the limiting reagent,

when considering the thermodynamics of the reaction. Adding excess aluminium to the reaction might increase the reaction kinetics in such a way as to increase the vanadium recovery. The two stage process entails that excess aluminium is added in the first stage whereafter the formed slag is removed, after which iron oxide is added in the second stage to reduce the aluminium content of the metal from the first stage. This will increase the vanadium recovery as well as produce a metal product with an aluminium content below 1.5 wt%.

Additionally, tests were done to determine which phases should be present at room temperature in the slag. These tests were not initially conceived, but after the results obtained from the various slags, the need for determining the Alkemade triangles of the slag compositions arose. An additional aim of the investigation was therefore to determine the effect of V_2O_3 present in the slag on the Alkemade triangles of the MgO-CaO- Al_2O_3 phase diagram.

1.5 Hypothesis

1. The rate of refractory wear will decrease if the slag is saturated in MgO.
2. The vanadium recovery of the single stage process can be increased by decreasing the spinel content of the slag.
3. The vanadium recovery in a two stage process will increase with an increase in excess aluminium added to the reaction in the first stage.
4. It is possible to reduce the aluminium content of the ferrovanadium by reacting the metal with Fe_2O_3 in the second stage of the two stage process.

Chapter 2: Literature review

2.1 Sources of vanadium

Vanadium is the 22nd most abundant element in the Earth's crust, is found in more than 50 different minerals and is spread at a mean concentration of 150 g/t (Habashi, 2002a). Vanadium is not present in nature in its pure state, but occurs in combination with various elements. Vanadium is found in minerals such as carnotite ($K_2(UO_2)_2(VO_4)_2 \cdot 3H_2O$), roscoelite ($K(V^{3+}, Al, Mg)_2AlSi_3O_{10}(OH)_2$), patronite (VS_4), vanadiferous clays. Vanadium is also hosted within titaniferous magnetite, siltstone and uraniumiferous sandstone deposits. Some deposits of crude oil also contain vanadium in the form of organic complexes. Coal, shale and tar sands may also contain some vanadium. The largest source of vanadium is the titaniferous magnetite deposits found in South Africa, China, Russia and Australia (Moskalyk and Alfantzi, 2003).

2.2 Iron-vanadium phase diagram

The steel industry is the largest consumer of vanadium and vanadium is therefore often produced in the form of ferrovanadium. Adding iron to vanadium reduces the temperature required to melt the vanadium present as well as the tendency of the vanadium to oxidise (Figure 2.1, Gasik, 2013).

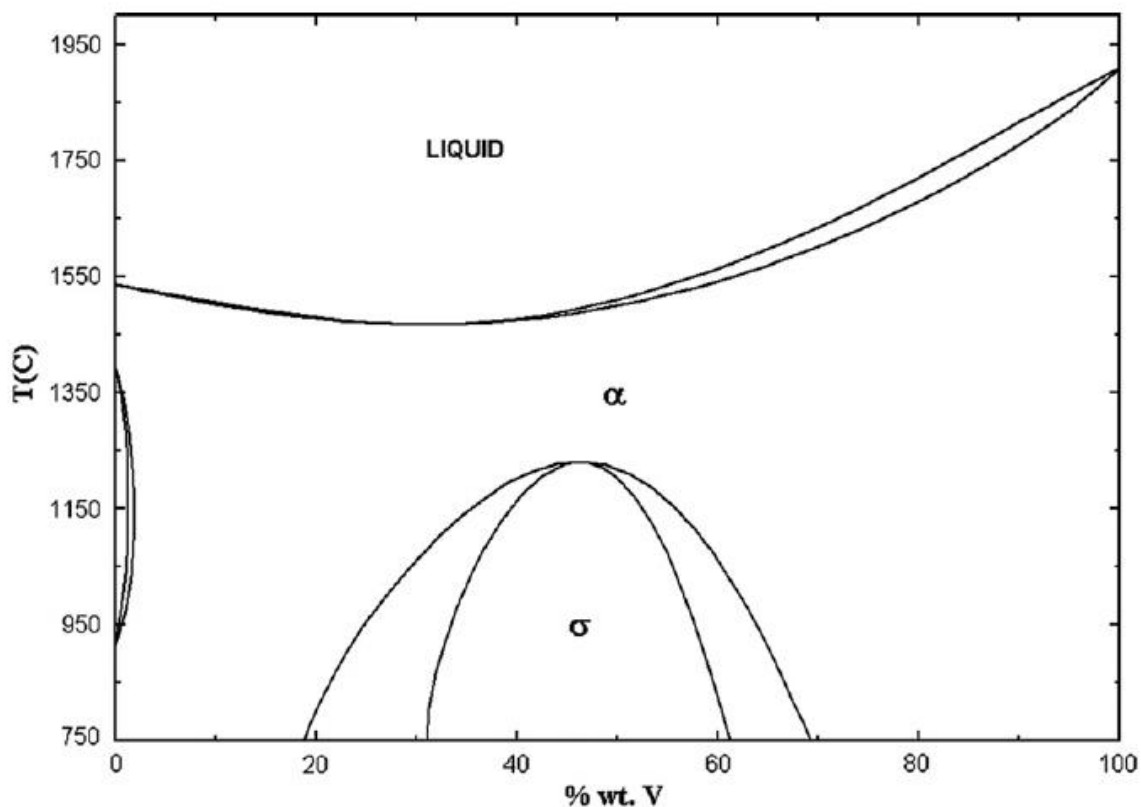


Figure 2.1: Binary phase diagram of the iron-vanadium system indicating the change of the melting point of vanadium with the addition of iron (Gasik, 2013).

Vanadium has a high melting point of 1910 °C (Gasik, 2013) and therefore requires a significant amount of energy to melt. An iron-vanadium solid solution constituted of 80 %

vanadium (typical composition of ferrovanadium) will be completely molten at a temperature of 1730°C. Vanadium also oxidises easily to higher oxidation states (V^{2+} , V^{3+} , V^{4+} and V^{5+}) at elevated temperatures in the presence of oxygen (Gasik, 2013).

2.3 Oxidation states of vanadium

Vanadium has various oxidation states of which, V^{2+} , V^{3+} and V^{5+} are the most common oxidation states, although V^{4+} can also be formed. The oxidation state of vanadium is dependent on the oxygen partial pressure and the temperature of the surroundings. A predominance diagram of oxygen partial pressure versus temperature is used to determine the oxidation state that will be present at different oxygen pressures and temperatures (Figure 2.2). Vermaak and Pistorius (2000) indicated that V_2O_3 is present in industrial Al_2O_3 -CaO based slags, and therefore at a temperature of 2113 K (1840 °C, the tapping temperature in the ferrovanadium industry) the oxygen partial pressure will be between 10^{-8} and 10^{-2} atm.

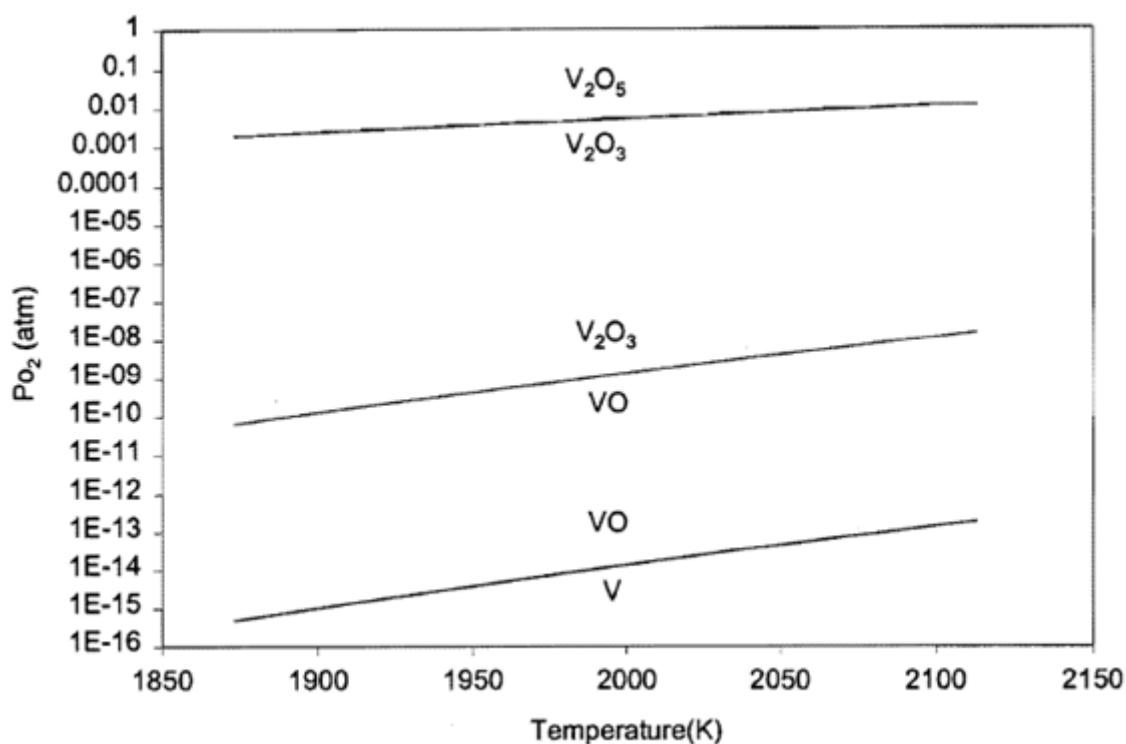


Figure 2.2: Predominance diagram indicating the regions where the various oxidation states of vanadium are dominant as a function of P_{O_2} and temperature (K) (Kubaschewski et al, 1992).

2.4 Factors influencing the equilibrium distribution of vanadium between the metal and slag

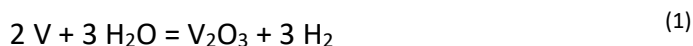
The tapping temperature during the ferrovanadium production process is approximately 1840 °C (metal temperature), which is required because of the high melting point of

ferrovanadium (Vermaak and Pistorius, 2000). The high temperature also aids the separation process of metal droplets entrained in the slag after the furnace content is tapped into a ladle. Metal entrainment in the slag is one of the factors resulting in vanadium loss to the slag (Vermaak and Pistorius, 2000).

Vanadium is also lost to the slag due to unreduced vanadium oxides reporting to the slag. Test work done on vanadium losses to the slag (Vermaak and Pistorius, 2000) indicate that losses up to 5 % (mass percent V_2O_3 in the slag) are common. The slag basicity has a strong influence on the vanadium losses (in the form of vanadium oxides) to the slag. The solidified slag consists mainly of $MgO \cdot Al_2O_3$ (MA), $CaO \cdot Al_2O_3$ (CA) and $CaO \cdot 2Al_2O_3$ (CA_2). The primary phase (MA spinel) contains most of the V_2O_3 content of the slag. Research done by Vermaak and Pistorius (2000) indicated that the primary spinel phase contained 93 % (molar basis) of the V_2O_3 content of the slag.

2.5 Activity coefficient of V_2O_3

The activity coefficient of V_2O_3 as a function of the $CaO:Al_2O_3$ molar ratio can be determined by fixing the vanadium and oxygen activities. This principle was used in experimental work done by Vermaak and Pistorius (2000). Vermaak and Pistorius (2000) controlled the vanadium activity coefficient, by using a pure vanadium crucible, and the activity of oxygen, by using a suitable fixed gas mixture. Slags containing different $CaO:Al_2O_3$ molar ratios (also containing V_2O_3 as "losses") were then melted in vanadium crucibles at constant oxygen partial pressure (Vermaak and Pistorius, 2000). The following reaction was the basis used to determine the V_2O_3 activity:



By using the Gibbs free energy of the reaction and knowing the temperature at which the reaction occurs, the equilibrium constant of equation 1 was determined (Vermaak and Pistorius, 2000):

$$K_2 = \frac{a_{V_2O_3} * p_{H_2}^3}{a_V^2 * p_{H_2O}^3} \quad (2)$$

The mole fraction of V_2O_3 present in the slag was determined using SEM-EDX analysis (Vermaak and Pistorius, 2000). The activity coefficient of V_2O_3 was determined from the equation:

$$\gamma_{V_2O_3} = \frac{a_{V_2O_3}}{X_{V_2O_3}} \quad (3)$$

2.5.1 Effect of basicity on vanadium losses to the slag

Research indicated (Vermaak and Pistorius, 2000) that there is a strong dependency between the activity coefficient of V_2O_3 and the slag basicity (CaO/Al_2O_3) at 1700°C (Figure 2.3). The V_2O_3 activity coefficient decreases sharply from a $CaO:Al_2O_3$ ratio of 0.6 to 0.9, but only a small decrease is associated with slags with basicity ratios higher than 0.9. The open triangle in Figure 2.3 represents a sample reacted at 1650 °C, from which it is evident that the activity coefficient is not very strongly dependent on temperature within this range (1650°C to 1700°C) (Vermaak and Pistorius, 2000).

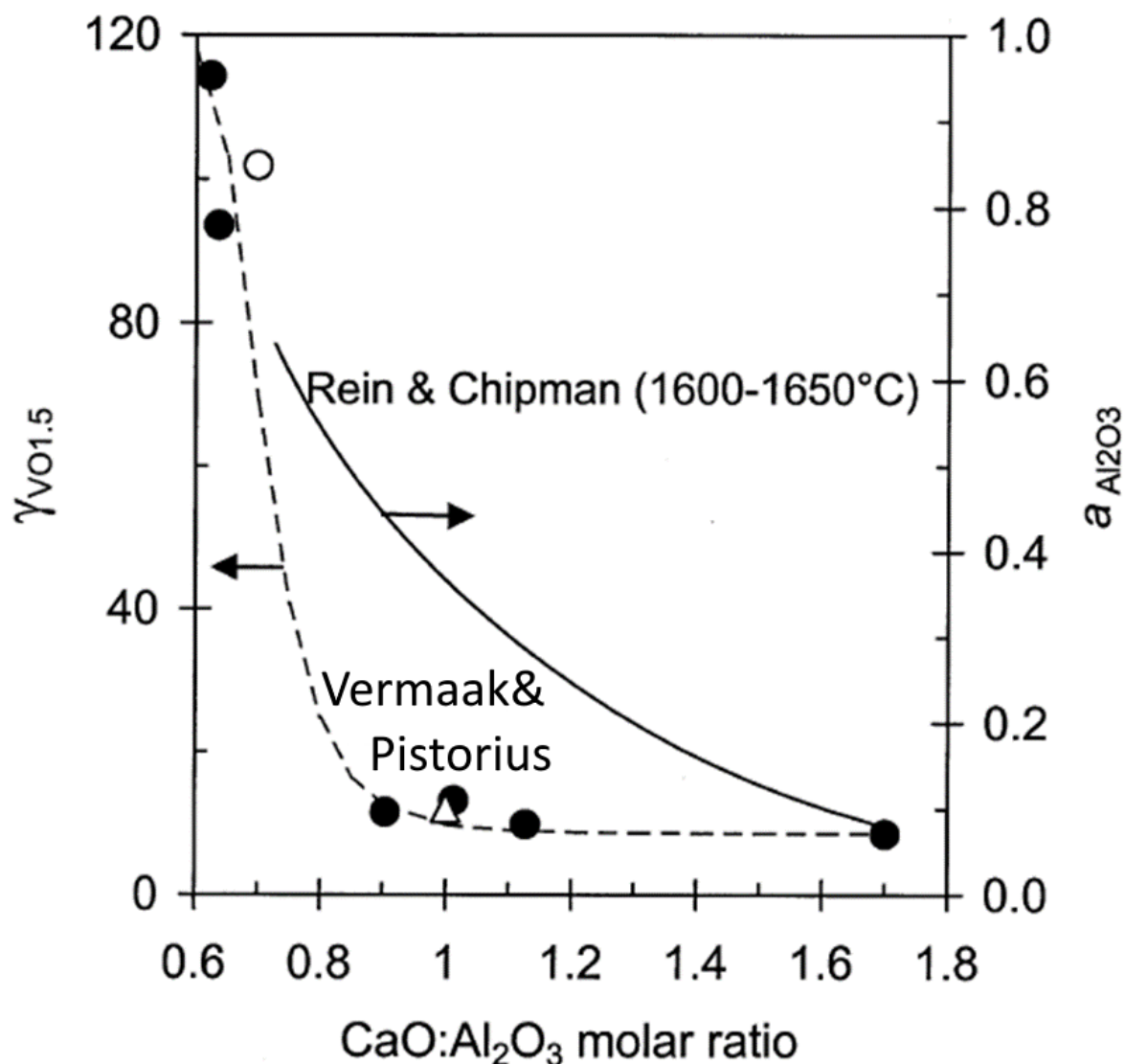


Figure 2.3: Relationship between the activity coefficient of V_2O_3 /activity of Al_2O_3 and the $CaO:Al_2O_3$ molar ratio. The dashed line represents tests done at $1700^\circ C$ (Vermaak and Pistorius, 2000) and the solid line tests done between $1600^\circ C$ and $1650^\circ C$ (Rein and Chipman, 1965). The open triangle is a test run at $1650^\circ C$ by Vermaak and Pistorius.

The mass percentage of V_2O_3 present in the slag or vanadium (as an oxide) reporting to the slag (per tonne of ferrovanadium produced), can be predicted using the activity coefficients given in Figure 2.3. An aluminium activity of 0.0003 was used, which was obtained by using the Raoultian law to obtain the aluminium activity coefficient (0.02) and the aluminium content in industrial ferrovanadium (<1.5 wt% aluminium). A vanadium activity of 0.7 was used, which is based on the ferrovanadium composition (70 % vanadium).

Vanadium oxide losses to the slag increases sharply as the molar ratio of $CaO:Al_2O_3$ increases from 0.7 to 1, which is due to the decrease of the V_2O_3 activity coefficient within the mentioned molar ratio range. A decrease in the mass percentage V_2O_3 in the slag at higher basicity values (molar ratios of 1 to 1.8) is the result of the Al_2O_3 activity decreasing as the basicity increases. A variation exists between the V_2O_3 % and mass of vanadium in the slag

per tonne of ferrovanadium produced due to an increase in the amount of slag formed as the basicity increases (therefore the variation of the dashed and solid line at 1800°C). From Figure 2.3 and Figure 2.4 it is evident that a small decrease in basicity (from a molar ratio of 1) will yield a higher recovery of vanadium to the metal. Aspects such as viscosity should also be considered, as lower CaO:Al₂O₃ ratios will result in an increase in viscosity and therefore influence the kinetics of metal-slag separation negatively (Vermaak and Pistorius, 2000).

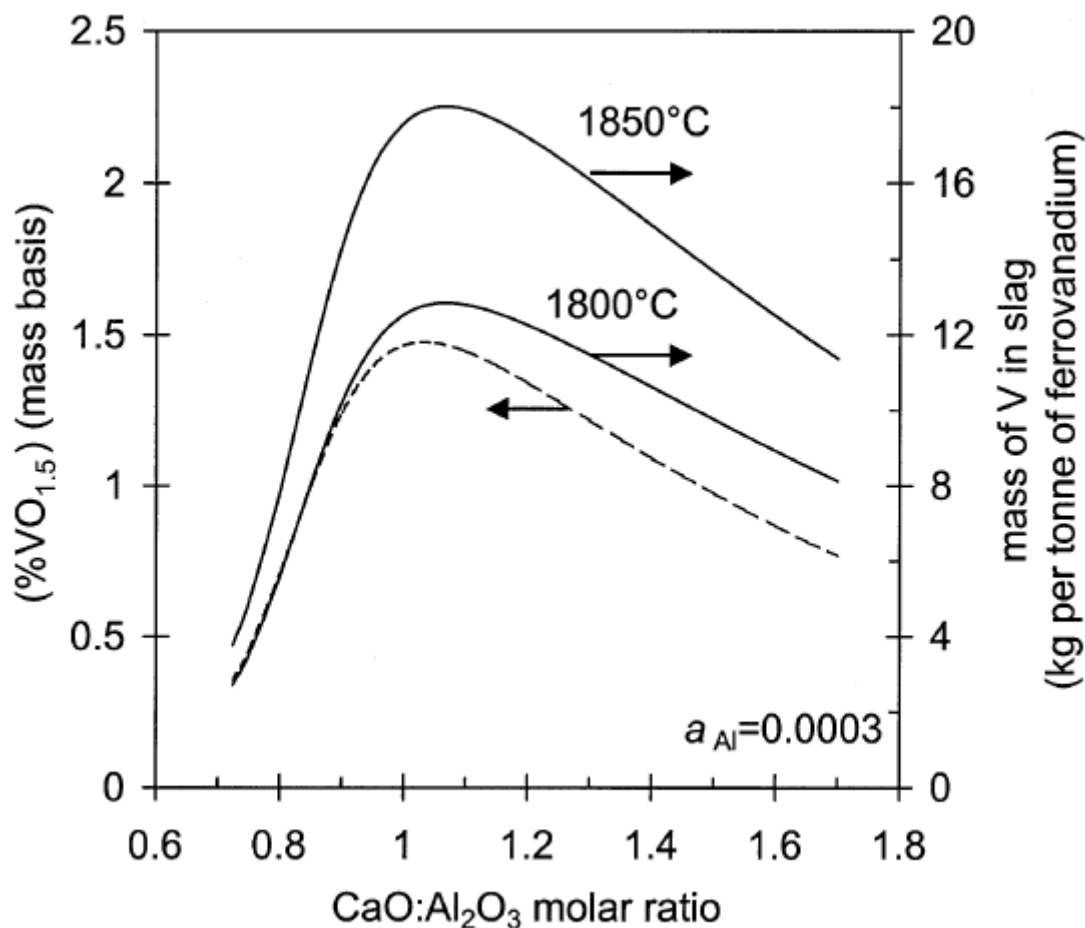


Figure 2.4: Vanadium losses to the slag due to the slag basicity, presented as both percentage V₂O₃ in the slag and mass vanadium in the slag per tonne of ferrovanadium produced (Vermaak and Pistorius, 2000).

The addition of MgO to the ferrovanadium production process results in an increase in V₂O₃ losses to the slag as a MgO-Al₂O₃ (a spinel-type) phase forms. Al₂O₃ in the spinel structure is easily substituted by V₂O₃. High alumina contents in the slag reduces the extent of Al₂O₃ substitution and therefore reduces V₂O₃ loss to the slag (Figure 2.5). The V₂O₃ losses to the slag is also reduced by decreasing the MgO content of the slag (Vermaak and Pistorius, 2000).

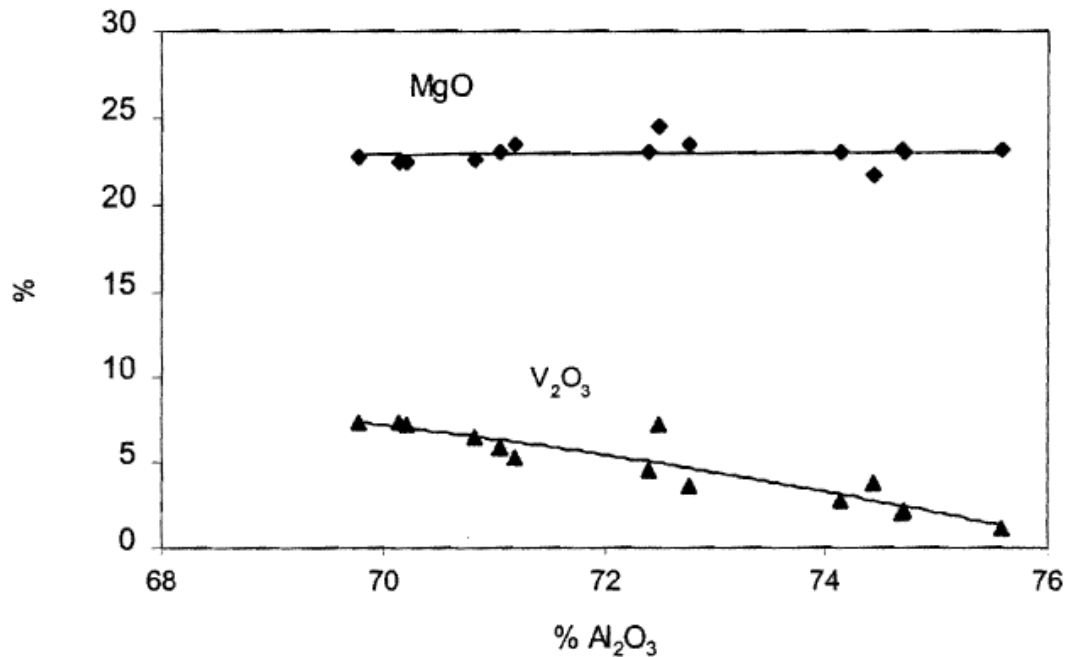


Figure 2.5: V₂O₅ content of the MgO- Al₂O₃ phase in the slag of a ferrovanadium process as the Al₂O₃ content is varied (Vermaak and Pistorius, 2000).

2.6 Metal droplet entrainment

In the base metal industry, copper losses through entrainment of matte in the slag accounts for 25 to 75% of the total copper losses to the slag (Minto and Davenport, 1973). Reasons for matte entrainment in the slag which may be relevant to ferrovanadium production includes:

- Fine dispersion of precipitated matte from the slag in regions where large temperature gradients exist in the furnace (Barnett and Jeffes, 1977).
- Introduction of matte in the slag by mixing (electromagnetic fields in the DC arc furnace).
- Matte from the lower part of the furnace rising upwards to the slag during tapping, which is the result of shear stress between the slag and the matte.
- High slag viscosity decreasing matte settling.
- Attachment of matte to solid phases.
- Matte spheres within the slag being too small to settle downwards (Liow and co-workers, 2003)

The settling of entrained matte in the slag is important and is influenced by factors such as the matte properties (e.g. viscosity, interfacial tension and composition), matte droplet size, slag layer depth and the probability of coalescence of entrained droplets (Floyd and Mackay, 1981). Larger droplets settle faster than smaller droplets and thinner slag layers result in shorter settling distances for entrained matte droplets. Stirring of slags and decreasing the slag viscosity are possible solutions for increasing the settling rate.

In a study done by Bellemans et al. (2017) it was found that copper losses due to metal entrainment in the slag account for 65%-80% of the total copper losses in the copper

production process. Copper losses to the slag are dependent on the slag viscosity, fluid motion of the slag, residence time, solid particles in the slag that entrap metal droplets, SO₂ generation in the slag, how the furnace is operated and matte-slag separation.

The copper losses to the slag are due to inadequate decantation of the metal droplets. Metal droplet settling through the slag can be described by Stokes's equation (Bellemans et al., 2017):

$$u = \frac{2 \cdot r^2 (\rho_{\text{sphere}} - \rho_{\text{fluid}}) g}{9\mu} \quad (4)$$

- u = settling rate (m/s)
- r is the radius of the droplet (m)
- ρ_{sphere} and ρ_{fluid} are the densities of the droplets and the surrounding phase respectively (kg/m³).
- g is the gravitational constant (m/s²)
- μ is the viscosity of the slag (Pa.s)

Stokes's equation is valid for laminar flow conditions and where rigid spheres are present. Laminar flow is characterised by a low Reynolds number. Laminar flow is usually present for liquid droplets moving through an immiscible medium. Where very low metal viscosities are present compared to the slag, Stokes's equation has to be corrected due to internal tensions within the droplets. Stokes's equation can be corrected by using the Hadamard-Rybczinski equation (Bellemans et al., 2017):

$$u = \frac{g \cdot r^2 \cdot \Delta\rho}{3\mu} \quad (5)$$

- $\Delta\rho$ is the density difference between the sphere and the fluid.

The work done by Bellemans et al. (2017) indicated that droplets with a size smaller than 0.1 mm behaved like rigid spheres, with their velocities being describes by Stokes's equation. The velocity of droplets larger than 0.1 mm was described by the Hadamard-Rybczinski equation.

Bellemans et al. (2017) state that fast decantation can be achieved by:

- Having a high density difference between the metal and the slag.
- Having large metal droplets present, which has a favourable outcome on the surface energy between the metal droplets and the slag.
- Having a slag with as low a slag viscosity as possible by changing the slag composition. The viscosity of the slag can also be influenced by the fraction of solid particles, which is described by the Einstein-Roscoe model equation (Bellemans et al., 2017):

$$\eta = \eta^0 (1 - af)^{-n} \quad (6)$$

- η = viscosity of the liquid-particle mixture (Pa.s)
- η^0 = liquid viscosity (Pa.s)
- a = the inverse of the maximum fraction of solid particles that the liquid can accommodate as the viscosity moves towards infinity.

- f = fraction solids present in the slag
- n = geometrical particle shape constant.
- For spherical mono-sized particles a and n have values of 1.35 and 2.5 respectively.

Metal droplets can also be retained on the metal-slag interface due to the surface tension that exists between the slag and the metal. A critical radius exists where metal droplets with a radius larger than the critical radius will cross the metal-slag boundary, whereas smaller droplets will float above the metal-slag boundary. The critical radius can be determined using the equation by Poggi et al. (1969):

$$R = \left(\frac{2 \cdot \gamma_{\text{slag}}}{\frac{4}{3} \cdot \rho_{\text{particle}} \cdot g} \right)^{0.5} \quad (7)$$

- R = critical radius of sphere (m)
- γ = surface tension (N/m)
- ρ = density (kg/m³)
- g = standard gravity (m/s²)

2.6.1 Metal droplet attachment to spinel phase

Metal-slag separation is mostly dependent on thermodynamic laws and are therefore influenced by factors such as composition, atmosphere and temperature (Bellemans et al., 2017). According to Bellemans et al. (2017) metal recovery is also influenced by interaction between the solid particles in the slag and the metal droplets present in the slag. Metal droplets attach to solid phases in the slag, inhibiting the settling of the droplet and thereby increasing metal losses through metal droplet entrainment.

Bellemans et al. (2017) investigated the interaction between the spinel phase and metal droplets. Tests were done where metal droplets were introduced either at random or by supersaturation of the liquid. The two situations correspond to two different scenarios:

- The metal droplets and slag phase formed separately.
- The metal droplets formed due to the presence of the slag phase (spinodal initialization).

The two different scenarios did not have any effect on the metal attachment, as in both scenarios metal droplets attached to the solid particles present in the slag. An observation was also made that in some instances the spinel phase grows on the edge of the pre-existing metallic droplets, therefore the metallic droplets act as sites for initiation and growth of the spinel phase.

The test work by Bellemans et al. (2017) also considered the influence of motion of the solid particles (spinel phase) in the slag on the amount of metal that attaches to the solid particles. These tests were conducted in non-wetting and low wetting conditions. The low wetting and non-wetting conditions were determined according to the parameter x_s in the formula:

$$f_{\text{solid}}(x_m) = \frac{A_s}{2} (x_m - x_s)^2 \quad (8)$$

- $f_{solid}(x_m)$ is the bulk contribution of the solid phase to the total Gibbs free energy
- A_s is the steepness of the parabola (J/m^3), where the parabola is the Gibbs energies as a function of the molar fraction of metal.
- x_s is a model parameter indicating the minimum of the parabola

Non-wetting conditions are where $x_s = 0.5$ and low wetting conditions where $x_s = 0.6$. Inducing movement of the particles only influenced the metal attachment for the low wetting conditions, but not for the non-wetting conditions. The amount of metal attachment (in the instance of wetting conditions) increased when movement of the particles were induced.

2.6.2 Viscosity

The viscosity of a CaO-Al₂O₃ slag is explained in terms of polymer formation, which is a result of bridging between compounds through O²⁻ ions. Tetrahedral SiO₄⁴⁻ forms a network through bridging of O²⁻ ions (Seetharaman, Mukai and du Sichen, 2004), but in the absence of SiO₄⁴⁻, amphoteric compounds such as Al₂O₃ may act as a network former. The result of network formation between Al₂O₃ (in the form of AlO₂⁻) structures is an increase of the viscosity of the slag. CaO in turn modifies the formed networks by breaking the chains and thereby decreasing the viscosity of the slag (Silva, 2012).

Various models have been considered for modelling of slag viscosities. Viscosity is related to the measurement of the resistance to motion when a shear stress is applied to the liquid and therefore entail the movement of layers of ions, molecules or atoms in a structure. The bonding forces between these layers follow an Arrhenius type relation as temperature is varied (Silva, 2012). Viscosity is therefore determined through the following equation:

$$\eta = A * \exp\left(\frac{E_A}{RT}\right) \quad (9)$$

- η is the viscosity (Pa.s)
- A is a pre-exponential coefficient (Pa.s)
- E_A is the activation energy required (J/mole)
- R is the universal gas constant (J/K/mole)
- T is the temperature in kelvin (K)

Slag composition may vary with temperature however, complicating the nature of the phases present in the slag, which resulted in another description of slag viscosity by Urbain (Silva, 2012):

$$\eta = A * T * \exp\left(\frac{E_A}{RT}\right) \quad (10)$$

- η is the viscosity (Pa.s)
- A is a pre-exponential coefficient (Pa.s)
- E_A is the activation energy required (J/mole)
- R is the universal gas constant (J/K/mole)
- T is the temperature in kelvin (K)

The presence of silicates in slags often result in a slight curvature when using the Urbain model, with an improved fit obtainable by using the Browstow relationship (Seetharaman, Mukai and du Sichen, 2004):

$$\eta = A_B + \frac{B_B}{T} + C_B \log(T) \quad (11)$$

- η is the viscosity (Pa.s)
- A_B is an empirical constant
- B_B is an empirical constant
- T is the temperature (K)
- C_B is an empirical constant

These models do not take chemical composition into consideration, which led to various studies regarding the incorporation of chemical composition in the computation of slag viscosities. Urbain and other authors proposed the grouping of slag forming oxides into modifier, amphoteric and glass forming groups in order to evaluate the effect of each group separately (Silva, 2012). The pre-exponential constant and activation energy is then determined by:

$$\ln(A_w) = A_0 + \sum_{\substack{\text{Component} \\ \text{of oxides } i}} A_i X_i \quad (12)$$

$$E_w = E_0 + \sum_{\substack{\text{Component} \\ \text{of oxides } i}} E_i X_i \quad (13)$$

- A_w is the total of the individual pre-exponential constants
- A_0 is the pre-exponential constant when chemical composition is not incorporated
- A_i is the individual pre-exponential constant of each component
- X_i is the mass fraction of component i
- E_w is the total of the individual activation energies (J/mole)
- E_0 is the activation energy when chemical composition is not incorporated (J/mole)
- E_i is the individual activation energy value of each component (J/mole)

The values obtained for A and E_A is only valid for limited ranges of composition and temperature (Silva, 2012).

2.6.2.1 Slag composition variations

Experimental work done by Arkhipov, Berezin and Shtengel'meier (1964) indicated that the addition of MgO as a flux (together with CaO) yields higher vanadium recoveries during FeV production than if only CaO was used. The increase in recovery (when adding MgO) was due to the reduction of both the slag viscosity as well as the liquidus temperature of the slag. The reduction of the slag viscosity results in less time being required for slag-metal separation,

whereas the lower slag liquidus temperature results in a longer period of time over which the metal droplets can separate from the slag.

The three different slags that were tested by Arkhipov et al. are given in Table 2.1, slag 1 is the result of a test where no flux was added, slag 2 is the result of a test where CaO was added and slag 3 is the result of a test where both MgO and CaO were added. The test work was conducted at 2000°C and the slag volumes for the three tests were identical. The results show an increase in vanadium yield with CaO addition and a further increase with the addition of MgO as well.

Table 2.1: Experimental work done by Arkhipov, Berezin and Shtengel'meier (1964), where three different slag compositions and the resulting vanadium yield were tested.

Slag	Content in slag (%)					Vanadium yield (%)	
	SiO ₂	Al ₂ O ₃	CaO	TiO ₂	MgO	Alloy	Slag
1	0.07	86.90	2.2	0.35	1.41	92	8
2	0.11	84.46	6.6	0.37	0.98	96.5	3.5
3	0.22	80.16	6.37	0.32	4.73	99.2	0.8

The viscosities of the different slag compositions were also measured over the temperature range 1800°C to 2000°C and is shown in Figure 2.6. The viscosity decreases from slag 1 to slag 3, due to the decrease in Al₂O₃ content from slag 1 to slag 3. An increase in slag basicity (ratio of MgO and CaO to Al₂O₃) results in a decrease in slag viscosity. Section 2.5.1 indicated a general increase in V losses in the form of V₂O₃ with an increase in slag basicity, which is contrary to the results obtained in Table 2.1 where the V losses decreased with an increase in slag basicity. The difference in results can be ascribed to two different mechanisms, where the work in section 2.5.1 refer to only losses in the form of V₂O₃ formation and the results in section 2.6.2.1 refer to losses in the form of both metal entrapment and V₂O₃ formation. The overall increase in V recovery as the basicity increases in section 2.6.2.1 would be due to the metal entrapment decreasing due to a decrease in viscosity. The losses due to V₂O₃ formation is not governed by viscosity, hence the difference in results between section 2.5.1 and section 2.6.2.1.

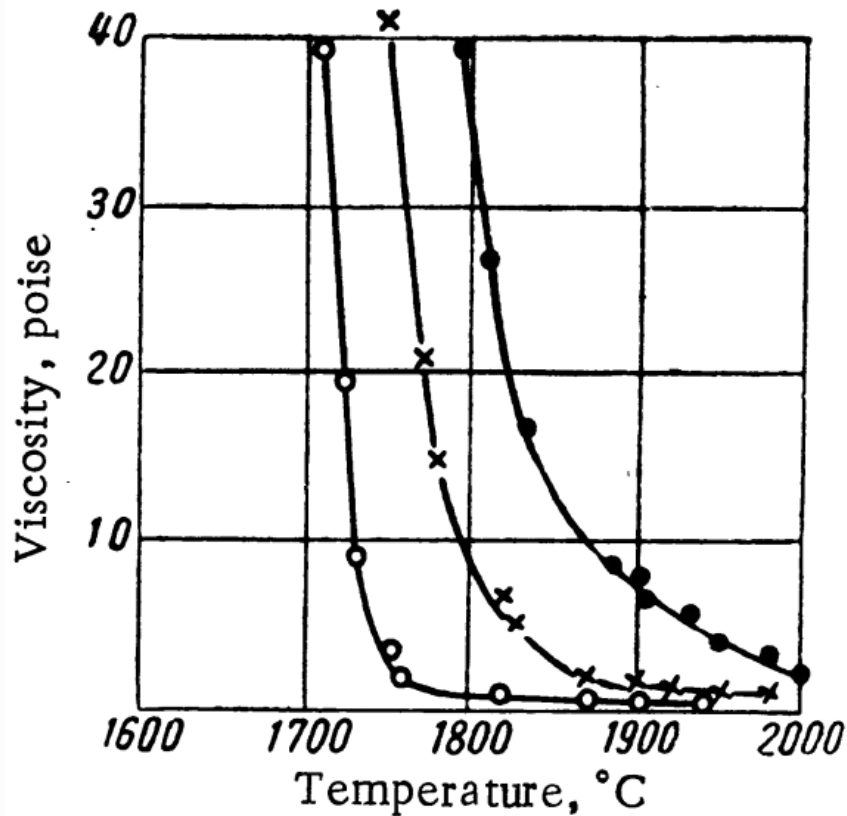


Figure 2.6: Viscosity of the three different tests that were done (o = slag 3, x = slag 2 and • = slag 1)

2.7 Refractory lining

Literature on refractory linings used in the ferrovanadium industry is limited. The work done by Vermaak and Pistorius (2000) mentions that MgO refractories are mostly used. The high operating temperature (tap temperature of 1900 °C), together with an incompatible slag (Al_2O_3 -rich slag) results in high refractory wear. The resulting slag from the process contains 11 wt% MgO, and as no MgO is added as a raw material, the MgO originates from the refractory (Vermaak and Pistorius, 2000).

2.8 Interpretation of literature

The recovery of ferrovanadium in the aluminothermic process is influenced by several factors, such as the melting temperature of the alloy, aluminium added, viscosity of the slag and the phases present in the slag.

The melting temperature of ferrovanadium is very dependent on the percentage vanadium present in the alloy as the melting temperature increases with vanadium content from 1470 °C (at 30 % wt vanadium) to 1910 °C (at 100 % wt vanadium) (Gasik, 2013).

Vanadium losses to the slag during ferrovanadium production are considerable as indicated in the literature (Vermaak and Pistorius, 2000). This is due to both metal droplet entrainment and unreduced vanadium oxides reporting to the slag. Vanadium oxide formation is mainly a function of the composition and basicity of the slag. The spinel phase $\text{MgO} \cdot \text{Al}_2\text{O}_3$ (MA) hosts

the majority of the V_2O_3 in the slag (Vermaak and Pistorius, 2000), which is a result of V^{3+} substituting for Al^{3+} .

The pronounced influence of slag basicity on the activity coefficient of V_2O_3 in the slag presents an opportunity to reduce vanadium losses to the slag. This can be achieved by operating with slags of $(CaO + MgO): Al_2O_3$ ratios in which the activity coefficient of V_2O_3 is high.

Using the $MgO-CaO-Al_2O_3$ ternary phase diagram, regions can be identified where the spinel phase will not form at temperature or upon cooling (Figure 2.7). Identifying compositional regions where the spinel phase does not form provides an opportunity to reduce vanadium losses to the slag, if the new phase(s) that form have a lower tendency to host V_2O_3 .

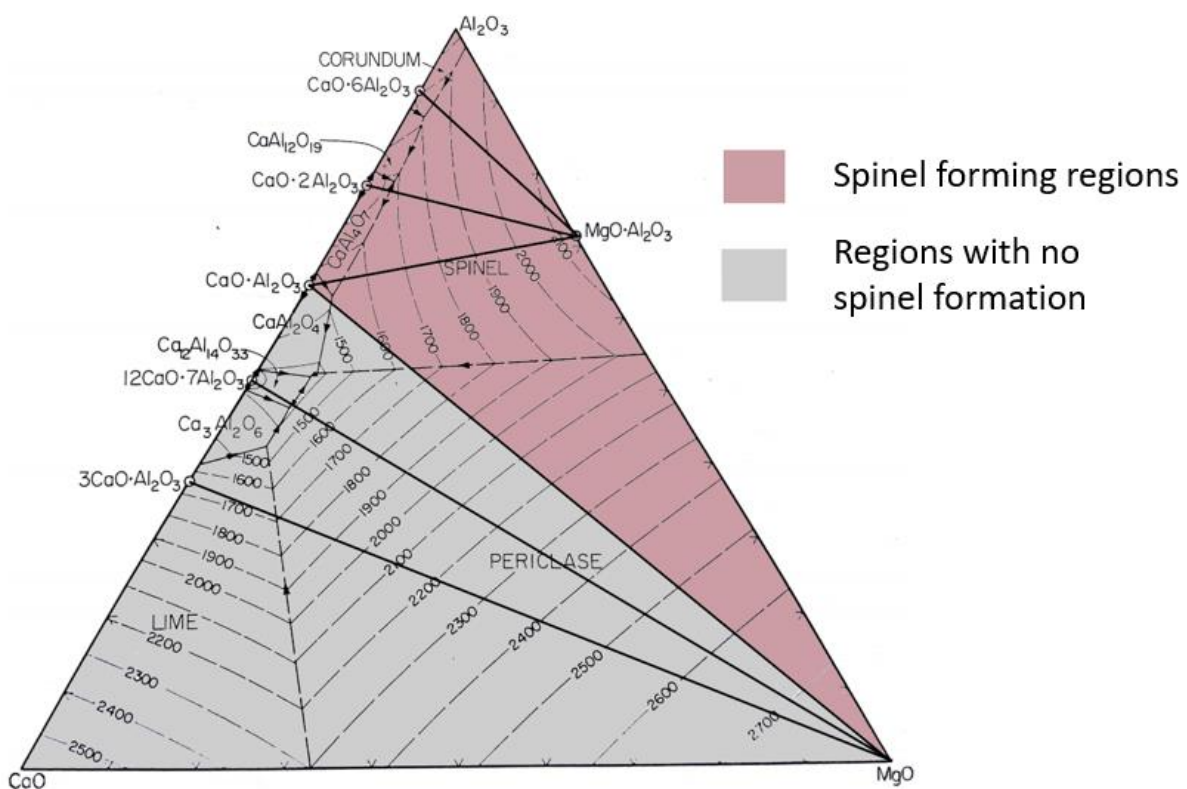


Figure 2.7: Alkemade triangles indicating the phases which will form at room temperature.

The work from Vermaak and Pistorius (2000) indicated a low amount of V_2O_3 in the slag at low basicity ratios, which is the result of a high V_2O_3 activity coefficient at low basicity values. Using low basicity values will however have adverse effects, such as a high viscosity which will result in slow reaction rates and a high amount of metal droplets being entrained. Metal droplets in the slag require both time and a net downward force to separate from the slag. The terminal velocity of the droplet will decrease as the viscosity increases due to increased drag forces exerted on the droplet. The results from Vermaak and Pistorius (2000) do however show that low amounts of V_2O_3 formation is possible at higher basicity values ($CaO: Al_2O_3 > 1.2$). Higher basicity values will result in slags of lower viscosities, but with higher slag

volumes, which implies that the separation distance for metal droplets in the slag will increase.

The question that arises is if the decrease in viscosity would offset the increase in slag volume. The possibility of achieving less metal entrainment and a higher activity coefficient of V_2O_5 in the slag, is worth investigating, with the possibility that the benefit of both these factors can outweigh the increased operational costs of adding more flux (in the form of both MgO and CaO).

The addition of MgO to the process would also decrease the wear of the MgO bricks. The addition of a sufficient amount of MgO to the process would saturate the slag in MgO, thereby terminating MgO brick dissolution into the slag. The suggested slag composition is shown in Figure 2.8. Within the suggested composition range the slag will be saturated in MgO, and spinel formation will not occur.

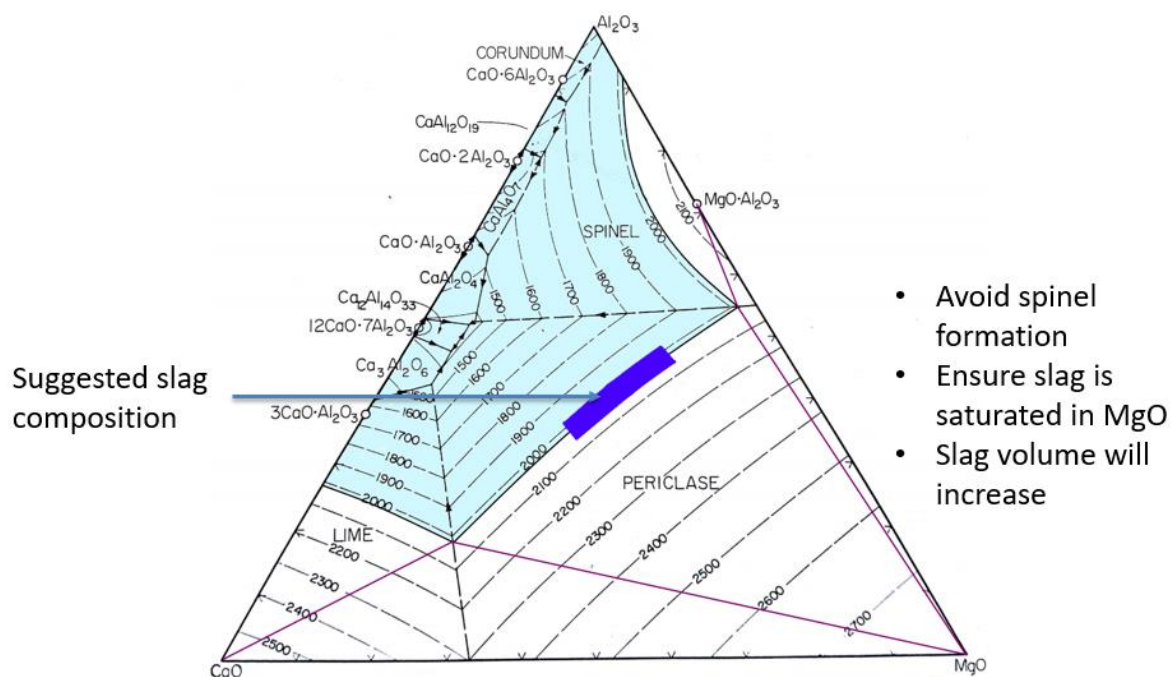


Figure 2.8: 2050°C isotherm projected onto the Al_2O_3 -CaO-MgO phase diagram, indicating where MgO slag saturation will occur.

Metal droplet entrainment can also contribute significantly towards vanadium losses to the slag. Metal droplet entrainment is largely affected by the droplet size and slag viscosity, as explained by Stokes's equation. It would therefore be beneficial to obtain larger metal droplets that settle faster than smaller droplets, which can be obtained by increasing the metal droplet interaction within the slag. The droplet interaction can be increased by decreasing the slag volume and by decreasing the slag viscosity. A low slag viscosity will also increase the droplet settling rate.

2.9 Conclusions

During ferrovanadium production vanadium is lost to the slag where it either reports to a spinel phase or is entrained in the slag as ferrovanadium droplets. The activity of V_2O_3 in the slag is dependent on the basicity of the slag. Ferrovanadium inclusions are dependent on both the metal droplet size, viscosity of the slag, as well as the distance the droplets have to travel in order to separate from the slag (slag volume is therefore important). The MgO-CaO- Al_2O_3 ternary phase diagram can be used to determine a slag composition where spinel formation is avoided, which can result in a decrease in vanadium losses to the slag (if the other phases formed have a lower V_2O_3 capacity). Adding MgO as a raw material in order to achieve MgO saturation of the slag will also reduce the refractory wear.

Chapter 3: Project aim and experimental design

3.1 Design of experiments

3.1.1 Response, factors and levels

Post mortem analysis done indicated that refractory wear is present due to insufficient magnesia present in the slag. The first test type conducted therefore entailed the magnesia content being varied and the two factors chosen were where the slag was not saturated in magnesia and where it was saturated, with the response being refractory wear.

From the literature study it was evident that spinel formation influences the recovery of vanadium and therefore the spinel content was varied, with the response being vanadium recovery.

Increasing vanadium recovery (response) by using a two stage process was also investigated, with the aluminium added in the first stage and iron oxide being added in the second stage being varied.

3.1.2 Test types

1. Refractory wear
2. Relation between spinel formation in the slag and vanadium recovery
3. Two stage smelting process

3.1.3 Factors for each test type

Test type 1: Slag composition (varied)

Test type 2: Slag composition (varied), aluminium added to the reaction (constant)

Test type 3: Slag composition (constant), aluminium added to the reaction (varied)

3.1.4 Levels for each test type

Test type 1

Table 3.1: Slag compositions for the slag-refractory interaction tests.

MgO (wt %)	Al ₂ O ₃ (wt %)	CaO (wt %)	Designation
2	82	16	A
8	78	14	B

Test type 2

Table 3.2: Slag compositions for the tests where the effect of spinel formation in the slag on the vanadium recovery was evaluated (varied).

MgO (wt %)	Al ₂ O ₃ (wt %)	CaO (wt %)	Designation
8	78	14	D
14	68	18	E
28	52	20	F
25	41	34	G

Table 3.3: Aluminium content in the metal for the tests where the effect of spinel formation in the slag on the vanadium recovery was evaluated (constant).

Aluminium (wt %)	Designation
1.5	D, E, F, G

Test type 3

Table 3.4: Slag composition for the two stage melting process tests (constant).

MgO (wt %)	Al ₂ O ₃ (wt %)	CaO (wt %)	Designation
8	78	14	C

Table 3.5: Aluminium content in the metal for the two stage melting process tests (varied).

Aluminium (wt %)	Designation
1.5	C1
3.5	C2
5.5	C3

3.1.5 Response

Test type 1: Extent of refractory wear

Test type 2: Vanadium recovery, spinel formation (also vanadium content of spinel)

Test type 3: Vanadium recovery

3.1.6 Measurement of responses

Test type 1 was analysed using SEM-EDS analysis. The extent of chemical interaction with the refractory was determined by analysing predetermined regions of the refractory. The regions analysed were at different distances from the slag-refractory interface. The same regions of the two different tests were then compared with each other in order to determine the extent of refractory wear and slag penetration. Additionally, the extent of chemical interaction between the slag and the refractory was also analysed and compared between samples.

The metal recovery was determined by separating the metal from the slag and then determining the mass of metal recovered versus the expected metal mass that should have formed. The vanadium recovery could then be determined knowing the composition of the metal.

The metal formed (ferrovanadium) was recovered by manually crushing the metal-slag sample and then separating the metal droplets by hand. Manual crushing (with a hammer) allowed for the slag to be crushed, while the metal droplets remained intact as it had a very high hardness. The metal droplets were round in shape which made them easy to separate from the slag by hand. Metal droplets were identified based on shape and hardness. Spherical shapes were identified using the naked eye and also by tilting the sample holder, allowing any spherical shapes to roll and therewith separate from the rest of the sample. The spherical shapes were then pressed on with a hammer, if the piece broke then it was an indication it was slag and not metal. Metal droplets that were too small to identify and separate using this method was accounted for as metal droplet entrainment in the slag. This would result in an under estimation of the metal recovery.

In order to determine the vanadium recovery as a function of spinel formation, both the vanadium recovery and the spinel content in the slag was determined. The vanadium recovery was determined by hand separation of the metal droplets as described in the previous paragraph concerning vanadium recovery. The spinel content of the slag was determined using a combination of SEM-EDS analysis and ImageJ. Using SEM-EDS analysis, low magnification electron backscatter images could be taken in order to obtain a 2-dimensional image showing the regions covered by the various phases. The area covered by the spinel phase could then be determined using the quantification function of ImageJ, where a phase can be isolated using the greyscale threshold function, where after the area of that phase could be determined. XRD analysis was also used to determine the spinel content of the slag samples.

3.1.7 Randomisation

In order to decrease the effect of noise factors, the order in which the tests were done was randomised (Table 3.6 and Table 3.7). Randomising the tests also reduces the tendency for biased analysis of the tests.

Table 3.6: Number allocation for the tests as defined in Table 3.1, Table 3.2 and Table 3.4.

Test number	Designated code
1	A
2	B
3	C1+D
4	C2
5	C3
6	E
7	F
8	G

Table 3.7: Random allocation of a run number to the various tests.

Test number	Run number	Designated code
1	2	A
2	1	B
3	4	C1+D
4	3	C2
5	5	C3
6	7	E
7	6	F
8	8	G

3.1.8 Blocking and controlling

The temperature and atmosphere inside the furnace was controlled in order to simulate industrial conditions. The temperature was controlled by continuous measurement using a pyrometer (the temperature was adjusted manually) and the atmosphere was controlled using argon gas (purity Ar \geq 99.997%).

3.2. Experimental setup

3.2.1 Furnace setup

Induction heating was used to heat the samples to the required temperature (1800°C). The power was supplied using a 15 kW Ecoheat power supply. The temperature was measured using an optical pyrometer and the temperature was controlled by manually changing the power input to the induction coil.

The furnace setup is shown in Figure 3.1. The furnace consisted of various refractory layers in the form of both MgO and Al₂O₃ refractories. The induction coil was made up of a copper coil which attached to the Ecoheat power supply. A quartz tube was used as a furnace shell in order to obtain a gastight environment, which allowed for the experiments to be conducted in a controlled atmosphere. The quartz tube also had the advantage of being transparent and therefore the inside of the furnace was visible while the experiments were conducted (the sample itself could not be seen, but the refractories around the sample could be inspected).

Steel plates were used to close the top and bottom of the furnace, with high temperature rubber being used to obtain a gastight seal between the quartz tube and the steel plates. The steel plates were designed to house the pyrometer holder at the top and also allow for a gas outlet at the bottom. The pyrometer holder housed the pyrometer and also had a gas inlet which was situated below the pyrometer. The pyrometer holder design has the advantage of having gas flowing away from the lens of the pyrometer, which enhances the view of the sample, ensuring accurate measurement of the temperature.

The MgO refractory in the centre of the furnace also served as a stage onto which the test samples were placed. The test setup for the different tests varied and is therefore explained in 3.2.2.

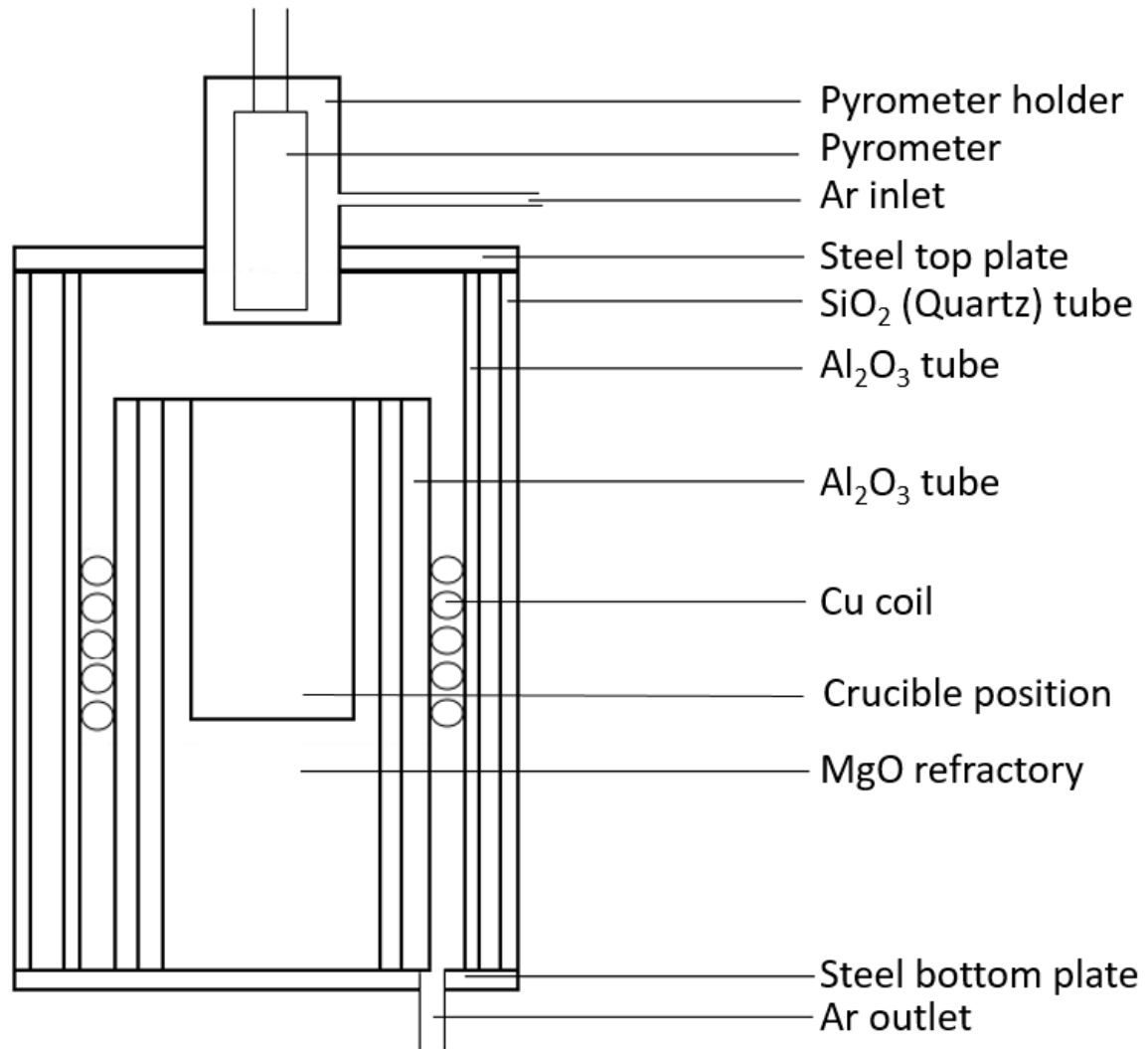


Figure 3.1: Induction furnace setup used to conduct tests A-G.

Additional test work was done to support results obtained from test types 2 and 3. The tests entailed synthesising the slag compositions obtained from tests D-G, as the presence of V₂O₃ resulted in the formation of phases not present on the MgO-CaO-Al₂O₃ phase diagram. The synthesised slag mixtures were pelletized and placed inside an Al₂O₃ crucible (used as a sample holder). The sample was reacted in a vertical tube furnace at a temperature of 1400°C for 24 hours in order to reach equilibrium. The setup of the furnace is shown in Figure 3.2.

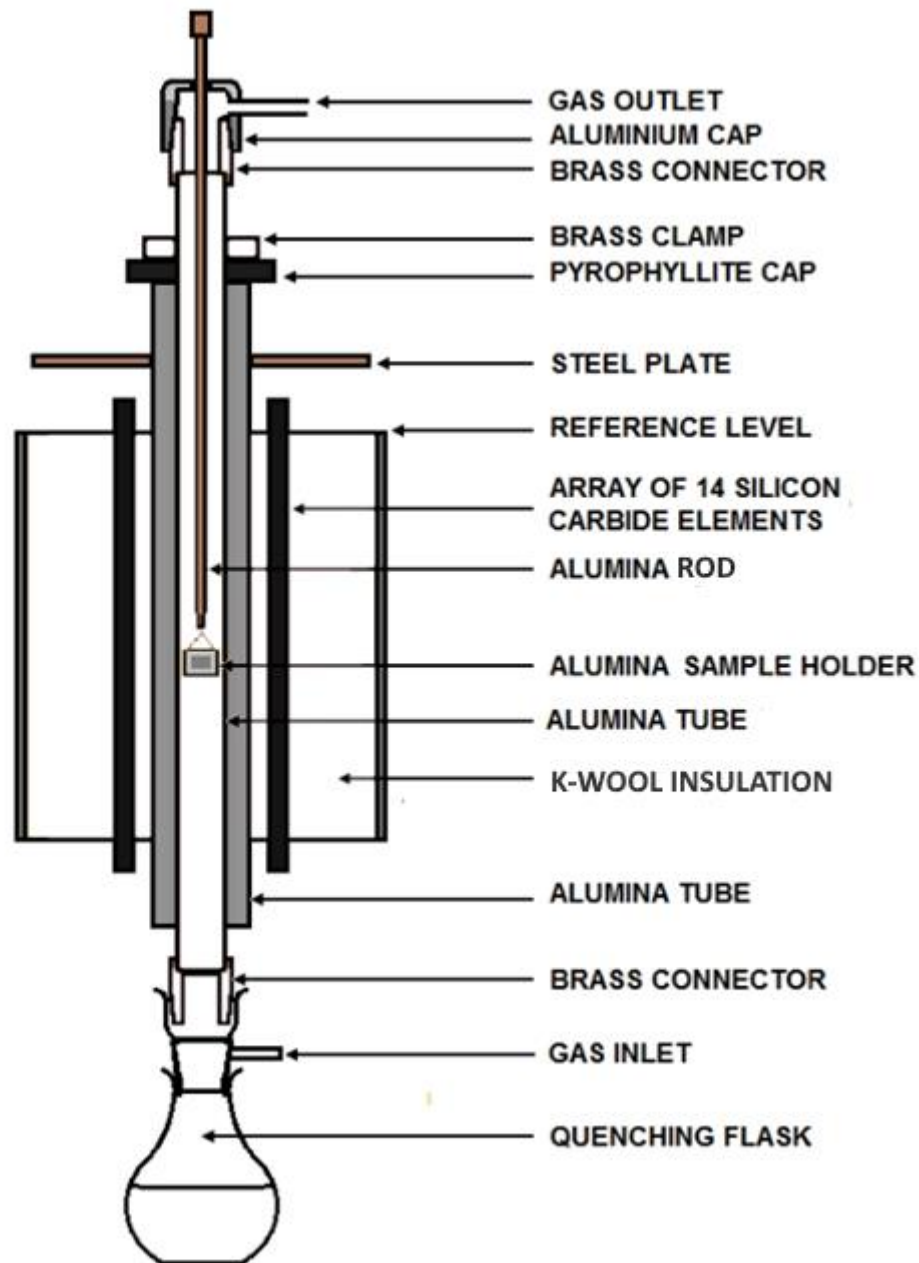


Figure 3.2: Furnace setup for the additional tests done to determine phase relations in the $\text{Al}_2\text{O}_3\text{-CaO-MgO-V}_2\text{O}_3$ system.

3.2.2 Test setup

The setup for the slag-refractory interaction tests is shown in Figure 3.3. Slag was pressed into a molybdenum crucible to fill a quarter of the crucible. A 15mm MgO refractory core was drilled using a core drill, which was then placed in the centre of the molybdenum crucible on top of the slag. The remainder of the slag was then added to the area surrounding the MgO crucible in order to ensure that a large area of the refractory was in contact with slag. The Mo crucible also served as the susceptor thereby producing the heat required for the tests.

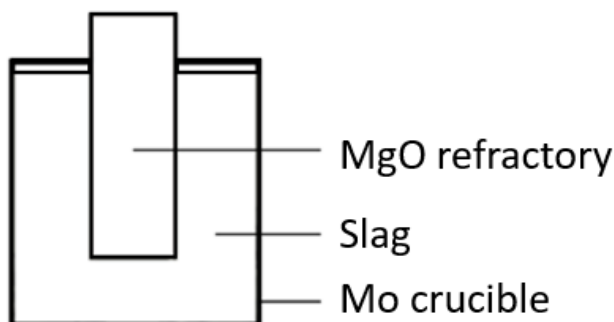


Figure 3.3: Test setup for the slag-refractory interaction tests.

The setup for the metal-slag interaction tests is shown in Figure 3.4. A mixture of V_2O_3 , aluminium, iron, MgO and CaO was placed inside a MgO crucible. The MgO crucible was then placed in the centre of the stage of the furnace. A hollow molybdenum cylinder was placed over the MgO crucible (surrounding the outside of the crucible). The molybdenum cylinder acted as a susceptor, producing heat in order to heat the test sample to the required temperature.

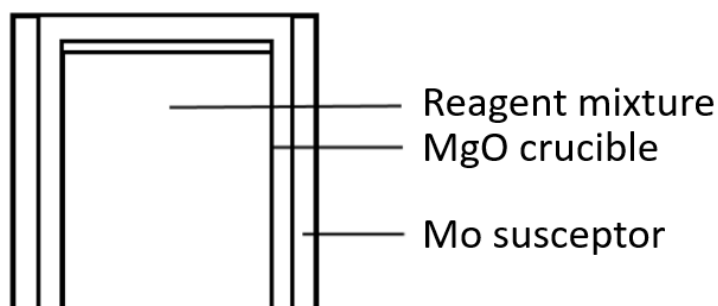


Figure 3.4: Test setup for the metal-slag interaction tests.

3.2.3 Raw materials

The raw materials that were used for the experiments are:

- $MgCO_3$
- $CaCO_3$
- $Al(OH)_3$
- V_2O_5
- Aluminium
- Iron

The $MgCO_3$, $CaCO_3$ and $Al(OH)_3$ were converted to MgO, CaO and Al_2O_3 respectively at $1300^\circ C$ for 3 hours in a muffle furnace before being used in the experiments. V_2O_5 was reduced to V_2O_3 at $650^\circ C$ in an atmosphere containing 4% hydrogen and 96 % argon. The time at temperature for the V_2O_5 reduction reaction was 8 hours and the reduction was carried out in a retort furnace. The conversion of V_2O_5 to V_2O_3 was confirmed using XRD analysis.

3.2.4 Experimental procedure

The test samples were prepared according to the compositions described in Section 3.1. The test sample was placed inside the furnace with the setup as explained in the Sections 3.2.1 (Furnace setup) and 3.2.2 (Test setup). The furnace was purged with Ar before the test commenced and a constant flow of Ar was supplied to the furnace throughout the tests (0.1 l/min). The test samples were heated at an average rate of 10°C/min (controlled manually) and also cooled at a rate of 10°C/min. All tests were conducted at a temperature of 1800 °C. The holding time for the slag-refractory interaction tests was 50 minutes and for the metal-slag interaction tests 2 hours.

3.3 Sampling

3.3.1 Slag samples from a ferrovanadium smelter

Industrial slag was sampled by dipping a steel rod into the slag through the inspection hole. Two samples were taken in order to obtain enough slag for the analysis. The samples were taken from the top part of the slag and about 1 m from the lining. Two samples were taken (samples 1 and 2) in a similar manner.

3.3.2 Post-mortem refractories samples from a ferrovanadium smelter

Refractory samples were taken from the DC arc furnace before it was relined. Two MgO bricks (one at the slag/refractory interface and one at the metal/refractory interface) and a MgO-C brick (situated above the slag line and tap hole) were taken. The samples were then sectioned in order to do an analysis of the profile of the bricks from the hot face to the cold face. The layout of the refractory bricks inside the DC arc furnace used on a South African plant is shown in Figure 3.5.

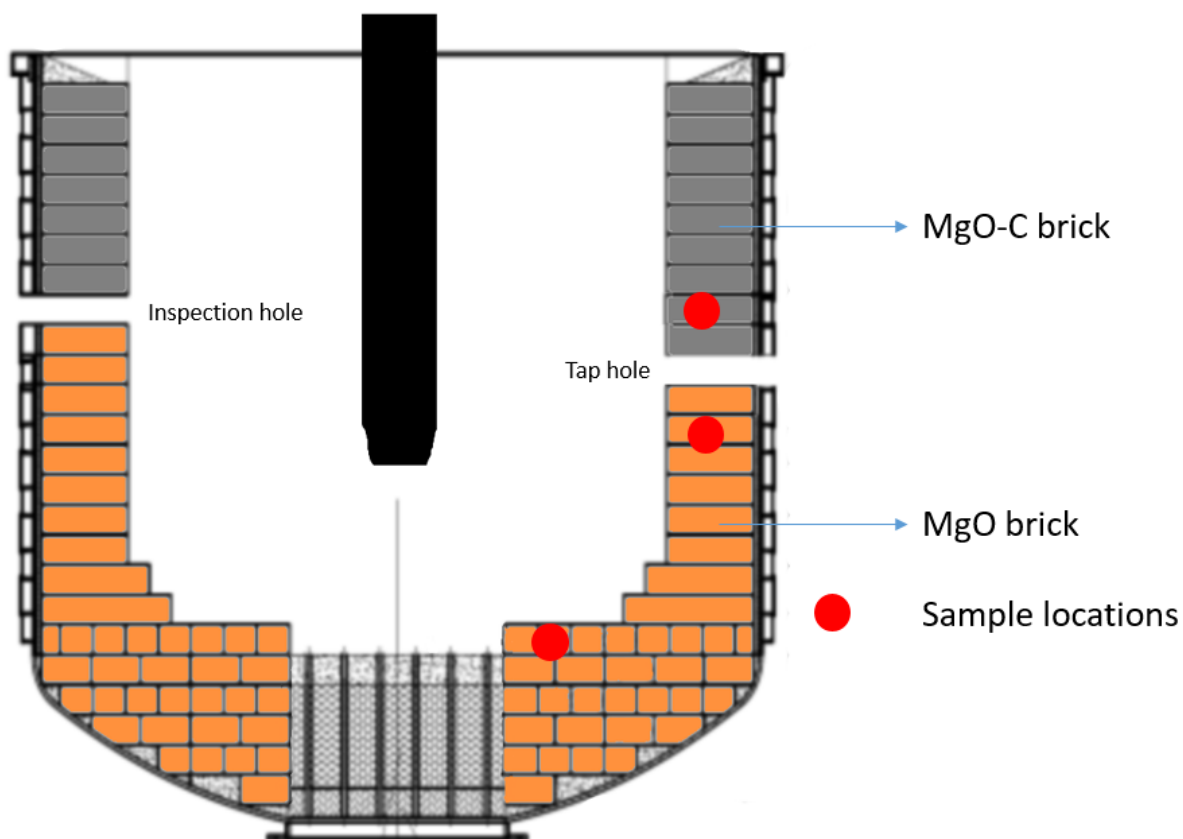


Figure 3.5: Schematic diagram of the lining design.

3.4. Sample analysis

3.4.1 XRF analysis

The samples were milled in a tungsten-carbide milling pot to achieve particles sizes below 75 μm . The samples were dried at 100°C, mixed with PVA binder and pressed in an aluminium cup at a pressure of 10 tons. XRF analysis was performed on a Thermo fisher ARL Perform'X Sequential XRF instrument, using OXSAS software.

3.4.2 XRD analysis

The samples were prepared according to the standardized Panalytical backloading system, which provides nearly random distribution of the particles.

The samples were analyzed using a PANalytical X'Pert Pro powder diffractometer in θ - θ configuration with an X'Celerator detector and variable divergence- and fixed receiving slits with Fe filtered Co-K α radiation ($\lambda=1.789\text{\AA}$). The mineralogy was determined by selecting the best-fitting pattern from the ICSD database to the measured diffraction pattern, using X'Pert Highscore plus software.

The relative phase amounts (weight% of crystalline portion) were estimated using the Rietveld method.

3.4.3 SEM-EDS analysis

After the slag-refractory interaction tests the crucibles were sectioned through the length of the sample, mounted in resin, ground and polished down to 1 μ m using a polishing machine. The polished sample was then coated with carbon using a carbon coater. The sample was then analysed using a Jeol JSM-IT300LV scanning electron microscope at 15kV fitted with an Oxford X-Max 50 EDS analyser. Areas to be analysed were identified, where after an electron backscatter image was taken of the area. The various phases present in the area were identified on the electron backscatter image, after which they were analysed using EDS.

3.4.4 Metal recovery

Metal recovery in the metal-slag interaction tests were prepared by removing the MgO crucible from the metal and slag using a diamond blade cutting machine. The sample was then crushed, by using a hammer, down to a top size of 1 mm diameter. The metal droplets did not break and were separated from the slag using hand separation (the metal droplets were round and could easily be identified using the naked eye). Metal droplets that were too small to be separated by hand were accounted for as metal droplets that were entrained in the slag. The mass of the metal droplets of each test was weighed (along with the mass of slag) and the vanadium metal recovery was calculated.

The metal droplets and slag were divided into two samples in order to conduct XRD and SEM-EDS analysis. The SEM samples were placed in a plastic ring and a resin mixture was added to the ring. After the resin had set, the sample was ground and polished down to 1 μ m. The samples were then analysed using SEM-EDS analysis. The XRD samples were pulverised to -50 μ m using a pulveriser, after which Si was added (known quantity) in order to determine the amount of MgO-Al₂O₃-CaO glassy phase present in each sample. The samples were then submitted for quantitative XRD analysis.

Chapter 4: Post mortem analysis of industrial slag and refractory samples

4.1 Post-mortem slag analysis

Post-mortem slag samples were taken at the end of the melting cycle, just before tapping the furnace content, in order to determine the composition of the slag as well as the phases present. The sample was taken through an inspection hole with a sampling rod. Only a small part of the top layer of slag could be sampled due to the size and position of the inspection hole.

4.1.1 Analysis using a CaO-Al₂O₃-MgO ternary phase diagram

The expected slag composition was calculated from the reagent ratio used in the industrial process (the addition of fettling material was not considered), while the actual slag composition was determined using SEM-EDS and XRD. The calculated slag composition as well as the analysed slag composition are shown in Figure 4.1. There was a significant difference between the calculated slag composition and the analysed slag composition. The analysed slag contained 21.8 wt % MgO, although MgO was not included in any of the raw material except the fettling material (Table 4.1). The increase in MgO content can be explained by examining the 2020 °C isotherm of the Al₂O₃-CaO-MgO system (Figure 4.2).

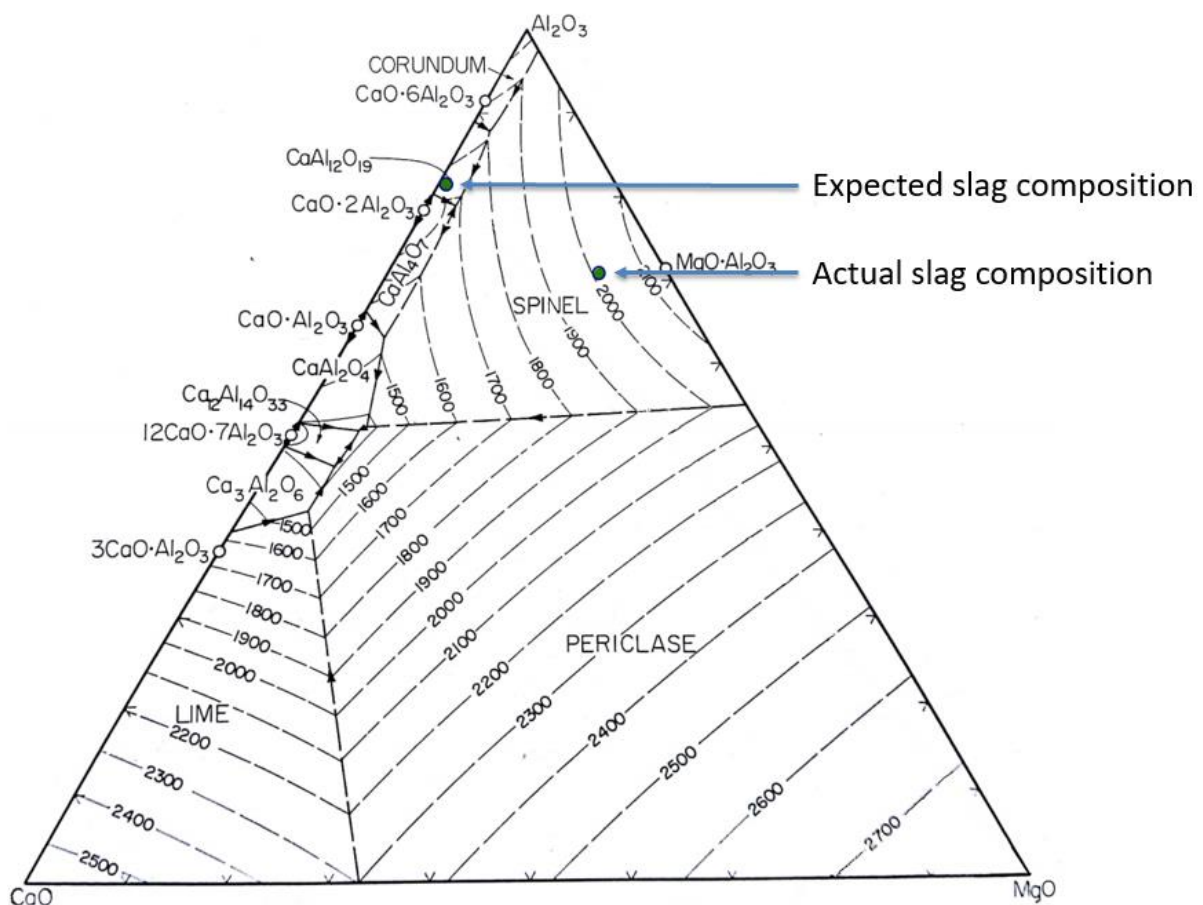


Figure 4.1: Representation of the estimated and analysed slag compositions on a CaO-Al₂O₃-MgO ternary phase diagram.

Table 4.1: Composition of the fettling material used in the industrial process.

Compound	Amount (wt %)
CaO	7.9
Fe ₂ O ₃	1.6
MgO	76.0
SiO ₂	1.4
Al ₂ O ₃	12.2
V ₂ O ₅	0.6
C	0.3

The change in slag composition from the expected slag composition to the actual slag composition is shown in Figure 4.2 (the 2020°C isotherm of the CaO-Al₂O₃-MgO system). The green line indicates the expected path along which the composition change occurred. The line emphasises the significant amount of MgO that dissolves into the slag. At a temperature close to 2000°C, the slag requires 21 wt % MgO in order to be saturated in MgO·Al₂O₃ (if the starting composition is that of the estimated slag). The slag does not contain MgO initially, but because it is in contact with MgO refractories, it will dissolve the refractory until the slag is saturated with MgO·Al₂O₃. This explains the aggressive refractory wear observed. Refractory wear can therefore be reduced by adding MgO as a raw material.

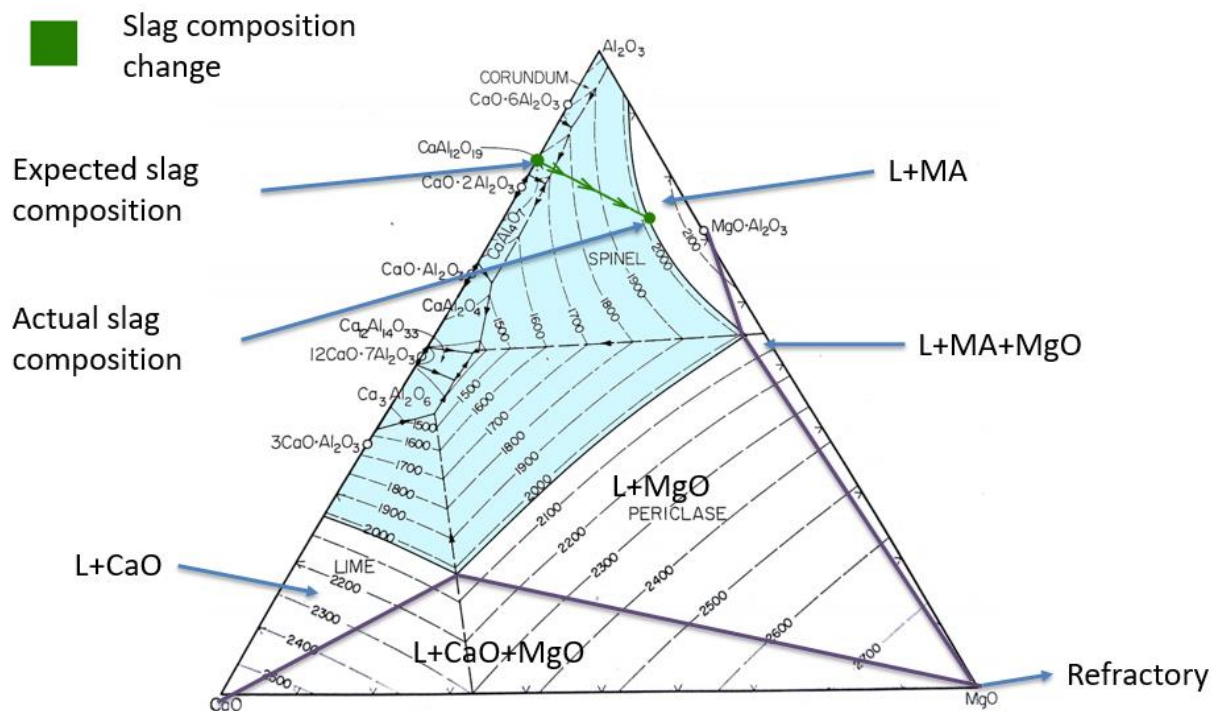


Figure 4.2: 2020°C isotherm of the CaO-Al₂O₃-MgO system.

The main concern with MgO addition as a raw material is that it results in the formation of the MA spinel phase, which is the main reason for vanadium losses in the form of V_2O_3 (V^{3+} substitutes for Al^{3+}). The slag will however be constituted of a certain minimum amount of MgO (enough to achieve saturation), irrespective of the amount of MgO added. It would therefore not be advisable to add less MgO (as a raw material) than would be required to achieve MgO saturation of the slag.

Using the MgO-CaO- Al_2O_3 ternary phase diagram, regions can be identified where the spinel phase will not form upon cooling (Figure 2.7). Identifying regions where the spinel phase does not form provides an opportunity to reduce vanadium losses to the slag, if the new phase(s) that form have a lower tendency to host V_2O_3 .

4.1.2 XRD-analysis

XRD analysis of the slag samples indicated that the slag consisted of the phases spinel ($MgAl_2O_4$), krotite ($CaAl_2O_4$) and grossite ($CaAl_4O_7$), while a glassy phase was also detected. (Table 4.2). The glassy phase was calculated by adding a predetermined amount of Si to the sample. The glassy phase contained MgO, Al_2O_3 and CaO as determined using SEM-EDS analysis. It is important to note that the spinel and glass contains MgO despite no MgO being added as a raw material. The MgO content of these phases is due to slag attack of the magnesia based refractory.

Table 4.2: XRD results of slag sample.

Phase	Stoichiometry	Quantity (wt %)	3- σ error
Spinel	$MgAl_2O_4$	57.6	0.90
Krotite	$CaAl_2O_4$	7.5	0.77
Grossite	$CaAl_4O_7$	14.3	0.89
Glassy	CaO-MgO- Al_2O_3	20.6	2.13

4.1.3 SEM-EDS analysis

SEM-EDS analysis was done in order to verify the phases identified by the XRD results. The backscatter electron image in Figure 4.3 and Figure 4.4 correspond with the observations from the optical analysis. It is evident that 3 crystalline phases were present in the slag. Using EDS analysis (SEM-EDS results in the Appendix under 1 Post-mortem slag analysis), it was confirmed that $MgO \cdot Al_2O_3$ (MA spinel), $CaAl_2O_4$ (krotite) and $CaAl_4O_7$ (grossite) were present. The $MgO-Al_2O_3-CaO$ glassy phase was also confirmed using SEM-EDS analysis. Vanadium was present in the $MgAl_2O_4$ (2.4 wt%), $CaAl_2O_4$ (0.6 wt%) and $CaAl_4O_7$ (0.5 wt%) phases, but no vanadium was present in the CaO-MgO- Al_2O_3 glassy phase.

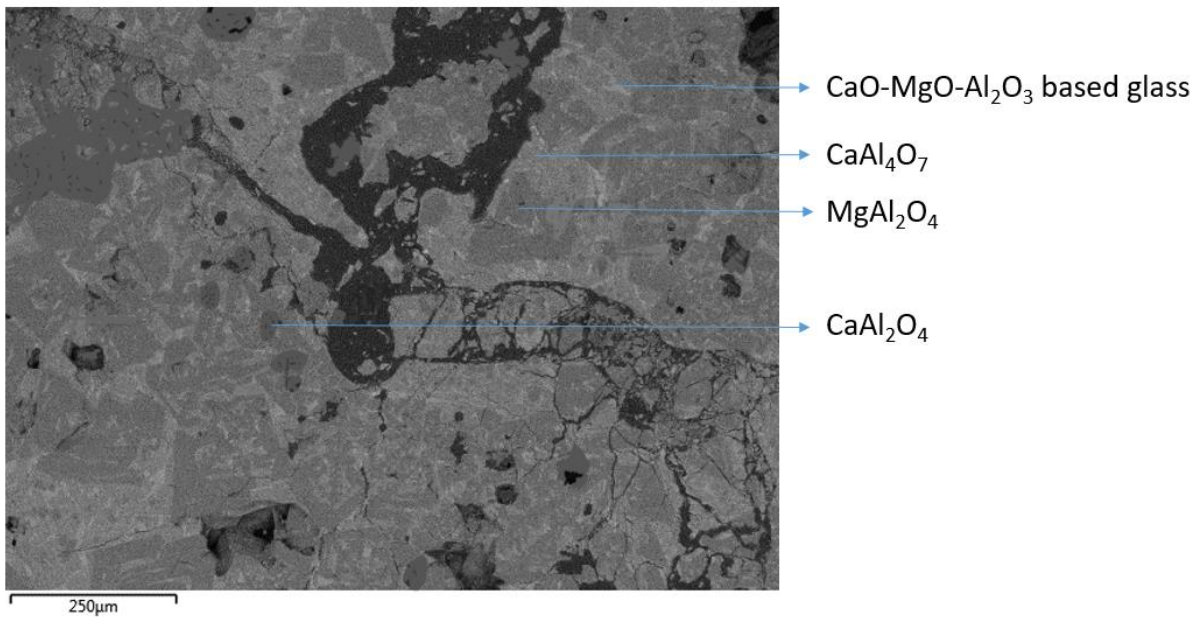


Figure 4.3: Backscatter electron image of slag sample.

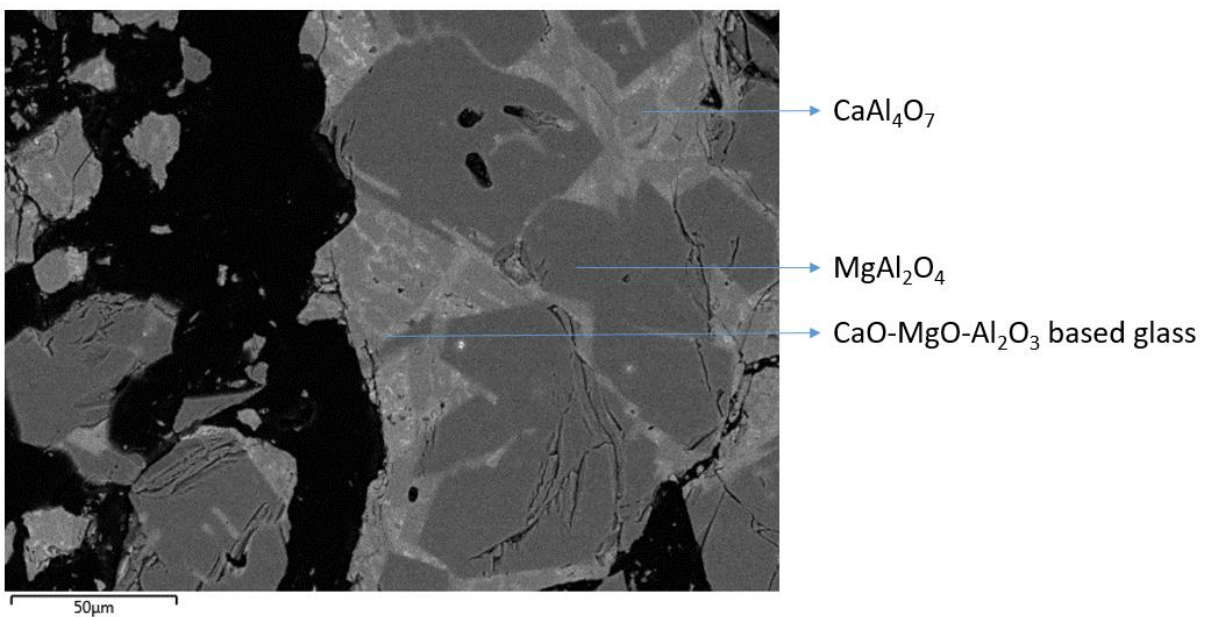


Figure 4.4: Backscatter electron image of slag sample.

The phases identified in the SEM-EDS analysis can be confirmed theoretically by drawing an Alkemade triangle around the composition locus on the CaO-MgO-Al₂O₃ phase diagram (as show in Figure 4.5). The endpoints of the Alkemade triangle indicate which phases are expected to be present after the slag has cooled down (equilibrium cooling) to room temperature. The theoretically identified phases coincide with the SEM-EDS analysis (being MgAl₂O₄, CaAl₂O₄ and CaAl₄O₇). The CaO-MgO-Al₂O₃ based glass is present in the SEM-EDS analysis due to non-equilibrium cooling conditions when the sample was taken (the sample was quenched in water).

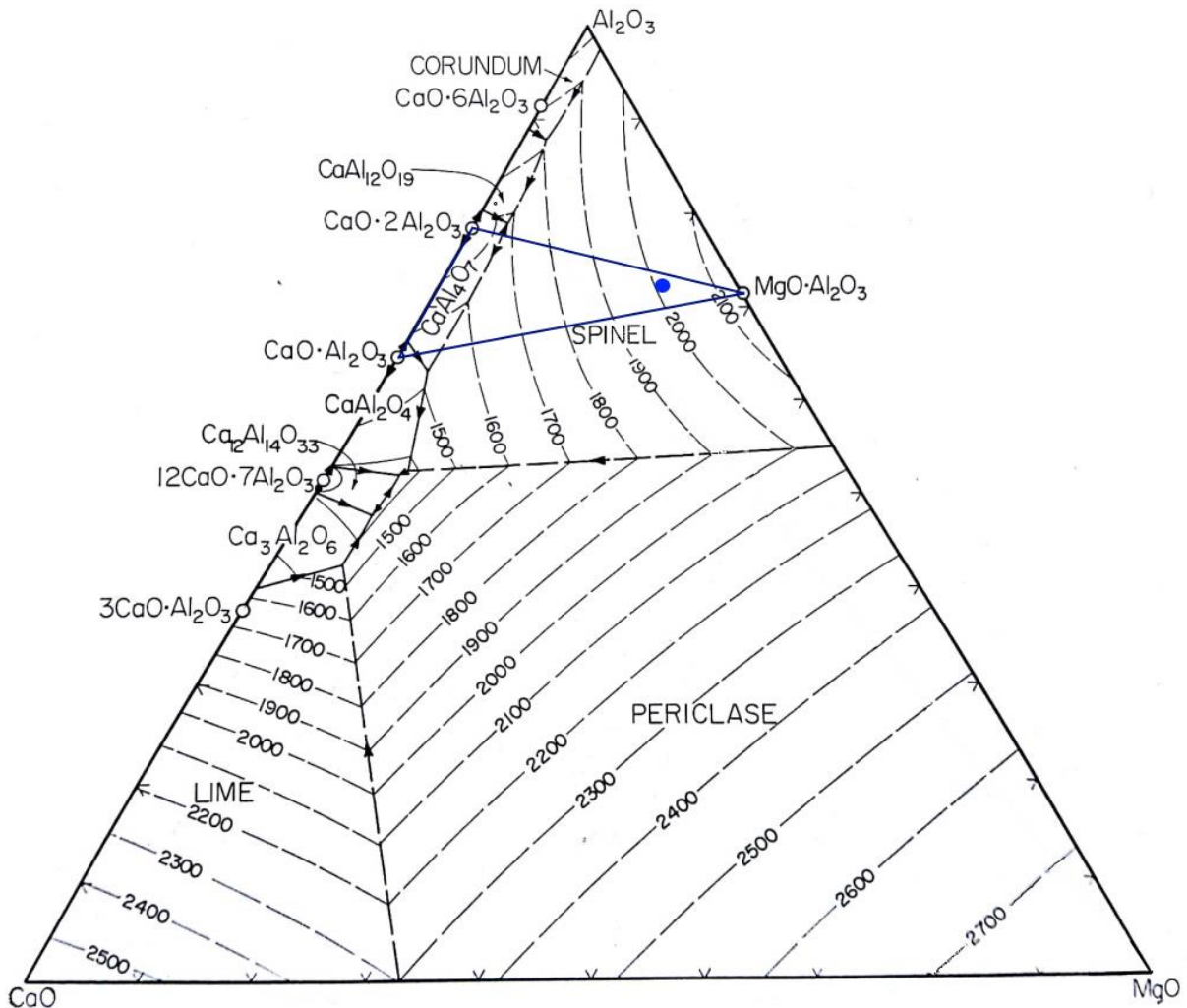


Figure 4.5: Plot of the slag composition on the CaO-MgO-Al₂O₃ ternary phase diagram.

Elemental analysis of the metal inclusions was also done. A backscatter electron image of a metal droplet is shown in Figure 4.6. From the image it is evident that two phases are present in the metal droplet. The elemental analysis indicated that the two phases present were the σ -ferrovanadium and α -ferrovanadium phases. The σ -ferrovanadium phase has a composition of 65.1 wt% vanadium; 34.9 wt% Fe and the α -ferrovanadium phase a composition of 98.1 wt% vanadium; 1.9 wt% Fe. The phase surrounding the metal droplet is the MA spinel phase. It is also important to note that the spinel phase has a vanadium content of 2.2 atom %, thus vanadium is present in the spinel phase. The vanadium (V^{3+}) substitutes the Al^{3+} ion in the spinel structure. Vanadium is therefore present in the form of vanadium in the metal inclusions and V^{3+} in the slag forming compounds.

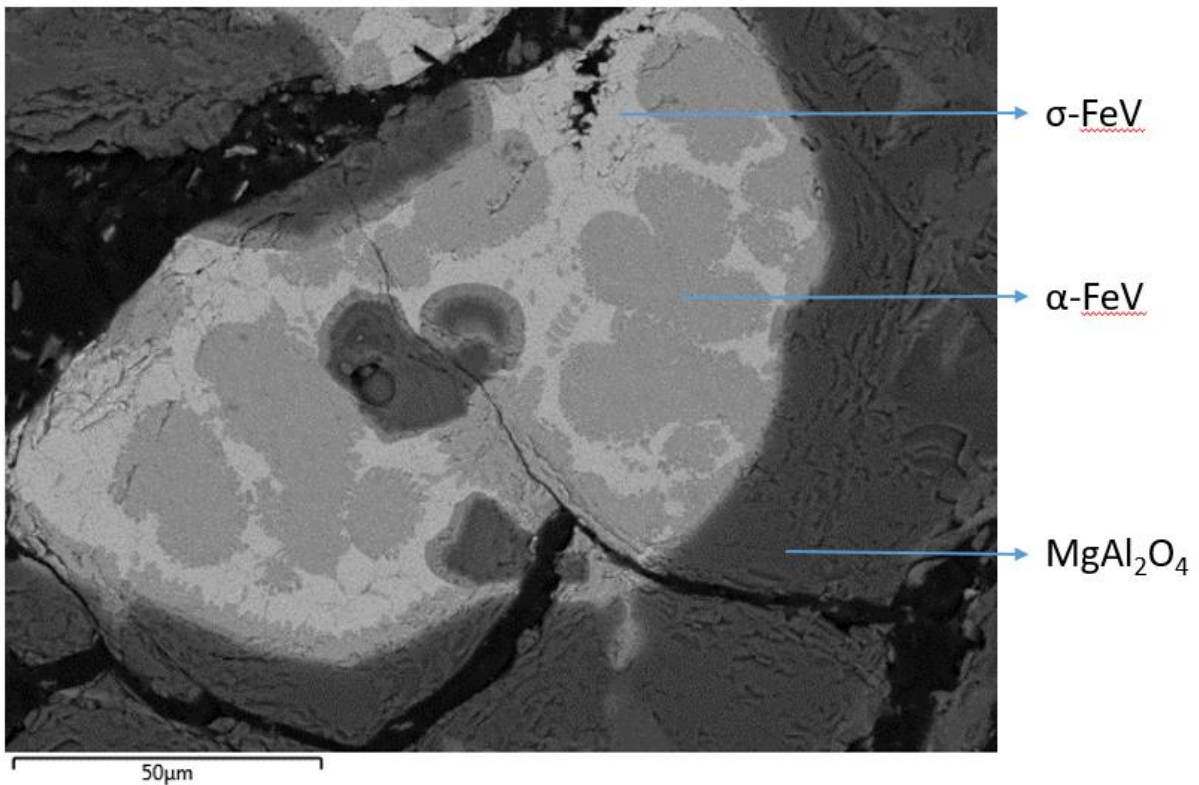


Figure 4.6: Electron backscatter image of a metal droplet inclusion in the slag.

4.2 Post-mortem refractory analysis

4.2.1 XRF results

Refractory samples were taken from the sampled refractory bricks that were in service. The profile across a magnesia brick which was in contact with the slag was taken, which consisted of 5 samples. The position of the samples relative to the hot and cold face is shown in Figure 4.7. There is also a change in colour of the refractory close to the hot face as shown in Figure 4.8.



Figure 4.7: Positions from where the magnesia brick samples were taken relative to the hot and cold faces.



Figure 4.8: Image of the hot face of the magnesia brick.

The MgO content across the brick is shown in Figure 4.9, with position 1 being the absolute hot face and position 5 being the absolute cold face. A sample was taken at the centre of each section and analysed. The MgO profile across the brick indicates that the MgO content in the brick decreases significantly from the cold face to the hot face, which indicated penetration of the slag into the brick. The presence of CaO and Al₂O₃ also indicates that slag penetration occurred (Figure 4.10).

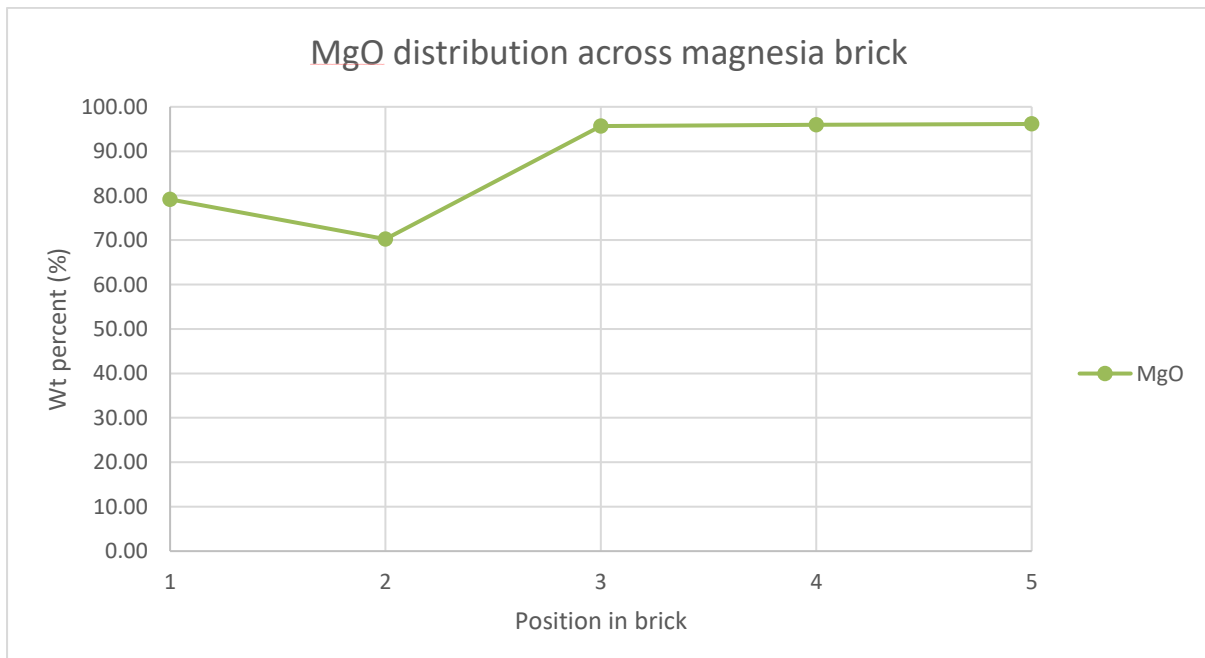


Figure 4.9: MgO profile from the hot face to the cold face of the brick.

The distribution of the two slag components Al₂O₃ and CaO across the magnesia brick is shown in Figure 4.10. The Al₂O₃ content is significantly higher at the hot face compared to the cold face and the same is true for CaO, indicating that a high amount of slag penetrated into

the refractories during the service life. The high amount of interaction present between the refractories and the slag is due to the slag being incompatible with the refractories (but the high operating temperature is also a contributing factor).

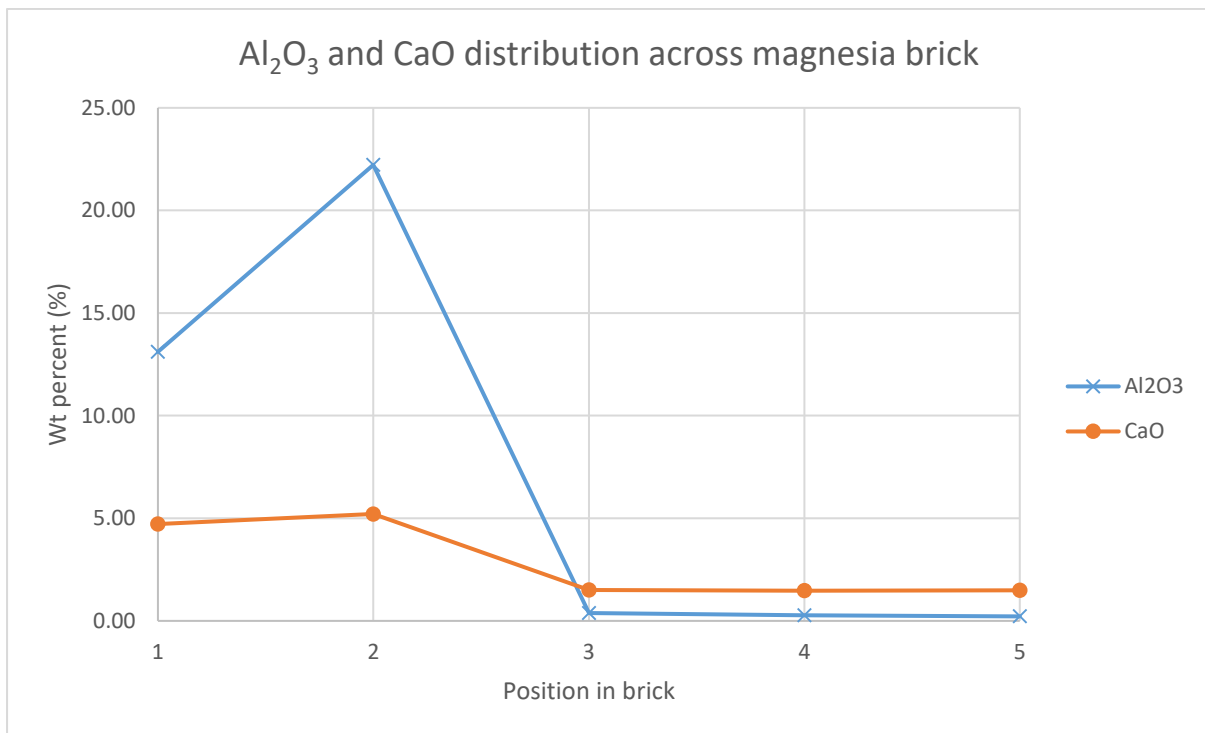


Figure 4.10: Distribution of Al₂O₃ and CaO across the magnesia refractory brick.

The distribution of vanadium and Fe across the brick was also analysed and yielded the results shown in Figure 4.11. The vanadium content is much higher at the hot face than at the cold face, indicating that vanadium also penetrated into the refractory together with the slag. Vanadium may also be present because of V³⁺ replacing Al³⁺ in the MgAl₂O₄ structure. Vanadium can also be hosted in other oxide phases and also go into solid solution with MgO (explained in subsequent sections). The form of the vanadium present at the hot face of the MgO brick cannot be determined from XRF results and require either XRD or SEM-EDS analysis. The change in iron content from the hot face to the cold face of the brick is not significant.

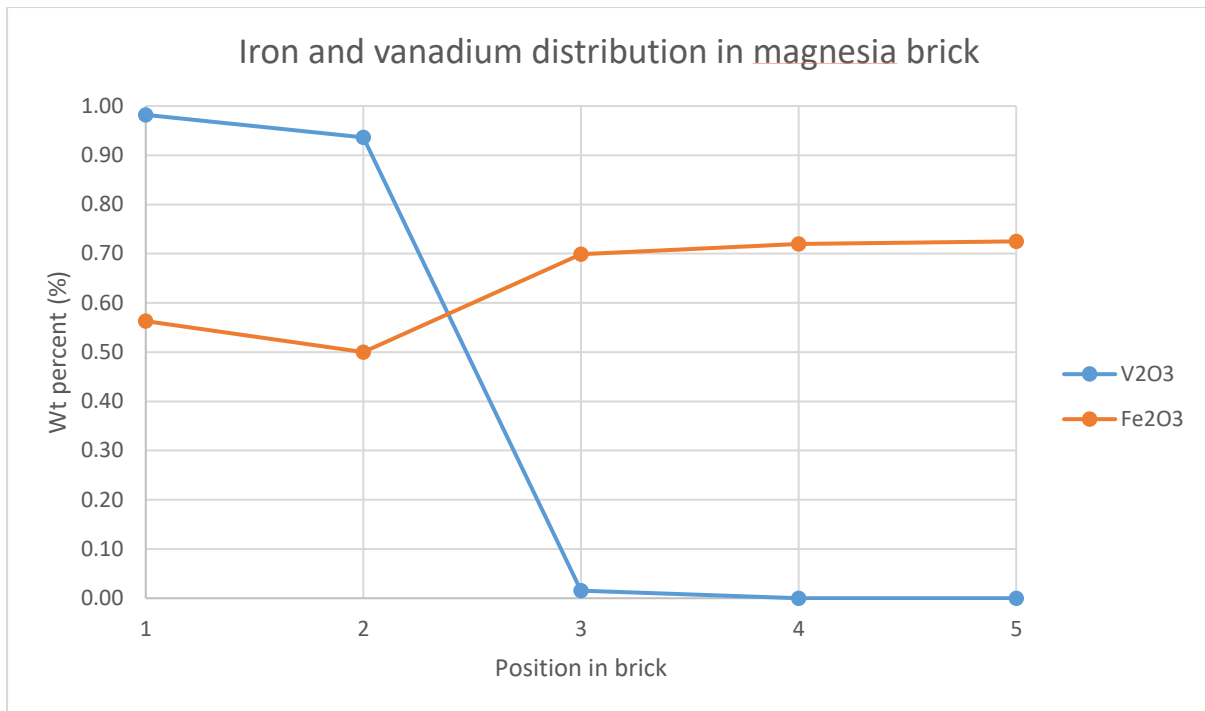


Figure 4.11: Distribution of vanadium and iron across the MgO brick.

A magnesia brick was also taken from the hearth of the furnace, where the metal is in contact with the MgO lining (bottom location in Figure 3.5). No significant chemical interaction or penetration was observed in the bottom MgO brick as can be seen in Table 4.3. The samples were taken from the centre of 3 sections, which are shown in Figure 4.12.

Table 4.3: XRF results of the MgO brick sample taken from the hearth of the furnace.

Component	Position			Brick specification
	1	2	3	
MgO (wt%)	94.49	95.72	95.77	96.5
Al ₂ O ₃ (wt%)	0.6	0.37	0.28	0.4
SiO ₂ (wt%)	1.25	1.11	1.2	0.6
CaO (wt%)	1.63	1.59	1.71	1.6
V ₂ O ₅ (wt%)	0.01	<0.01	<0.01	0
Fe ₂ O ₃ (wt%)	0.74	0.72	0.72	0.8
P ₂ O ₅ (wt%)	0.17	0.16	0.17	0

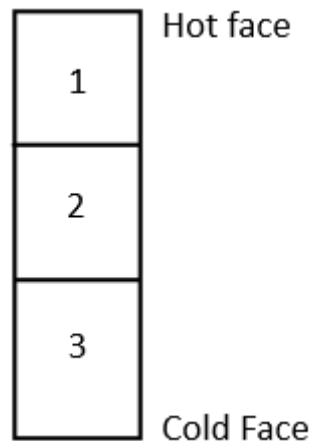


Figure 4.12: Orientation of the samples relative to the hot face.

The MgO-C refractory brick was taken in order to investigate the chemical wear of the bricks above the tap hole. The MgO-C bricks used were anti-oxidant free bricks. Visual inspection indicated that a layer had deposited onto the refractory. XRF analysis of the samples yielded the results shown in Table 4.4. The difference between the hot and cold face of the MgO-C brick is small, however, it can be noted that the MgO and CaO content has increased slightly whereas the other components have decreased slightly.

The deposited layer shown in Figure 4.13 therefore consists mainly of MgO, SiO₂, Al₂O₃ and CaO, resulting in the shift in composition as stated above. The deposited layer can be a result of the intensive mixing occurring inside the furnace, resulting in slag coming in contact with bricks above the tap hole. The carbon content at the hot face is also lower than the cold face due to the oxidising atmosphere present when raw materials are loaded into the furnace (the furnace roof is opened when raw materials are loaded).

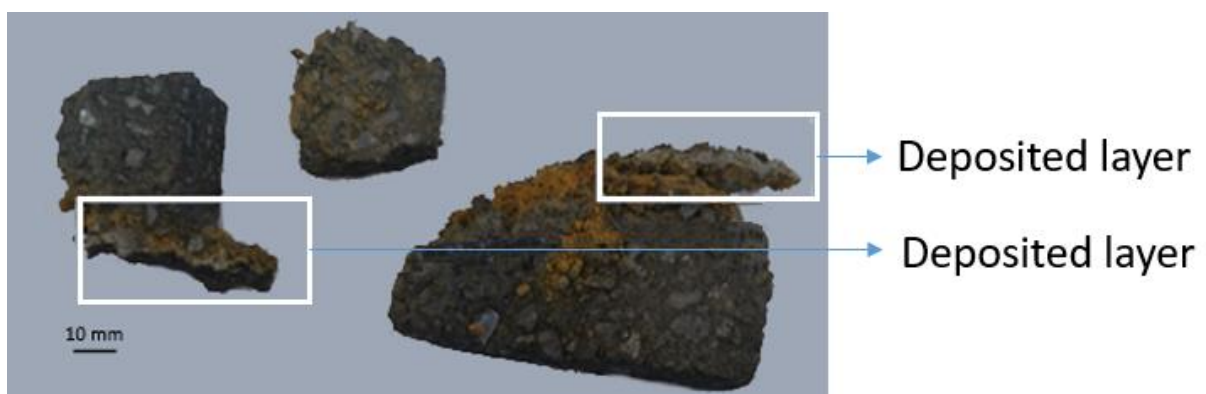


Figure 4.13: MgO-C refractory with deposited layer.

Table 4.4: XRF results of the hot and cold face of the MgO-C brick.

	MgO-C hot face	MgO-C cold face	Brick specification
MgO (wt%)	90.59	89.57	97.2
Al₂O₃ (wt%)	1.57	2.55	0.1
SiO₂ (wt%)	3.34	4.16	0.6
CaO (wt%)	2.38	2.18	1.5
V₂O₃ (wt%)	0.02	0.01	0
Fe₂O₃ (wt%)	1.00	1.13	0.6
P₂O₃ (wt%)	0.21	0.17	0

4.2.2 XRD results

4.2.2.1 MgO brick from the slag line

The XRD results of the MgO brick situated at the sidewall is shown in Table 4.5. The presence of mayenite ($\text{Ca}_{12}\text{Al}_{14}\text{O}_{33}$) and spinel (MgAl_2O_4) in sample 1 and sample 2 indicate that slag penetrated into the refractory. Considering the SEM-EDS results, it is evident that sample 2 was taken at the slag-refractory interface whereas sample 1 was taken further away from the hot face than sample 2. The XRD results for samples 1 and 2 support the SEM-EDS results, as sample 2 contained a higher amount of spinel and mayenite.

Table 4.5: XRD results of the MgO brick from the slag line.

	Periclase (MgO) %	Spinel (MgAl₂O₄) %	Mayenite (Ca₁₂Al₁₄O₃₃) %
sample 1	97.54	1.82	0.57
sample 2	73.69	23.03	2.82
sample 3	100.00		
sample 4	100.00		
sample 5	100.00		

4.2.2.2 MgO-C brick

The XRD results in Table 4.6 indicate a decrease in the graphite content at the hot face of the MgO-C brick. The decrease is presumably be the result of the graphite oxidising at the high operating temperature. The presence of spinel indicates that a small amount of slag was present at the hot face of the brick. Monticellite (CaMgSiO_4) is present due to SiO_2 and

CaO being present in the main raw material (magnesite) used for the production of MgO-C bricks. The low CaO/SiO₂ ratio in the brick results in the formation of a small amount of liquid at the operating temperature, which solidifies in the form of monticellite upon cooling.

Table 4.6: XRD results of the MgO-C brick situated above the tap hole.

	Periclase %	Spinel %	Graphite %	Monticellite (CaMgSiO ₄) %
Hot face	86.78	0.47	11.87	0.87
Cold face	80.59	0.00	19.41	

4.2.2.3 MgO brick from the hearth of the furnace

The XRD analysis of the samples from the three regions of the MgO brick situated at the bottom of the furnace is shown in Table 4.7. The results indicated that no significant interaction between the metal and the refractory had occurred, which is also supported by the SEM-EDS results.

Table 4.7: XRD results of the MgO brick taken from the hearth of the furnace.

	Periclase %
Sample 1	100
Sample 2	100
Sample 3	100

4.2.3 SEM-EDS analysis

The post mortem analysis on the refractory bricks included SEM-EDS analysis in order to identify the phases present and also to obtain high magnification images of the microstructures.

4.2.3.1 MgO brick situated in the slag line

The brick sampled from the side wall was analysed by sectioning the brick and then analysing the various areas of the brick. The locations of the various samples taken from the brick are indicated in Figure 4.14. The samples were taken in the centre of each region.

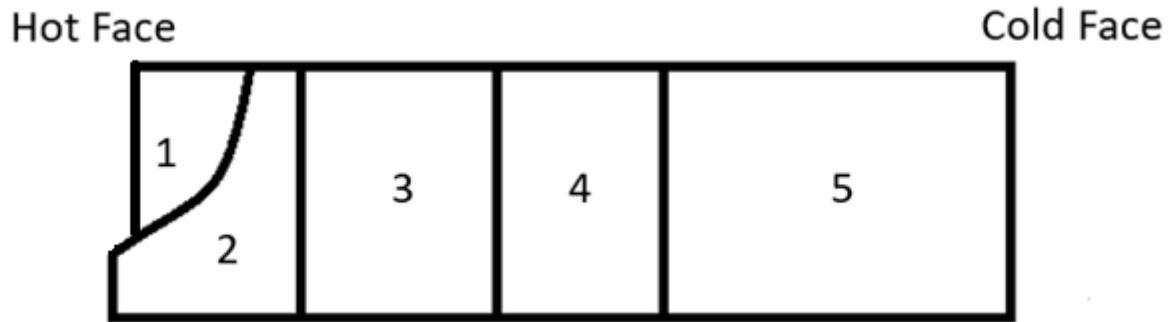


Figure 4.14: Position of the MgO samples relative to the hot and cold face.

The MgO cold face (sample number 5) indicates that the main phase present in the brick is MgO. A small amount of another phase is present, which consists of a combination of CaO, MgO and SiO₂ was identified as monticellite.

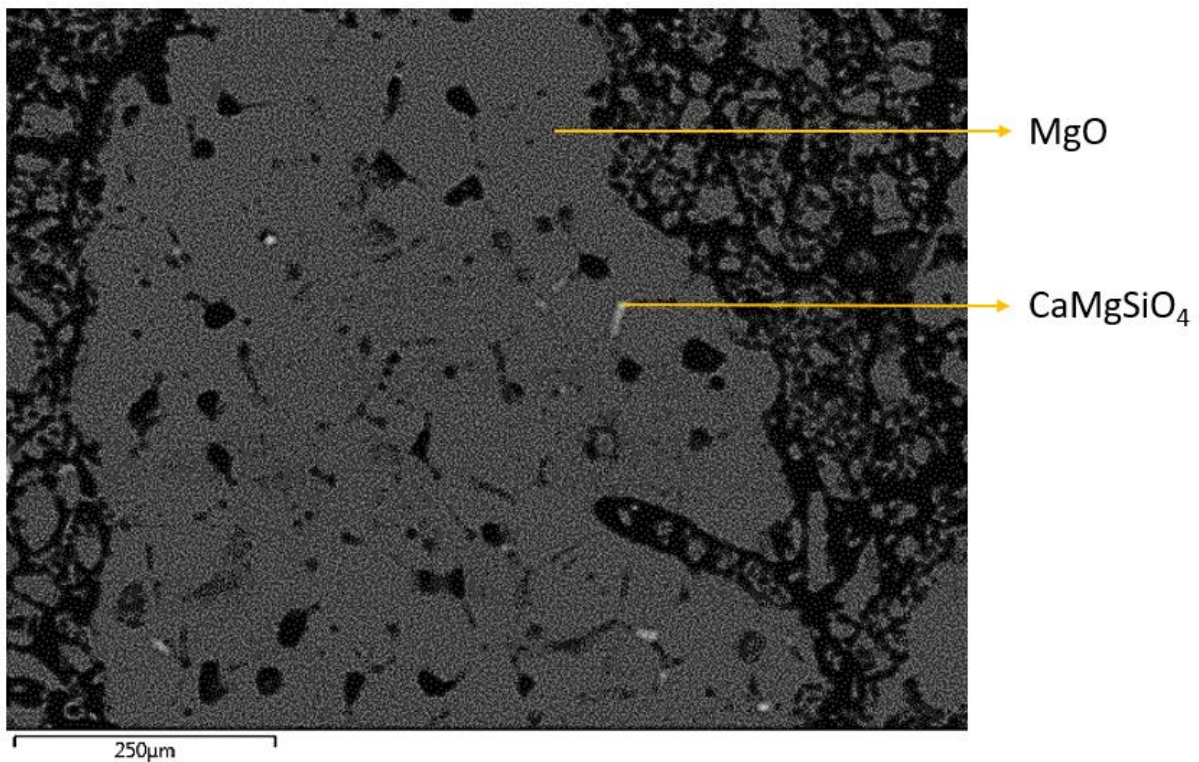


Figure 4.15: Backscatter electron image of the cold face of the MgO brick sampled from the slag line.

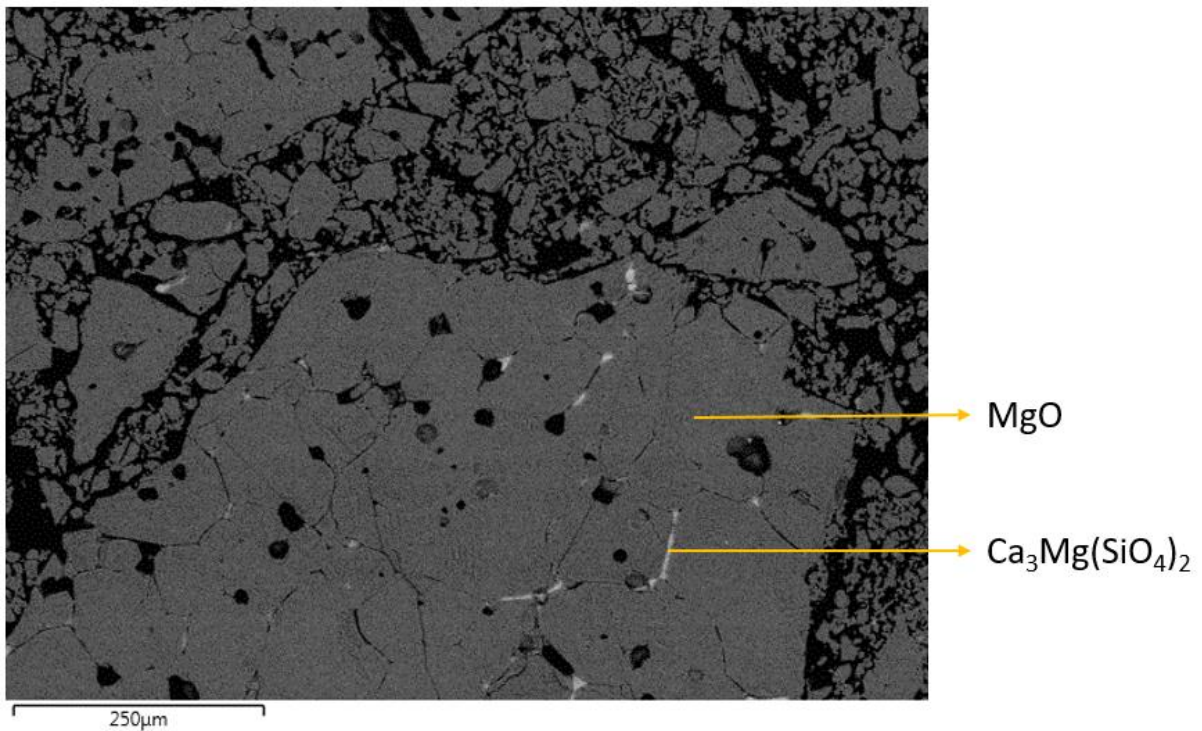


Figure 4.16: Backscatter electron image of sample 4 situated closer to the hot face than sample 5.

The MgO sample shown in Figure 4.17 was situated relatively near the hot face (sample 3). The analysis of the sample is similar to samples 4 and 5, with the MgO phase being the main phase present and an impurity phase ($\text{Ca}_3\text{Mg}(\text{SiO}_4)_2$) being present in small amounts.

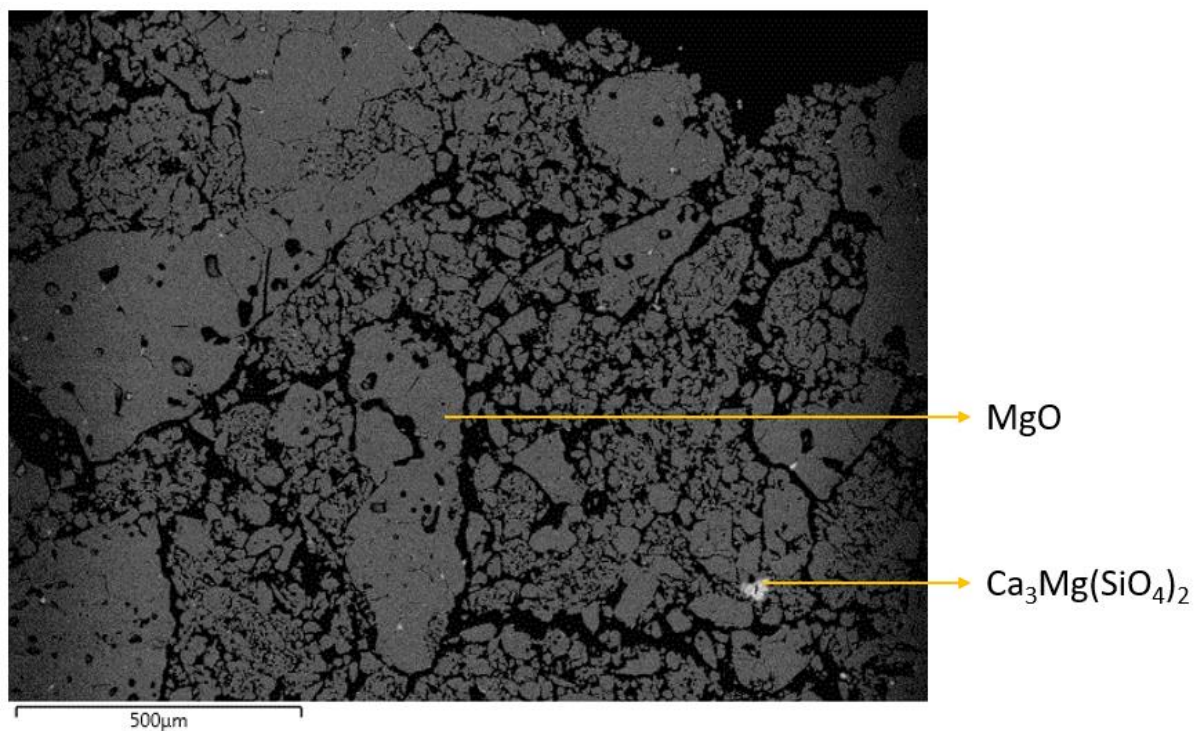


Figure 4.17: Backscatter electron image of sample 3 situated near the refractory zone that was affected by slag penetration.

Samples 1 and 2 were almost parallel to each other, with sample 2 having a different appearance than sample 1. It is evident from Figure 4.18 that sample 2 had a microstructure similar to that of the solidified slag. Refractory material dissolved in the slag, after which it combined with Al_2O_3 to form the MgAl_2O_4 spinel phase. Since the original slag contained no MgO, high refractory wear occurred due to the dissolution of MgO brick into the slag and the resulting formation of MgAl_2O_4 .

Metal inclusions were also present in the slag sample, which were analysed as being ferrovanadium. CaAl_2O_4 and CaAl_4O_7 are constituted of CaO and Al_2O_3 in different ratios, which also originated from the slag. Slag refractory interaction took place and formed an interfacial layer of MgAl_2O_4 between the slag and refractory.

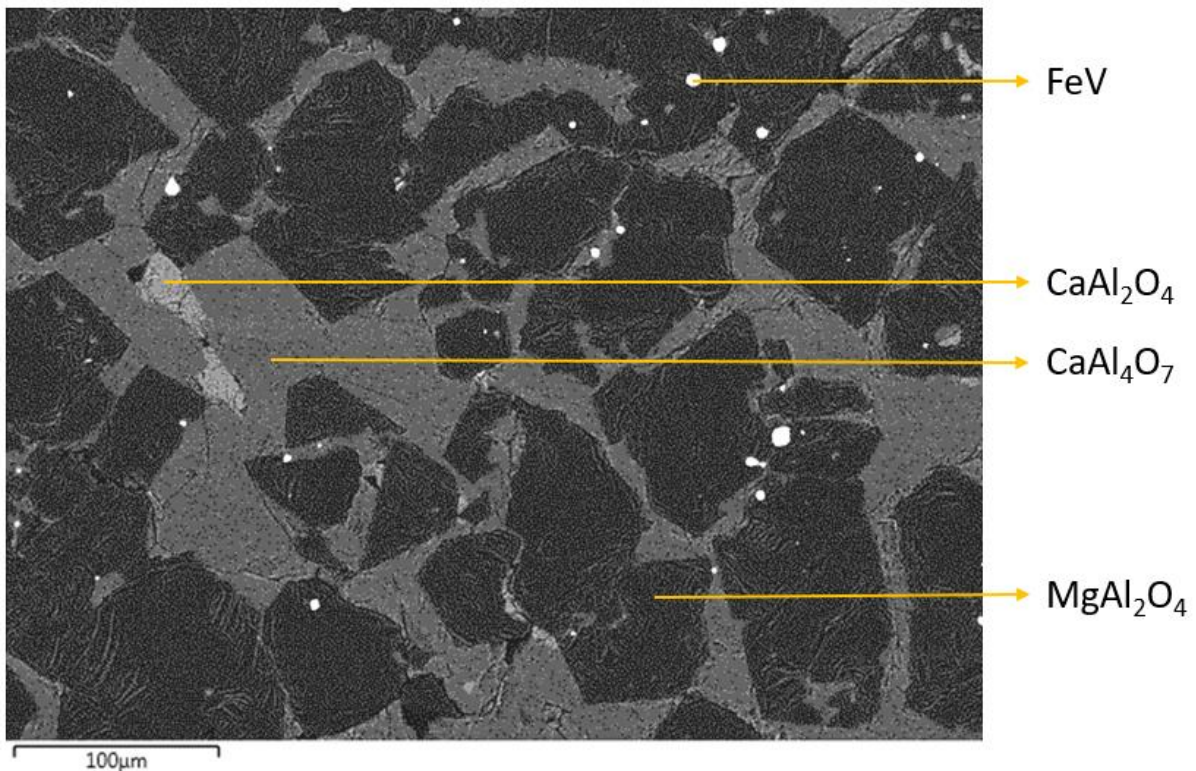


Figure 4.18: Backscatter electron image of the MgO hot face, situated at the slag-refractory interface, containing only slag (sample 2).

Another site of sample 2 that was analysed is shown in Figure 4.19. The analysis indicates that some refractory is still present (because of the presence of MgO), but that a high amount of slag is also present. Visual inspection suggests that the sample contained more slag than refractory, which indicated that a high amount of refractory wear occurred due to slag dissolving the refractory. The small amount of MgO present indicated that very aggressive refractory wear had occurred, which resulted in the eventual disintegration of the surface of the brick in contact with the slag. Metal inclusions are also present in the form of ferrovanadium.

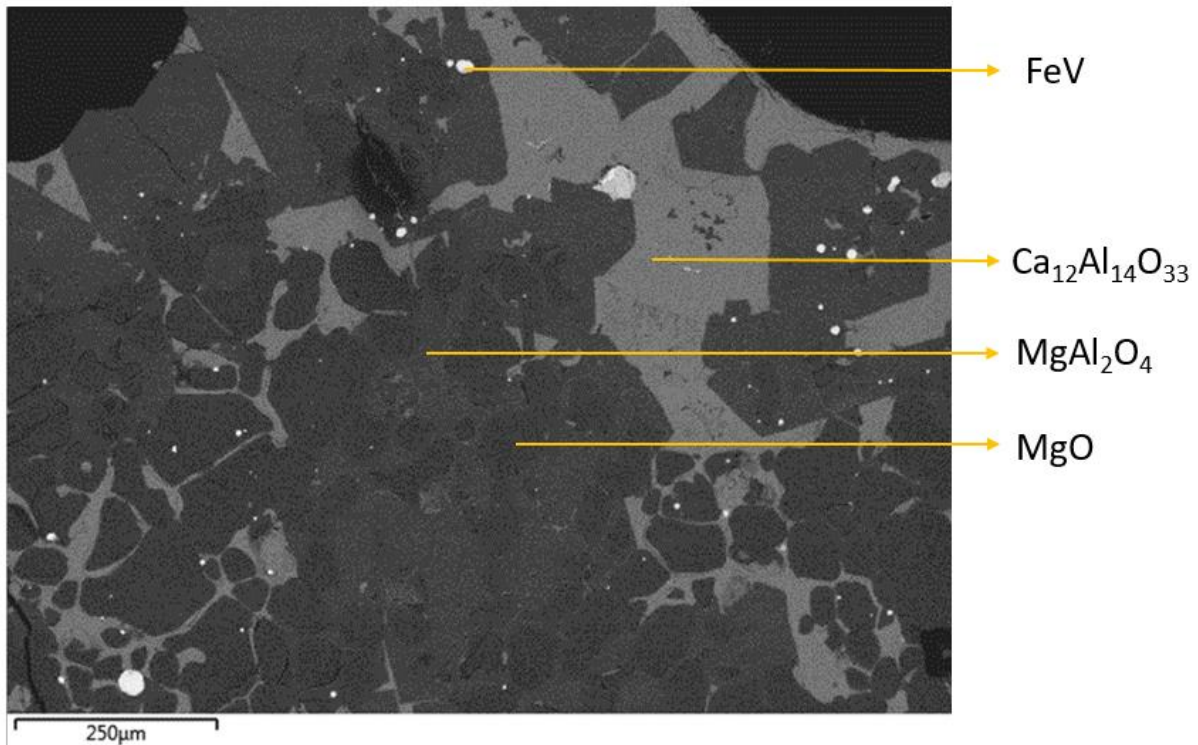


Figure 4.19: Electron backscatter electron image of the MgO hot face on the refractory side of the slag-refractory interface (sample 2).

The analysis of sample 1 is shown in Figure 4.20. The darkest phase present is the MgO refractory and the slightly lighter phase is MgAl_2O_4 (spinel). The small bright spheres are metallic inclusions. The presence of the spinel phase supports the hypothesis that slag penetrates into the refractory. Visual inspection of the electron backscatter image indicated that slag dissolved the matrix of the refractory first. The reason for the penetration phenomenon was a combination of the slag not being saturated in MgO and the matrix dissolving before the aggregate grains. The matrix is constituted of finer grains and will therefore dissolve faster into the slag.

Since the operating temperature exceeded the solidus temperature of the matrix of the brick (1800°C) a high amount of liquid formed in the matrix, through which the slag could penetrate into the refractory. The penetrating slag then reacted with the MgO grains to form MgAl_2O_4 , resulting in further refractory wear. The metal inclusions were present due to a high metal inclusion content in the slag, which then penetrated into the refractory with the liquid slag. The CaO-MgO- Al_2O_3 based slag that penetrated the refractory also formed $\text{Ca}_{12}\text{Al}_{14}\text{O}_{33}$ upon cooling. At the operating temperature the slag was saturated with MgO and MgAl_2O_4 .

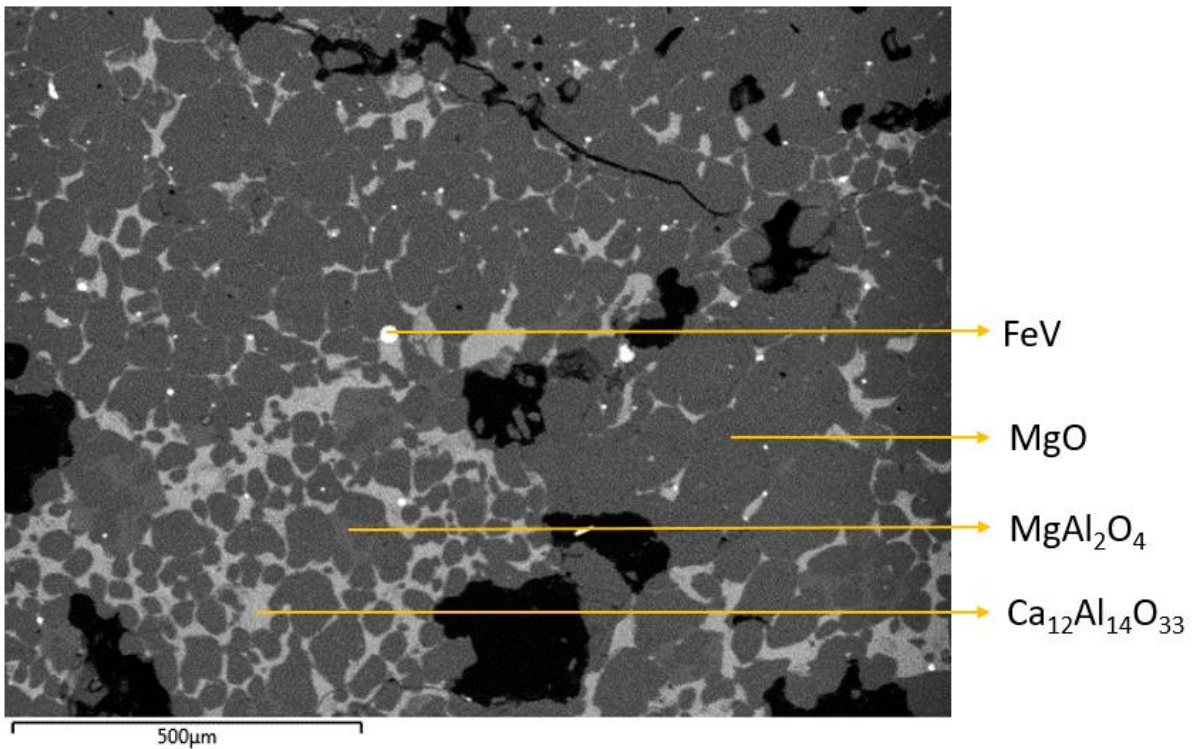


Figure 4.20: Electron backscatter image of MgO sample near the hot face (sample 1).

4.2.3.1.1 Summary of SEM-EDS results

The SEM-EDS analysis of the post mortem MgO brick is summarised in Table 4.8. Slag (CaO-Al₂O₃ – based) is present in samples 1 and samples 2, which confirms that slag penetration into the refractory brick occurred. Metal inclusions were also present in the refractory, which is the result of metal inclusions being present in the penetrating slag. The presence of MgAl₂O₄ suggested that a reaction occurred between the slag and the refractory. Merwinite (Ca₃Mg(SiO₄)₂) and monticellite (CaMgSiO₄) are impurity phases that are typically associated with magnesia bricks.

Table 4.8: Summary of the phases present in the post mortem MgO taken from the slag line.

	1 Hot face	2	3	4	5 Cold face
Phases	<ul style="list-style-type: none"> • MgO • MgAl₂O₄ • Ca₁₂Al₁₄O₃₃ • Ferrovandium 	<ul style="list-style-type: none"> • MgAl₂O₄ • MgO • CaAl₂O₄ • CaAl₄O₇ • Ferrovandium • Ca₁₂Al₁₄O₃₃ 	<ul style="list-style-type: none"> • MgO • Ca₃Mg(SiO₄)₂ • CaMgSiO₄ 	<ul style="list-style-type: none"> • MgO • Ca₃Mg(SiO₄)₂ • CaMgSiO₄ 	<ul style="list-style-type: none"> • MgO • CaMgSiO₄ • Ca₃Mg(SiO₄)₂

4.2.3.2 MgO brick from the hearth of the furnace

A MgO brick that was taken from the hearth of the furnace (that was in contact with the metal) indicated that MgO and small amounts of merwinite and monticellite were present. No evidence of metal penetration could be found.

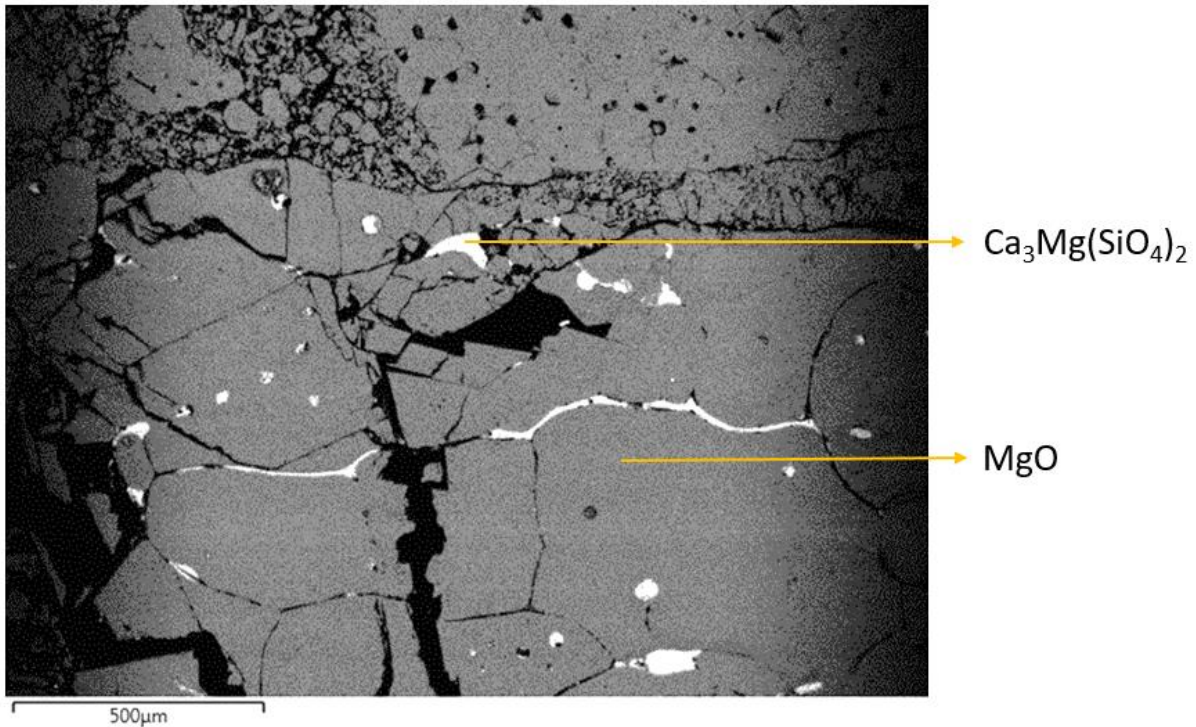


Figure 4.21: Backscatter electron image of the cold face of the MgO brick that was removed from the hearth of the furnace.

A backscatter electron image of the area between the hot face and cold face is shown in Figure 4.22. No evidence of metal penetration was present and the microstructure appears to be fully intact. There was however a small number of bright inclusions present, which was identified as being ZnS inclusions. The presence of ZnS may be a result of contamination during polishing.

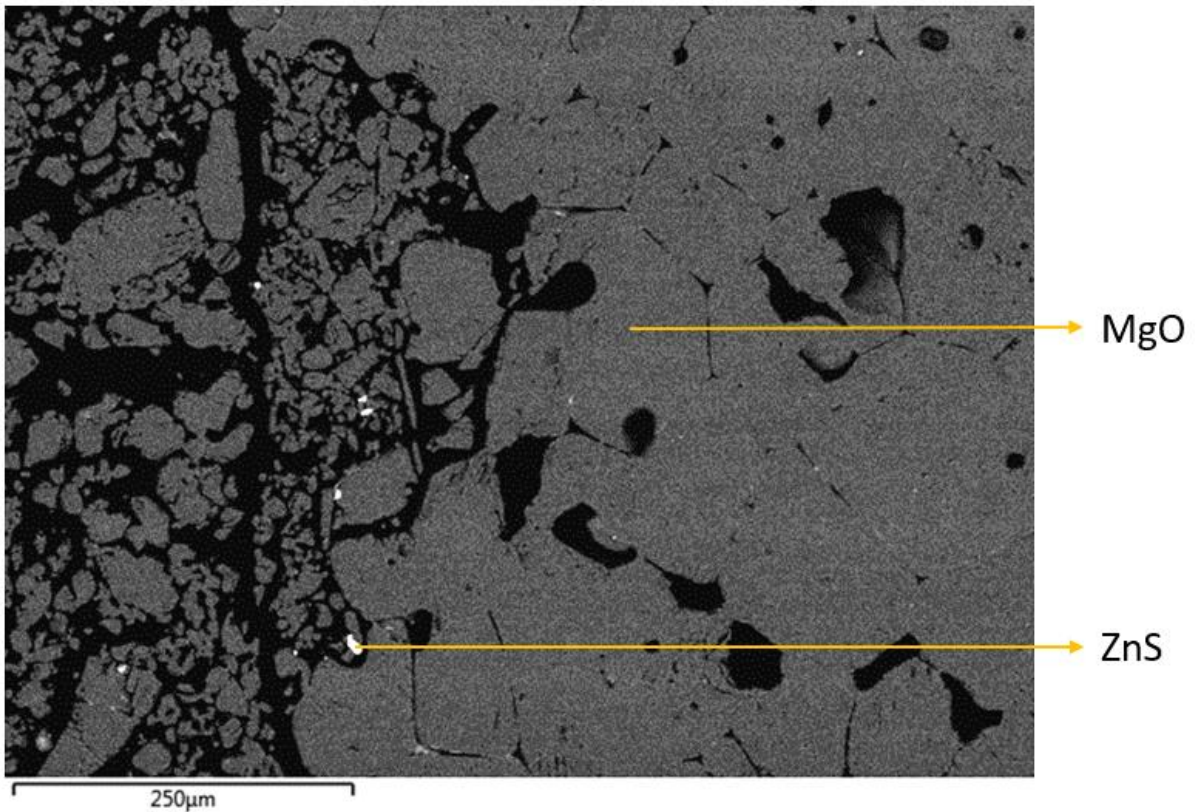


Figure 4.22: Backscatter electron image of the MgO brick removed from the hearth of the furnace.

The SEM-EDS analysis of the hot face (sample 1) indicated that MgO was present together with a small amount of a MgO-CaO-SiO₂ glassy phase. It is evident from Figure 4.23 that there was no penetration of metal into the refractory. The phases present at the hot and cold faces were identical and indicated that no metal penetration occurred at the bottom of the furnace and therefore very little refractory wear occurred.

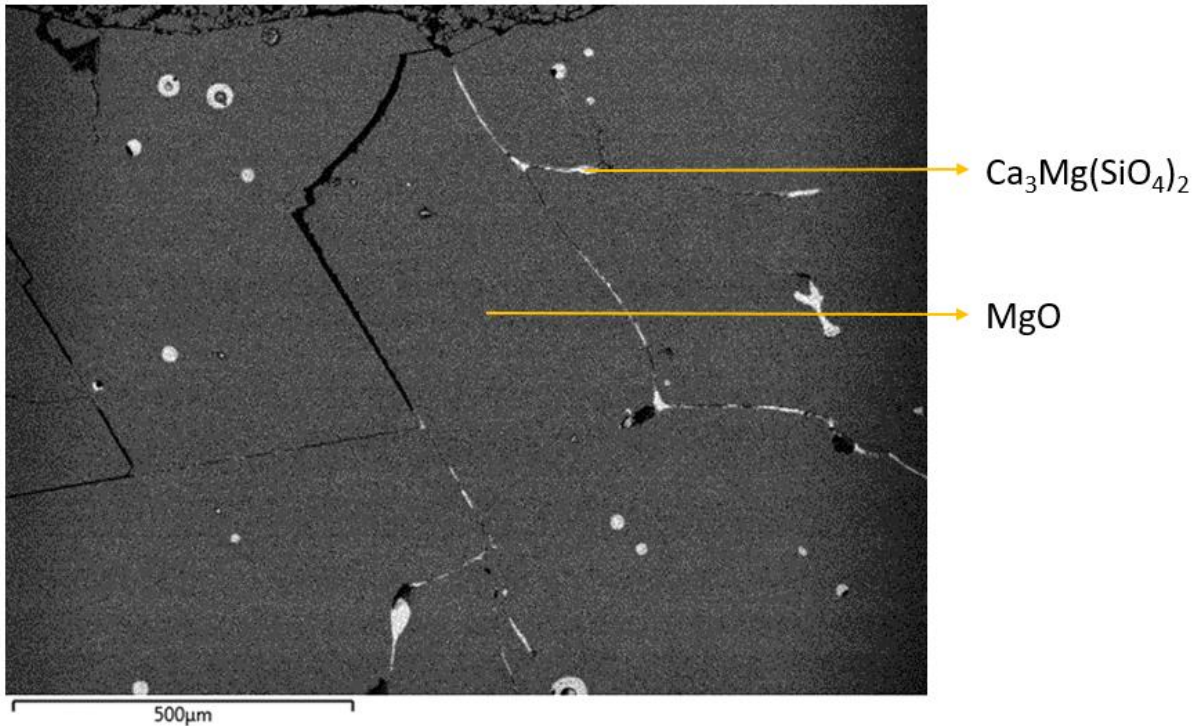


Figure 4.23: Backscatter electron image of the hot face of the MgO brick that was removed from the hearth of the furnace.

4.2.3.2.1 Summary of the SEM-EDS results

The SEM-EDS analysis of the samples taken from the MgO brick that was removed from the hearth of the furnace is summarised in Table 4.9 (the positions from where the samples were taken are shown in Figure 4.12). No interaction was present between the refractory and the metal. ZnS was present in one polished sample, which is presumably not representative of the hearth bricks. ZnS is not expected to be present in the brick.

Table 4.9: Summary of the SEM-EDS analysis of the MgO brick situated at the furnace hearth.

	1 Hot face	2	3 Cold face
Phases	<ul style="list-style-type: none"> • MgO • Glassy phase (MgO-CaO-SiO₂ – based) 	<ul style="list-style-type: none"> • MgO • ZnS 	<ul style="list-style-type: none"> • MgO • Glassy phase (MgO-CaO-SiO₂ – based)

4.2.3.3 MgO-C brick situated above the tap hole.

A MgO-C brick present above the tap hole was sampled in order to determine if any interaction between the atmosphere and the brick had occurred. Both the hot and cold faces were analysed.

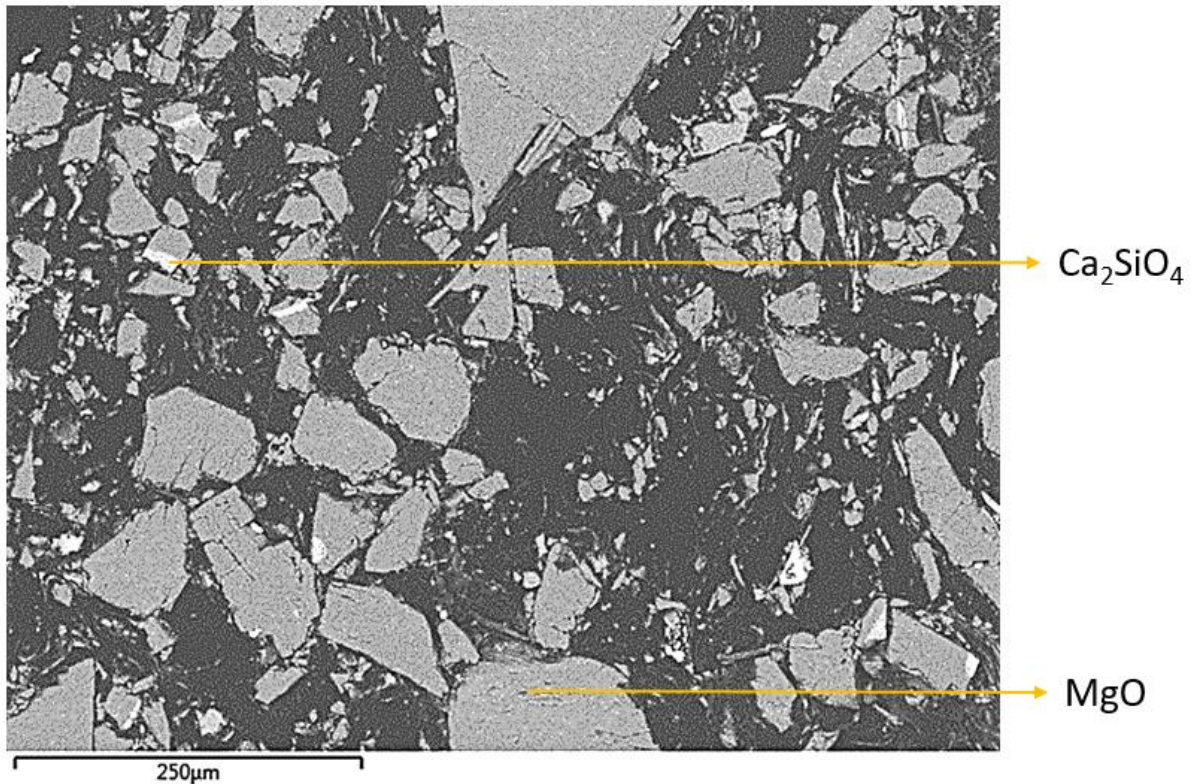


Figure 4.24: Backscatter electron image of a MgO-C sample at the cold face of the brick.

The MgO-C hot face contained MgAl_2O_4 , which is formed through the reaction of aluminium that oxidised and MgO. The presence of slag (evident from Figure 4.25) in the MgO-C indicated that contact between the slag and the MgO-C brick had occurred. The presence of slag in the refractory is a result of the porosity of the brick allowing penetration of slag into the brick, with the porosity being a result of graphite oxidation. The Ca_2SiO_4 phase is formed due to the impurities of CaO and SiO_2 present in the brick before being used in the furnace, as evident by the brick specifications in Table 4.4. Although CaMgSiO_4 is expected to form during cooling, Ca_2SiO_4 is readily present at high temperatures when considering compositions in the MgO region of the CaO-SiO₂-MgO phase diagram. The presence of Ca_2SiO_4 rather than CaMgSiO_4 is due to high operating temperatures and rapid cooling rates. No anti-oxidants were identified in the MgO-C brick, which are usually present in the form of metallic aluminium or Al_4C_3 .

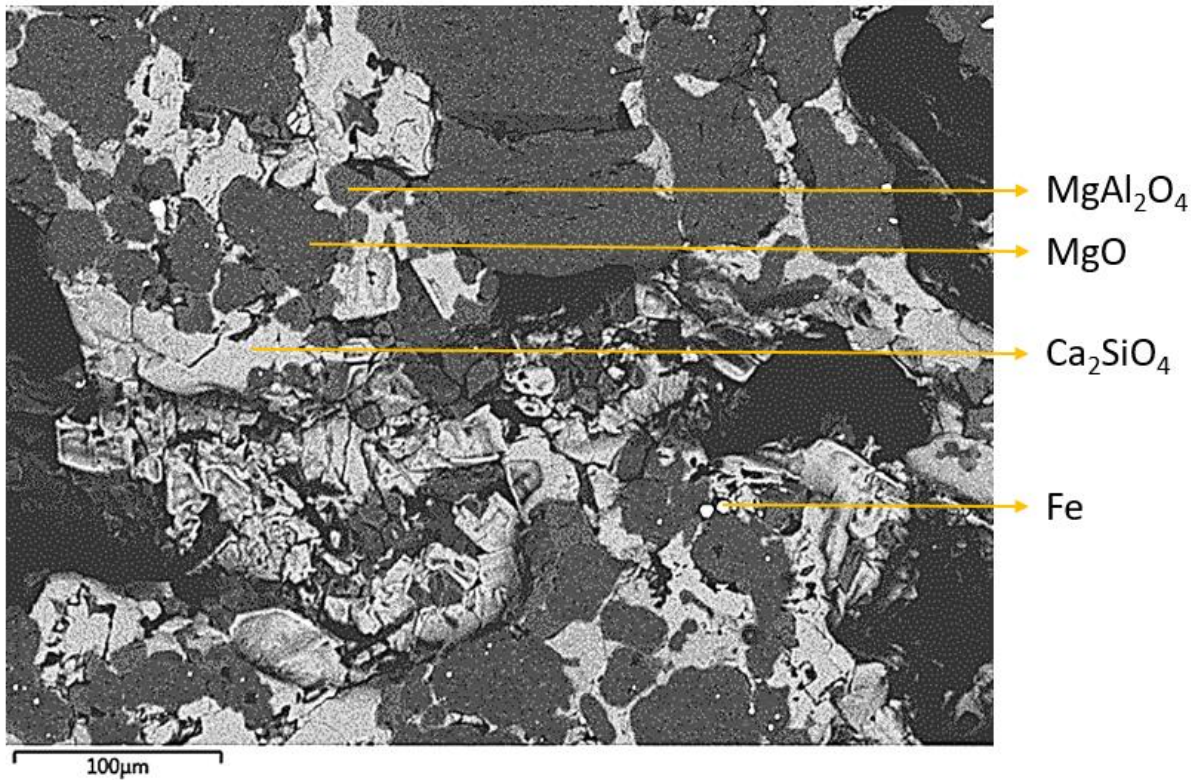


Figure 4.25: Backscatter electron image of the MgO-C hot-face that contained a precipitate on the surface.

The SEM-EDS results of the MgO-C brick is summarised in Table 4.10. The results indicate that slag was present at the hot face of the brick, penetrating into the brick. Visual inspection of the sample indicated that slag was present at the surface of the brick, supporting the suggestion that the brick was exposed to slag. Oxidation of the carbon resulted in the porosity of the brick increasing, allowing the slag to penetrate into the brick.

Table 4.10: Summary of the SEM-EDS results of the MgO-C brick situated above the tap hole.

	MgO-C Hot face	MgO-C Cold face
Phases	<ul style="list-style-type: none"> • MgO • Ca₂SiO₄ • MgAl₂O₄ • Fe 	<ul style="list-style-type: none"> • MgO • Ca₂SiO₄

4.3 Conclusions

The slag analysis indicated that vanadium losses are due to both vanadium in metal inclusions and V³⁺ in the slag (related to the formation of the MA spinel phase in the slag). The slag also contained 20.7 wt % MgO, which originated from the MgO lining. This was supported by the analysis of the MgO refractory in contact with the slag, which indicated that the MgO content

in the hot face decreased when slag penetrated into the brick. The reason for the difference in MgO content between the hot face and cold face is that the MgO refractory dissolved into the slag in order to obtain MgO saturation of the slag. A significant amount of Al_2O_3 and CaO was present at the hot face of the brick, indicating that the slag penetrated into the brick.

In order to reduce refractory wear, sufficient MgO must be added to obtain a MgO saturated slag. The vanadium losses can be reduced by reducing the viscosity of the slag and also by avoiding spinel formation. This can be obtained by changing the MgO and CaO content to a slag composition of $\text{Al}_2\text{O}_3 = 40 \text{ wt\%}$, $\text{MgO} = 40 \text{ wt\%}$ and $\text{CaO} = 20 \text{ wt\%}$, as shown in Figure 2.8.

Chapter 5: Experimental results

5.1 Slag-refractory interaction

5.1.1 Background

Slag-refractory interaction tests were done in order to determine the effect of slag composition (by increasing the MgO content) on refractory wear in the ferrovanadium production process. Two slag compositions were prepared with compositions given in Table 3.1. The one slag sample was not saturated in MgO (Sample A), whereas the other slag sample was saturated in MgO (Sample B) at 1800°C. The slag was placed inside a molybdenum crucible, in contact with a MgO refractory (15mm diameter cylinder) as indicated in Figure 5.1. The tests were conducted for 50 minutes at 1800°C. The samples were analysed using SEM-EDS analysis.

Numerous backscatter electron images were taken at different locations on the sectioned samples. The different locations are indicated in Figure 5.2. The locations are indicated in the analysis by first mentioning the y position (top, centre, bottom), followed by the x position (centre or side).

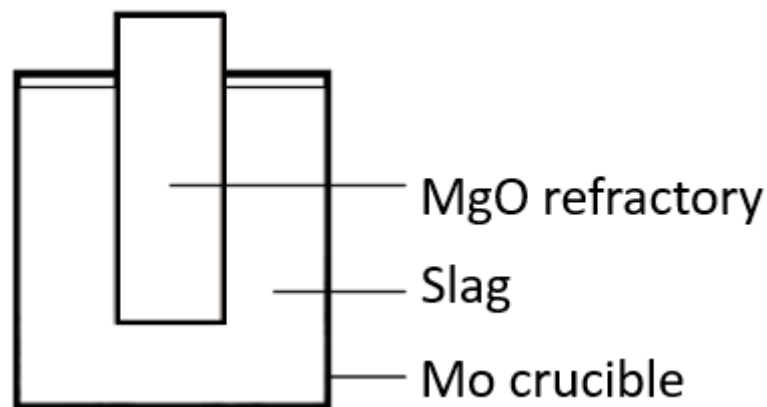


Figure 5.1: Schematic diagram of the setup before the slag-refractory tests were conducted.

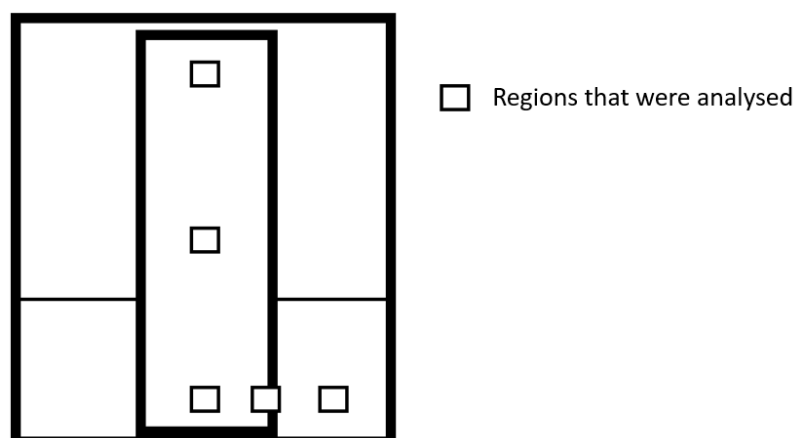


Figure 5.2: Schematic diagram of the sectioned crucible with indicated regions that were analysed.

5.1.2 Sample A

The initial composition of sample A is given in Table 3.1.

5.1.2.1 Refractory analysis

The region at the top-centre that was analysed indicated that slag was present between the MgO grains of the refractory (Figure 5.3). The refractory region was well above the slag line, indicating that the slag had wicked into the refractory. The matrix binding the aggregate grains have been replaced with slag to a large extent, which indicates that slag penetration occurred with little difficulty.

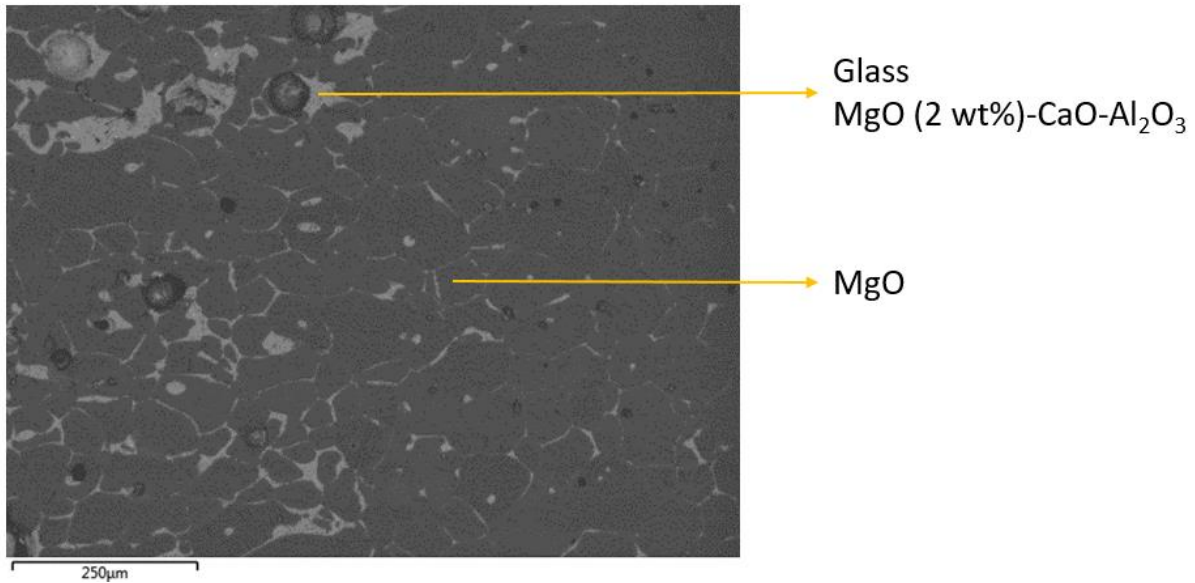


Figure 5.3: Electron backscatter image of the top-centre refractory region that was analysed.

Two slag phases were present in the centre-centre region, one constituted of MgO, CaO and Al_2O_3 (glassy phase) and the other constituted of CaO and Al_2O_3 (dendritically precipitated CaAl_2O_4). The analysed region indicated that slag penetration had occurred and the presence of CaAl_2O_4 indicates that the slag is enriched in MgO. The MgO grains were not affected by the penetration, but the binding matrix had been replaced by slag. Trace amounts of oxidised molybdenum was present in the slag. The molybdenum oxide was only present in the CaAl_2O_4 phase in quantities of less than 1 wt%. The presence of the molybdenum oxide is not indicated in the work to follow, as it is only present in trace amounts and should not influence the slag-refractory interaction.

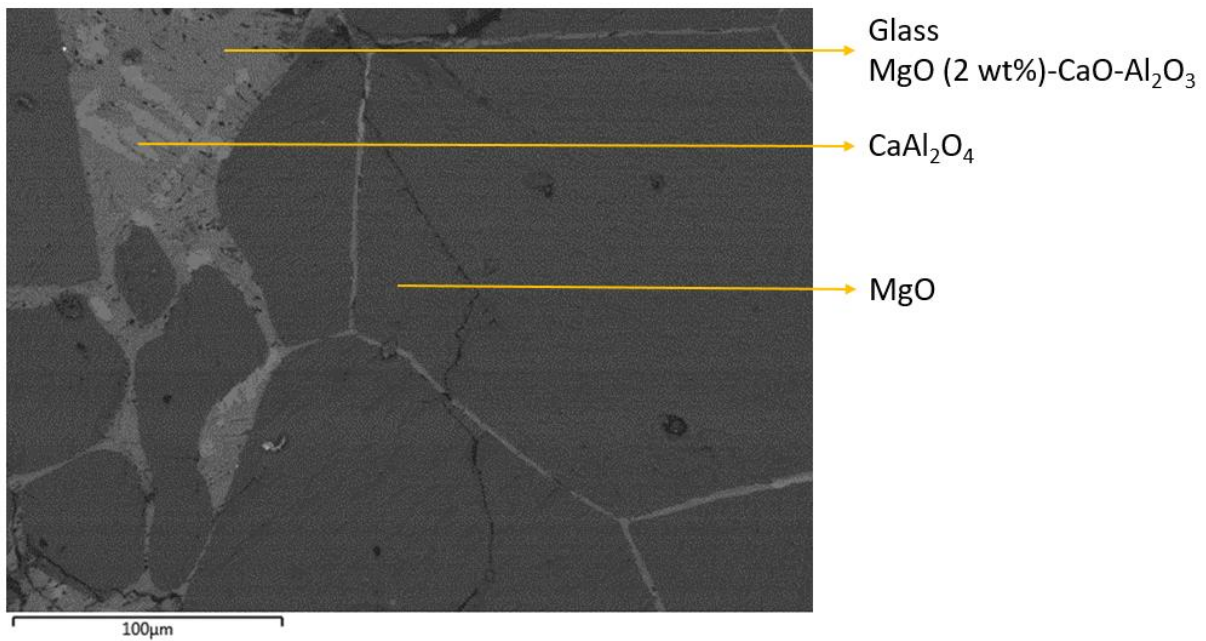


Figure 5.4: Electron backscatter image of the region analysed at the centre-centre region of the refractory.

The bottom-centre region that was analysed (Figure 5.5) indicated extensive infiltration of the slag into the refractory. It is also evident that a reaction had occurred between the slag and the refractory to form MgAl_2O_4 . Most MgO grains were still intact, but some grains have disappeared as MgAl_2O_4 started to form (evident by the large regions of MgAl_2O_4).

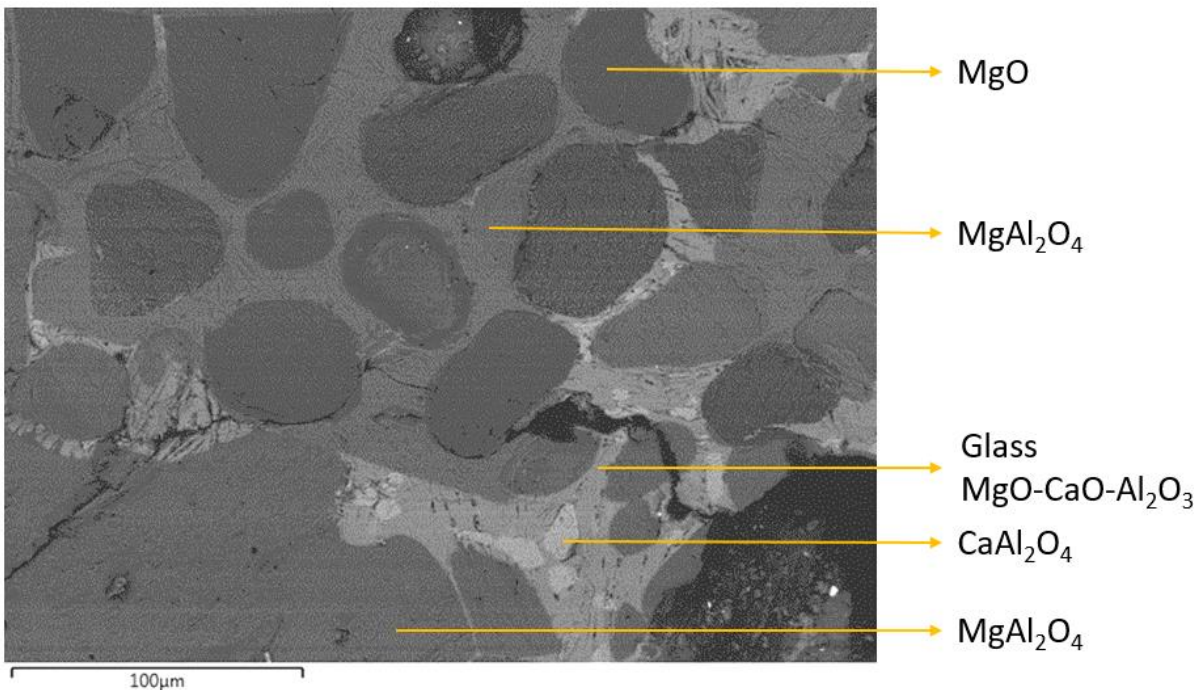


Figure 5.5: Electron backscatter image of the region analysed at the bottom-centre of the refractory.

The bottom-edge region of the refractory indicated aggressive interaction with the slag (Figure 5.6). The slag had penetrated into the refractory, as well as reacted with the refractory to form MgAl_2O_4 . The MgO grains are rounded whereas the MgAl_2O_4 crystals are cubic in form.

The area covered by MgO (38.5% as analysed using imageJ) has reduced significantly compared to the bottom-centre region (52.8%). The mechanism of refractory wear is penetration of the slag into the refractory, together with a reaction between the slag and the refractory. CaAl_2O_4 precipitated dendritically from the liquid matrix, but the sample consisted of liquid, MgO and MgAl_2O_4 at temperature. Molybdenum is also present, which originated from the molybdenum crucible used.

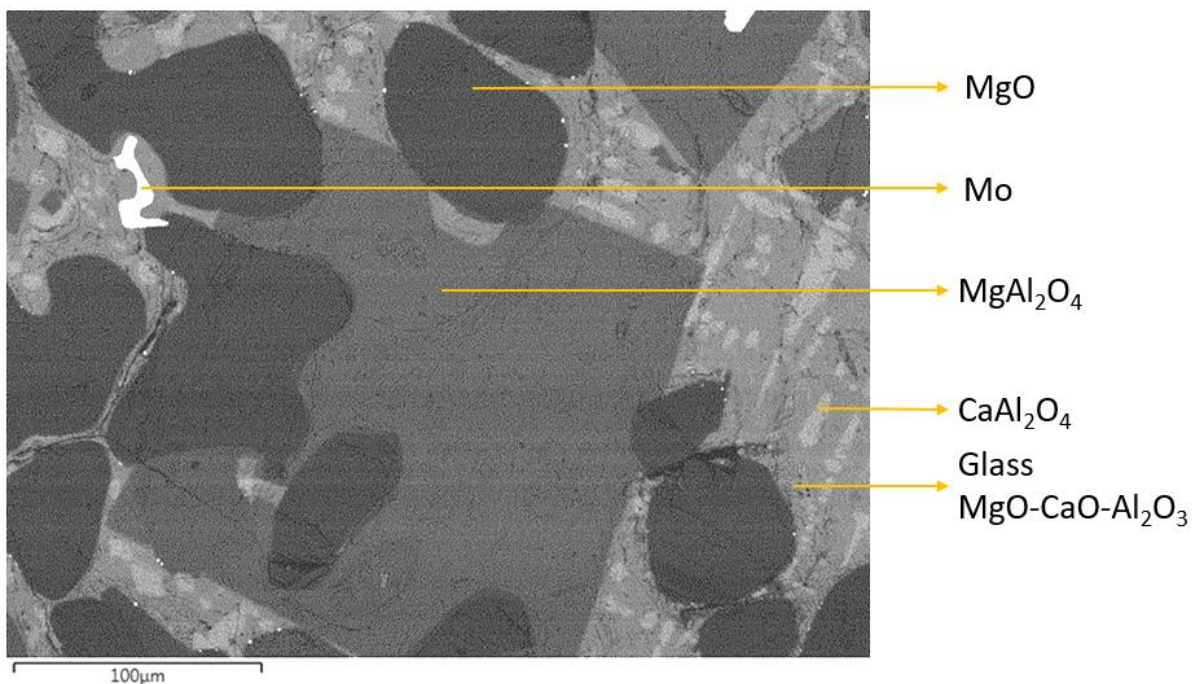


Figure 5.6: Electron backscatter image of the region analysed at the bottom-edge area of the refractory.

5.1.2.2 Slag analysis

The bottom-side region that was analysed contained four phases as well as a small amount of molybdenum inclusions (Figure 5.7). The slag phases present in the slag were MgAl_2O_4 , MgO , CaAl_2O_4 and a glassy $\text{CaO-MgO-Al}_2\text{O}_3$ based slag matrix phase. The CaAl_2O_4 phase should not have formed when considering the starting composition of the slag (Figure 5.8), as the slag should contain $\text{CaO} : \text{Al}_2\text{O}_3$ ratios smaller or equal to 0.5. The $\text{CaO} : \text{Al}_2\text{O}_3$ ratio of 1 indicated that the liquid composition had shifted from the initial composition. The presence of MgO and MgAl_2O_4 in the slag supports the remarks regarding slag penetration being present and that a reaction occurred between the slag and the refractory.

The reason for the penetration is due to the high temperature of the slag, as well as the initial slag not being saturated in MgO (by means of adding MgO as a flux). The reaction of the slag with the refractory is also due to the slag not being saturated in MgO . The slag forms MgAl_2O_4 up to an extent where the slag is saturated in MgAl_2O_4 , but because only a small amount of

MgO was added as flux, slag saturation only occurred after a significant amount of MgO (originating from the refractory) dissolved into the slag.

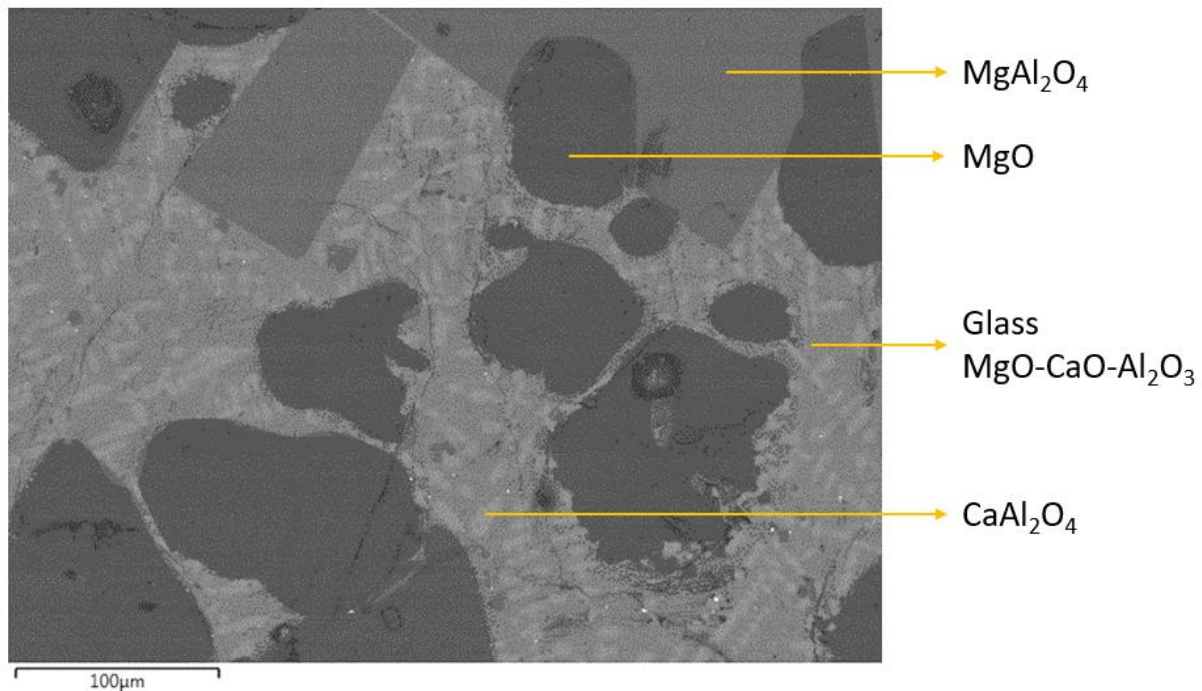


Figure 5.7: Electron backscatter image of the analysed slag region.

Three low magnification (60x) electron backscatter images of the slag were used to analyse the composition of the slag. The total composition of all three areas were analysed and the average taken as the final slag composition. The final slag composition is shown in Table 5.11. The phase diagram (Figure 5.8) indicates the initial slag composition (A_i), which is the composition that should have been obtained had the slag not reacted with the refractory. The phase diagram also indicates the actual final slag composition (A_f), as analysed after the test. The change in composition is due to the slag not being saturated in MgO, resulting in MgO being dissolved into the slag (as well as reacting with the slag).

The composition is expected to change along the line drawn from A_i to the MgO corner of Figure 5.8. The composition did change along this line as can be seen by A_f (which is almost on the line). The position of A_f does however indicate that the slag was at a temperature of 1900 °C and not at 1800 °C, as the total slag composition is on the 1900 °C isotherm (although the tests were done at a reading of 1800 °C). Temperature calibration was done up to 1700 °C by setting the power source at a certain power value and then measuring the temperature using both the pyrometer and a type-R thermocouple. The temperature readings were similar between the pyrometer and type-R thermocouple and the pyrometer was therefore deemed to be accurate.

The difference in actual and measured temperature can be ascribed to the fact that the pyrometer reads the temperature at the top of the sample, whereas most of the heat is generated at the bottom of the sample which can result in a difference in the measured temperature versus the actual temperature (at the lower section of the sample). The

temperature gradient is a result of the shape of the susceptor (in this case the crucible), which is closed at the bottom (Figure 3.3), resulting in more heat being generated at the bottom of the sample.

Table 5.11: Initial slag composition (A_i) and final composition (A_f) of slag in contact with refractory sample (Slag composition of slag A (A_f) in contact with a MgO refractory core based on three areas analysed at 60x).

Slag component	Initial composition (wt %)	Final composition (wt %)
MgO	2	35
Al ₂ O ₃	82	54.7
CaO	16	10.3

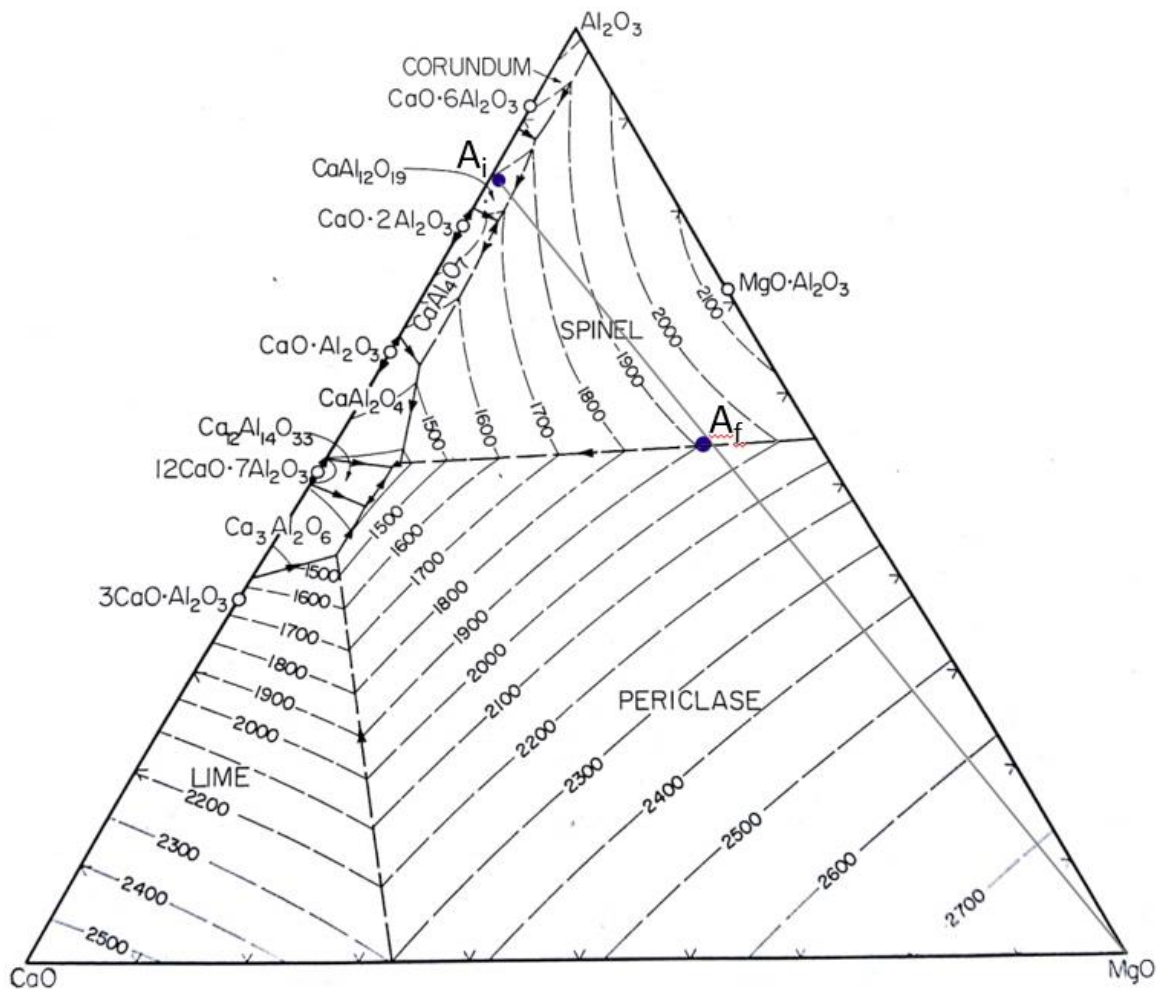


Figure 5.8: Ternary phase diagram indicating the change in total composition of the initial slag (A_i) versus the final slag (A_f).

5.1.3 Sample B

5.1.3.1 Refractory analysis

The analysis at the top-centre of the sample indicated that minimal slag penetration was present (Figure 5.9). The slag that was present however was due to the slag being wicked into the sample as the slag line was below the analysed refractory area. The MgO grains were still intact, but the binding matrix had been replaced by slag to a large extent.

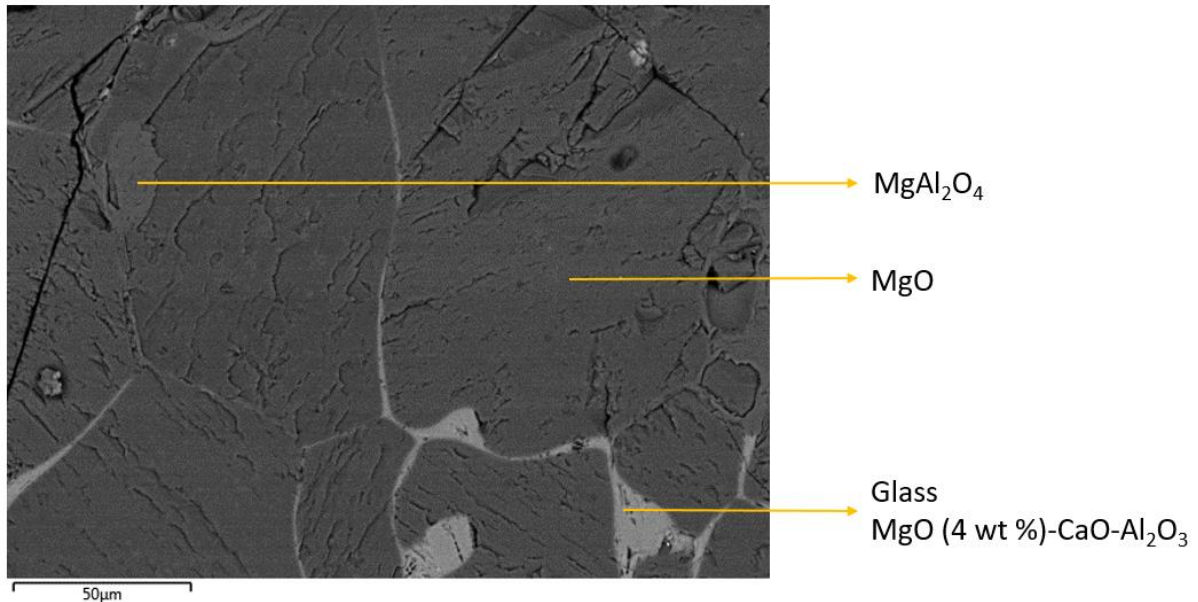


Figure 5.9: Electron backscatter image of the top-centre of the MgO refractory.

The centre-centre region that was analysed indicated that slag had penetrated into the refractory (Figure 5.10). The presence of MgAl_2O_4 also suggests that a reaction occurred between the slag and the refractory and therefore refractory wear occurred. At a temperature of 1800°C slag B should consist of liquid only. It is however important to note that the slag already contained MgO, as MgO was added as a flux, therefore the presence of MgAl_2O_4 is not necessarily only due to interaction with the refractory.

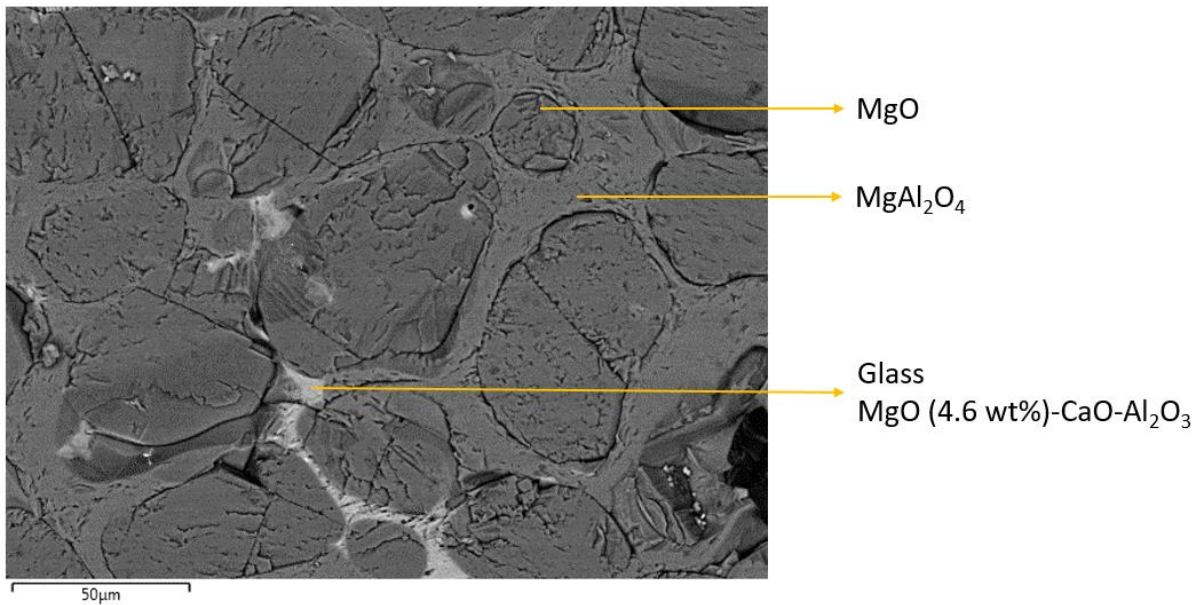


Figure 5.10: Electron backscatter image of the centre-centre region of the MgO refractory.

Analysing the bottom-centre region of the refractory sample indicated that the slag had penetrated into the refractory and that a reaction had taken place (Figure 5.11). The area covered by MgO grains were less than at the top-centre (68.1% versus 73.8% respectively), which indicated that a reaction did take place to reduce the size of the MgO grains. Comparing the bottom-centre regions for slag B to slag A, it is evident that a larger area is still covered by MgO for the test of slag B (68.1%), which suggests that the extent of refractory wear is less for the test of slag B than for slag A (52.8%).

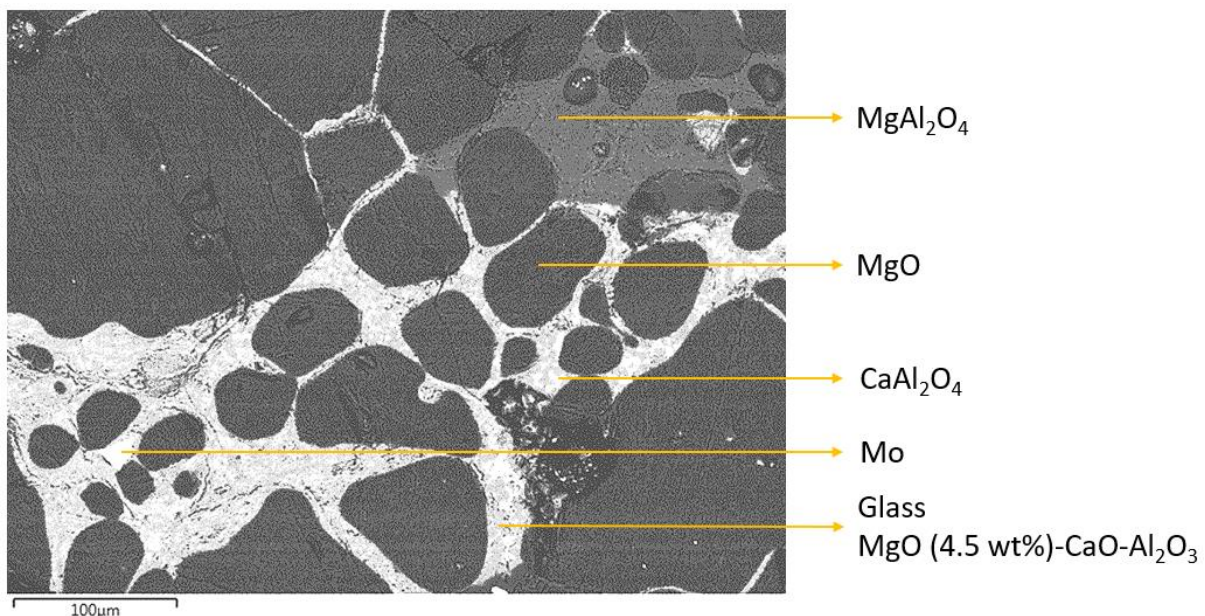


Figure 5.11: Electron backscatter image of the bottom-centre of the MgO refractory.

The bottom edge region (slag-refractory interface) that was analysed indicated that significant penetration and reaction had taken place between the slag and the refractory (Figure 5.12). MgO grains were still present, but the slag covered most of the analysed region

(52.7% slag). MgAl_2O_4 formed as a primary phase and also precipitated out upon cooling as is expected from the initial slag composition. The area covered by MgO (47.3%) is also less than in the bottom-centre region (68.1%).

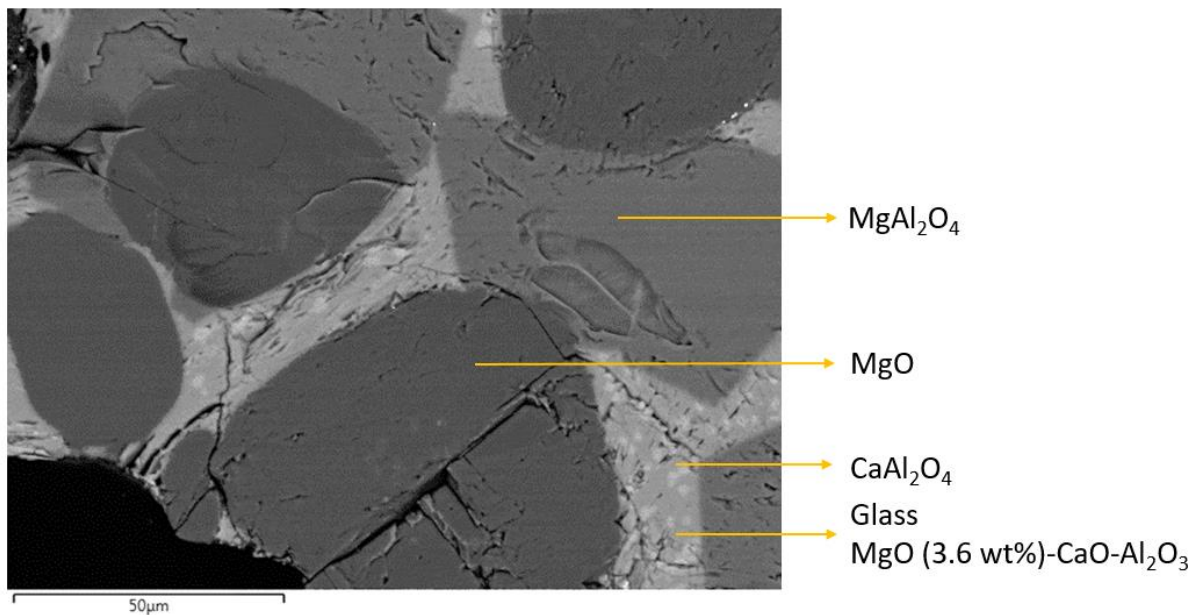


Figure 5.12: Electron backscatter image of the bottom edge region of the MgO refractory.

5.1.3.2 Slag analysis

The bottom-side region that was analysed indicated that the slag was mainly composed of MgAl_2O_4 (Figure 5.13). Small amounts of MgO were present, which indicate that the slag was saturated in MgO . There is still considerable wear present as indicated in the bottom-centre and bottom-side regions.

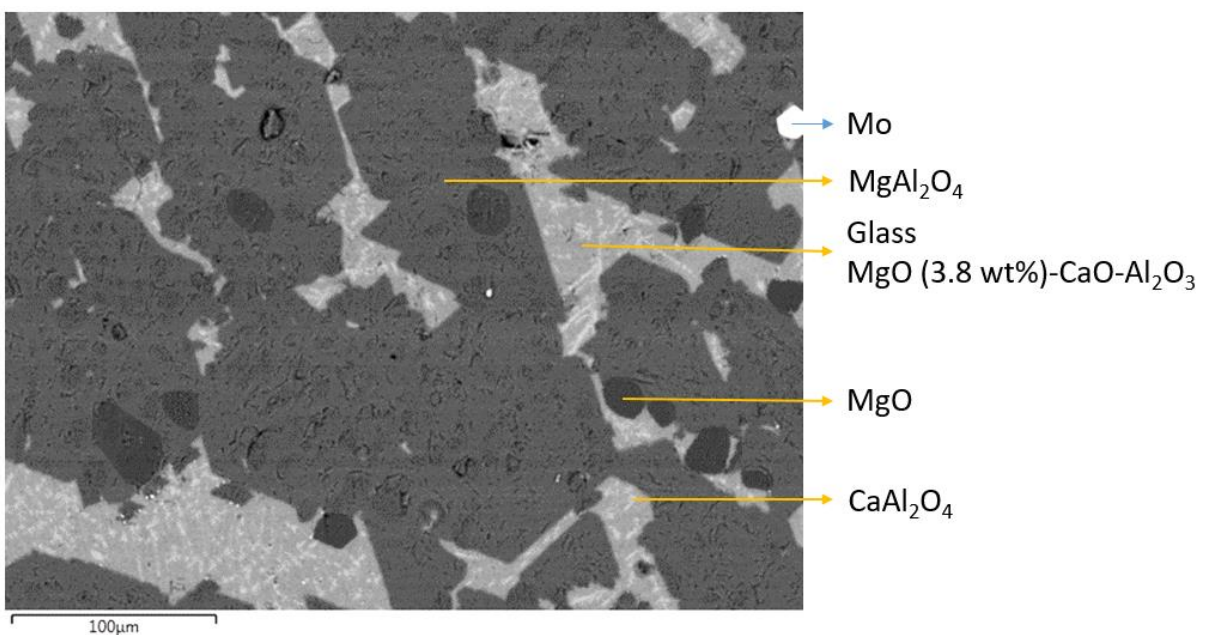


Figure 5.13: Electron backscatter image of the slag at a magnification of 70x.

Three low magnification electron backscatter images (70x) of the slag were used to analyse the composition of the slag. The total composition of all three areas were analysed and the average taken as the final slag composition. The final slag composition is shown in Table 5.12. Figure 5.14 indicates the change in composition of the slag (from B_i to B_f). The slag composition is changed along the line from B_i towards the MgO corner of the phase diagram, as indicated in Figure 5.14.

The change in slag composition B_i is due to the slag not being saturated in MgO for an operating temperature of just below 1900°C, resulting in MgO being dissolved into the slag (as well as reacting with the slag).

Table 5.12: Initial composition (A_i) and the final composition (A_f) of the slag in contact with the refractory.

Slag component	Initial composition (wt%)	Final composition (wt %)
MgO	8	32.3
Al ₂ O ₃	78	56.2
CaO	14	11.5

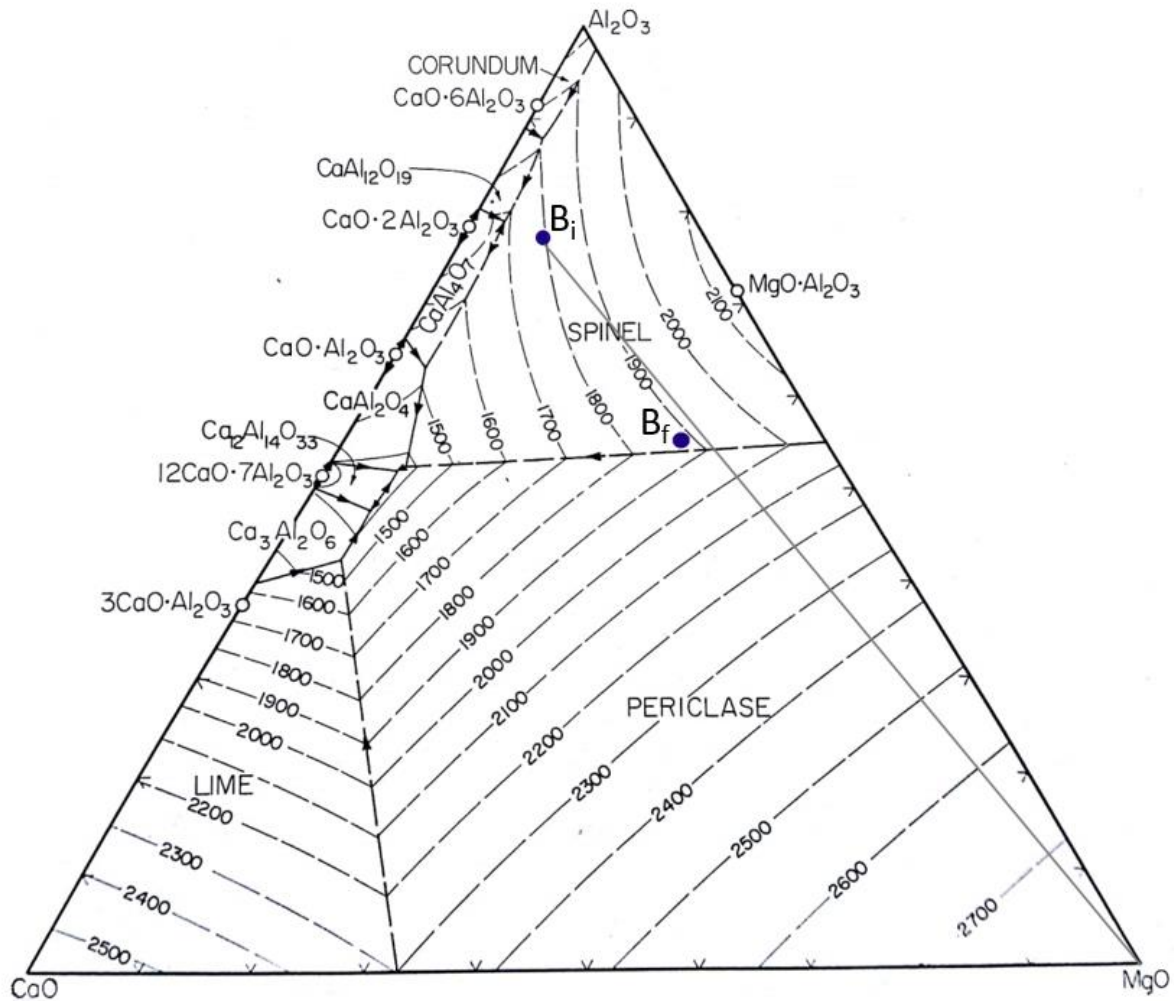


Figure 5.14: Ternary phase diagram indicating the change in composition of the expected slag (B_i) versus the actual slag (B_f).

An indication of the difference in refractory wear for test specimens A and B was obtained by investigating the sectioned test specimens (Figure 5.15 and Figure 5.16). Almost no slag is present between the refractory core and crucible wall, as the slag was wicked into the refractory, leaving only a small amount of slag as indicated. Both tests initially had refractory cores with a height of 28 mm, therefore the change in height was assumed to give an indication of the amount of refractory wear present due to MgO dissolution and liquid phase formation.

Visual inspection of the refractory cores A and B also indicate a densified structure for test A compared to test B, indicating that more liquid is present in test core A. The change in height of the refractory core from test A (Figure 5.15) was more than the change in height for test B (Figure 5.16), which therefore confirms the importance of MgO saturation of the slag. Test B had a slag composition closer to the MgO saturation composition compared to test A, which resulted in a smaller change in height and therewith less refractory wear.

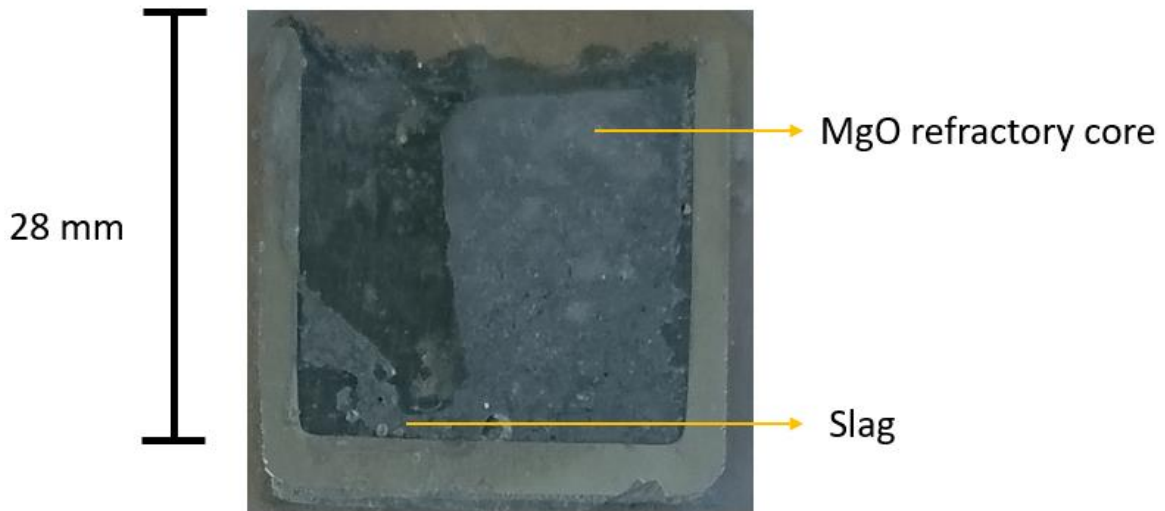


Figure 5.15: Section through test A (molybdenum crucible with MgO core and slag).

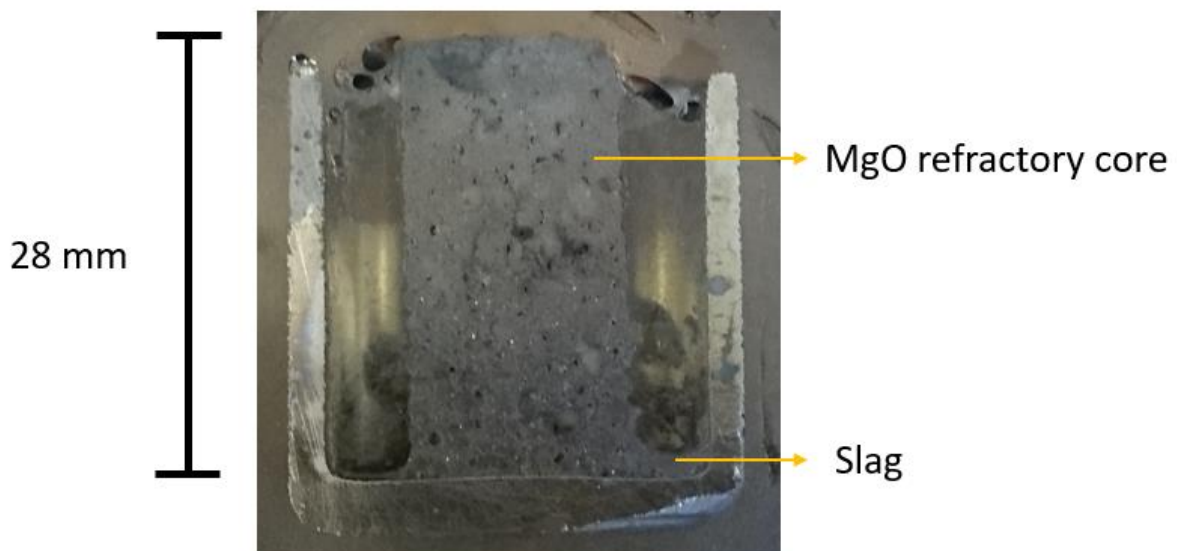


Figure 5.16: Section through test B (molybdenum crucible with MgO core and slag).

5.2 Metal and vanadium recovery

5.2.1 Metal and vanadium recovery as a function of slag composition

The vanadium recovery as a function of slag composition was tested by changing the slag composition as shown in Figure 5.17 (1800°C isotherm on the MgO-CaO-Al₂O₃ phase diagram). The V₂O₅, aluminium and iron added remained constant, which resulted in a change in slag volume as the composition was altered. The change in slag composition changed the slag viscosity. A decrease in slag viscosity will reduce the amount of metal retained in the slag if the slag volume remains constant, but for these experiments a decrease in slag viscosity was also accompanied with an increase in slag volume. The aim was therefore to determine if the decrease in slag viscosity offsets the increase in slag volume.

The ferrovanadium metal droplets were separated from the slag by hand, as previously discussed. Droplets with a diameter smaller than 0.5 mm accounted for metal droplets that were entrained in the slag. The separation method used will result in an under estimation of the metal recovery. Small metal droplets have a slower settling rate than larger droplets as explained by Stokes's equation (section 2.6 Metal droplet entrainment):

From Stokes's equation it is evident that a smaller droplet radius (r) decreases the settling rate of the metal droplet, which results in an increase in metal losses due to metal droplet entrainment.

Metal and vanadium recovery in this section was calculated by using the following equations:

$$\text{Metal recovery} = \frac{\text{Mass of metal recovered after the test}}{\text{Mass of metal theoretically expected to form}} \times 100 \quad (14)$$

$$\text{Vanadium recovery} = \frac{\text{Mass of metal} \times \text{wt\% V in metal}}{\text{wt\% V in } V_2O_3 \times V_2O_3 \text{ added to reaction}} \times 100 \quad (15)$$

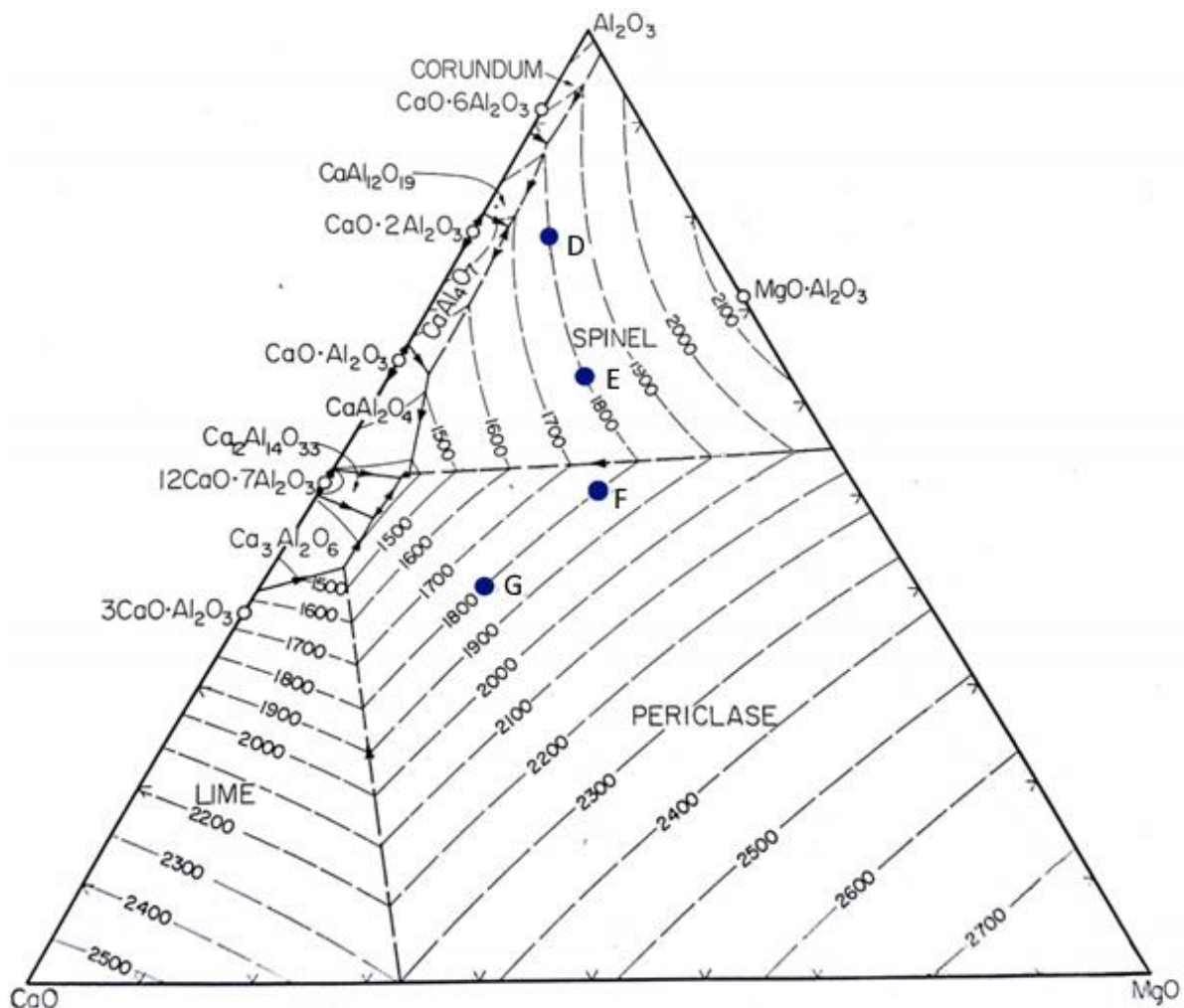


Figure 5.17: Slag compositions used to examine recovery as a function of slag composition.

The metal recovery versus slag composition graph (Figure 5.18) indicated that the metal recovery decreased as the slag composition was changed from composition D to G (with slag composition D having the lowest slag volume and highest viscosity and slag composition G having the highest slag volume and lowest expected viscosity). The decrease in metal recovery as the composition was changed from composition D to G indicated that the increase in slag volume had a bigger influence on metal recovery than viscosity. The increase in slag volume resulted in the formation of a high amount of metal droplets with a diameter smaller than 0.5 mm, resulting in a high amount of metal droplet entrainment in the slag.

The larger slag volume increased the settling distance for the metal droplets, decreasing the recovery of the metal droplets. The interaction between metal droplets (metal droplets coalescing) also decreased, resulting in more small droplets that settled slower as explained by the relation between settling rate and droplet radius (Stokes's equation). The slag composition that yielded the highest metal recovery was slag composition D due to slag composition D having the lowest slag volume.

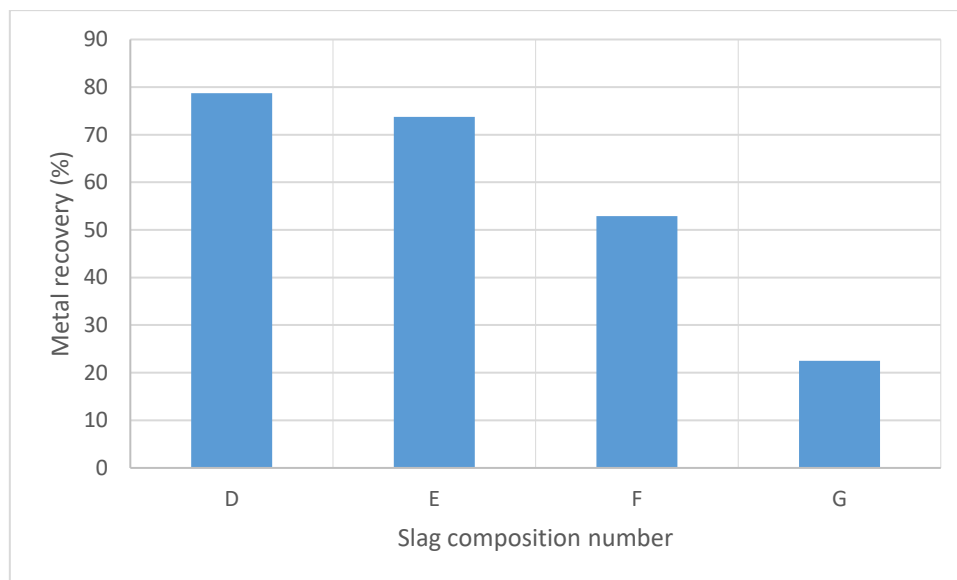


Figure 5.18: Metal recovery as a function of slag composition. (I removed the heading in the graph, as it is repeated in the heading of the Figure.)

The trend for the vanadium recovery was similar to the trend for the metal recovery (Figure 5.19). The vanadium recovery reduced with a change in slag composition from composition D to G as a result of the increase in slag volume. The loss of vanadium can also be ascribed to the formation of vanadium containing oxide phases such as the spinel phase and $\text{Ca}_2(\text{Al},\text{V})_2\text{O}_7$.

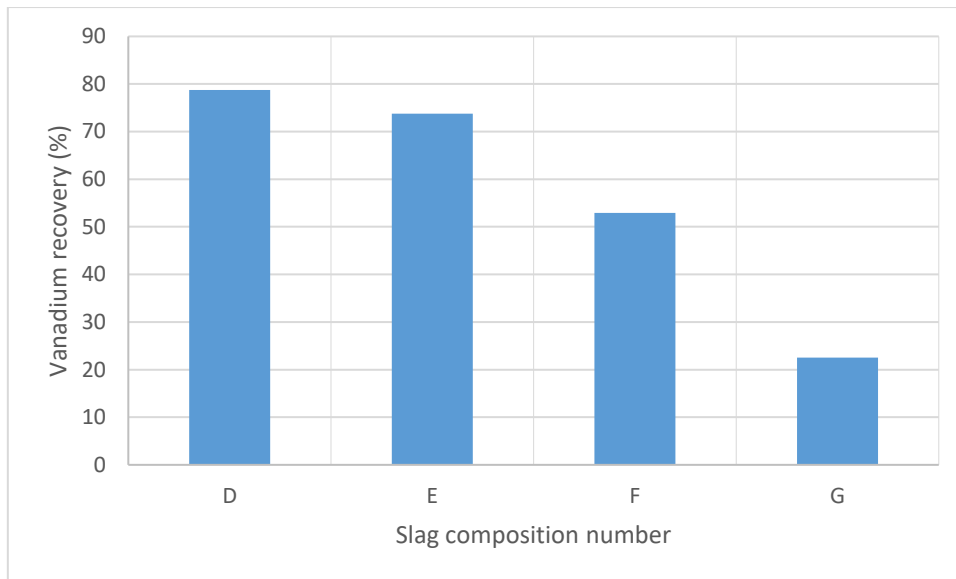


Figure 5.19: Vanadium recovery as a function of the slag composition.

The slag masses of the various slag compositions are shown in Figure 5.20. The mass of the slag increased with a factor of 1.25 from slag D to slag G.

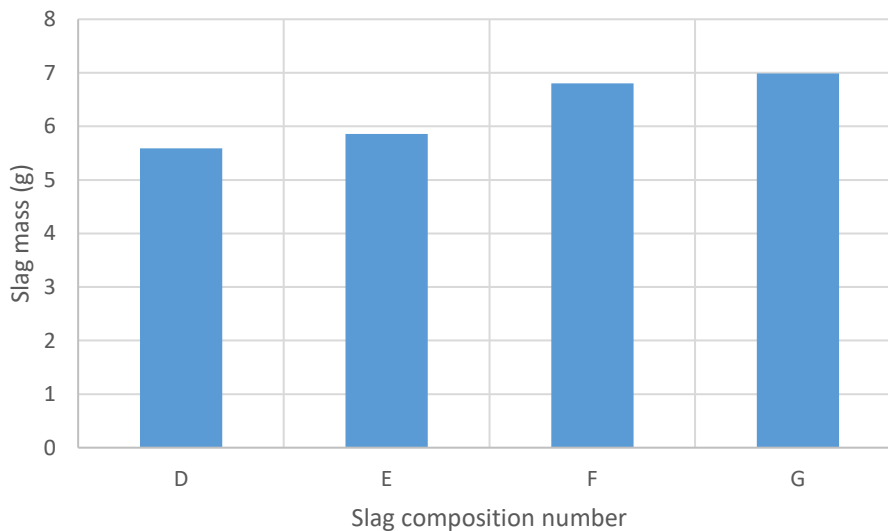


Figure 5.20: Slag mass of the various slag compositions.

The particle size distribution of the metal droplets is an indication of the efficiency of the metal recovery of the process. In order to obtain a good recovery efficiency, the size distribution should show that a small amount of small metal particles are present and that most of the droplets are large particles. The ideal situation would be to have one large metal droplet. Stokes's equation indicates that a larger metal droplet radius will result in a faster settling rate, resulting in an increase in recovery.

The size of the biggest droplets obtained from the tests decreased as the slag composition was changed from slag composition D to G (Figure 5.21 to Figure 5.24). The amount of small metal droplets also increased from slag composition D to G (Figure 5.21 to Figure 5.24). The

particle size distribution indicated that as the slag mass (volume) increased, the particle size distribution shifted to smaller particle sizes. The amount of metal droplets also increased, which indicated that the contact between metal droplets were less (due to the increased distance between metal droplets).

The average size (radius) of the particles is also indicative of the probability of recovering the metal droplets. A higher average particle radius implies a higher probability of recovering the metal droplets. The average particle radius were 1.45 mm, 1.05 mm, 0.75 mm and 0.6 mm for slag compositions D, E, F and G respectively. The decrease in average particle radius as the slag mass increased indicates that as the slag mass increased, the probability of recovery the metal droplets decreased. Slag composition D therefore had the highest probability of recovering all the metal droplets that formed.

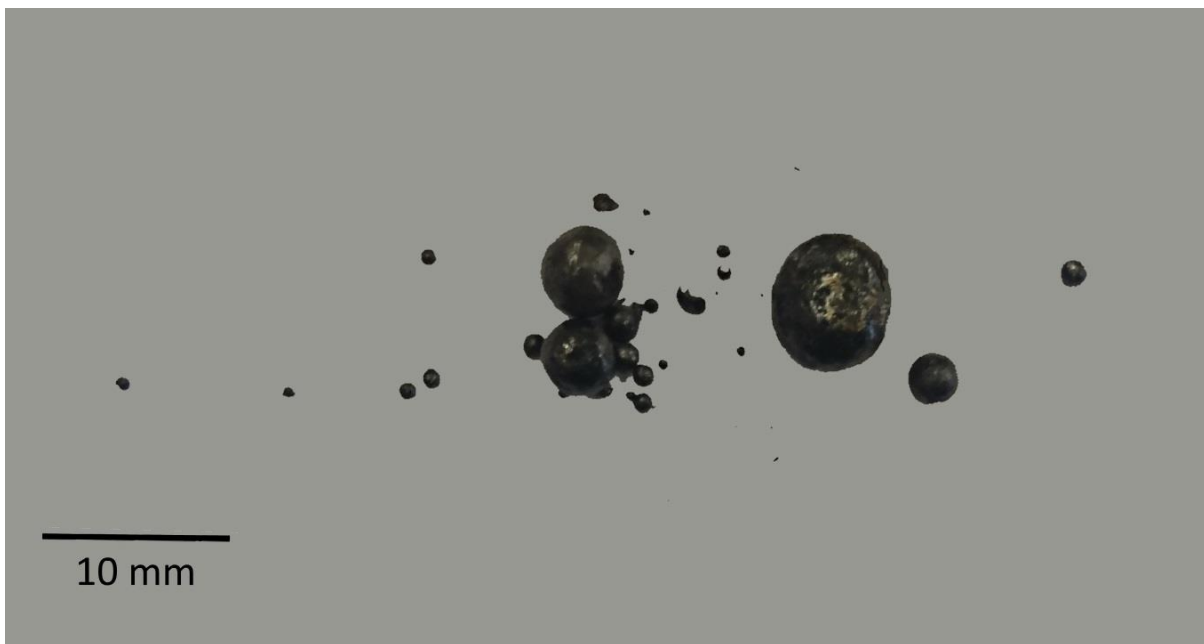


Figure 5.21: Metal droplets recovered from the test where slag composition D was used.

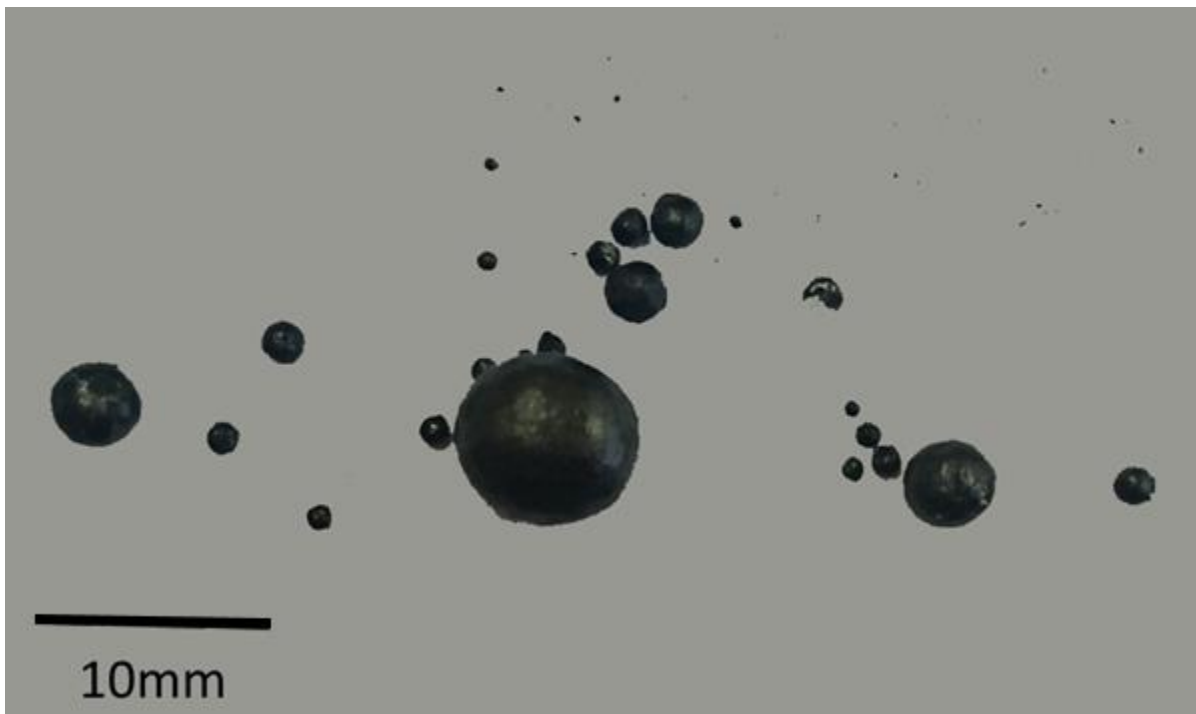


Figure 5.22: Metal droplets recovered from the test where slag composition E was used.

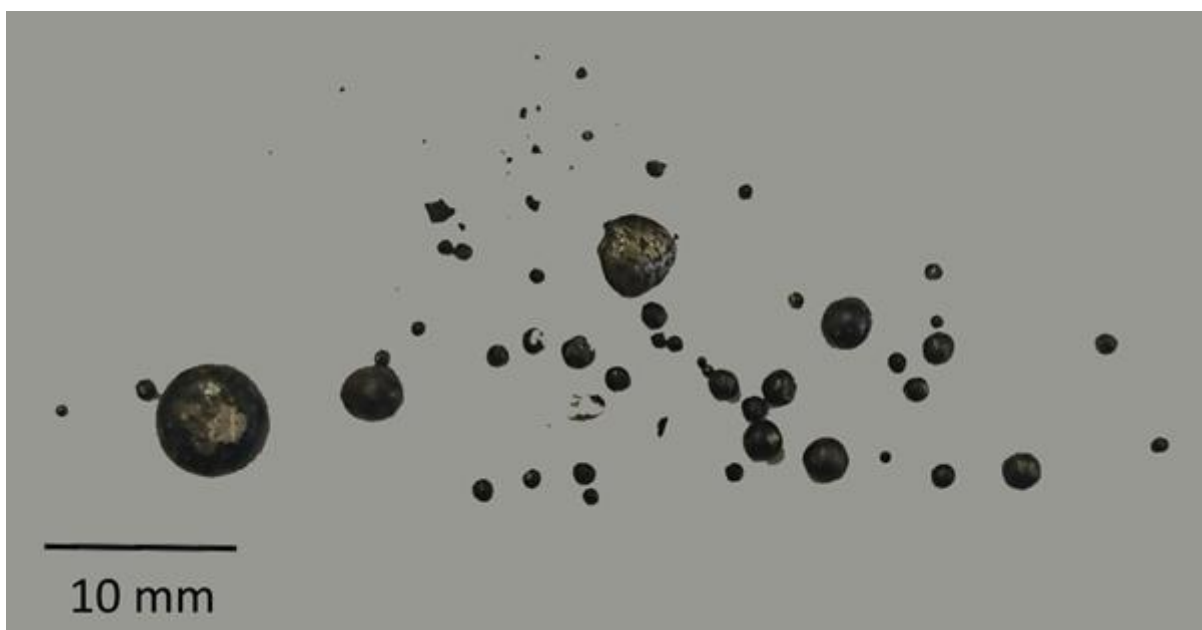


Figure 5.23: Metal droplets recovered from the test where slag composition F was used.

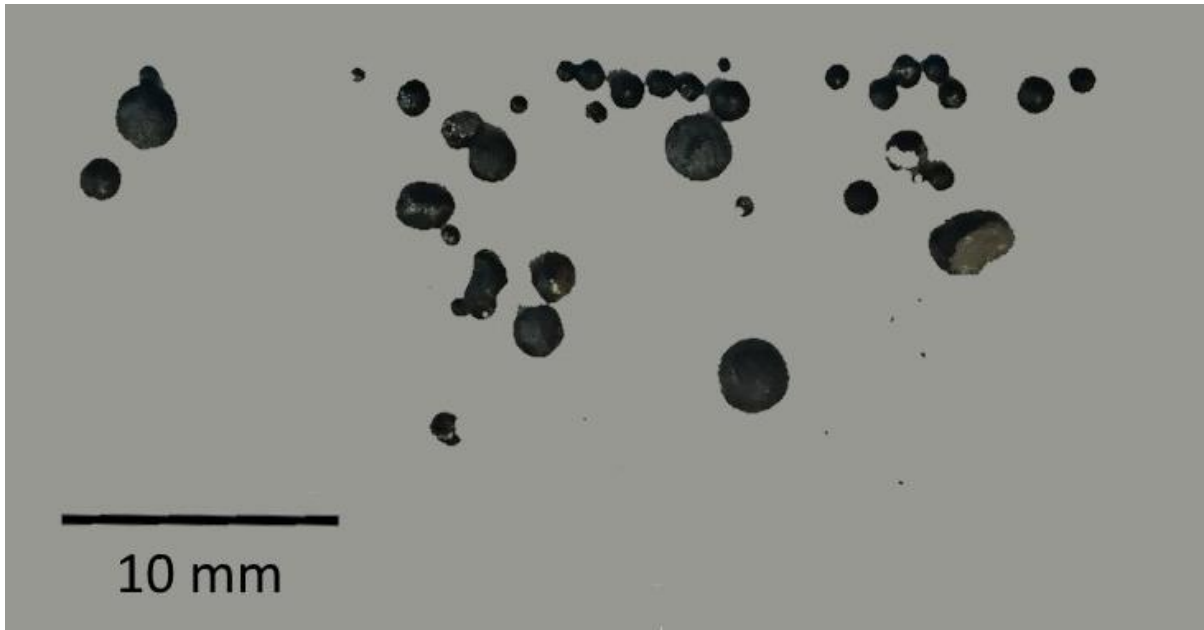


Figure 5.24: Metal droplets recovered from the test where slag composition G was used.

The mass distribution of the metal according to metal droplet size is shown in Figure 5.25. The cumulative mass recovered increased from slag composition D to slag composition G up to a metal droplet radius of 1.5 mm, which indicated that a larger amount of small droplets exist as the slag volume increased.

The trend reversed between metal droplet radiuses of 1.5 mm and 3.5 mm, which then resulted in the cumulative mass increasing from slag composition G to slag composition D for metal droplet sizes larger than 3.5 mm. The mass distribution of the metal droplets therefore shifted towards larger particle sizes as the slag composition changed from G to D. This is because the decrease in volume will result in an increase in the probability of droplets coalescing. An increase in slag viscosity is expected from composition G to D, which should result in a decrease in particle settling rate from sample G to D, which would result in decreasing droplet size from sample G to D, although this was not the result (Figure 5.25).

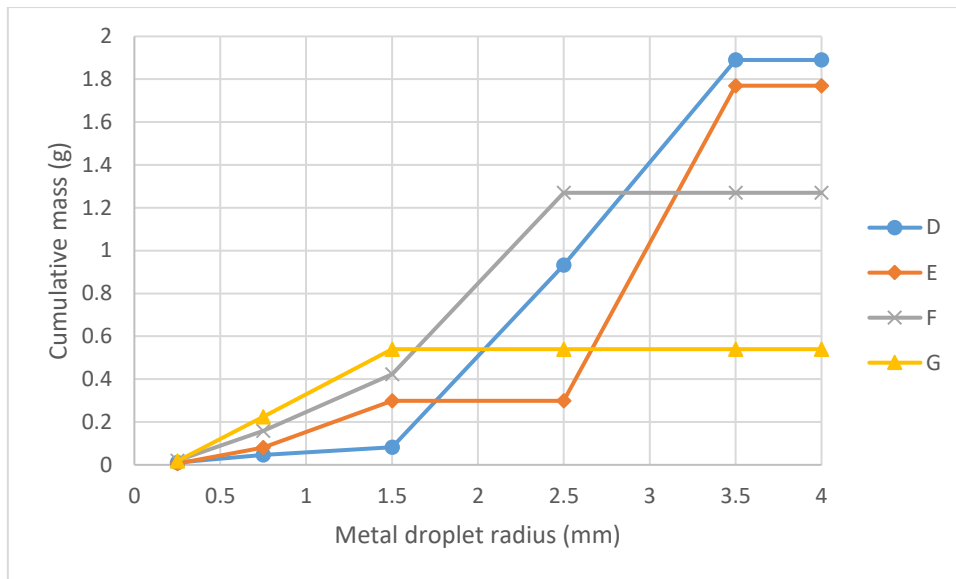


Figure 5.25: Cumulative mass distribution of the metal droplets according to metal droplet radius.

5.2.2 Metal recovery as a function of spinel phase formation

The metal recovery as a function of the amount of the spinel phase present (after cooling to room temperature) in the slag was also investigated. The slag composition was changed in order to form slags with different amounts of spinel phase present. The phases present were analysed using SEM-EDS analysis and the amount of spinel phase present was determined using ImageJ (area covered by spinel phase).

The expected phases for tests D and E at 1800°C are liquid and primary spinel, whereas for tests F and G it is liquid and primary MgO. Therefore the spinel phase present for tests D and E would be a primary phase, whereas it will be a secondary phase for tests F and G, formed upon cooling.

Similar phases are present in samples D and E (Figure 5.26 and Figure 5.27). The area covered by the spinel after cooling in Figure 5.27 (test E) is 15.4 % (error of 6.9 %), which is less than the 23.6 % present (error of 5.6 %) in Figure 5.26 (test D).

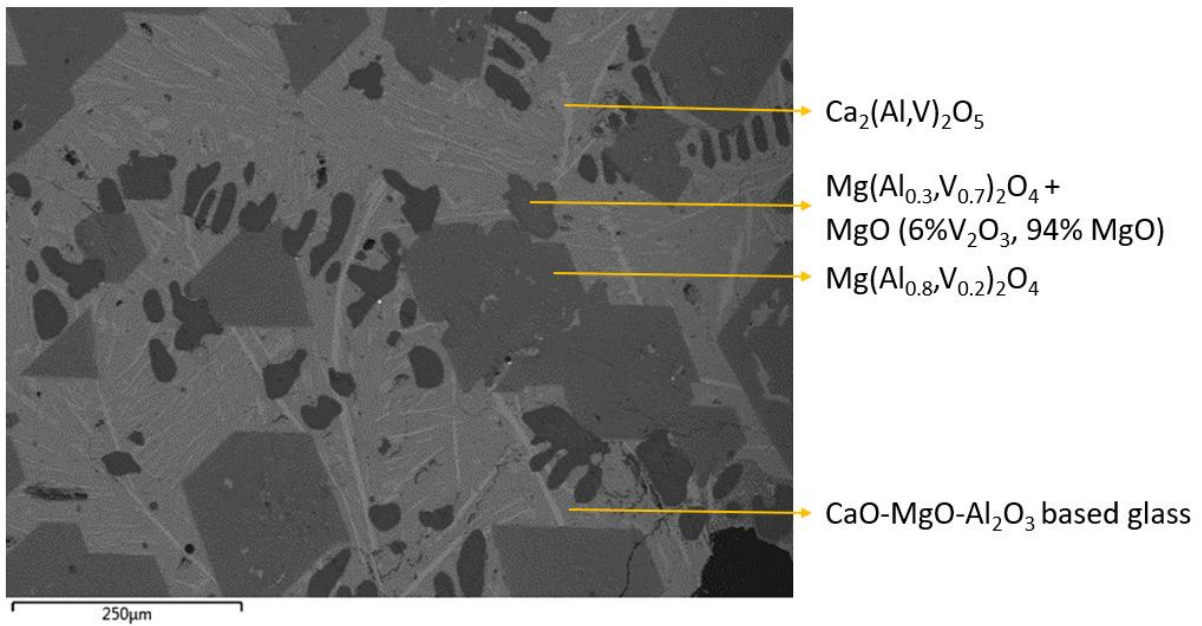


Figure 5.26: Electron backscatter image of the slag formed in test D.

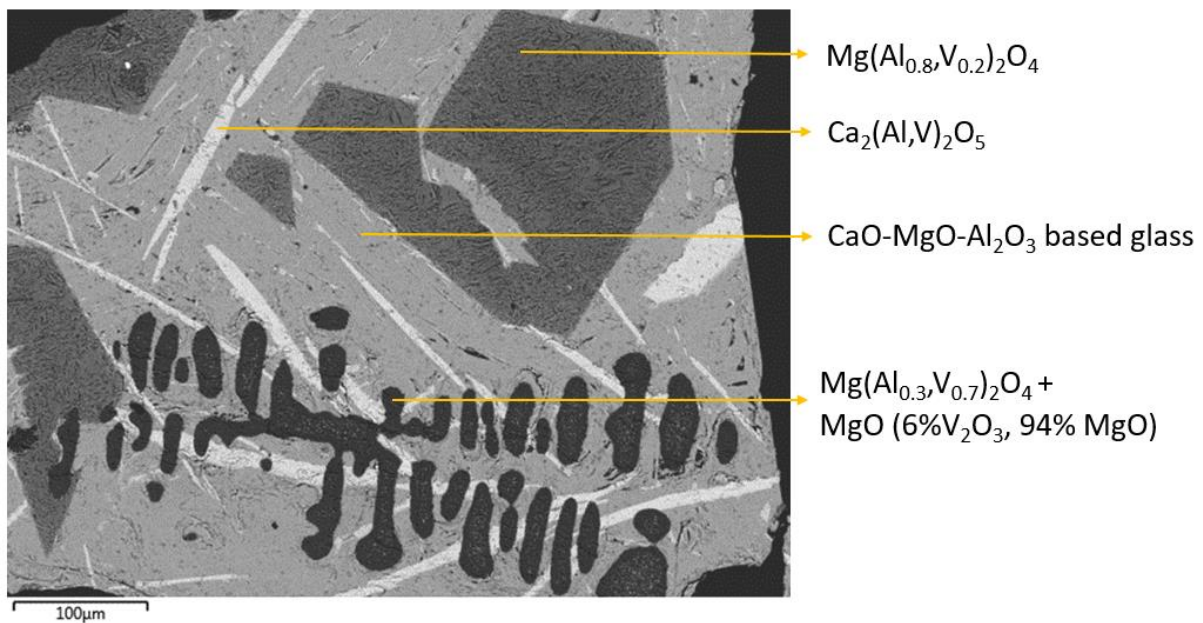


Figure 5.27: Electron backscatter image of the slag formed in test E.

A metal droplet recovered from test E is shown in Figure 5.28. The metal droplet had some slag entrained inside the droplet. The compositions of the metal droplet was 70.5 wt% V, 28.8 wt% Fe and 0.7 wt% Al. The composition of the metal from the baseline test D and test E are almost the same.

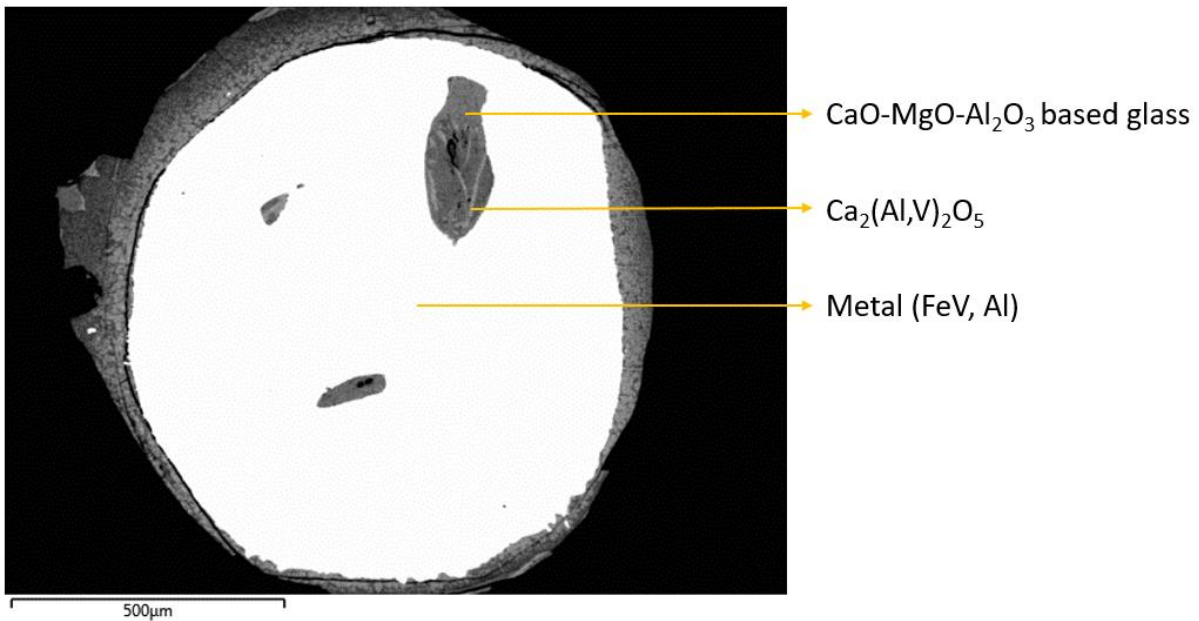


Figure 5.28: Electron backscatter image of a metal droplet recovered from test E.

The phases present in the slag of test F (Figure 5.29) are the same as the phases present in test E. The amount of each phase changed from test E to test F. The spinel content decreased from 15.4 % to 4 % and the $\text{Ca}_2(\text{Al},\text{V})_2\text{O}_5$ phase increased from 5.4 % to 10.6 %. An increase in the $\text{Ca}_2(\text{Al},\text{V})_2\text{O}_5$ phase will increase vanadium losses to the slag and is therefore detrimental to metal recovery.

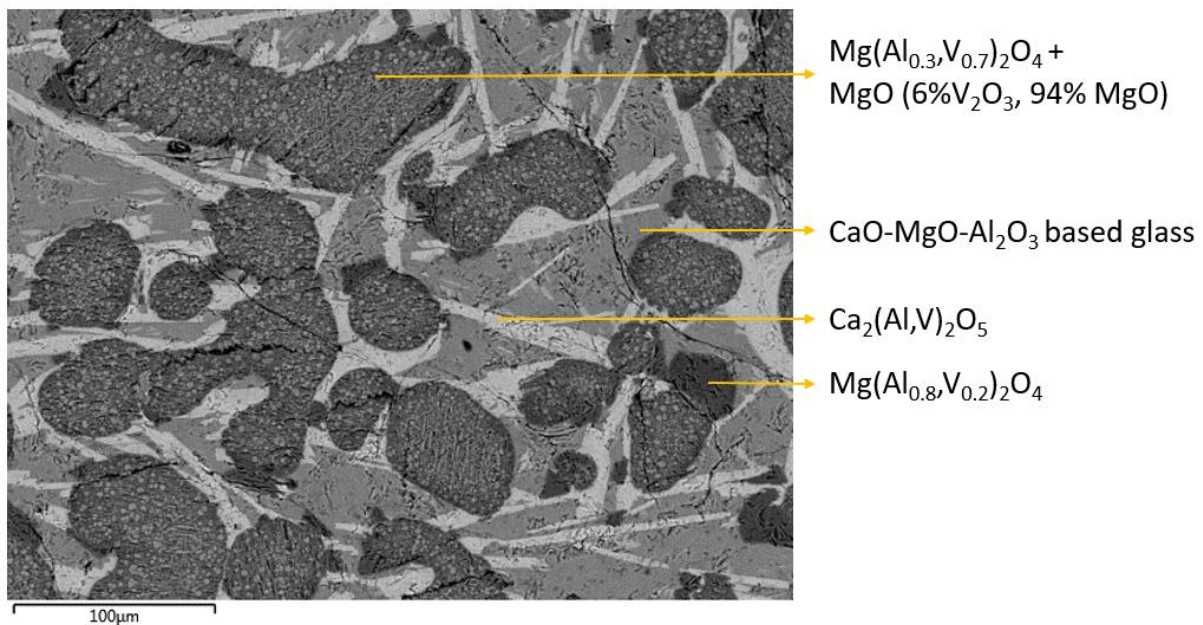


Figure 5.29: Electron backscatter image of the slag formed in test F.

The metal composition of test F (Figure 5.30) was 72 wt% V, 27.5 wt% Fe and 0.5 wt% Al. The vanadium and aluminium content of the metal from test F was slightly lower than for test E.

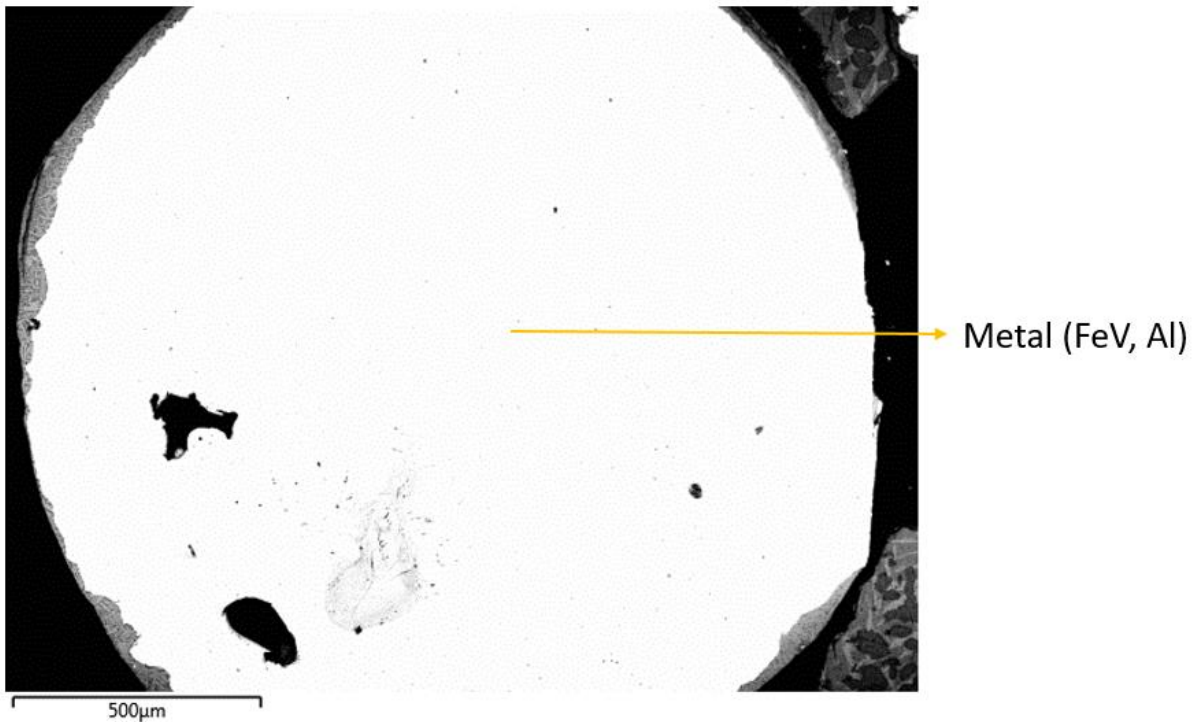


Figure 5.30: Electron backscatter image of a metal droplet recovered from test F.

The composition of the slag of test G contained $\text{Ca}_2(\text{Al},\text{V})_2\text{O}_5$, $\text{Mg}(\text{Al}_{0.3},\text{V}_{0.7})_2\text{O}_4$, MgO_{ss} , $\text{Ca}_3\text{Al}_2\text{O}_6$ and a CaO-MgO- Al_2O_3 based glassy phase (Figure 5.31). The same oxide phases, $\text{Ca}_2(\text{Al},\text{V})_2\text{O}_5$, $\text{Mg}(\text{Al}_{0.3},\text{V}_{0.7})_2\text{O}_4$ and MgO_{ss} , were also present in test F, but the phase $\text{Ca}_3\text{Al}_2\text{O}_6$ was not present in test F. The spinel phase ($\text{Mg}(\text{Al}_{0.8},\text{V}_{0.2})_2\text{O}_4$) is present in test F but not in test G, which can be explained by plotting the slag compositions on a ternary phase diagram (Figure 5.32).

The slag compositions for tests E, F and G are shown in Figure 5.32. The slag compositions E and F are in the MgAl_2O_4 - CaAl_2O_4 - MgO Alkemade triangle, which indicated that MgAl_2O_4 , CaAl_2O_4 and MgO (in this instance CaAl_2O_4 is replaced by $\text{Ca}_2(\text{Al},\text{V})_2\text{O}_5$ due to the presence of vanadium) will be present at 25°C. Composition G is in the $\text{Ca}_{12}\text{Al}_{14}\text{O}_{33}$ - $\text{Ca}_3\text{Al}_2\text{O}_6$ - MgO Alkemade triangle which explains the presence of $\text{Ca}_3\text{Al}_2\text{O}_6$. Although MgAl_2O_4 should not be present, a fair amount of $\text{Mg}(\text{Al},\text{V})_2\text{O}_4$ exsolved from the MgO , presumably due to cooling. The $\text{Ca}_{12}\text{Al}_{14}\text{O}_{33}$ phase is not present because of the presence of vanadium, which results in the formation of $\text{Ca}_2(\text{Al},\text{V})_2\text{O}_5$ rather than $\text{Ca}_{12}\text{Al}_{14}\text{O}_{33}$.

Metal inclusions were also present in the slag (metal inclusions in the slag were visible in all the tests, but were not always present in the electron backscatter images chosen). The concentration of $\text{Ca}_2(\text{Al},\text{V})_2\text{O}_5$ increased from 10.6 % to 28 % of the surface area in tests E to G.

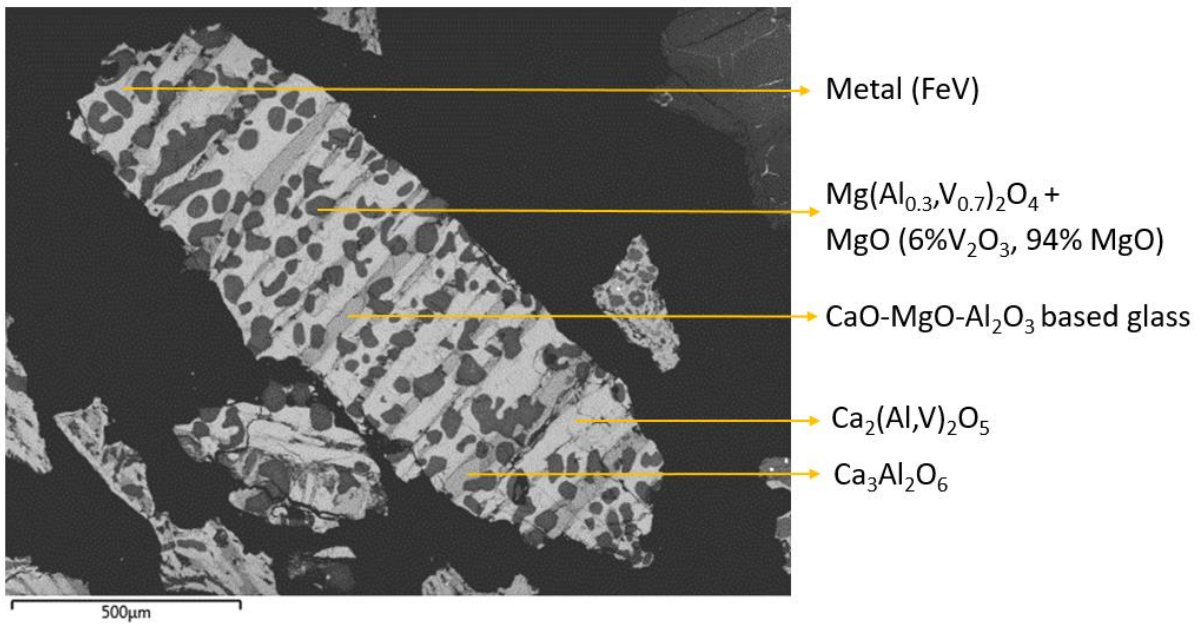


Figure 5.31: Electron backscatter image of the slag formed in test G.

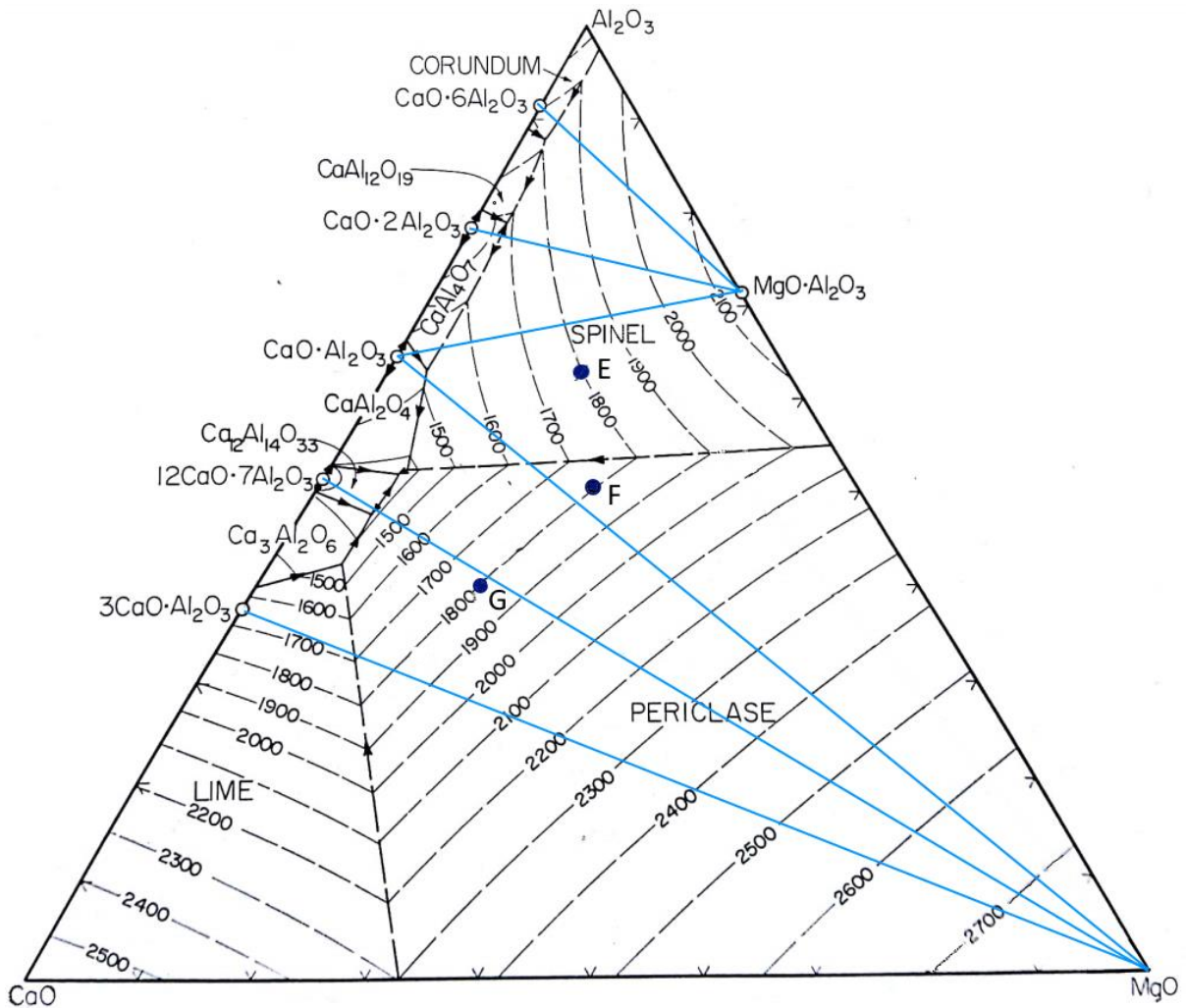


Figure 5.32: CaO- Al₂O₃ -MgO ternary phase diagram with slag compositions of tests E, F and G and Alkemade triangles projected onto it.

The composition of the metal in test G was 69 wt % V, 30.1 wt % Fe and 0.9 wt % Al. The vanadium content of the metal from test G is slightly lower than in the other three tests.

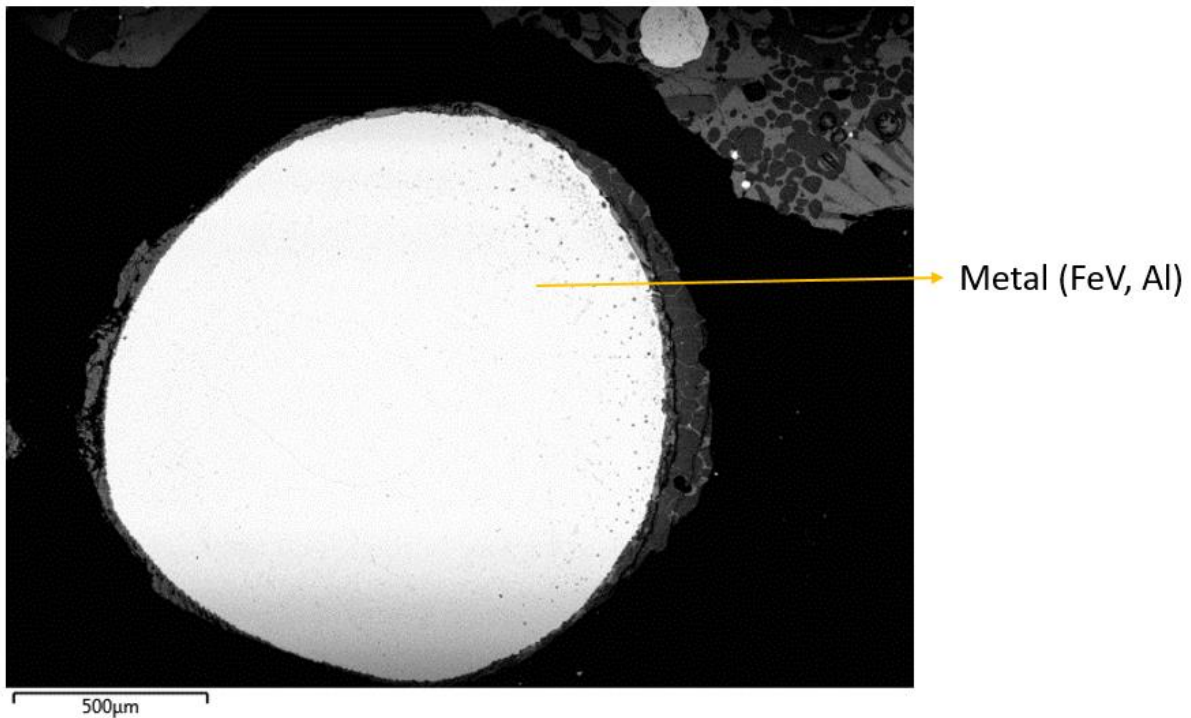


Figure 5.33: Electron backscatter image of a metal droplet recovered from test F.

5.2.3 XRD results versus SEM-EDS results

Comparisons of the results obtained using XRD and SEM-EDS for the spinel and $\text{Ca}_2(\text{Al},\text{V}_2)_2\text{O}_7$ phases are shown in Table 5.13 and

Table 5.14. The comparison between the SEM-EDS and XRD results correlate well. The amount of each phase present cannot be compared to the theoretical values because a ternary phase diagram containing $\text{Ca}_2(\text{Al},\text{V}_2)_2\text{O}_7$ would be required to determine such values. The values obtained for the amount of spinel and $\text{Ca}_2(\text{Al},\text{V}_2)_2\text{O}_7$ phases present can be accepted as accurate due to the good correlation between the SEM-EDS and XRD results. The area analyses using ImageJ was conducted by analysing three areas of each sample at magnifications between 100x and 150x.

Table 5.13: Comparison of the amount of spinel present in the different slag samples determined using XRD and SEM-EDS (in conjunction with ImageJ).

Slag sample	SEM-EDS (Image J) (wt%)	Standard deviation	XRD (wt%)	Standard deviation
D	23.6	0.9	26.1	1.1
E	15.4	0.8	14.7	0.7
F	4.0	0.3	4.3	0.3
G	0.0	-	0.0	-

Table 5.14: Comparison of the amount of $\text{Ca}_2(\text{Al,V}_2)_2\text{O}_7$ present in the different slag samples determined using XRD and SEM-EDS (in conjunction with ImageJ).

Slag sample	SEM-EDS (Image J) (wt%)	Standard deviation	XRD (wt%)	Standard deviation
D	3.0	0.3	2.7	0.2
E	5.4	0.4	3.9	0.3
F	10.6	0.6	9.2	0.6
G	28.0	0.7	26.5	0.8

5.3 The effect of adding excess aluminium to the recovery of vanadium

5.3.1 Background

Metal-slag interaction tests were done to determine the effect of changing the amount of aluminium added on the vanadium recovery in the ferrovanadium production process. Three tests were done, each with a different amount of aluminium added to the reagent mixture. V_2O_3 , iron, aluminium and flux (CaO and MgO) were crushed and mixed, where after the mixture was added to a MgO crucible. The test sample was then heated to 1800°C and held at this temperature for 2 hours, where after the sample was manually cooled at an estimated rate of 20°C/min to room temperature. It was notable that the cooling rate for sample C2 was higher than for samples C1 and C3. The sample was then sectioned in order to do SEM-EDS analysis.

5.3.2 XRD results

XRD analysis was performed on the slag retrieved (Table 5.15) from the excess aluminium tests (C1-C3) and slag composition tests (D-G). The slag analyses for tests C1 and C3 were almost identical, but C2 indicated a variation in the amount of each component present. The reason for the variation is due to the MgO-CaO- Al_2O_3 based glassy phase content being higher for C2 than for C1 and C3, which would be due to a higher cooling rate for test C2 (as the solidus temperature of the slag remained the same, the glassy phase content is dependent on the cooling rate).

The cooling rate was controlled manually and although care was exercised to replicate the cooling rate, some variation would have occurred between tests. The increased cooling rate resulted in less time being available for the MgO and $\text{Mg}(\text{Al,V})_2\text{O}_4$ to precipitate out of the liquid before the solidus temperature was reached, which resulted in less MgO and $\text{Mg}(\text{Al,V})_2\text{O}_4$ being present and more MgO- Al_2O_3 -CaO glassy phase being present.

Tests D-G also showed a change in MgO- Al_2O_3 -CaO glassy content, with the MgO- Al_2O_3 -CaO glassy content decreasing from D-G (with the exception of D-E). In the case of tests D-G, it

was not certain if the MgO-Al₂O₃-CaO glassy content is due to the cooling rate or the solidus temperature, because the presence of vanadium changes the slag system from the CaO-MgO-Al₂O₃ ternary system to the quaternary CaO-MgO-Al₂O₃-V₂O₃ system. A clear trend is however present for the Ca₂(Al,V)₂O₅ and Mg(Al,V)₂O₄ phases. The Ca₂(Al,V)₂O₅ phase increased as the composition was changed from D to G and the Mg(Al,V)₂O₄ content decreased as the composition was changed from D to G. Mg(Al,V)₂O₄ was not present in test G, where Ca₃Al₂O₆ formed instead of Mg(Al,V)₂O₄.

Table 5.15: XRD results of the slag compositions for tests C1-C3 and D-G (wt. %).

Sample	MgO	Ca ₂ (Al,V) ₂ O ₅	Mg(Al,V) ₂ O ₄	Ca ₃ Al ₂ O ₆	Glassy phase
C1 and D	20.6	2.7	26.1	0	50.6
C2	9.8	2.8	21.9	0	65.5
C3	20.9	1.4	29	0	48.7
E	16.5	3.9	14.7	0	64.9
F	42.2	9.2	4.3	0	44.3
G	36.0	26.5	0	4.1	33.4

A relationship between the metal recovery with changing spinel content could not be established, since the recovery decreased as the total spinel content decreased. This is the opposite of what should have been observed if there were to be a relationship between the metal recovery and the spinel content. A factor contributing to this phenomenon is the increase in MgO-V₂O₃ solid solution and Ca₂(Al,V)₂O₅ formation as the spinel content decreases. The aforementioned phases contain V₂O₃, therewith decreasing the vanadium recovery even though the spinel phase content decreased. The increase in MgO-V₂O₃ solid solution and Ca₂(Al,V)₂O₅ formation as the composition is changed from D to G resulted in higher V₂O₃ losses to the slag even though the spinel phase content decreased. The other factor that contributes to this phenomenon is the increase in slag volume as the composition is changed from D to G.

5.3.3 Sample C1 (1.5 wt% Al) SEM-EDS analysis

5.3.3.1 Metal analysis

The metal that had formed consisted of two phases as indicated in Figure 5.34. The compositions of the phases were determined as the average of three areas analysed on the sample. The bright phase is ferrovandium (29.3 wt% Fe, 70 wt% V, 0.7 wt% Al) and the darker phase is vanadium (100% V). The total composition of the metal was 28.6 wt% Fe, 71 wt% V and 0.4 wt % Al.

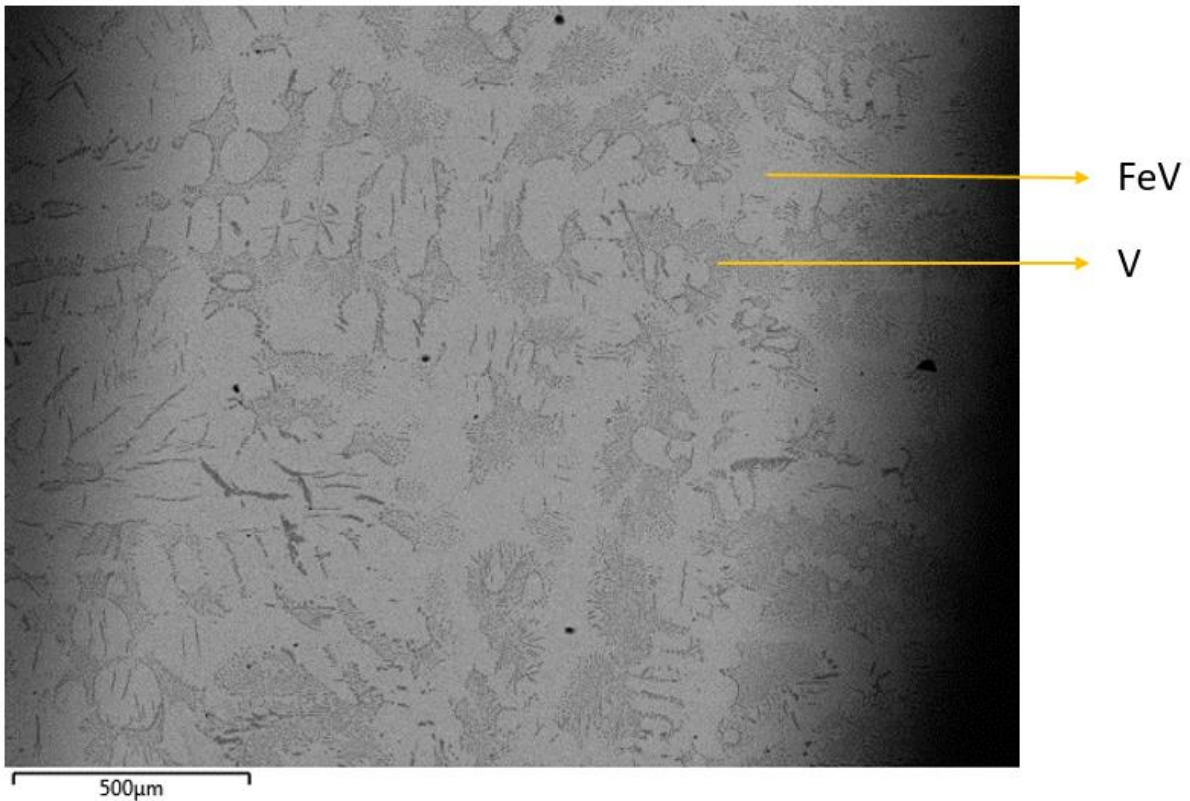


Figure 5.34: Electron backscatter image of the metal that separated from the slag of sample C1 (magnification of 60x).

Figure 5.35 is a higher magnification image of the metal (Figure 5.34), from which it is evident that two phases were present in the metal, one consisting of ferrovanadium and one consisting of vanadium. The crystal structure indicated that ferrovanadium formed as a primary phase (evident by the presence of round ferrovanadium nodules). The secondary phases consisted of a combination of ferrovanadium and vanadium. The secondary phases form upon cooling when the sample enters the $\alpha+\sigma$ region, which results in the formation of σ (35 wt% Fe, 65 wt% V) and α (13 wt% Fe, 87 wt% V) according to the Fe-V phase diagram (Figure 5.36).

The compositions obtained from the SEM-EDS analysis of the two phases present in the metal differs from the compositions reported in the iron-vanadium phase diagram, with both phases containing a higher vanadium content than was expected (the values obtained from the iron-vanadium phase diagram).

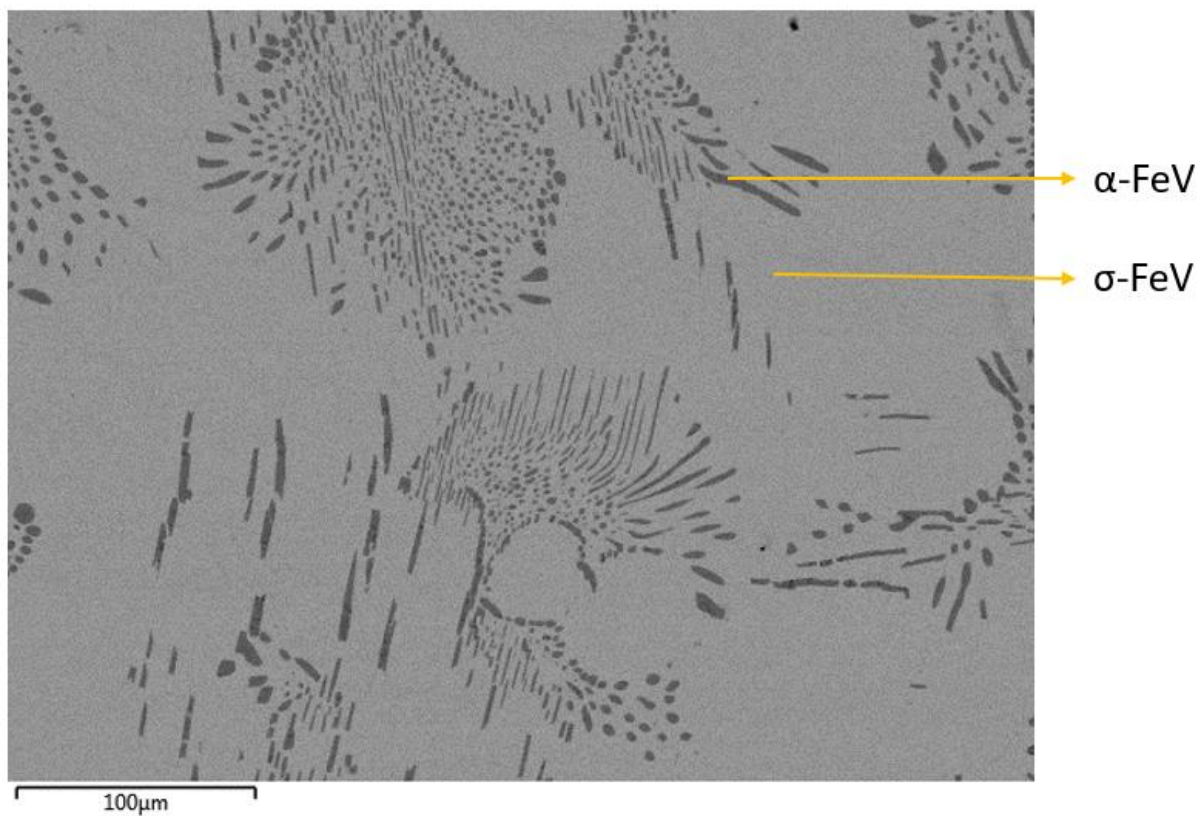


Figure 5.35: Electron backscatter image of the metal that separated from the slag of sample C1 (magnification of 300x).

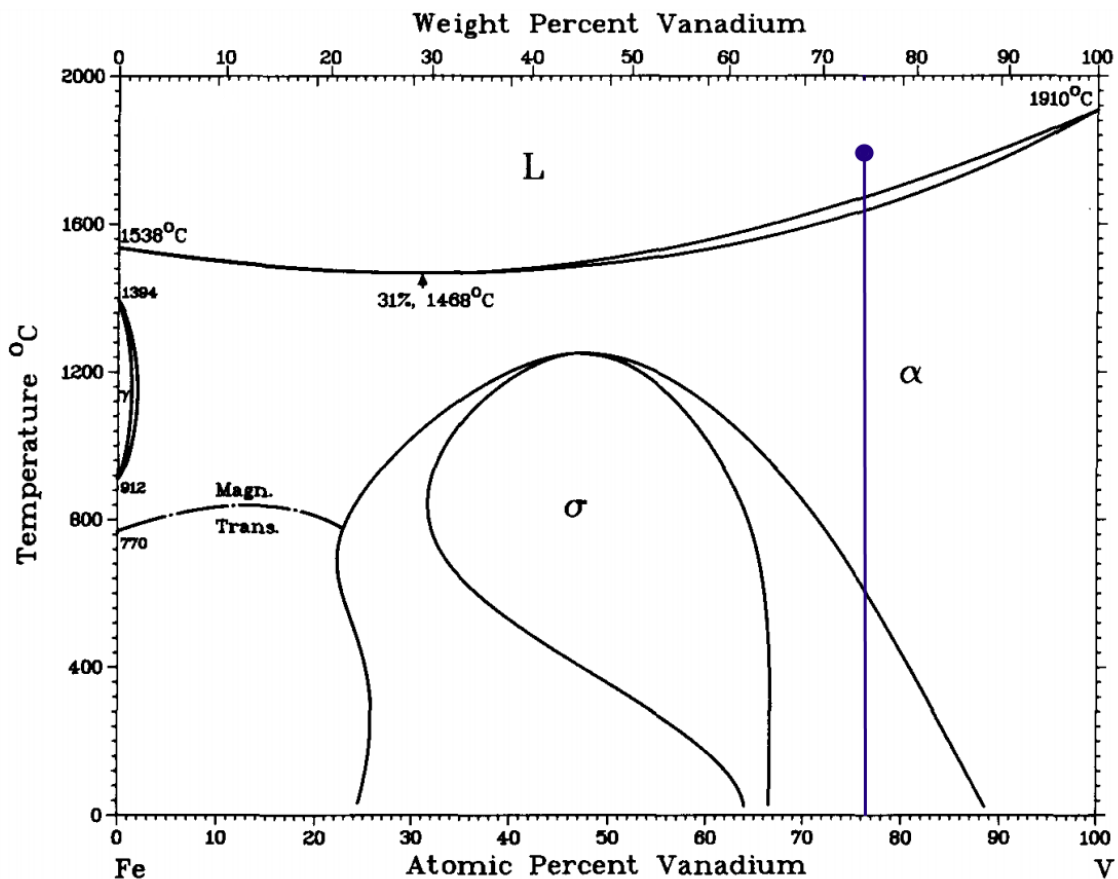


Figure 5.36: Iron-vanadium phase diagram indicating the equilibrium phases that are expected to form from a liquid consisting of 26 wt% Fe, 74 wt% V on cooling (Smith, 1984).

5.3.3.2 Slag-metal interface analysis

The slag-metal interface region of sample C1 is shown in Figure 5.37, from which it is evident that an interfacial layer formed between the slag and the metal. The interfacial layer also contained a high concentration of small metal droplets. The slag contained $\text{Mg}(\text{Al}_{0.88}, \text{V}_{0.12})_2\text{O}_4$, $\text{Ca}_2(\text{Al}, \text{V})_2\text{O}_4$, MgO_{ss} , $\text{Mg}(\text{Al}_{0.3}, \text{V}_{0.7})_2\text{O}_4$ and a glassy $\text{CaO-MgO-Al}_2\text{O}_3$ oxide phase. The slag-refractory interaction tests indicated that the slag phases MgAl_2O_4 , CaAl_2O_4 and $\text{Ca}_{12}\text{Al}_{14}\text{O}_{33}$ were present. The slag phases present in the metal-slag interaction tests differ from the slag phases in the slag-refractory interaction tests due to the presence of vanadium. The presence of vanadium resulted in the formation of $\text{Ca}_2(\text{Al}, \text{V})_2\text{O}_4$ instead of CaAl_2O_4 , as well as substitution of V^{3+} into the Al^{3+} position of the MgAl_2O_4 phase to form $\text{Mg}(\text{Al}_{0.88}, \text{V}_{0.12})_2\text{O}_4$ and $\text{Mg}(\text{Al}_{0.3}, \text{V}_{0.7})_2\text{O}_4$. Vanadium present as V_2O_3 also went into solid solution with MgO (the possibility of this is evident from the MgO_{ss} region in Figure 5.38)

The interfacial layer is constituted of a spinel structure and a $\text{MgO-V}_2\text{O}_3$ solid solution. The spinel structure contained both V^{3+} and Al^{3+} in the second cation position. The phase contained more V^{3+} than Al^{3+} and acted as a barrier between the slag and the metal phases.

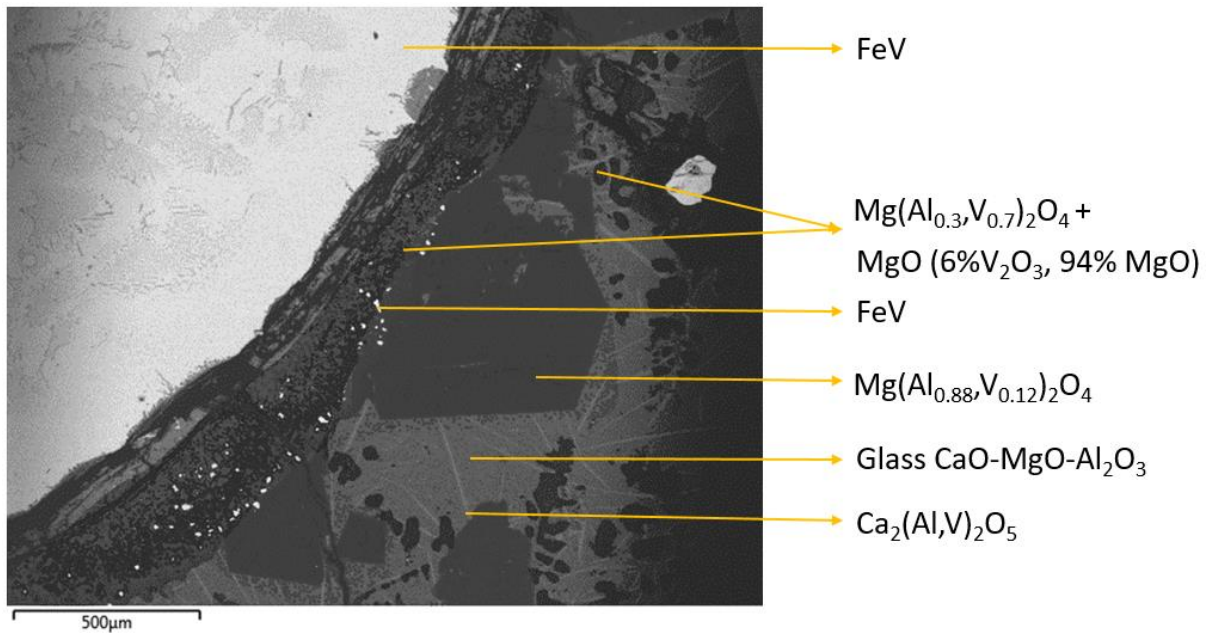


Figure 5.37: Electron backscatter image of the interface between the slag and the metal of sample C1 (magnification of 60x).

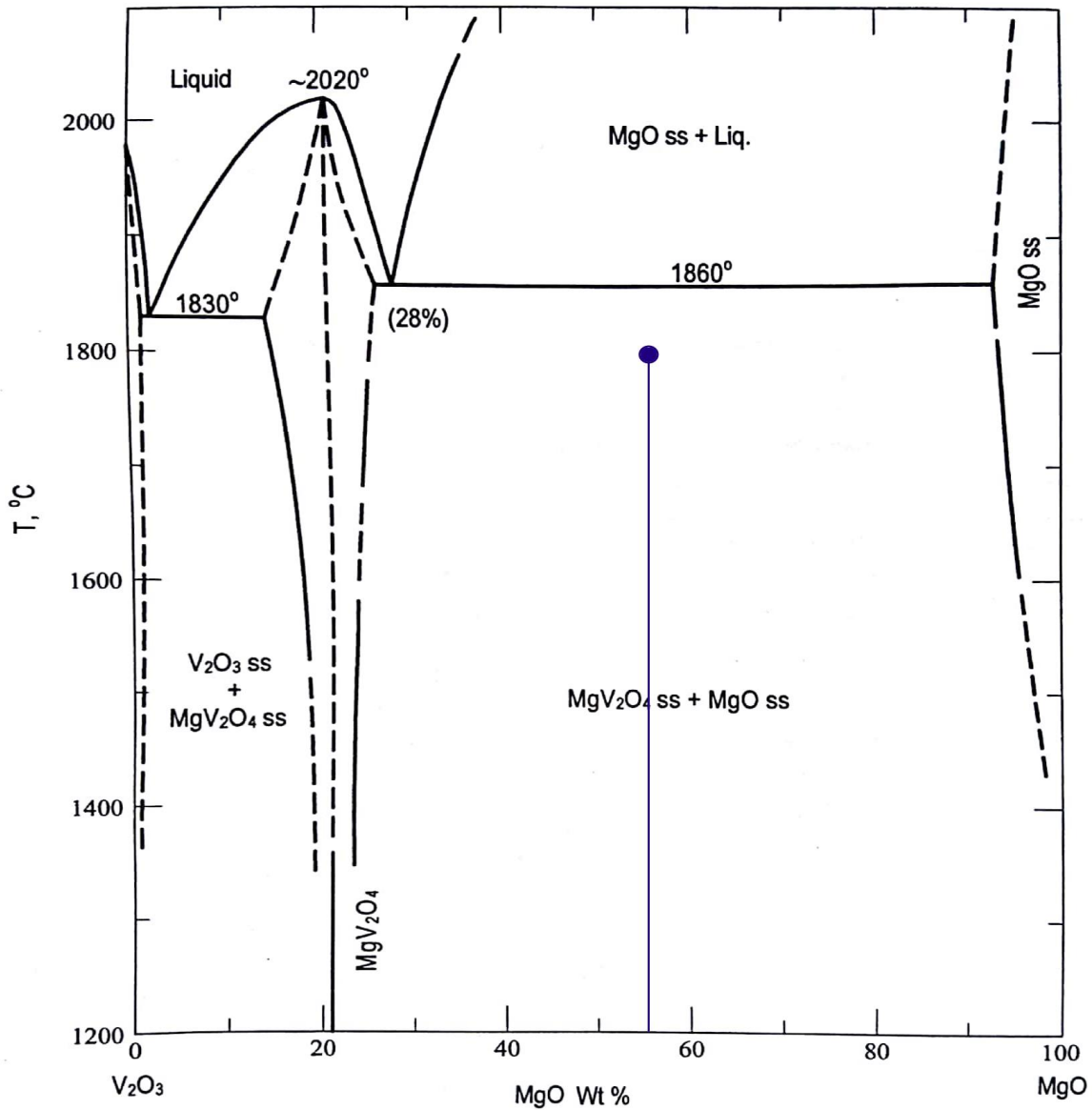


Figure 5.38: MgO-V₂O₃ phase diagram with a plot of the localised cooling of the double phase region (Cini, 1968).

The interface between the metal and the slag is shown under high magnification in Figure 5.39. The interfacial layer consisted of two oxide phases and a high concentration of ferrovanadium inclusions. The two oxide phases were Mg(Al_{0.3},V_{0.7})₂O₄ and a MgO solid solution phase with a composition of 94% MgO and 6% V₂O₃.

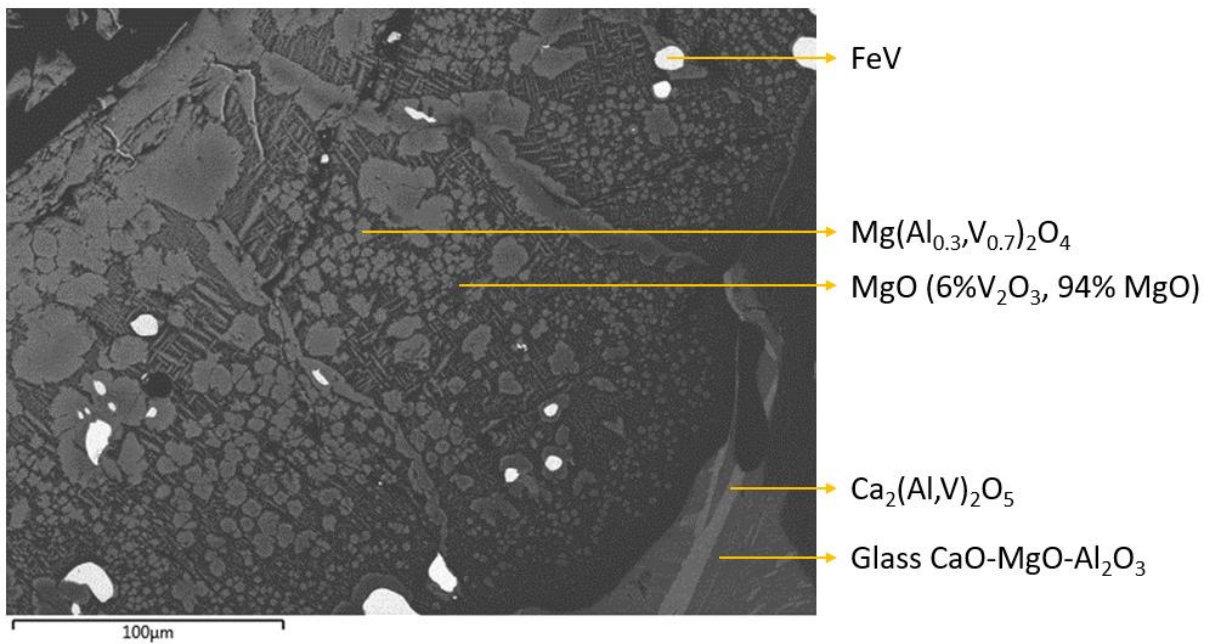


Figure 5.39: Electron backscatter image of the interface between the slag and the metal of sample C1 (magnification of 430x).

The upper region of the slag (Figure 5.40) contained only trace amounts of ferrovanadium metal droplets, indicating that good separation had taken place. The slag was constituted of three oxides that contained vanadium, two of which were due to V^{3+} substituting for Al^{3+} and one phase where MgO and V_2O_3 were in solid solution. Vanadium was therefore lost mainly due to the ability of the slag phases to accommodate V^{3+} in their respective structures. The presence of the MgO- V_2O_3 solid solution phase indicated that it not only forms at the interface between the metal and the slag, but also forms part of the phase chemistry of the slag. The V^{3+} containing spinel, $Mg(Al_{0.3},V_{0.7})_2O_4$, was however not present in the upper region of the slag.

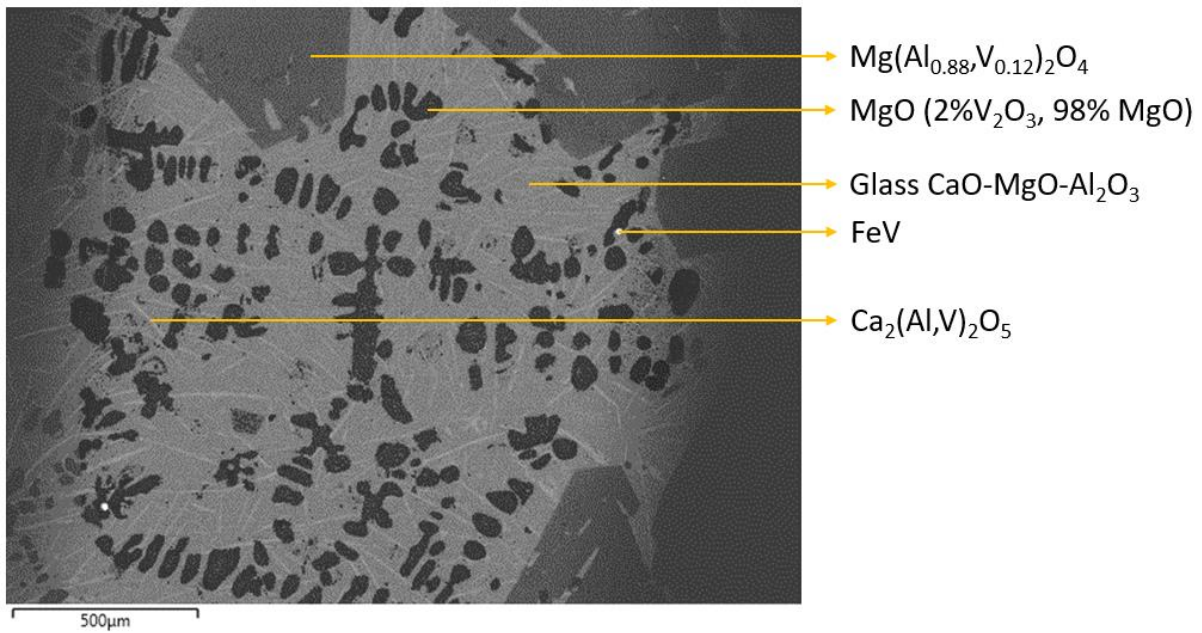


Figure 5.40: Electron backscatter image of the upper region of the slag of sample C1 (magnification of 110x).

The lower region of the slag (Figure 5.41) contained a larger amount of ferrovanadium inclusions compared to the upper region of the slag. The MgO solid solution phase contained a higher concentration of V_2O_3 in the lower region of the slag.

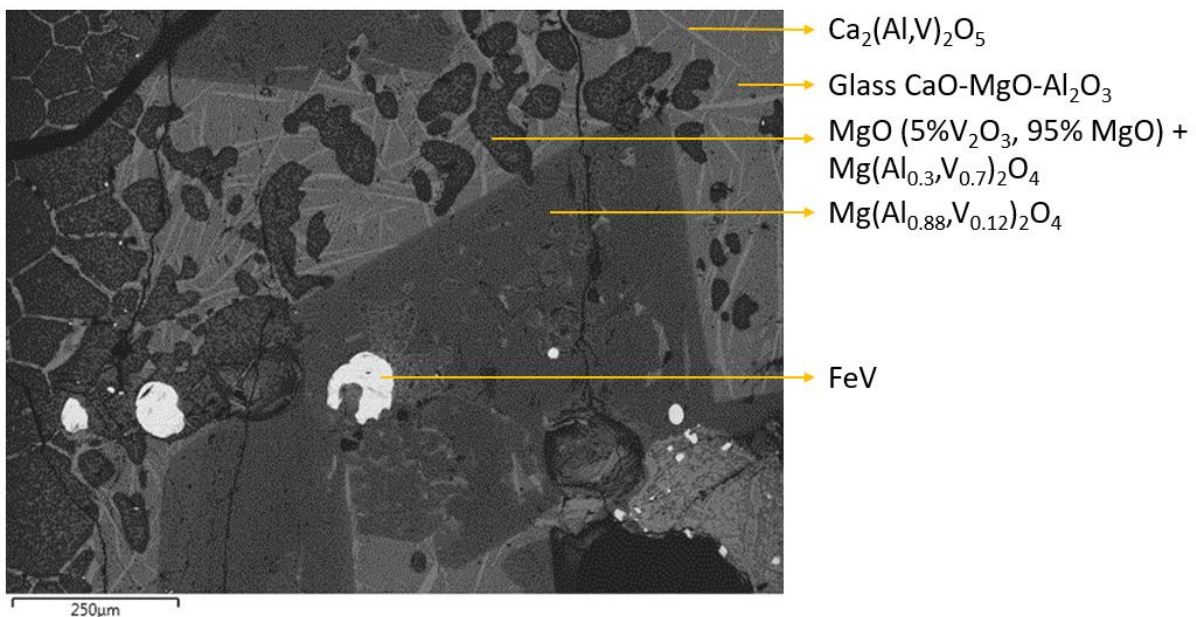


Figure 5.41: Electron backscatter image of the bottom region of the slag of sample C1 (magnification of 110x).

The $\text{MgO-V}_2\text{O}_3$ solid solution phase that precipitated $\text{Mg}(\text{Al}_{0.3}, \text{V}_{0.7})_2\text{O}_4$ crystals is visible in Figure 5.42. The $\text{MgO-V}_2\text{O}_3$ solid solution phase hosted the $\text{Mg}(\text{Al}_{0.3}, \text{V}_{0.7})_2\text{O}_4$ phase, which formed as small precipitates within the hosting phase. The reason for both phases being present is that the V_2O_3 concentration is high, which results in a vanadium rich spinel phase

precipitating out on cooling, as indicated in Figure 5.38. The total composition of the region where $\text{MgO}_{(ss)}$ and $\text{MgV}_2\text{O}_4_{(ss)}$ are present is plotted on the $\text{MgO-V}_2\text{O}_3$ phase diagram in Figure 5.38.

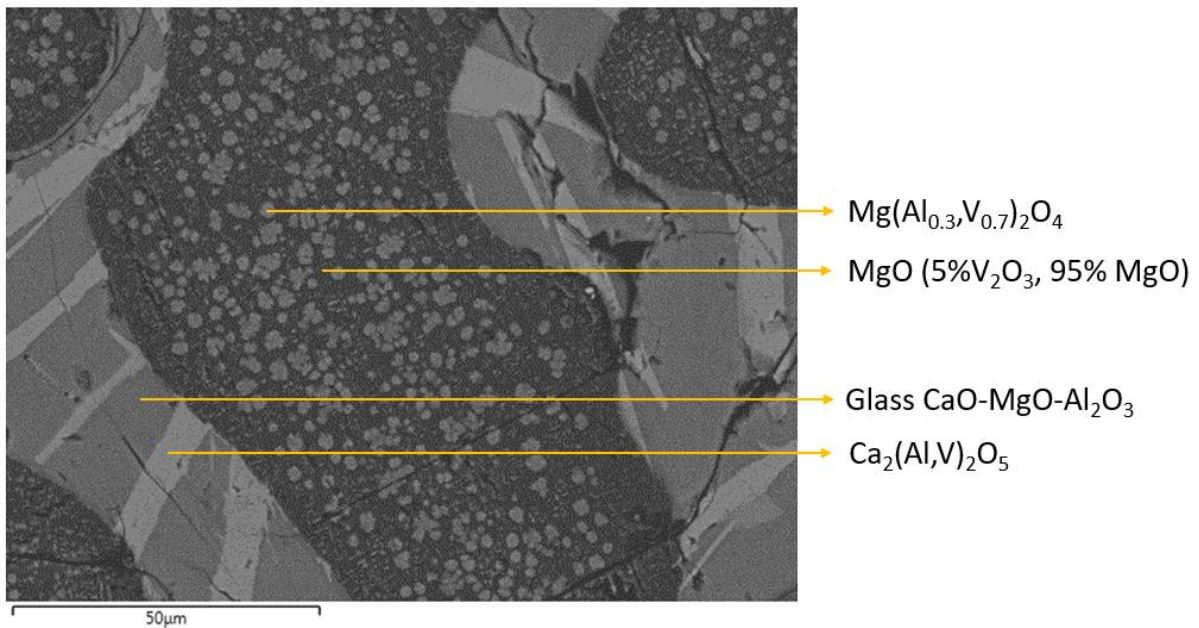


Figure 5.42: Electron backscatter image of sample C1 at a higher magnification of the bottom region of the MgO solid solution phase containing a vanadium rich spinel phase.

5.3.3.3 Slag-refractory interaction

The interface between the slag and the MgO crucible was analysed (Figure 5.43) as it represents the interaction of the slag with the MgO refractory in industry. The slag consisted mainly of $\text{CaO-Al}_2\text{O}_3$ components, but also contained MgAl_2O_4 and trace amounts of the MgO solid solution phase. In order to obtain a better idea of what occurred at the interface of the refractory, an image was analysed at a higher magnification (Figure 5.44).

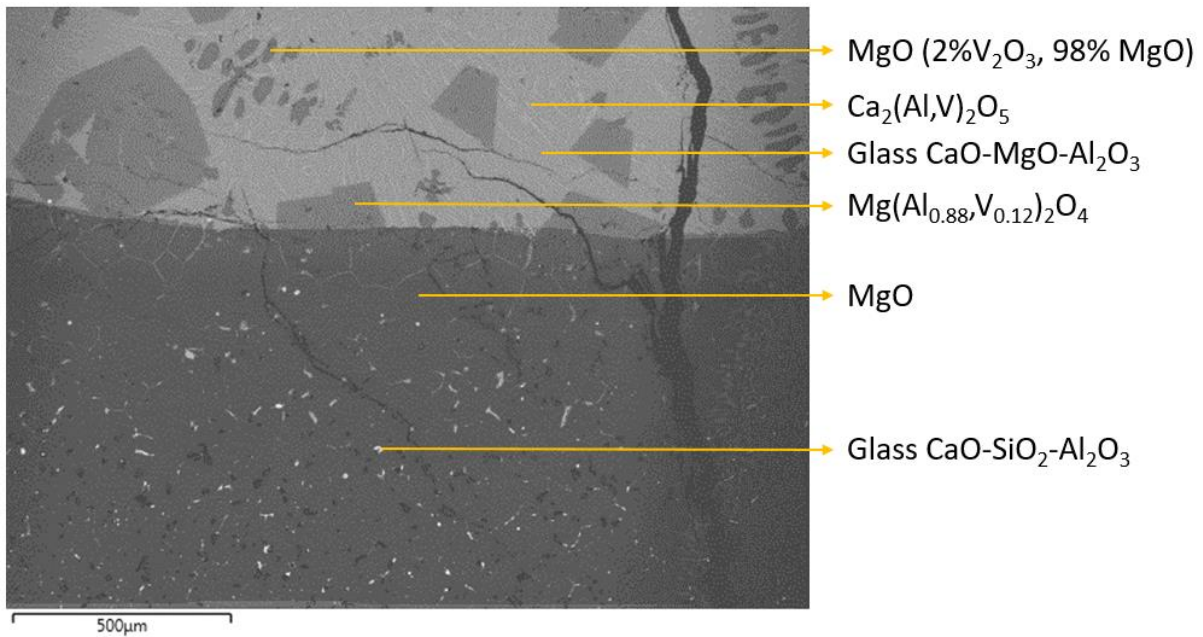


Figure 5.43: Electron backscatter image of the slag-refractory (MgO crucible) interface.

The interaction between the slag and the refractory is evident in Figure 5.44. The MgAl₂O₄ spinel phase (containing V³⁺) formed on the surface of the refractory, as well as in the pores of the refractory. The refractory region in contact with the slag also contained V₂O₃, which was in solid solution with MgO. Refractory wear occurs when the slag diffuses into the MgO refractory and then reacts with the MgO to form MgAl₂O₄.

MgO dissolution into the slag will occur until the slag is saturated in MgO, which highlights the importance of adding enough MgO to the slag in order to prevent refractory wear. MgAl₂O₄ has the ability to accommodate V³⁺ within its structure, resulting in vanadium losses to the slag. MgO can also take V₂O₃ into solid solution, which resulted in further losses of vanadium.

Tests D to G indicated that the solid solution between MgO and V₂O₃ had vanadium contents between 14 wt% and 20 wt%. The contribution of MgO-V₂O₃ solid solution to the total loss of vanadium as V₂O₃ were 35 %, 47 %, 75 % and 58 % for tests D, E, F and G respective. The contribution was determined based on average vanadium content determined in each test for the various phases, along with the phase composition of the slag.

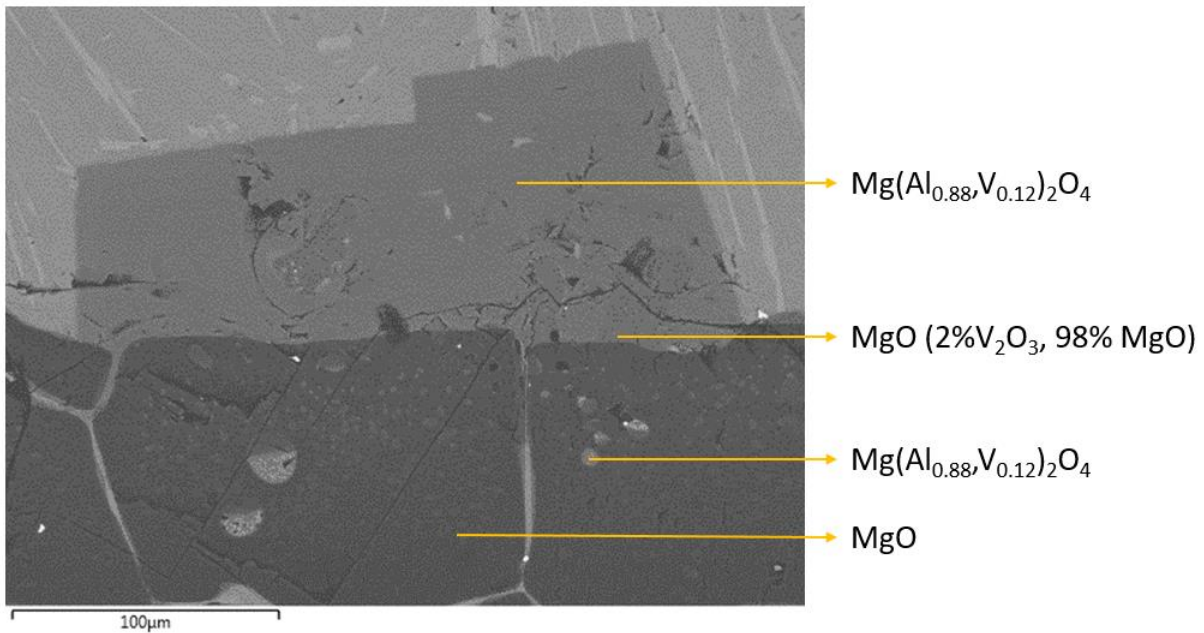


Figure 5.44: Electron backscatter image of the slag-crucible interface at a magnification of 430x.

5.3.4 Comparison between samples C1, C2 and C3

SEM-EDS analysis was used to determine the slag phases that were present, as well as determining the composition of the metal that had formed.

5.3.4.1 Metal recovery as a function of aluminium added

The amount of aluminium added was varied in order to determine the effect of adding excess aluminium to the reaction on the amount of metal recovered. The excess aluminium added to the reaction should reside in the metal if it does not oxidise. The slag composition was held constant and should therefore contain the same slag phases (for all 3 tests that were done).

The phases that formed in sample C1 are MgO_{ss} , $\text{Mg}(\text{Al}_{0.3}, \text{V}_{0.7})_2\text{O}_4$, $\text{Mg}(\text{Al}_{0.8}, \text{V}_{0.2})_2\text{O}_4$, $\text{Ca}_2(\text{Al}, \text{V})_2\text{O}_5$ and a $\text{CaO-MgO-Al}_2\text{O}_3$ based glassy phase (Figure 5.45).

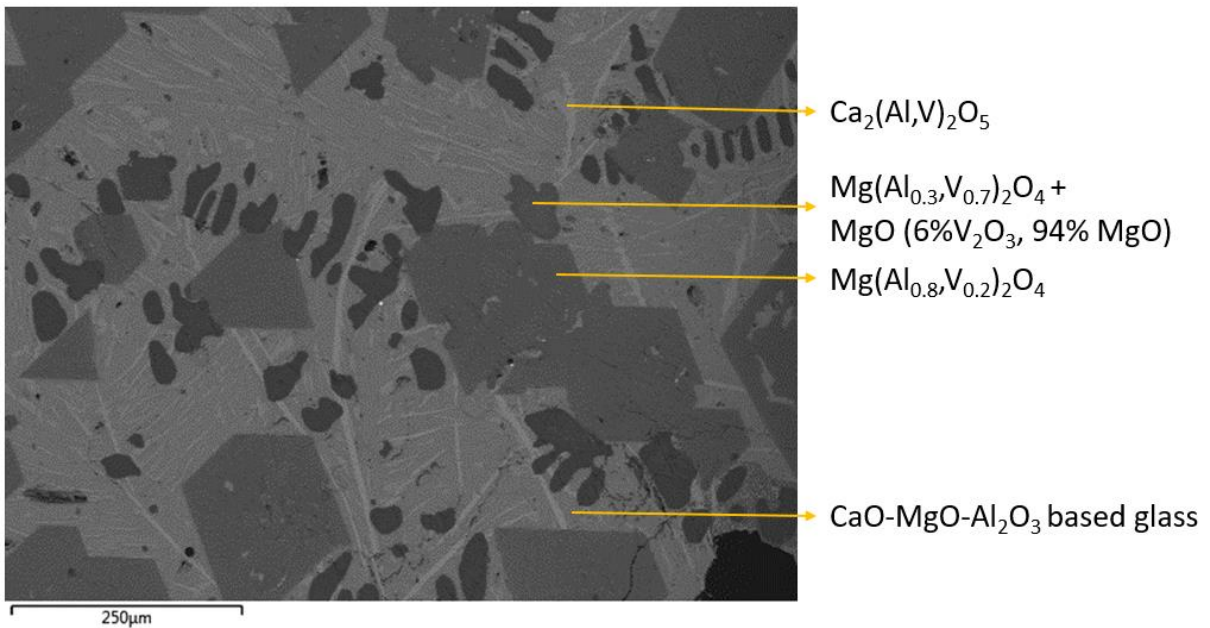


Figure 5.45: Electron backscatter image of the slag formed in the test of sample C1 where 1.5wt% excess aluminium was added.

The composition of the metal of sample C1 (Figure 5.45) was 28.6 wt% Fe, 71 wt% V and 0.4 wt % Al. The expected aluminium content was 1.5 wt % Al because 1.5 wt% excess aluminium was added to the reaction. The difference in expected and actual aluminium content suggested that the aluminium had reacted with other components in the furnace. The probable reaction is the reaction between aluminium and trace amounts of O_2 present in the furnace, with the O_2 being present because of the constant flow of Ar (purity Ar \geq 99.997%) into the system.

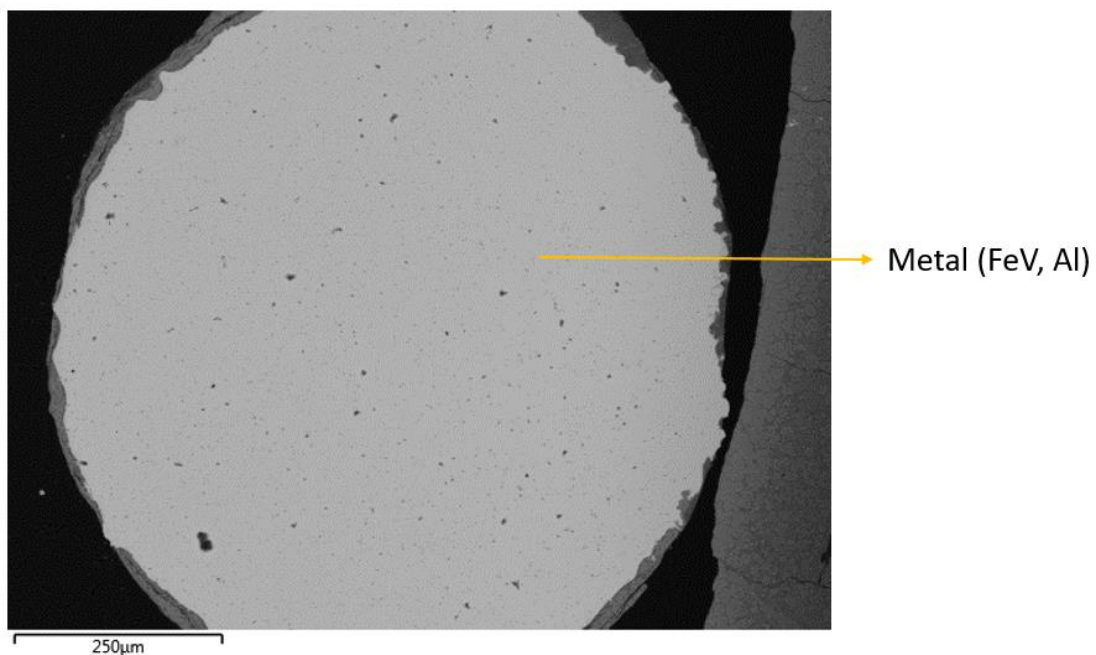


Figure 5.46: Electron backscatter image of the metal formed of sample C2 that contained slag in the centre of the metal drop.

The various phases present in the slag from the test where 3.5 wt% excess aluminium was added is shown in Figure 5.47. It is evident from the image that the same phases were present compared to the results from the 1.5 wt% excess aluminium test.

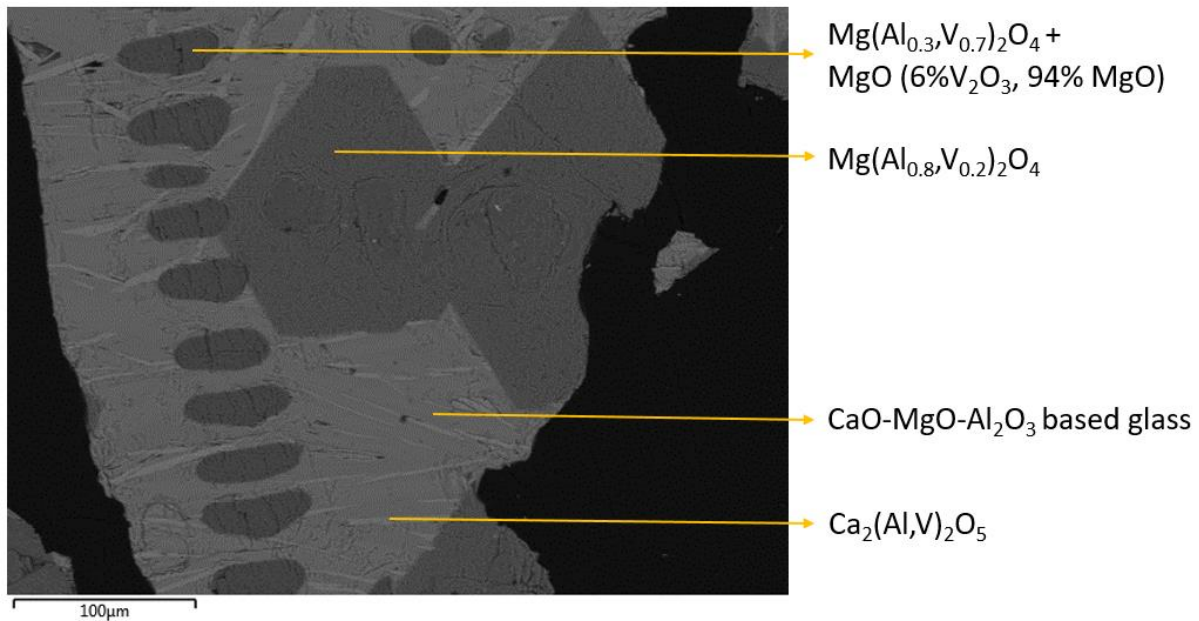


Figure 5.47: Electron backscatter image of the slag of sample C2.

The metal consisted of 68.6 wt% V, 30 wt% Fe and 1.4 wt% Al. The aluminium content increased from the 1.5 wt% excess aluminium test, but was lower than the 3.5 wt% aluminium content that was expected. The difference was due to aluminium oxidation that occurred inside the furnace. The metal did contain entrained slag as indicated in Figure 5.48. The metal also contained a region where two metal phases were present as indicated in Figure 5.48 and Figure 5.49. The σ -ferrovanadium phase had a composition of 68 wt% V; 32 wt% Fe and the α -F phase had a composition of 98 wt% V; 2 wt% Fe.

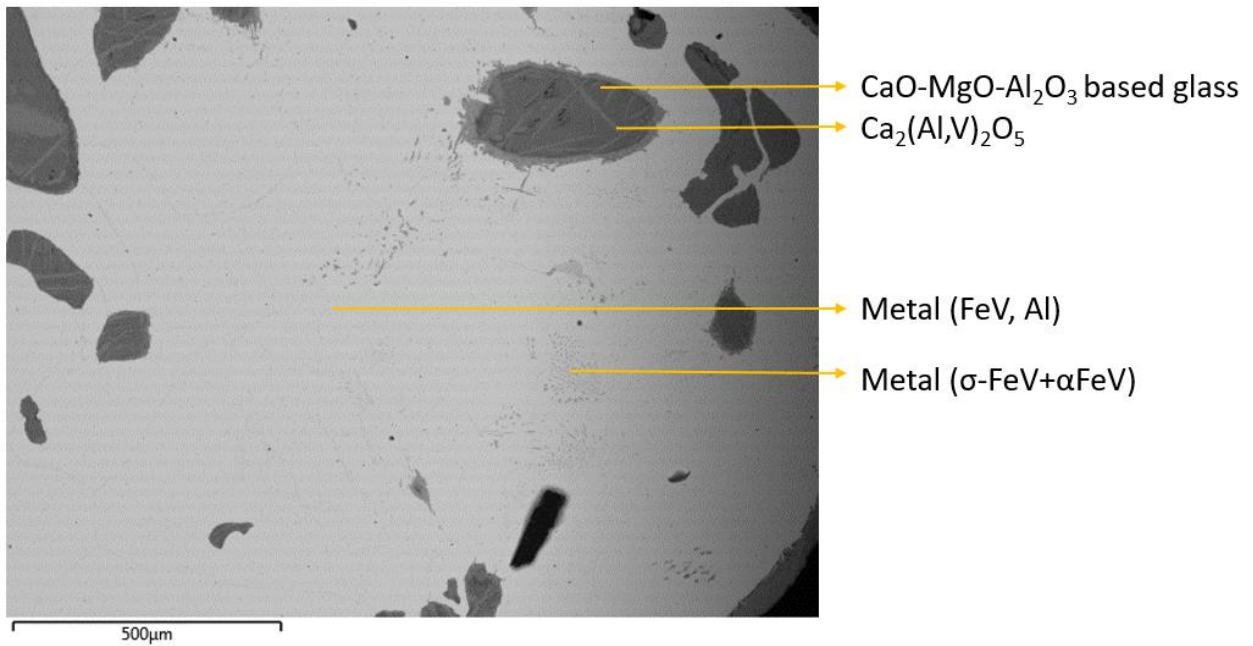


Figure 5.48: Electron backscatter image of the metal (with entrained slag) from test sample C2.

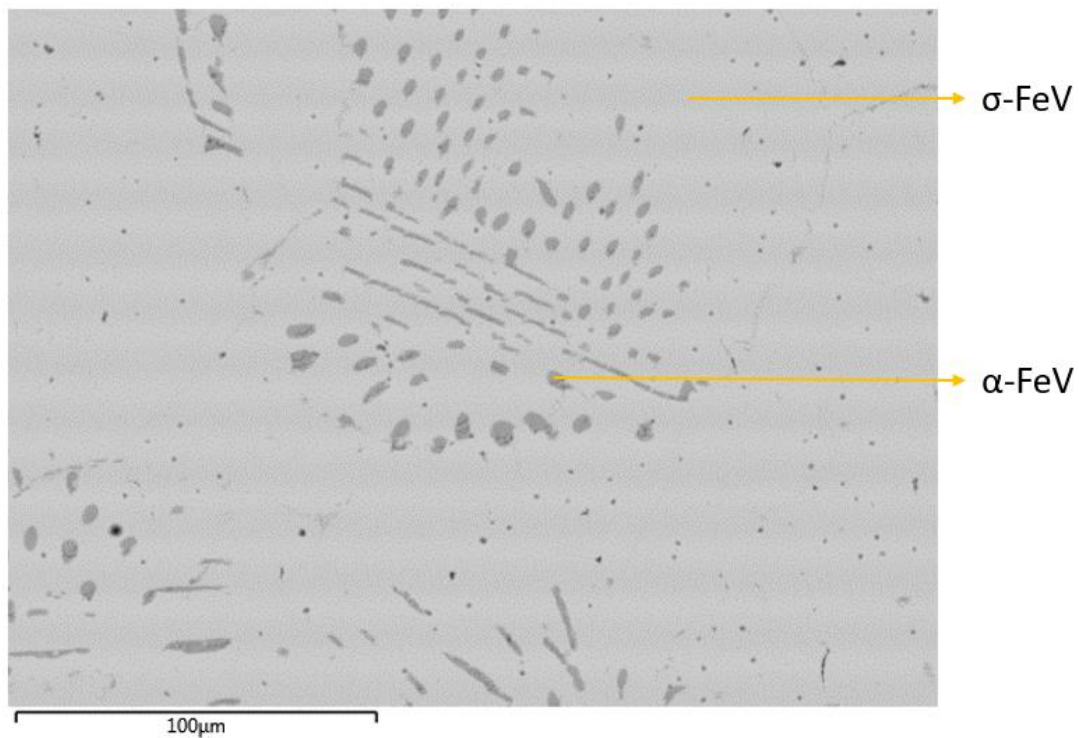


Figure 5.49: Electron backscatter image of the metal from the test where 3.5 wt% excess aluminium was added

The phases that formed in test sample C3 is shown in Figure 5.50. The phases that formed are MgO, $\text{Mg}(\text{Al}_{0.8}\text{V}_{0.2})_2\text{O}_4$, $\text{Ca}_2(\text{Al,V})_2\text{O}_5$ and a CaO-MgO- Al_2O_3 based glassy phase. The phases that formed are similar to the phases formed in sample C1 (section 5.3.3 Sample C1), with the exceptions of the MgV_2O_4 and MgO_{ss} (containing vanadium) phases that formed at the

interphase between the slag and the metal. The slag also contained small metal droplet inclusions which were not recovered (the size was too small to be recovered).

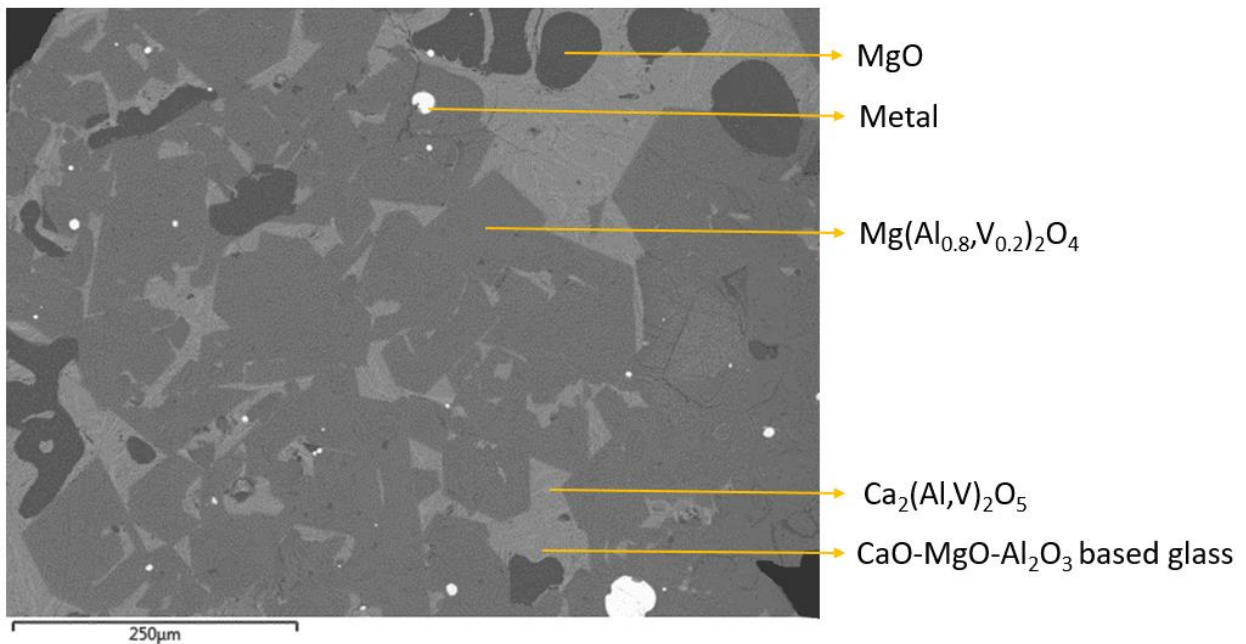


Figure 5.50: Electron backscatter image of the slag formed in test sample C3.

When a different slag region of the same slag sample was analysed (Figure 5.51), it also contained MgO_{ss} (where MgO is in solid solution with V_2O_3) and a vanadium containing spinel phase, $\text{Mg}(\text{Al}_{0.3},\text{V}_{0.7})_2\text{O}_4$. The slag is therefore identical to the baseline test. The slag region did not contain any entrained metal droplets.

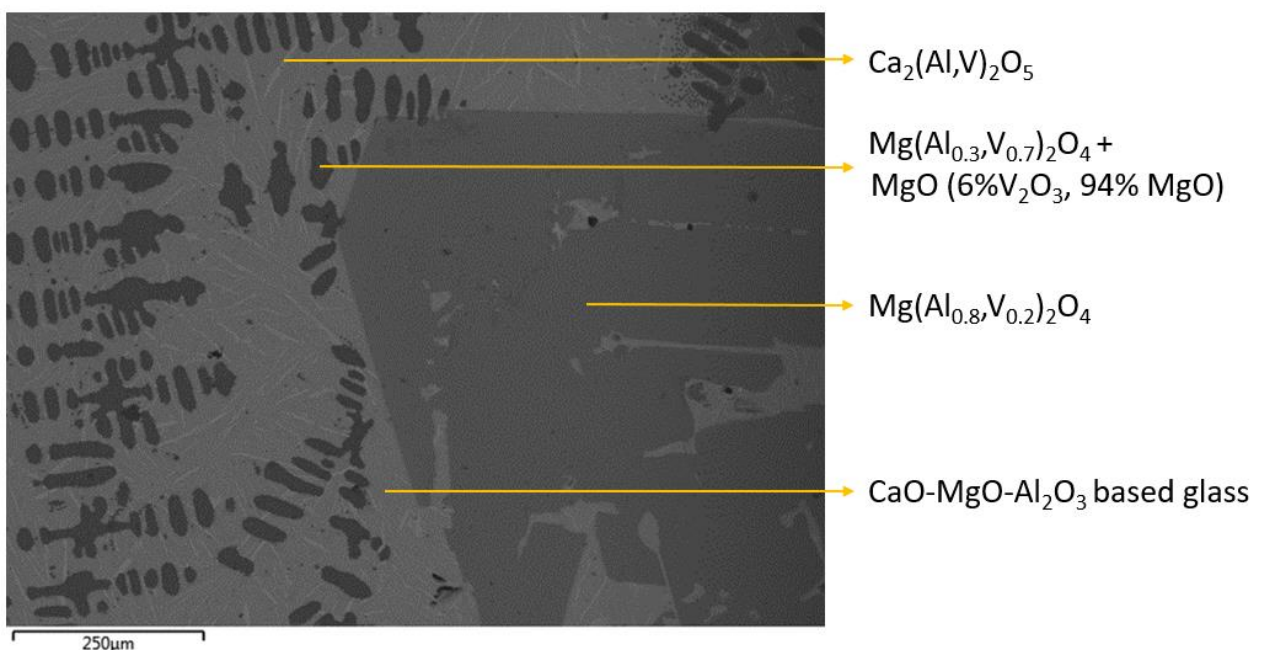


Figure 5.51: Electron backscatter image of the slag formed in test sample C3.

The composition of the metal of sample C3 (Figure 5.52) was 27.7 wt% Fe, 70.5 wt% V and 1.8 wt % Al. The expected aluminium content was 5.5 wt % Al, therefore a difference between the expected and actual aluminium content is present.

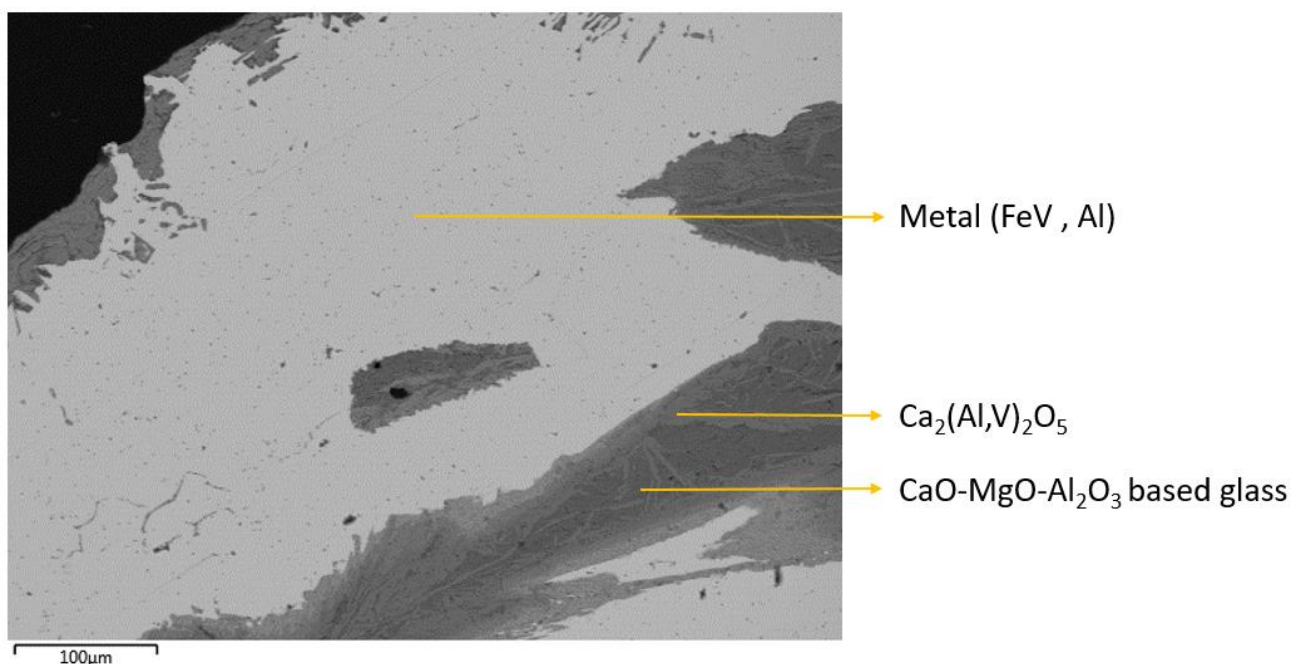


Figure 5.52: Electron backscatter image of the metal droplet with entrained slag of test sample C3.

5.4 Two stage process

The vanadium recovery is dependent on the extent to which V_2O_3 is reduced to vanadium and also on the separation of the formed ferrovanadium from the slag. Complete V_2O_3 reduction is achieved by adding excess reductant (aluminium) to the reaction. The separation of the metal (ferrovanadium) from the slag is mainly dependent on the slag viscosity, slag volume and metal droplet size. The effect of changing the amount of reductant added to the reaction was investigated in the first part of this section by varying the amount of aluminium added to the reaction and holding other variables (the slag composition and reaction time) constant. The second part requires that Fe_2O_3 be reacted with the metal to reduce the aluminium content of the metal.

5.4.1 Metal and vanadium recovery as a function of aluminium (first stage)

The vanadium recovery as a function of excess aluminium added to the reaction was tested by adding enough aluminium to the reaction to obtain excess aluminium contents equal to 1.5 wt% Al, 3.5 wt% Al and 5.5 wt% Al respectively. The vanadium metal droplets were separated from the slag by hand, as droplets with a diameter larger than 0.5 mm could easily be identified using an optical microscope. Droplets with a diameter smaller than 0.5 mm accounted for metal droplets that were entrained in the slag. The recovery was determined using equations 14 and 15.

The results for the metal recovery as a function of aluminium added are shown Figure 5.53. A large increase (1.7 % increase) in metal recovery occurred as the excess aluminium added was

increased from 1.5 wt% to 3.5 wt% Al. The increase in metal recovery as the excess aluminium added was increased from 3.5 wt% to 5.5 wt% Al was only marginal (0.1 wt%). The vanadium recovery curve (Figure 5.54) has a similar trend to the metal recovery curve. An increase in aluminium concentration would result in a higher driving force for the reduction reaction, converting a higher percentage of V_2O_3 to vanadium.

The most suitable option for a two stage process would therefore be to add enough aluminium to obtain an excess of 3.5 wt% Al as a significant change in metal recovery occurred between 1.5 wt% and 3.5 wt% Al added.

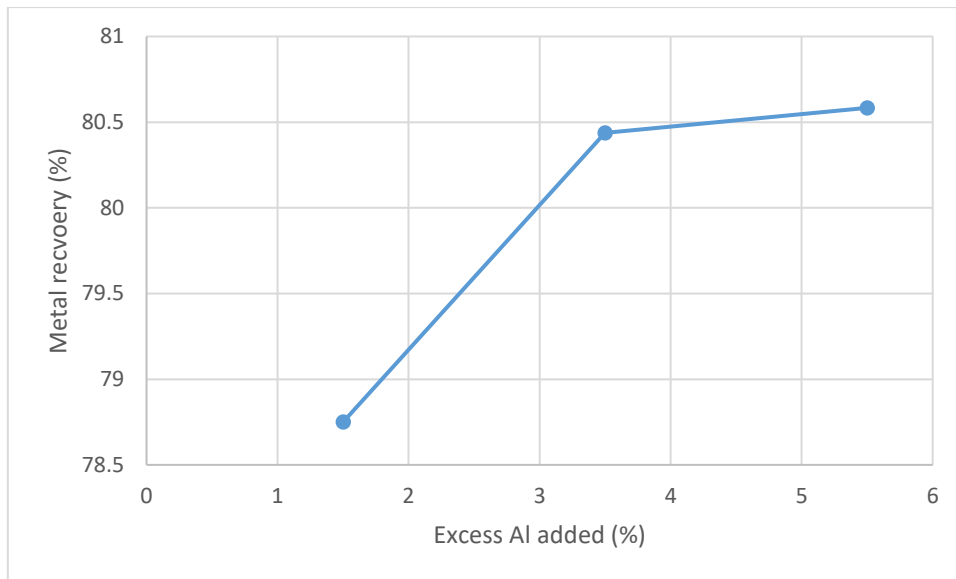


Figure 5.53: Metal recovery as a function of excess aluminium added.

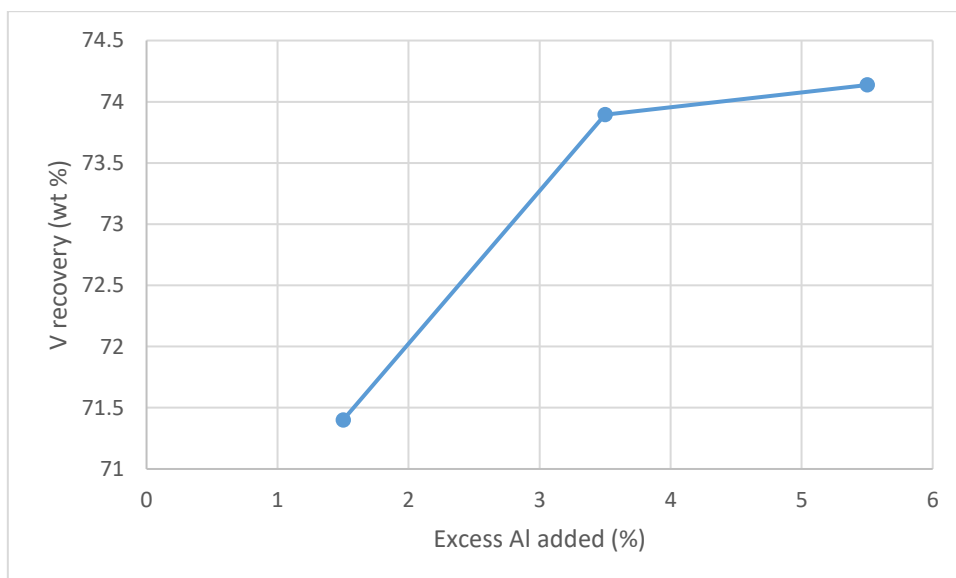


Figure 5.54: Vanadium recovery as a function of excess aluminium added.

The particle size distribution of the metal droplets was an indication of the efficiency of the metal recovery of the process. In order to obtain a good recovery efficiency, the size

distribution should show that a small amount of small metal particles are present and that most of the droplets are large particles (Figure 5.55). The ideal situation would be to have one large metal droplet.

The metal droplets that were obtained from the metal recovery tests as a function of the aluminium added are shown in Figure 5.55 to Figure 5.57. A large amount of small metal droplets formed in tests C1 and C2 (Figure 5.55 and Figure 5.56), while a smaller amount of small particles formed in test C3 (Figure 5.57). The amount of small particles can influence the recovery of the metal, as small particles tend to remain entrained in the slag.

The average size of the particles was also indicative of the probability of recovering the metal droplets, with a higher average particle size indicating a higher probability of recovering the metal droplets. The average metal droplet sizes (radius) were 1.45 mm, 1.7 mm and 2.35mm for 1.5 wt% excess Al (test C1), 3.5 wt% excess Al (test C2) and 5.5 wt% excess Al (test C3) respectively, which indicated that test C3 had the highest probability of recovering most of the metal droplets.

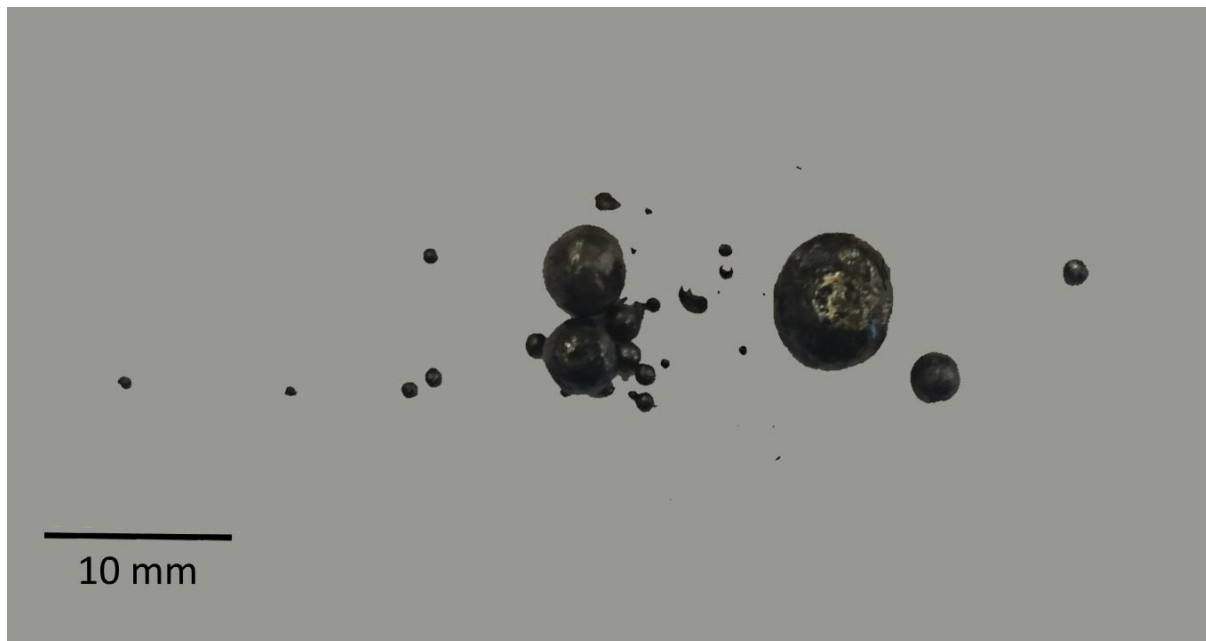


Figure 5.55: Metal droplets obtained from the test where 1.5 wt% excess aluminium was added (test C1).

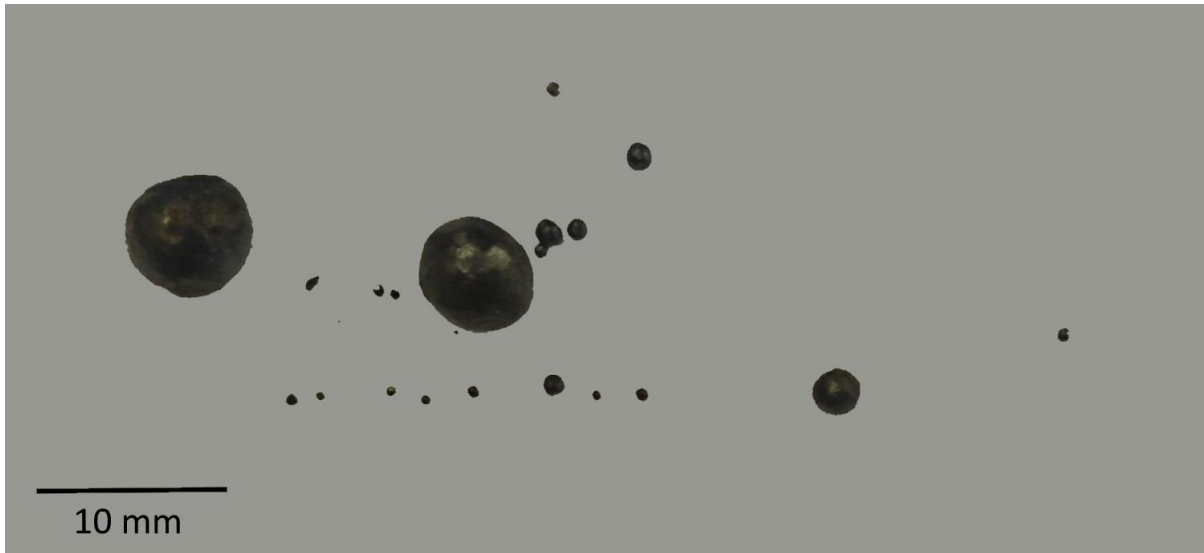


Figure 5.56: Metal droplets obtained from the test where 3.5 wt% excess aluminium was added (test C2).

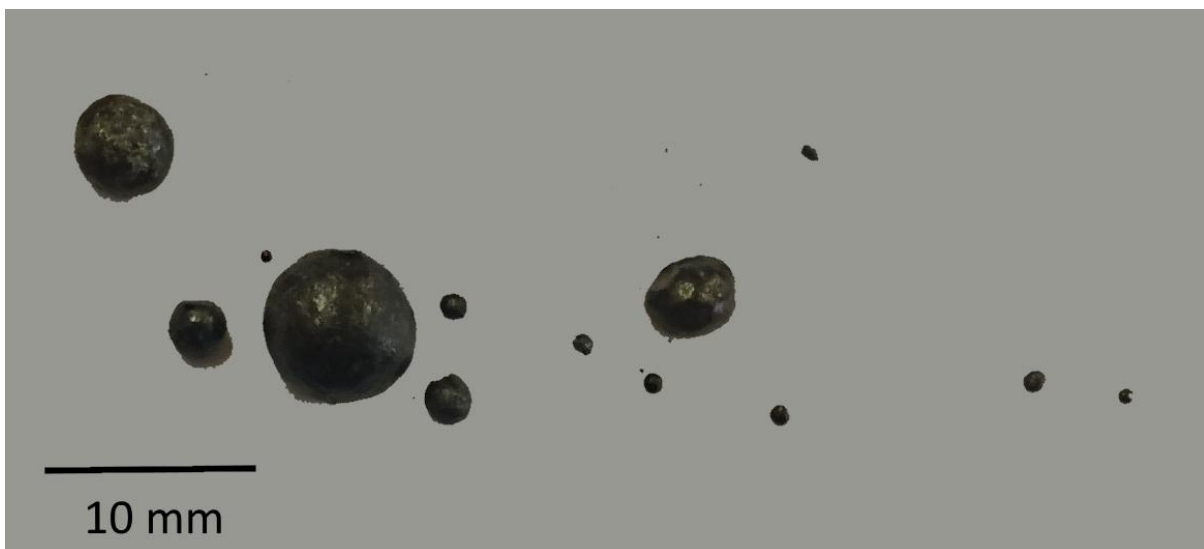


Figure 5.57: Metal droplets obtained from the test where 5.5 wt% excess aluminium was added (test C3).

The density of the metal and the volume of the droplets were used to determine the mass distribution of the metal droplets (Figure 5.58). It is evident from Figure 5.58 that no significant difference in droplet size was present between tests C1, C2 and C3. This is in contradiction with the average droplet radius determined for tests C1, C2 and C3. The discrepancy is a result of the number of smaller particles present in each test. The highest number of small particles were found in test C1, followed by C2 and then C3, resulting in the average radius being the lowest for C1, then C2 followed by C3. Even though the number of particles differ significantly for the different tests, the mass contribution of each size fraction was similar (Figure 5.58) because the difference in particle quantity was mainly due to smaller particles.

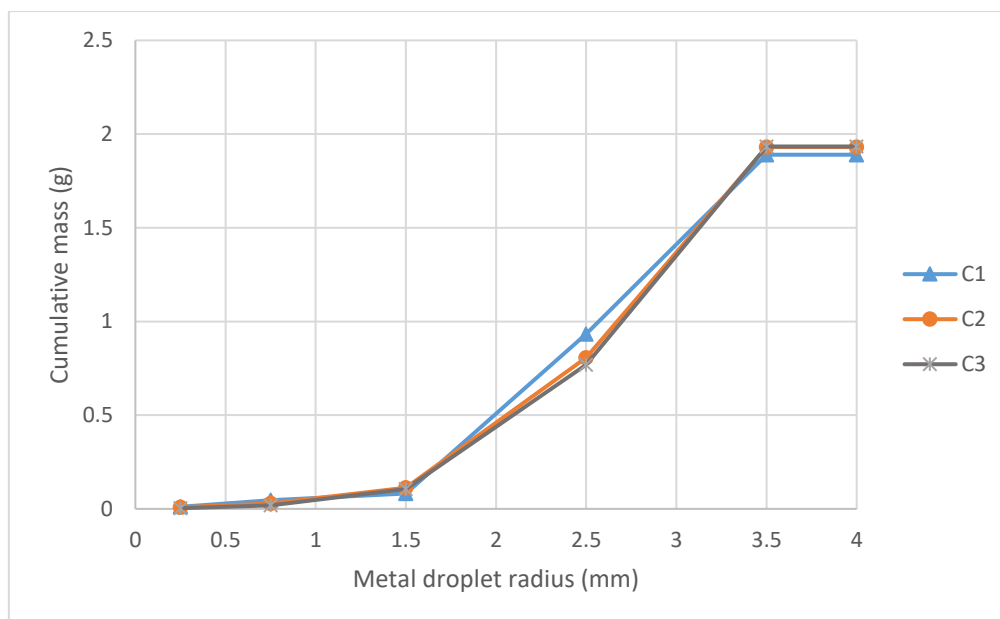


Figure 5.58: Cumulative mass distribution of the metal as a function of metal droplet size.

5.4.2 First stage summary

Tests were done where 1.5 wt% (C1), 3.5 wt% (C2) and 5.5 wt% (C3) excess aluminium were added to a mixture of V_2O_3 , Fe, CaO and MgO, reacted at 1800°C , after which the vanadium recoveries of the respective tests were determined. The results indicated that test C2 was the best option for the first stage of the melting process, as it had only a slightly lower vanadium yield than test C3, but a significantly higher vanadium yield than test C1.

The composition of the metal from test C2 is indicated in Table 16. Although the metal should contain 3.5 wt% excess aluminium, the aluminium content was determined to be 1.4 wt%. Additional aluminium was added to the mixture of the second stage in order to simulate a metal containing 3.5 wt% aluminium.

Table 16: Composition of the metal obtained from test C2 using SEM-EDS analysis.

First stage	Test C2	Standard deviation
Iron (wt%)	30.0	0.9
Vanadium (wt%)	68.6	1.4
Aluminium (wt%)	1.4	0.3

5.4.3 Second stage

Fe_2O_3 was reacted with the aluminium containing ferrovanadium from the first stage at 1800°C to form Al_2O_3 and ferrovanadium with a lower aluminium content. CaO and MgO was also added in order to produce a fluid slag which is compatible with the MgO lining. The aim of the two second stage tests (H1 and H2) was to reduce the aluminium content in the metal

from 3.5 wt% to 1.5wt% (H1) and 1.0 wt% (H2). Due to the aluminium in the ferrovanadium being lower than the expected 3.5 wt% Al, more aluminium was added to the reaction in order to achieve the 3.5 wt% Al.

The slag compositions of both slags were the same and is shown in Table 5.17. The slag composition together with the mass of Al_2O_3 that would form for a complete reaction was used to determine the slag mass. The slag mass and vanadium content in the slag was then used to determine the mass of vanadium in the slag, which can then be used to determine the vanadium recovery of the second stage.

Table 5.17: Average composition of slag that formed during the second stage of the melting process, using SEM-EDS analyses of both slags H1 and H2.

Slag component	Composition (Wt %)	Standard deviation
MgO	6.7	0.5
Al_2O_3	65.5	1.7
CaO	11.8	0.6
V_2O_3	16.0	

The vanadium content in the slag amounted to 16.0 wt% of the slag, but because of the relatively low volume of slag formed, the respective vanadium recoveries for the second stage of the melting process was 98.4 % and 98.3 % for tests H1 and H2 respectively.

The metal composition for the two respective tests is shown in Table 5.18. Similar metal compositions were obtained, with both metals having lower aluminium contents than the intended aluminium. The reason for the lower aluminium content was due to oxidation occurring in the furnace. Small amounts of O_2 were present in the furnace (O_2 was measured to be $P_{\text{O}_2} = 10^{-11} \text{ atm}$), which resulted in aluminium reacting with O_2 .

The vanadium content of the metal after the second stage of melting (63.5 wt%) was lower than the vanadium content after the first stage of melting (68.6 wt%). The reason for the decrease in vanadium content in the metal was because of the increase in the amount of iron present in the metal and to a smaller extent because of the vanadium lost to the slag. The iron formed during the reaction between Fe_2O_3 and aluminium reported to the metal, in effect increasing the iron content of the metal and therefore increasing the Fe: V ratio. The amount of vanadium decreased slightly from 63.7 wt% to 63.3 wt%, which is insignificant when considering the experimental error derived from the standard deviation.

Table 5.18: Metal composition of the two tests done (H1 and H2) for the second stage of the melting process.

Second stage	Test H1	Standard deviation	Test H2	Standard deviation
Iron (wt%)	35.5	0.8	36.0	0.3
Vanadium (wt%)	63.7	1.7	63.3	0.8
Aluminium (wt%)	0.8	0.2	0.7	0.1

A theoretical metal composition of the expected composition after the second stage of melting is shown in Table 5.19. The composition was determined by using the composition obtained from the first stage of melting and then calculating the average (between tests H1 and H2) amount of Fe, vanadium and aluminium that was expected to form.

Comparing the theoretical values (Table 5.19) with the actual values (Table 5.18), it was evident that the theoretical vanadium and aluminium contents were slightly higher than the actual values, whereas the theoretical iron content was lower than the actual compositions. The reason for the small deviation is because the theoretical composition does not account for vanadium losses to the slag and the reaction between aluminium and oxygen, which is why the actual vanadium and aluminium content would be lower. The lower amount of vanadium and aluminium also resulted in the iron content increasing even though the actual mass of Fe from the actual test cannot be more than the theoretical Fe mass.

Table 5.19: Theoretical metal composition after the second stage of melting.

Second stage	Theoretical composition
Iron (wt%)	34.4
Vanadium (wt%)	64.4
Aluminium (wt%)	1.2

An electron backscatter image of the slag that formed for the second stage melting process is shown in Figure 5.59. Both tests yielded slags of similar composition and the same phases. The slag contained a vanadium rich spinel phase ($\text{Mg}(\text{Al}_{0.3}, \text{V}_{0.7})_2\text{O}_4$), a $\text{MgO-V}_2\text{O}_3$ solid solution phase, $\text{Ca}_2(\text{Al}, \text{V}_2)_2\text{O}_5$ and a glassy phase containing CaO , MgO , V_2O_3 and Al_2O_3 . The $\text{Mg}(\text{Al}_{0.3}, \text{V}_{0.7})_2\text{O}_4$ phase formed inside the $\text{MgO-V}_2\text{O}_3$ solid solution phase and had a needle-like or round shape. It is assumed that the $\text{Mg}(\text{Al}_{0.3}, \text{V}_{0.7})_2\text{O}_4$ crystals precipitated from the $\text{MgO-V}_2\text{O}_3$ solid solution phase on cooling.

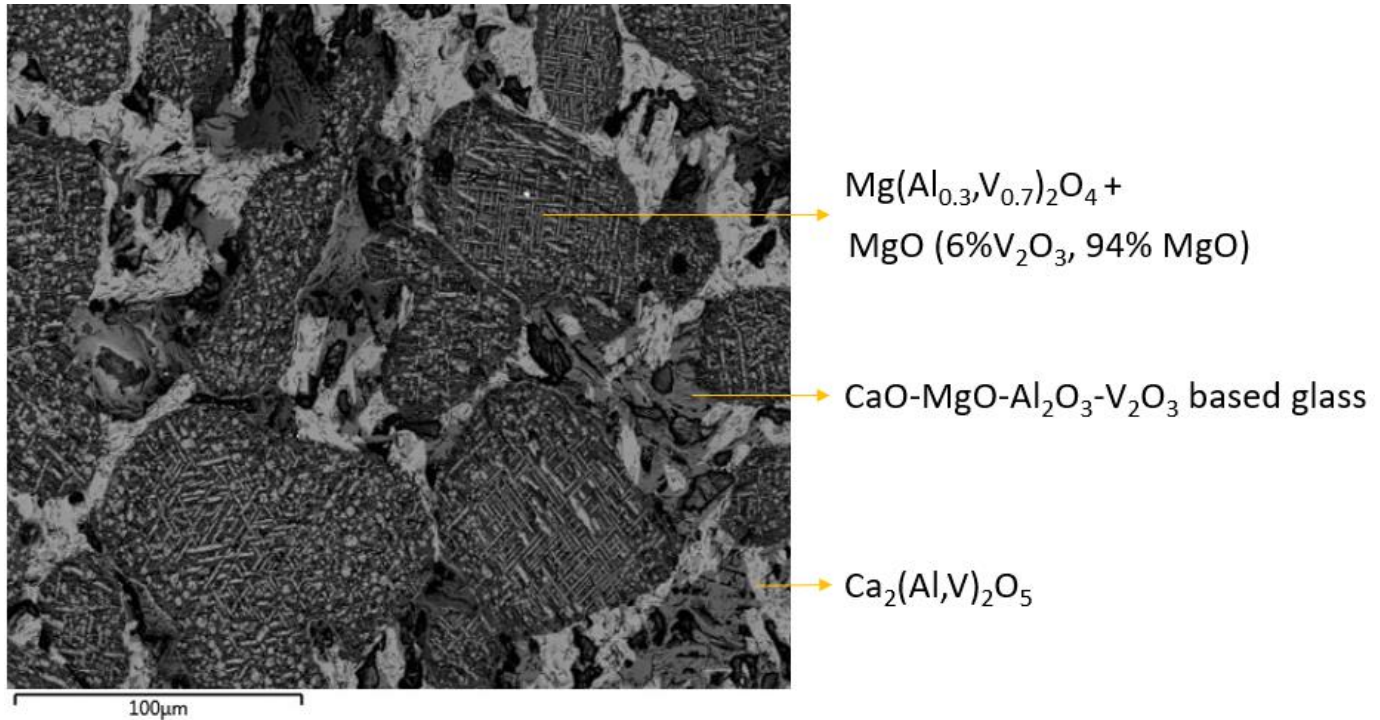


Figure 5.59: Electron backscatter image of the slag formed in test H1.

An electron backscatter image of the metal and slag that formed in the second stage of the melting process is shown in Figure 5.60. The metal consisted of α -ferrovanadium (darker phase) and σ -ferrovanadium. α -ferrovanadium had a composition of 1.5 wt% Fe, 98.5 wt% V and σ -ferrovanadium had a composition of 29 wt% Fe, 71 wt% V.

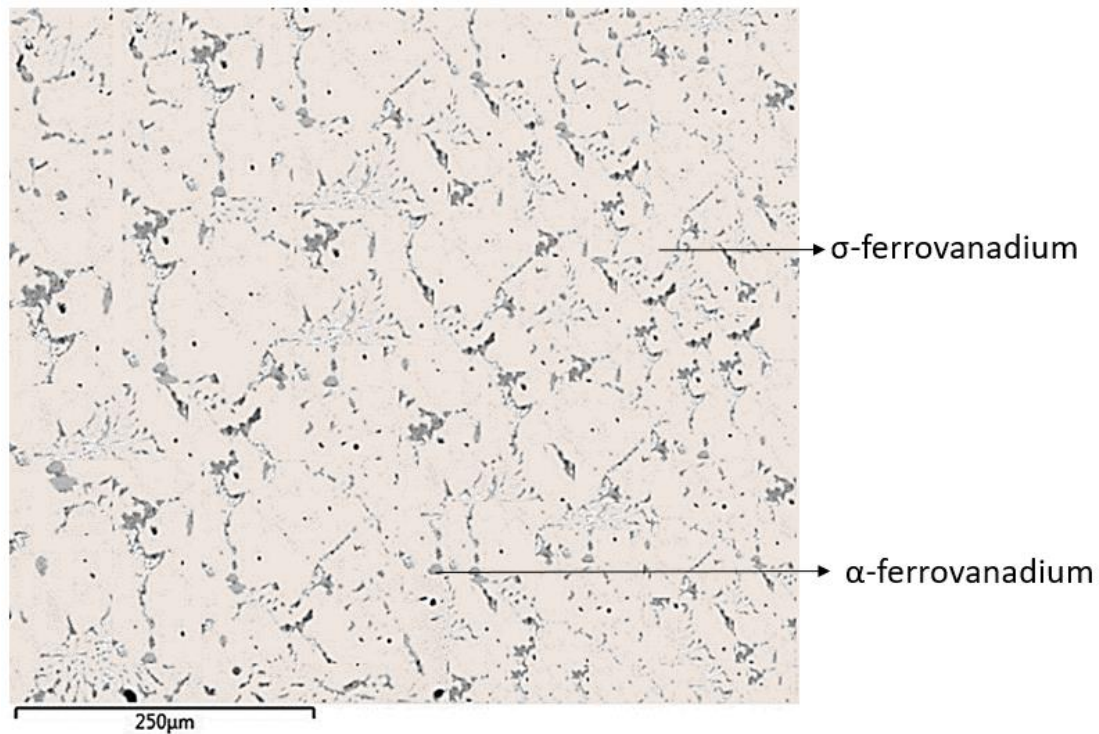


Figure 5.60: Electron backscatter image of the metal that had formed during the second stage of the melting process.

5.4.4 Vanadium recovery for the second stage

The recovery of the second stage can be estimated by using the mass of slag formed, together with the percentage of vanadium present in the slag. The estimated mass of vanadium present in the slag was then subtracted from the original mass of vanadium present in the metal, which was used to determine the recovery of the second stage. The recovery and the values calculated to determine the recovery is shown in Table 5.20.

The vanadium content of both slags was high (approximately 16 wt%), but a high vanadium recovery was obtained because of the small amount of slag which formed compared to the amount of metal that formed.

Table 5.20: Determining the recovery for the second stage of the two stage melting process.

	Test H1	Test H2
Mass of metal	1.9	1.9
Mass of V in metal	1.21	1.20
Mass of slag	0.12	0.13
V wt% in slag	15.9	15.8
Mass of V in slag	0.019	0.021
Vanadium recovery (wt %)	98.4	98.3

The vanadium recovery was higher for the two stage process compared to the one stage process (Table 5.21). Vanadium recovery can therefore be increased by dividing the ferrovanadium production process into two stages, where 3.5 wt% excess aluminium is added in the first stage and Fe_2O_3 is added in the second stage.

Table 5.21: Comparison between the recoveries obtained for the one stage process and the two stage process.

	Single stage	Two stage
Vanadium recovery (wt%)	71.4	72.6
Standard deviation	0.7	0.4

Chapter 6: Summary and discussion

Chapter 6 summarises and elaborates on the analysis of the test results obtained in Chapter 5. The chapter covers the slag-refractory interaction tests where both an unsaturated and saturated slag was brought into contact with a MgO refractory. The metal and vanadium recovery tests are also analysed in more detail, considering the effect of slag volume, viscosity and composition on the recovery. The two stage melting process results are also discussed, with the chapter concluding by drawing comparisons between the laboratory and industrial results.

6.1 Slag-refractory interaction tests

Both the unsaturated and MgO saturated slag samples penetrated into the respective refractory cores and reacted with the refractory. The mechanism of refractory wear is therefore a combination of slag penetration and chemical reaction between the slag and the refractory. The refractory wear in the case of test A was more than the wear in test B, as indicated by comparing the amount of MgO present in the bottom-middle and bottom-edge regions.

The slag surrounding the refractory core consisted of MgAl_2O_4 , CaAl_2O_4 , MgO and a glassy MgO-CaO- Al_2O_3 phase. As slag A starts to pick up MgO it will remain liquid at 1800°C until it contains approximately 10 wt % MgO, which is the saturation point for MgAl_2O_4 in the liquid phase.

The final slag compositions of both tests were almost the same, where both compositions followed the interaction line from the initial composition towards the MgO corner of the ternary phase diagram. The difference in refractory wear can be ascribed to the difference in starting composition of the two slag compositions. The difference in degree of MgO saturation of the slag resulted in different amounts of refractory wear.

6.2 Metal recovery as a function of slag composition

6.2.1 The effect of slag volume and viscosity

The metal recovery as a function of slag mass is shown in Figure 6.61. The metal recovery is strongly dependant on the slag mass. The lower slag mass resulted in more interaction between metal droplets as the distance between droplets were less, resulting in larger metal droplets forming. The larger metal droplets will experience a stronger gravitational force, which then resulted in increased metal-slag separation.

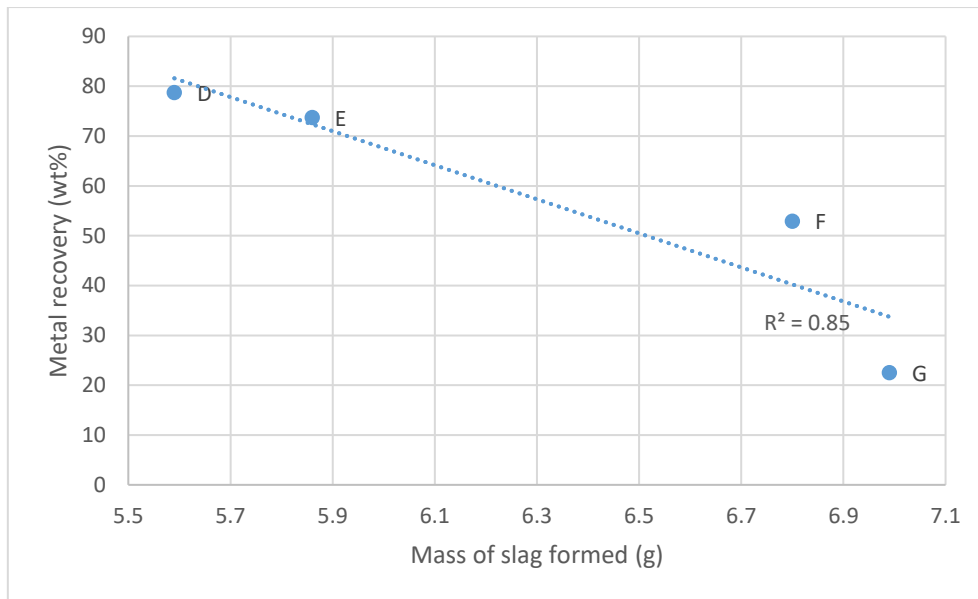


Figure 6.61: Metal recovery as a function of slag mass (g).

The slag viscosity was calculated using the Urbain and Einstein-Roscoe viscosity models. The fully liquid viscosity was determined using the Urbain method which is based on the slag composition and temperature. The Einstein-Roscoe viscosity model was then used to determine the effect of solid particles on the viscosity value obtained from the Urbain model. The assumption of spherical solid particles was made when using the Einstein-Roscoe model. The solid fraction of the Einstein-Roscoe model was estimated as half of the maximum solids fraction present at 1800°C. The maximum solids fraction was obtained from the XRD results (Table 5.15). The metal recovery as a function of calculated viscosity (Figure 6.62) indicated that the metal recovery decreased with an increase in viscosity from slag composition D to G. A linear trend ($R^2 = 0.91$) is evident from the metal recovery versus slag viscosity results.

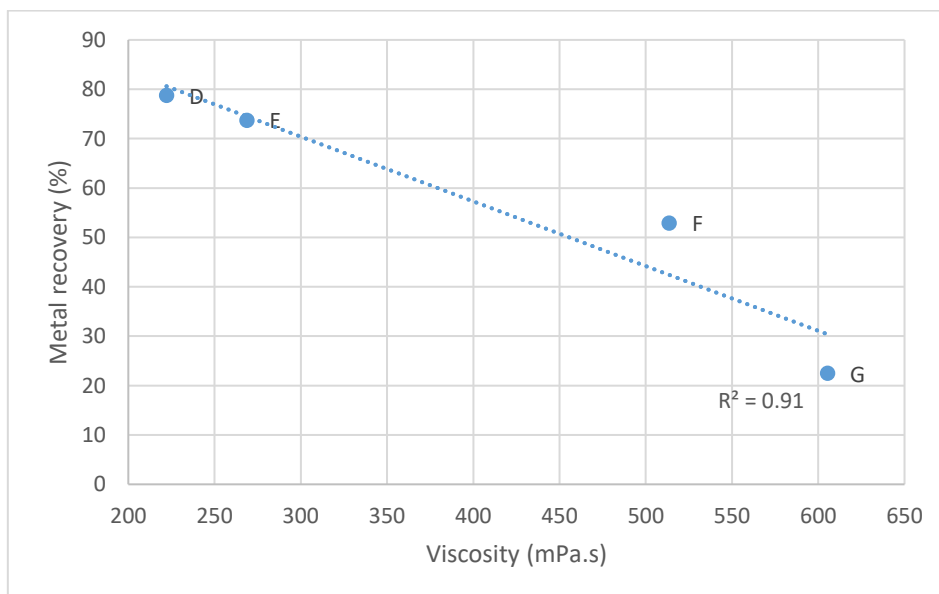


Figure 6.62: Metal recovery as a function of the calculated slag viscosity.

The slag volume was determined by using a calculated density value (based on the slag composition) and the slag mass (measured value). The metal recovery decreased as the slag volume increased (Figure 6.63), due to the increase in distance that metal droplets have to travel through the slag before crossing the slag-metal interface. The metal recovery therefore has a strong dependency on the slag volume as well as the slag viscosity.

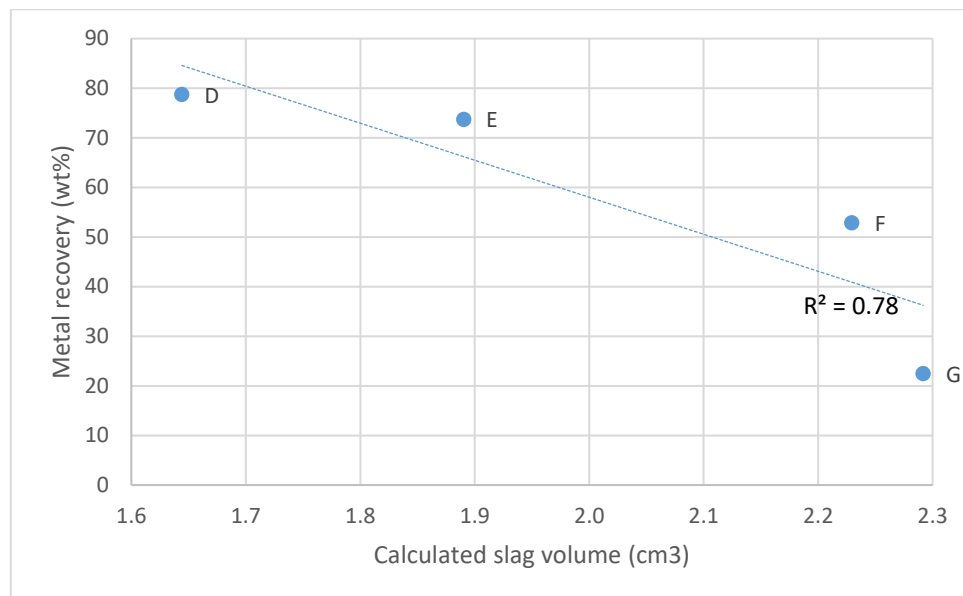


Figure 6.63: Metal recovery as a function of the calculated slag volume.

The metal recovery is dependent on both the slag volume and viscosity. The metal recovery decreased as the slag volume increased and the slag viscosity increased. The average metal droplet size decreased as the slag volume increased, resulting in a lower probability of recovering the metal droplets as the slag volume increased. Smaller metal droplets formed as the slag volume increased, due to less droplets coalescing. The preferred slag composition for the highest metal recovery was 8 wt% MgO, 78 wt% Al₂O₃ and 14 wt% CaO (composition D).

6.2.2 The effect of the (CaO+MgO): Al₂O₃ ratio

The slag components changed as the composition was changed from test E to G (an increase in the (CaO+MgO): Al₂O₃ ratio). The most important changes were the decrease in spinel (Mg(Al_{0.8}, V_{0.2})₂O₄) content from test E to G, with no primary spinel being present in test G. The decrease in spinel content will decrease the vanadium lost at temperature to the spinel phase (with the spinel phase contributing the most to vanadium losses as indicated by Vermaak and Pistorius (2000)). The Ca₂(Al,V)₂O₅ content of the various slags increased from test E to G. From microstructural observations it can be concluded that the Ca₂(Al,V)₂O₅ precipitated from the liquid phase on cooling. It can therefore be assumed that vanadium dissolved in the liquid phase at temperature preferentially reported to the Ca₂(Al,V)₂O₅ on cooling.

The vanadium recovery decreased linearly as the (CaO+MgO): Al₂O₃ ratio increased (Figure 6.64). An important factor to keep in mind when considering the (CaO+MgO): Al₂O₃ ratio is that the Al₂O₃ mass in the slag remains fixed. The Al₂O₃ mass in the slag is fixed due to the amount of reductant required in the process, therefore an increase in the (CaO+MgO): Al₂O₃

ratio increases the slag mass (and therefore volume). The linear shape of Figure 6.64 is largely dictated by the slag volume, as is evident when considering Figure 6.63. The contribution of basicity was minimal, as it would have resulted in a bell-shaped curve as was shown by the results of Vermaak and Pistorius (2000).

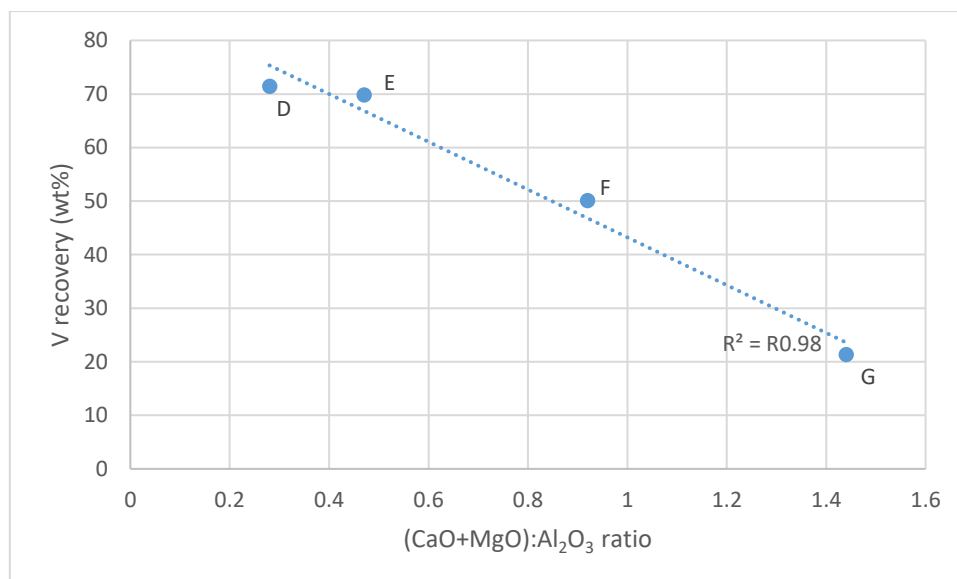


Figure 6.64: The V recovery as a function of slag composition.

Activity coefficient values based on the CaO: Al₂O₃ ratio of the slag was obtained from the work done by Vermaak and Pistorius (Figure 2.3). The vanadium recovery increased (although not linearly) as the activity coefficient of V₂O₃ increased (Figure 6.65). The results in Figure 6.65 agreed with the results from Vermaak and Pistorius (Figure 2.3 and Figure 2.4), which indicated that a high V₂O₃ activity coefficient results in a slag with a low vanadium content.

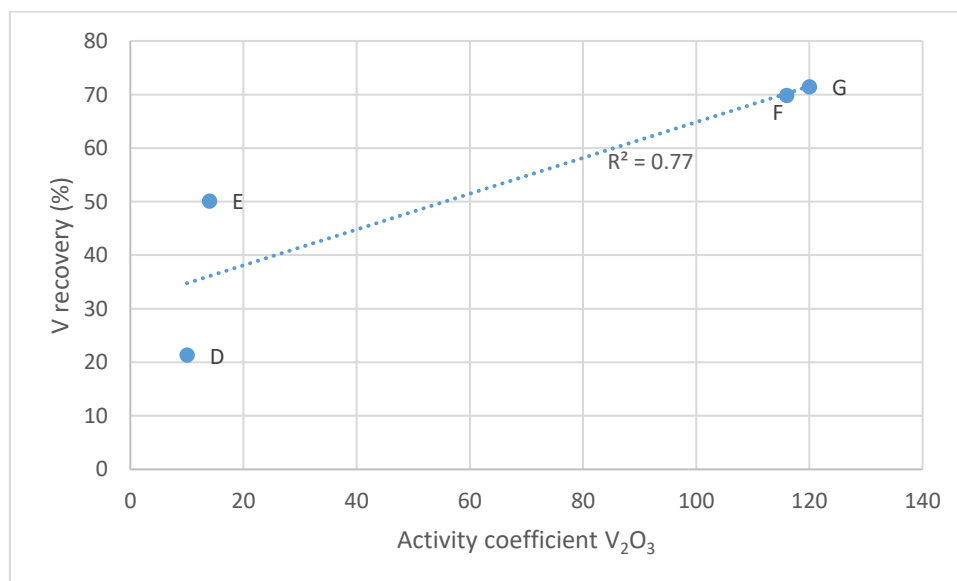


Figure 6.65: Vanadium recovery as a function of the V₂O₃ activity coefficient.

The vanadium recovery is dependent on the slag composition, with the results indicating a linear decrease in vanadium recovery as the (CaO+MgO): Al₂O₃ ratio increased. The vanadium recovery is also dependent on the V₂O₃ activity coefficient, with the vanadium recovery increasing as the V₂O₃ activity coefficient increased.

6.3 Two stage smelting process

6.3.1 Phases formed in stage 1

The metal that formed consisted of two phases, ferrovanadium and vanadium. Ferrovanadium was present as both primary and secondary phases, whereas vanadium formed as a secondary phase. The overall composition of the metal was 26 wt% Fe, 74 wt% V. An interfacial layer that formed between the metal and the slag consisted of MgO_(ss) and MgV₂O_{4(ss)}. The MgO solid solution phase contained 6 wt% V₂O₃. A high concentration of ferrovanadium inclusions was also present in the interfacial layer. The interfacial layer was not present with every ferrovanadium inclusion, indicating the stability of the interfacial layer is dependent on the surrounding conditions.

The slag consisted of the phases Mg(Al_{0.88},V_{0.12})₂O₄, Ca₂(Al,V)₂O₅, MgO_{ss}, Mg(Al_{0.3},V_{0.7})₂O₄ and a CaO-MgO-Al₂O₃ based glassy phase, with Mg(Al_{0.88},V_{0.12})₂O₄ and Mg(Al_{0.3},V_{0.7})₂O₄ being present at 1800°C. Vanadium losses at 1800°C therefore occurred due to ferrovanadium inclusions and V³⁺ substitution of Al³⁺ in the MgAl₂O₄ crystal structure. Upon cooling vanadium reported to the Ca₂(Al,V)₂O₅ phase and some of the V₂O₃ that went into solid solution with MgO, exsolved as very fine grained Mg(Al,V)₂O₄.

Interaction on the surface of the MgO crucible was present, with MgAl₂O₄ forming on the surface of the refractory, as well as in the pores. The phenomenon of MgAl₂O₄ formation in these regions indicated that refractory wear was a result of both slag penetration into the refractory, as well as chemical interaction between the slag and the refractory. V₂O₃ also went into solid solution with the MgO on the surface of the crucible, which contributed to vanadium losses.

6.3.2 Comparison between samples C1, C2 and C3 of stage 1

The phases present in the slag were the same for the three tests (sample C1 to C3) that were done. The iron and vanadium content was almost the same for the three tests, but the aluminium content differed. The aluminium content of the metal increased as the amount of aluminium added increased, but there was a difference in the aluminium content in the metal and the excess aluminium added to the reaction. The difference between the excess aluminium added and the aluminium content in the metal was due to the aluminium oxidising inside the furnace to form Al₂O₃.

The results obtained from Figure 5.53, Figure 5.54 and Figure 5.58 indicate that adding 3.5 wt% excess aluminium to the reaction would yield the best results in terms of metal recovery. Adding more aluminium would only result in marginally better results (which may not be attractive from a commercial point of view due to extra reagent costs). The results obtained from the average metal droplet size suggest that adding 5.5 wt% excess aluminium would result in the highest probability of recovering all the metal droplets that formed.

6.3.3 Second stage of the smelting process

It was possible to reduce the aluminium content in the metal (ferrovanadium) by reacting the metal with Fe_2O_3 at 1800°C . A small amount of vanadium was lost to the slag because of the presence of $\text{Mg}(\text{Al}_{0.88},\text{V}_{0.12})_2\text{O}_4$ at 1800°C . Upon cooling vanadium is also present in other slag phases in the form of $\text{Ca}_2(\text{Al},\text{V})_2\text{O}_5$, $\text{Mg}(\text{Al}_{0.3},\text{V}_{0.7})_2\text{O}_4$, and a $\text{MgO}-\text{V}_2\text{O}_3$ solid solution. Although the vanadium content in the slag is high (14.5 wt%), the vanadium recovery is 98.8 % because of the low volume of the slag compared to the amount of metal formed. The vanadium content of the metal obtained from stages 1 and 2 decreased from 68.6 wt% to 63.5 wt% because of the formation of Fe from Fe_2O_3 during the second stage of melting. A small amount of aluminium was oxidised to Al_2O_3 by oxygen present inside the furnace.

The vanadium recoveries obtained (Table 5.20) were used together with the vanadium recoveries for test C2 to determine an overall vanadium recovery for the proposed two stage melting process as opposed to a single stage melting process (vanadium recovery from test C1). The vanadium recovery obtained from the two stage process was 72.6 wt%, which was higher than the 71.4 wt% obtained for the single stage process (Table 5.21). A two stage process is therefore feasible from a technical point of view as it would yield a higher vanadium recovery. An economic feasibility study would however have to be conducted to determine its feasibility for industrial applications. The aluminium fade at lab scale and plant scale would also vary, with the percentage aluminium fade in industry expected to be less due to the lower O_2 : Al ratio in an industrial scale furnace.

6.4 Comparison of the industrial slag and the laboratory scale slag

A water quenched industrial slag sample was composed of spinel ($\text{Mg}(\text{Al},\text{V})_2\text{O}_4$), krotite (CaAl_2O_4), grossite (CaAl_4O_7) and a glassy phase (Al_2O_3 - CaO - MgO). The spinel and krotite phases contained 2.5 wt% and 0.3 wt% vanadium respectively. The phase composition of the slag was 57.6 wt% $\text{Mg}(\text{Al},\text{V})_2\text{O}_4$, 7.5 wt% CaAl_2O_4 , 14.3 wt% CaAl_4O_7 and 20.6 wt% $\text{MgO}-\text{Al}_2\text{O}_3$ - CaO glassy phase. The slag temperature was close to 2000°C and the sample was taken at the top region of the slag. The metal composition of metal droplets in the slag was 81 wt% V, 19 wt% Fe. The metal was composed of two phases, α -ferrovanadium and σ -ferrovanadium.

The slag obtained from the laboratory scale tests was constituted of the phases spinel ($\text{Mg}(\text{Al}_{0.88},\text{V}_{0.12})_2\text{O}_4$), MgO_{ss} (94 wt% MgO , 6 wt% V_2O_3), $\text{Mg}(\text{Al}_{0.3},\text{V}_{0.7})_2\text{O}_4$, $\text{Ca}_2(\text{Al},\text{V})_2\text{O}_5$ and $\text{MgO}-\text{Al}_2\text{O}_3$ - CaO glassy phase. The slag from the laboratory scale tests were slow cooled inside the furnace to avoid the MgO crucible from cracking due to thermal shock. The slag contained 26.1 wt% spinel phase (total spinel phase), 20.6 wt % MgO_{ss} , 2.7 wt% $\text{Ca}_2(\text{Al},\text{V})_2\text{O}_5$ and 50.6 wt% $\text{MgO}-\text{Al}_2\text{O}_3$ - CaO glassy phase. The metal composition of the metal droplets in the slag was 74 wt% V, 26 wt% Fe. The metal was composed of two phases, α -ferrovanadium and σ -ferrovanadium.

The primary phase for both slags were MgAl_2O_4 (which would be present at 1800°C) and contained 2.5 wt% and 4.5 wt% vanadium for the industrial and laboratory scale slag samples respectively. The difference in vanadium content can possibly be attributed to where the industrial slag was sampled, which was at the upper region of the slag. The upper region of the slag would have a lower concentration of vanadium compared to the lower region) due

to the density of ferrovanadium being higher than that of the slag components), resulting in a lower driving force for Al^{3+} substitution in the upper slag region. The laboratory scale slag was representative of the entire slag volume and would therefore have a higher vanadium concentration than the upper region of the slag.

Both slags contained MgAl_2O_4 , but the laboratory scale slag contained a high vanadium containing spinel as well. The slags also differed in that the industrial slag contained CaAl_2O_4 and CaAl_4O_7 , but the laboratory scale slag did not contain these phases. The reason for the laboratory scale slags not containing CaAl_2O_4 and CaAl_4O_7 is that the lab scale slag contained more MgO than the industrial slag to ensure MgO saturation of the slag, which resulted in the slag composition not being in the same Alkemade triangle as the industrial slag composition. The change in slag composition, as well as a higher amount of vanadium present in the slag resulted in different phases being present in the industrial slag and the laboratory scale slag.

The vanadium content of the laboratory scale slag (3.8 wt% V) was higher than the vanadium content of the industrial slag (1.5 wt% V). The higher vanadium content in the laboratory scale slag resulted in the formation of vanadium bearing phases forming. The phases $\text{Ca}_2(\text{Al},\text{V})_2\text{O}_5$, high vanadium containing spinel ($\text{Mg}(\text{Al}_{0.3},\text{V}_{0.7})_2\text{O}_4$) and MgO_{ss} (94 wt% MgO , 6 wt% V_2O_3) were all a result of the high vanadium content in the laboratory scale slag. The laboratory scale slag had a higher vanadium content because the samples were representative of the entire slag (top and bottom regions), whereas the samples from industry were taken from the top region of the slag, where the vanadium content would be less than the average amount of vanadium in the slag due to metal droplets settling to the lower part of the slag.

Metal droplets in the slag both contained the α -ferrovanadium and σ -ferrovanadium phases. The composition of the metal falls into a two phase region on the iron-vanadium phase diagram, resulting in the formation of an alloy containing two phases. The vanadium content of the industrial metal (81 wt% V) was higher than the vanadium content of the lab scale metal (74 wt% V), which was expected because the lab scale metal composition was altered in order to decrease the melting point of the metal. The aim of the laboratory scale tests was to produce a metal with a vanadium content of 75 wt%, with the resulting metal composition (74 wt%) being very close to the intended composition.

6.5 Comparison of the post mortem refractory analysis and slag-refractory interaction tests

The phases present in the post mortem refractory analysis can be compared to the phases present in the slag-refractory interaction tests in order to determine how representative the laboratory scale tests were to what had occurred in industry. The phases that were present in the post mortem refractory analysis were CaAl_2O_4 , CaAl_4O_7 , MgAl_2O_4 , $\text{Ca}_{12}\text{Al}_{14}\text{O}_{33}$, MgO , CaMgSiO_4 , $\text{Ca}_3\text{Mg}(\text{SiO}_4)_2$. The phases that were present in the slag-refractory analysis were MgO , CaAl_2O_4 , MgAl_2O_4 and glassy $\text{CaO-MgO-Al}_2\text{O}_3$.

The phases that were not present for both the analyses were CaAl_4O_7 , $\text{Ca}_{12}\text{Al}_{14}\text{O}_{33}$, CaMgSiO_4 and $\text{Ca}_3\text{Mg}(\text{SiO}_4)_2$ which were present in the post mortem refractory tests but not in the laboratory scale tests. The slag composition of the industrial slag falls within the MgAl_2O_4 - CaAl_4O_7 - CaAl_2O_4 Alkemade triangle, resulting in the formation of CaAl_4O_7 upon cooling.

CaAl_4O_7 was not present in the laboratory scale tests as the slag composition shifted from the MgAl_2O_4 - CaAl_4O_7 - CaAl_2O_4 Alkemade triangle to the MgAl_2O_4 - MgO - CaAl_2O_4 Alkemade triangle, resulting in the formation of MgO rather than CaAl_4O_7 . $\text{Ca}_{12}\text{Al}_{14}\text{O}_{33}$ was also present in the post mortem refractories, which should not form when considering the slag composition from the industrial slag. A possible reason for the presence of $\text{Ca}_{12}\text{Al}_{14}\text{O}_{33}$ is that the local slag composition (in certain areas of the refractory) was different from the bulk slag composition, resulting in the formation of $\text{Ca}_{12}\text{Al}_{14}\text{O}_{33}$. CaMgSiO_4 and $\text{Ca}_3\text{Mg}(\text{SiO}_4)_2$ are present in the post mortem analysis but not in the laboratory scale tests. CaMgSiO_4 and $\text{Ca}_3\text{Mg}(\text{SiO}_4)_2$ are impurity phases associated with magnesite. Purer raw materials are used to manufacture laboratory MgO crucibles compared to MgO bricks in industry, resulting in the present of CaMgSiO_4 and $\text{Ca}_3\text{Mg}(\text{SiO}_4)_2$ in industrial MgO bricks, but not in laboratory scale MgO crucibles.

6.6 Metal droplet interaction with spinel phase

The electron backscatter images indicated that metal droplets tend to be associated with the spinel phase (both high vanadium containing and low vanadium containing) in the slag. Bellemans et al. (2017) investigated the interaction between metal droplets and spinel phase present in the slag. Particles present in the slag affected the metal recovery due to the tendency of metal droplets to attach to these particles. Metal droplets attaching to spinel particles were also observed in the ferrovanadium recovery investigation, as can be observed in Figure 6.66.

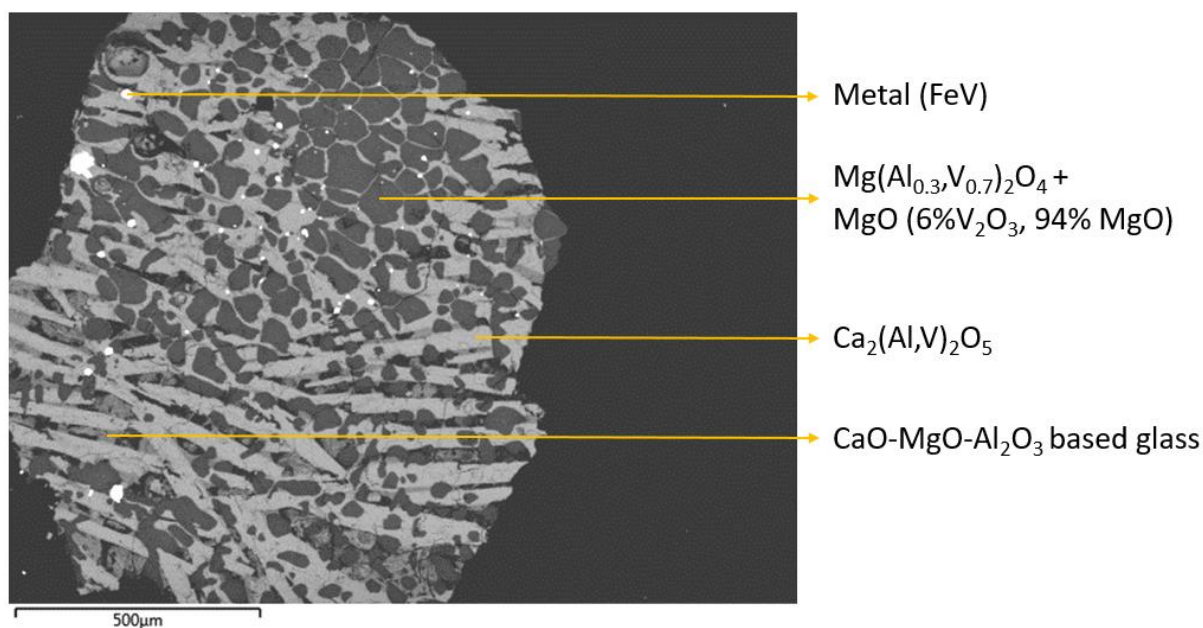


Figure 6.66: Electron backscatter image of the slag formed in test G where metal droplet attachment to spinel particles is present.

Metal droplets were also observed inside spinel particles (Figure 6.67), which indicated that the metal droplets did not attach to the particles, but that the spinel phase grew around the metal droplets. The metal droplets serve as a nucleation site for the spinel phase. The vanadium content of the metal droplets between the two phenomena differed considerably, for the case where spinel grew around the droplet the vanadium content was on average 55

wt% V, whereas when the droplet was attached to the spinel phase it was 75 wt% V on average. Formation of spinel phase around a metal droplet would result in interaction between the metal and spinel phase, with vanadium diffusing into the spinel phase resulting in a lower vanadium content in the metal droplet.

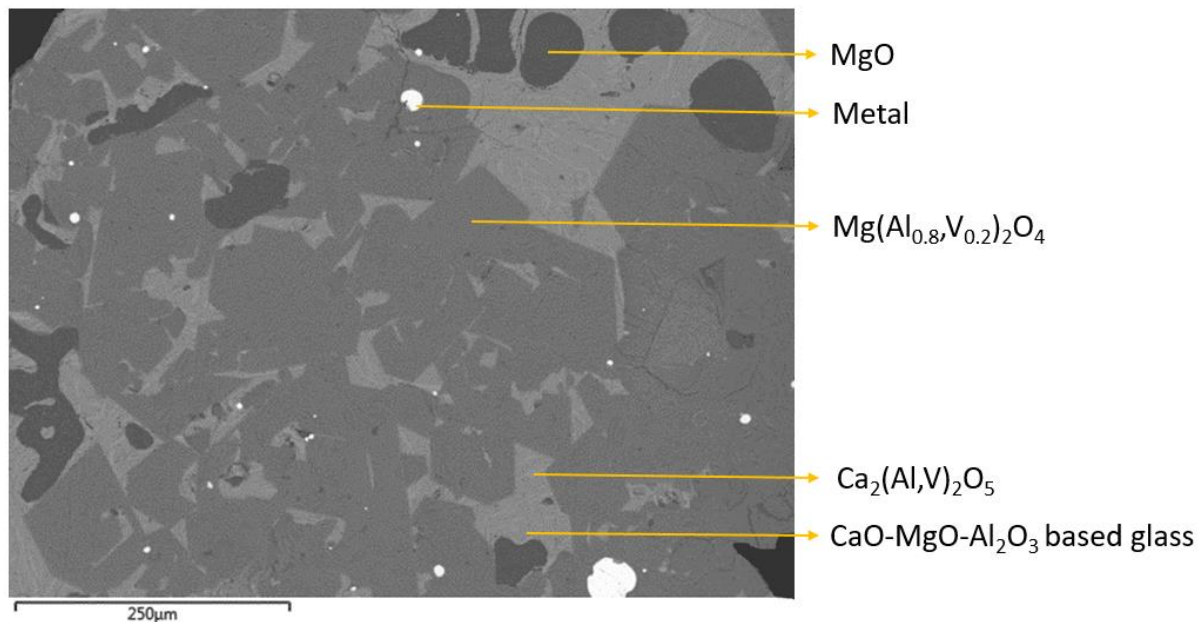


Figure 6.67: Electron backscatter image of the slag formed in the test C3, where spinel phase grew around metal droplets.

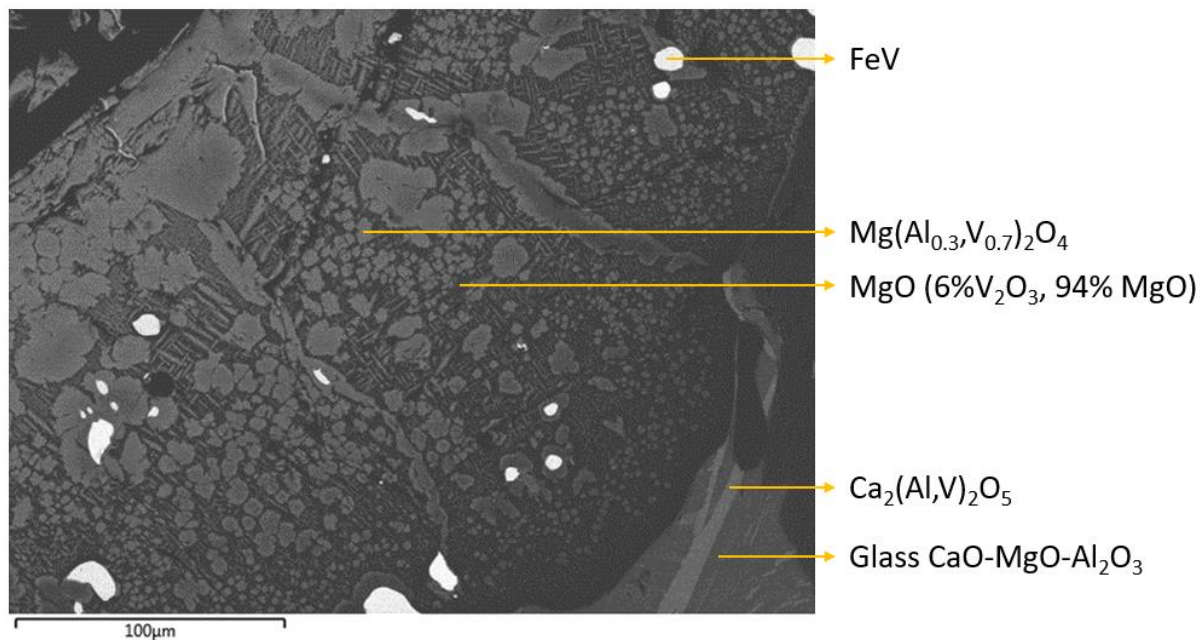


Figure 6.68: Electron backscatter image of the interface between the slag and the metal at a magnification of 60x for test C1.

6.7 Equilibrium tests

Equilibrium tests were done in order to determine which phases are present below the solidus temperature. Tests D, E, F and G that were done to determine the recovery as a function of

spinel formation were repeated, but in this instance the test temperature was 1400°C. 1400 °C was chosen because it is just above the solidus temperature of 1380°C, allowing liquid to form. The holding time of the tests were 24 hours and the heating and cooling rates were 3.8 °C/min. The atmosphere was controlled by introducing purified argon gas into an isolated system, which had a P_{O_2} of 10^{-12} atm at 1400°C. The tests were conducted in a vertical tube furnace.

SEM-EDS analysis was used to obtain an elemental analysis of the samples, which in combination with electron backscatter images were used to determine the phases present in the samples.

The SEM-EDS analysis indicated that the phases $Mg(Al,V)_2O_4$ (spinel) and $Ca_2V_2O_5$ were present in all four samples (D, E, F and G). Sample D also contained a small amount of glassy phase which consisted of CaO, MgO and Al_2O_3 . Sample F also contained a small amount of MgO_{ss} , which hosted a high vanadium spinel.

Comparing the slag formed in the non-equilibrium test (Figure 6.69) to the equilibrium test (Figure 6.70), it is evident that the spinel and $Ca_2V_2O_5$ phases were present in both slags. The amount of $Ca_2V_2O_5$ present did differ, as the non-equilibrium test contained thin needles of $Ca_2V_2O_5$, whereas the equilibrium tests contained large amounts of $Ca_2V_2O_5$. The reason for the change in quantity can be ascribed to the cooling rate, where a fast cooling rate resulted in the formation of thin needles of $Ca_2V_2O_5$, whereas a slow cooling rate allowed for more time for the $Ca_2V_2O_5$ crystals to grow.

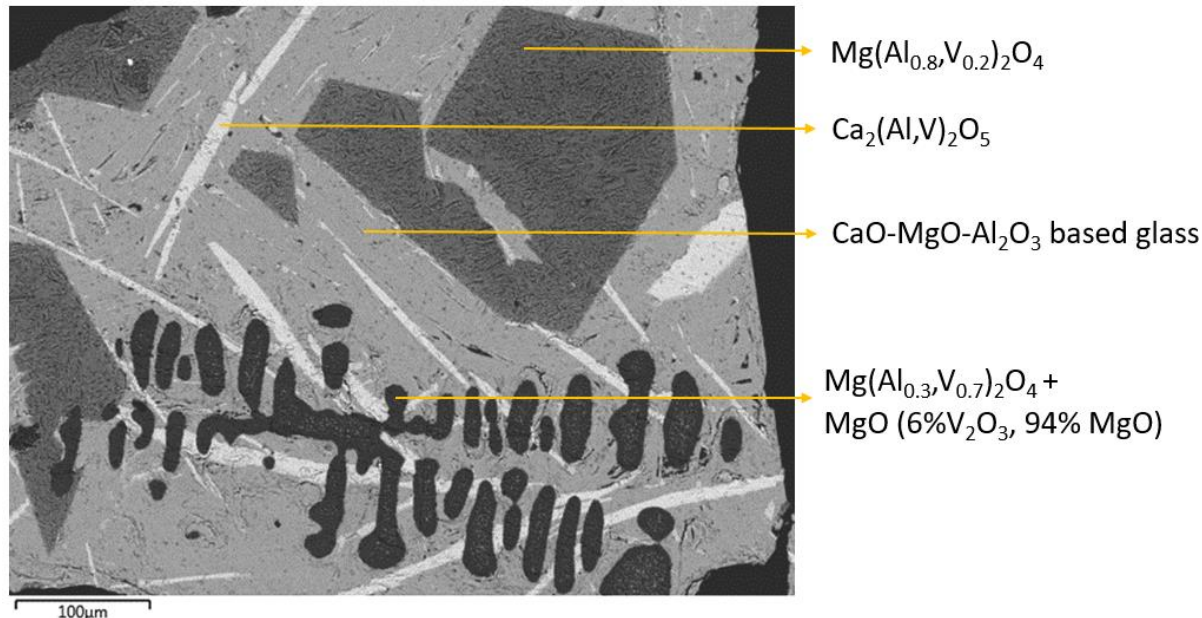


Figure 6.69: Electron backscatter image of the slag formed in test E (non-equilibrium).

It was also observed that the $Ca_2V_2O_5$ that formed under non-equilibrium (Figure 6.69) conditions contained Al^{3+} and had the chemical composition of $Ca_2(Al,V)_2O_5$, whereas the $Ca_2V_2O_5$ formed under equilibrium conditions (Figure 6.70) did not contain Al^{3+} and had the chemical composition $Ca_2V_2O_5$.

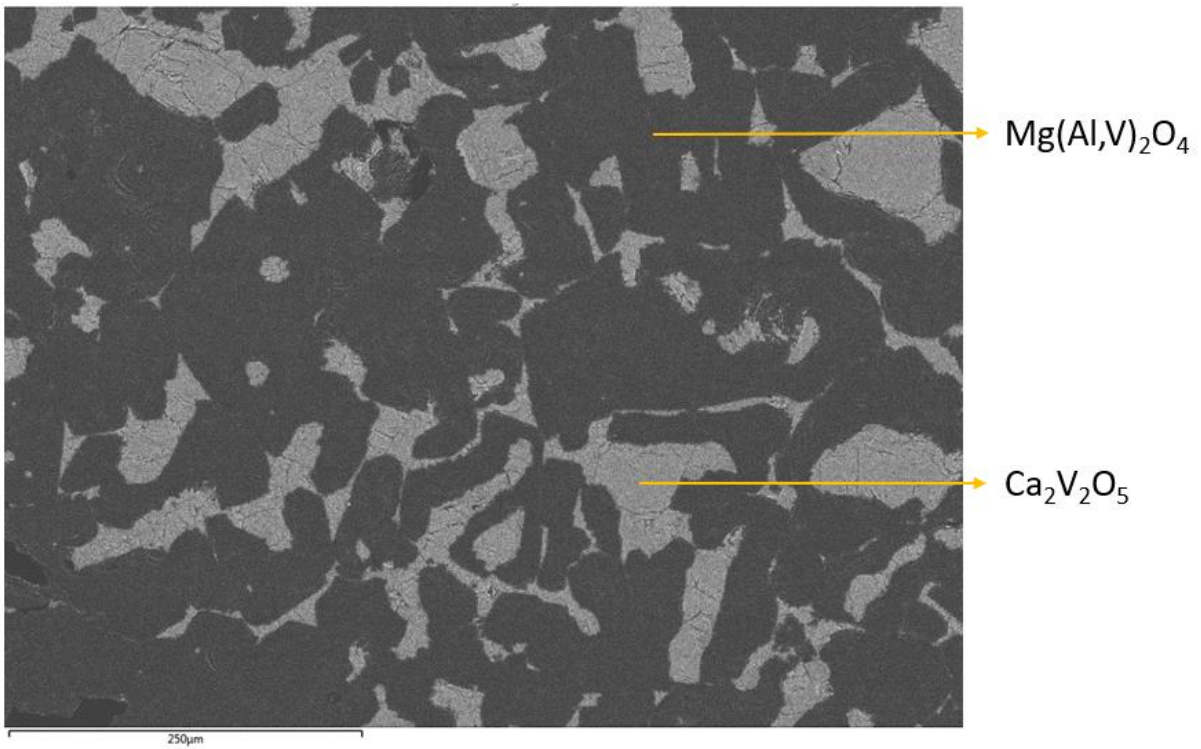


Figure 6.70: Electron backscatter image of the slag formed in equilibrium test E.

Chapter 7: Conclusions

The importance of slag composition on refractory wear was investigated in this study along with two different methods of possibly increasing the vanadium recovery in the ferrovanadium production process. The section on refractory wear focused on the importance of having a slag that is saturated in the main refractory constituent, in this case being MgO. The section on vanadium recovery focused on the effect of spinel content on recovery, as well as the possibility of increasing the vanadium recovery by producing ferrovanadium in two smelting steps.

The post-mortem slag and refractory analysis indicated that interaction between the slag and refractory resulted in a change in composition of the slag and MgO refractory brick that was in contact with the slag. The interaction resulted in an increase the MgO content of the slag and the presence of CaO and Al₂O₃ in the refractory brick. The presence of MgAl₂O₄ in the refractory indicated that a chemical reaction occurred between the slag and the refractory.

Increasing the MgO content of the slag in order to obtain a slag saturated in the main component of the refractory decreased the refractory wear rate. The decrease in refractory wear rate was evident by the difference in height of the refractory core in contact with a slag not saturated in MgO and a MgO saturated slag respectively. The height of the refractory core that was in contact with the slag not saturated in MgO decreased significantly compared to the refractory core that was in contact with the MgO saturated slag, indicating that the refractory wear was reduced by adding MgO to the slag. The rate of refractory wear will therefore decrease with an increase of MgO added to the slag.

Changing the slag composition to reduce the spinel content of the slag did not yield higher vanadium recoveries. The vanadium recovery decreased as the amount of spinel phase present in the slag decreased (change from slag composition D to G), indicating that spinel formation is not the main driving force for vanadium recovery. The vanadium recovery increased with a decrease in calculated slag viscosity and decreased as the calculated slag volume increased, which is in agreement with what would be expected in terms of slag viscosity and volume.

The vanadium recovery did decrease linearly with an increase in the (CaO+MgO): Al₂O₃ ratio of the slag composition. The vanadium recovery decreased linearly from 75 % to 25 % as the (CaO+MgO): Al₂O₃ ratio increased from 0.30 to 1.43. The (CaO+MgO): Al₂O₃ ratio influences the activity coefficient of V₂O₃, resulting in different vanadium partitioning between the slag and metal with a change in the (CaO+MgO): Al₂O₃ ratio. The vanadium recovery increased as the V₂O₃ activity coefficient increased, agreeing with the literature on vanadium recovery versus V₂O₃ activity coefficient by Vermaak and Pistorius (2000). The vanadium recovery is therefore strongly influenced by the slag volume and the (CaO+MgO): Al₂O₃ ratio of the slag composition.

The vanadium recovery increased as the excess aluminium added to the reaction increased. An increase in the recovery of 2.5 wt% vanadium was observed as the excess aluminium content was increased from 1.5 wt% to 3.5 wt% aluminium. The vanadium recovery only

increased by 0.2 wt% for an increase from 3.5 wt% to 5.5 wt% excess aluminium. Adding 3.5 wt% excess aluminium was identified as the optimum aluminium addition for the first stage of the two stage smelting process based on the recovery results. Aluminium fade did occur in each test, in test C1 the ferrovanadium had an excess aluminium content of 0.4 wt% instead of 1.5 wt%, in test C2 an excess aluminium content of 1.4 wt% instead of 3.5 wt% and in test C3 an excess aluminium content of 1.8 wt% instead of 5.5 wt%. It can be concluded that the vanadium recovery can be increased by increasing the excess aluminium added to the reaction.

Reacting the metal obtained from the first smelting step with Fe_2O_3 successfully reduced the aluminium content of the metal. The aluminium content of the metal reduced from 3.5 wt% to 0.8 wt% (test H1) and to 0.7 wt% (test H2) respectively. The vanadium recovery of the second stage was 98.3 wt%, which resulted in an overall vanadium recovery of 72.6 wt% for the two stage process compared to 71.4 wt% for the single stage process. It is therefore feasible to use Fe_2O_3 to implement a two stage melting process to increase the vanadium recovery of the process and to obtain a ferrovanadium product with an aluminium content below 1.5 wt% Al. The vanadium content of the metal decreased from 68.6 wt% to 63.5 wt%, indicating that the vanadium to iron ratio would have to be increased for the first melting stage in order to achieve the required vanadium content in the metal after the second stage.

Chapter 8: Recommendations

Adding MgO as a raw material will increase the lifespan of the refractories used in industry and it is recommended that enough MgO be added to obtain saturation. At temperatures slightly above 2000°C (approximate operating temperature), saturation can be achieved by adding enough MgO to form a slag consisting of 10 wt% MgO.

The vanadium recovery is strongly influenced by the slag volume and it is recommended that the slag volume be kept as low as possible. This can be done by minimising the amount of MgO and CaO added as a flux (10 wt% MgO and 5 wt% CaO at a temperature of 2000°C). The vanadium recovery is also influenced by the $(\text{CaO}+\text{MgO}):\text{Al}_2\text{O}_3$ ratio, with higher vanadium recoveries obtained at lower ratios. It is therefore recommended to use a low $(\text{CaO}+\text{MgO}):\text{Al}_2\text{O}_3$ ratio when calculating the raw material recipe.

Implementing a two stage smelting process will increase the overall vanadium recovery. It is recommended that an excess of 3.5 wt% aluminium be used in the first stage to optimise vanadium recovery. Millscale can then be used in a second smelting stage to decrease the aluminium content in the metal obtained from the first stage to customer specifications.

Chapter 9: Recommendations for future work

The formation of $\text{Ca}_2\text{V}_2\text{O}_5$ is a relatively unknown phenomenon in the ferrovanadium field. $\text{Ca}_2\text{V}_2\text{O}_5$ was identified in all of the metal-slag interaction tests in the form of $\text{Ca}_2(\text{Al},\text{V})_2\text{O}_5$. It would be beneficial to determine if the difference can be ascribed to a difference in cooling rate.

High vanadium containing phases such as $\text{Ca}_2\text{V}_2\text{O}_5$ and a $\text{MgO-V}_2\text{O}_3$ solid solution which hosted a high vanadium spinel phase was observed in multiple tests done at laboratory scale. These phases were however not observed in the post mortem analysis of industrial slag. The reason for this occurrence was ascribed to the difference in vanadium concentration, as the industrial slag sample was taken from the top part of the slag, whereas the laboratory scale slag sample was representative of the entire slag. Future work can focus on if the presence of these phases are a function of vanadium concentration (which can vary in different regions of the slag).

References

- Arkipov, O. A., Berezin, N. M. and Shtengel'meier, S. V., 1964, Influence of the physicochemical properties of the slag on the separation of liquid phases in the production of high-percentage ferrovanadium by the aluminothermic method, Surface phenomena in metallurgical processes, Metallurgizdat, Moskow, pp. 224-226
- Barnett, S.C.C. and Jeffes, J.H.E., 1977, Recovery of nickel from Thompson Smelter electric furnace slag. Trans. Inst. Min. Metall. C, 86: C155-C157
- Bellemans I., Cnockaert vanadium., De Wilde E., Moelans N. and Verbeken K., 2017, Metal losses in pyrometallurgical operations, Advances in Colloid and Interface science, <http://dx.doi.org/10.1016/j.cis.2017.08.001>, pp. 6-8
- Bellemans I., Cnockaert V., De Wilde E., Moelans N. and Verbeken K., 2017, Metal droplet entrainment by solid particles in slags: a combined phase field model and experimental approach, Proceedings of EMC 2017, Presented at the European Metallurgical conference 2017 pp.1525-1540
- Cini, L., 1968, System V_2O_3 -MgO under nonoxidizing conditions, Radex Rundsch, No. 2, pp. 102-112
- Eissa M., Ahmed A. and El-Fawkhry, 2015, Conversion of Mill scale waste into valuable products via carbothermic reduction, Hindawi publishing corporation, Journal of Metallurgy, Volume 2015, pp.1-9
- Floyd, J.M. and Mackey, P.J., 1981, Developments in the pyrometallurgical treatment of slag: a review of current technology and physical chemistry, Proceedings of Extraction Metallurgy 81: 345-371
- Gasik, M., 2013, Handbook of ferroalloys: Theory and technology, Elsevier, Waltham, pp. 397-409
- Gupta, C. K., and Krishnamurthy, N., 1992, Extractive metallurgy of vanadium, Process metallurgy 8, Amsterdam, Netherlands
- Habashi, F., 2002a. Two hundred years of vanadium. In: Tanner, M.F., Riveros, P.A., Dutrizac, J.E., Gattrell, M., Perron, L. (Eds.), Vanadium, Geology, Processing and Applications, Proceedings of the International Symposium on Vanadium, Conference of Metallurgists, Montreal, Canada , pp. 3–15
- Joerissen, L., Garche, J., Fabjan C. and Tomazic G., 2004, Possible use of vanadium redox-flow batteries for energy storage in small grids and standalone photovoltaic systems, Journal of power sources, vol. 127, pp. 98-104

Katsumata, M., Ishiyama, O., Inoue, T. and Tanaka, T., 1991, Microstructure and mechanical properties of bainite containing martensite and retained austenite in low carbon HSLA steels, materials transactions, vol. 32, pp. 715-728

Kekkonen, M., Oghbasilasie, H. and Louhenkilpi, S., 2012, Viscosity models for molten slags, School of Chemical technology, pp. 19-22

Kubaschewski, O., Alcock, C. B. and Spencer, P.J., 1993, Materials Thermodynamics, 6th edition, Pergamon, Oxford, pp. 258-338.

Lea, F. M. and Desch, C. H., 1956, The Chemistry of Cement and Concrete, 2nd edition, Edward Arnold and co., London, p. 52

Liow, J.L., Juusela, M., Gray, N.B. and Sutalo, I.D., 2003, Entrainment of a two-layer liquid through a taphole, Metall. And Materials trans. B 34B: 821-832

Minto, R. and Davenport, W. G., 1972, Entrapment and flotation of matte in molten slags. Trans. Inst. Min. Metall., 81: C36-C41

Moskalyk, R. R. and Alfantazi, A. M., 2003, Processing vanadium: A review, Minerals Engineering, volume 16, pp. 793-805

Poggi D, Minto R, Davenport W. Mechanisms of metal entrapment in slags. J Met 1969;21 40-44

Rein, R. H. and Chipman, J., 1965, Trans. TMS-AIME, volume 233, pp. 415-425

Sandford, S. C. and Breitenstein, 1951, Recovery of Vanadium from Titaniferous Magnetite, Journal of Metals, vol. 3, pp. 1133-1137

Seetharaman, S., Mukai, K. and du Sichen, 2004, Viscosities of slags-an overview, VII International Conference on Molten Slags Fluxes and Salts, The South African Institute of Mining and Metallurgy, pp. 31-40

Silva, A. C., 2012, Estimating viscosities in iron and steelmaking slags in the CaO- Al₂O₃-MgO-SiO₂-(TiO₂) system with basis on a thermodynamic model, Journal of materials research and technology, Elsevier, Brazil, pp. 154-160

Smith J.F, 1984, The Fe-V (iron-vanadium) system, Bulletin of alloy phase diagrams, Iowa state University, vol. 5 no.2, p. 184

Vermaak, M. K. G. and Pistorius, P. C., 2000, Equilibrium Slag Losses in Ferrovandium Production, Metallurgical and materials transactions B, volume 31B, pp. 1091-1097

Appendix

1 Post-mortem slag analysis

Table 1: XRD results of the post mortem slag samples taken from an industrial ferrovanadium production process.

Ferrovanadium slag sample 1			Ferrovanadium slag sample 2			Ferrovanadium slag sample 3		
	wt%	3 σ error		wt%	3 σ error		wt%	3 σ error
Amorphous	48.81	2.31	Amorphous	20.84	1.77	Amorphous	7.31	2.4
Grossite	12.87	1.11	Grossite	14.47	0.29	Grossite	21.86	0.99
Krotite	17.33	1.38	Krotite	7.63	0.63	Krotite	13.52	1.05
Spinel	20.97	0.14	Spinel	57.05	0.57	Spinel	56.30	1.38

Table 2: Composition of the post mortem slag.

Slag component	Amount (wt%)
Al₂O₃	71.6
CaO	6.6
MgO	21.8

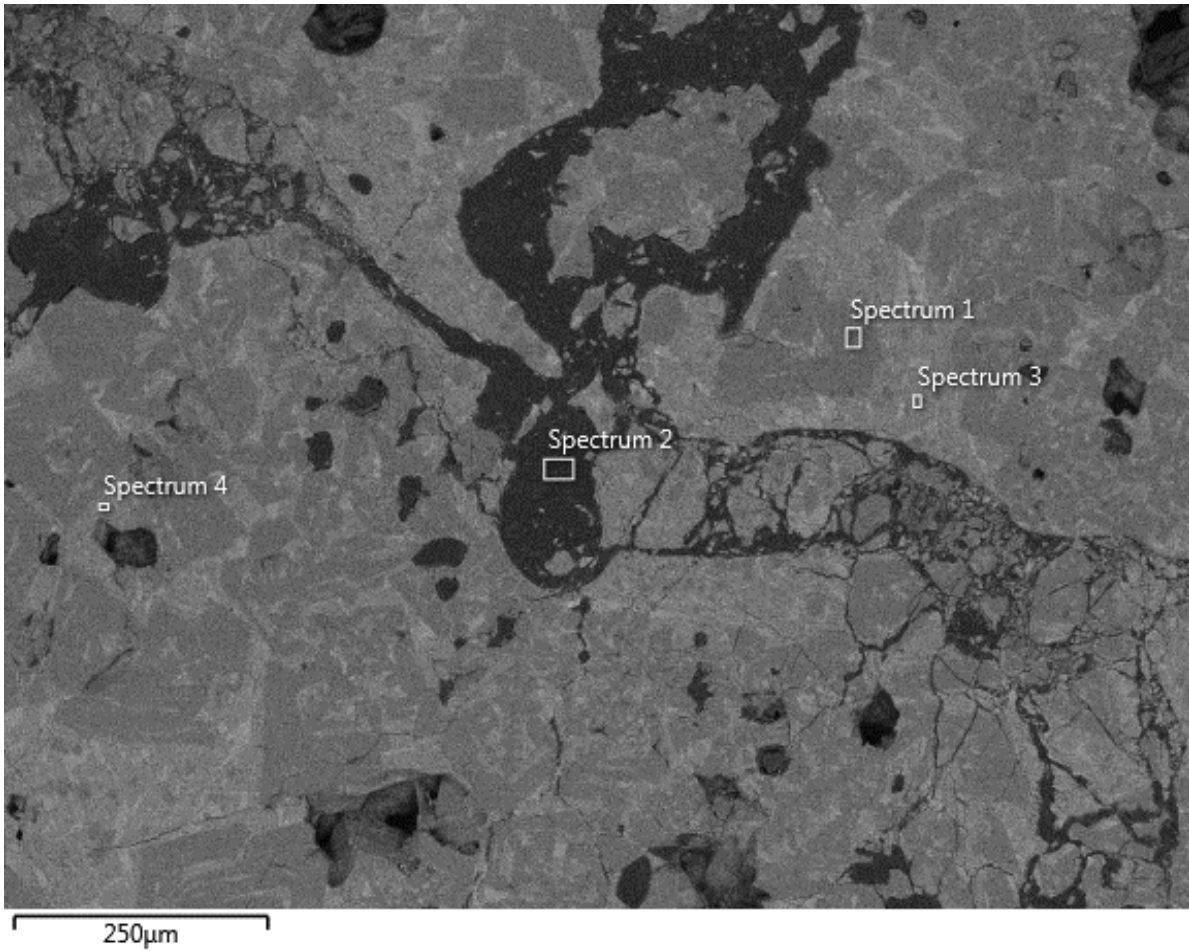


Figure 1: Electron backscatter image of a post mortem slag sample from the ferrovanadium industry.

Table 3: Spectrum data for Figure 1.

Component	Spectrum 1	Spectrum 3	Spectrum 4
O (At %)	58	61.3	61
Al (At %)	28	29	32
Mg (At %)	13		
Ca (At %)		8.8	7.7



Figure 2: Electron backscatter image of a metal droplet inclusion in the slag.

Table 4: Elemental analysis of the two phases present in the metal inclusion.

Component	Spectrum 5	Spectrum 6
V (wt%)	98.1	65.1
Fe (wt%)	1.9	34.9

Table 5: Elemental analysis of the phase surrounding the metal droplet (spinel phase).

Component	Spectrum 7
O (At%)	56
Al (At%)	27.9
Mg (At%)	13.9
V (At%)	2.2

2 Post-mortem refractory analysis

Table 6: XRF analysis of the MgO brick in contact with the slag.

Component	Position				
	1	2	3	4	5
MgO (wt %)	79.18	70.23	95.7	95.97	96.14
Al ₂ O ₃ (wt %)	13.11	22.22	0.38	0.27	0.22
SiO ₂ (wt %)	1.11	0.69	1.29	1.11	1.12
CaO (wt %)	4.72	5.21	1.5	1.47	1.49
V ₂ O ₅ (wt %)	0.98	0.94	0.02	<0.01	<0.01
Fe ₂ O ₃ (wt %)	0.56	0.5	0.7	0.72	0.73
P ₂ O ₅ (wt %)	0.1	0.03	0.21	0.19	0.19

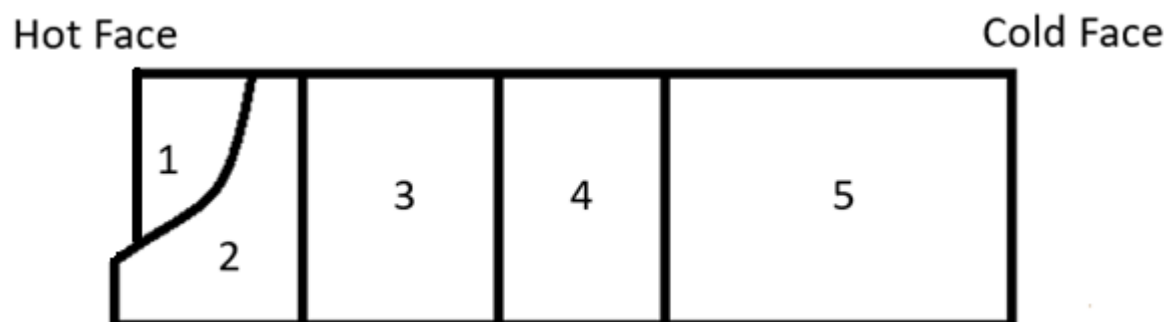


Figure 3: Schematic of the position of the samples that were taken from the MgO brick.

2.1 SEM-EDS results

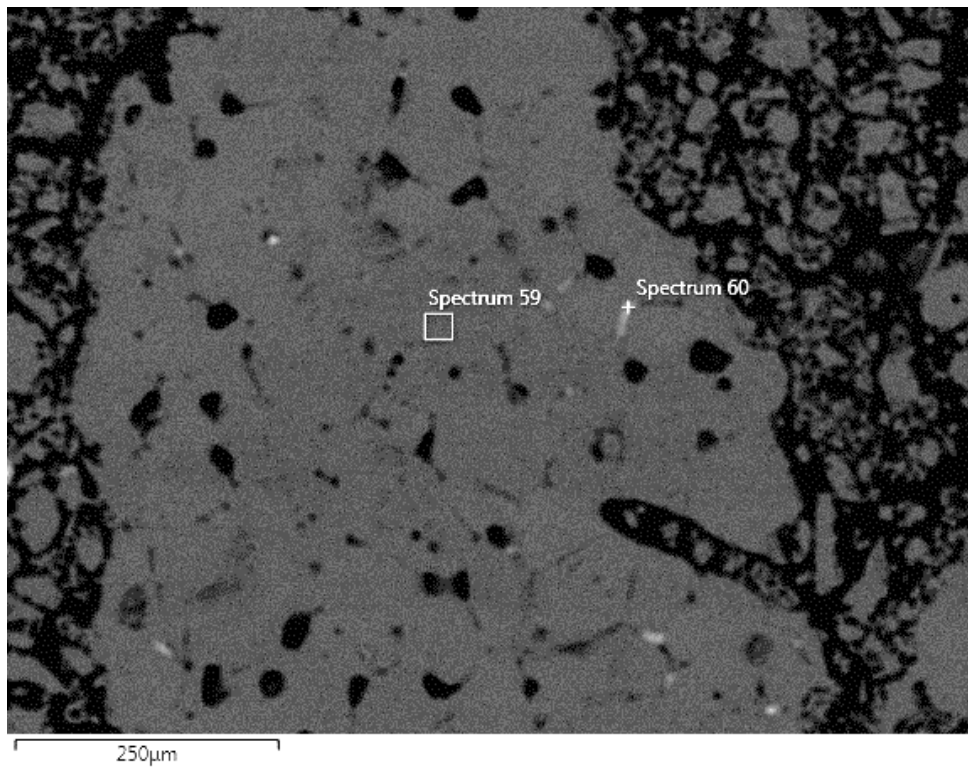


Figure 4: Electron backscatter image of the cold face of a post mortem MgO brick sampled from the side wall where the slag is in contact with the brick.

Table 7: SEM-EDS analysis of Figure 4.

	Spectrum 59	Spectrum 60
Mg (At %)	53.2	14.4
O (At %)	46.8	56.5
Ca (At %)		16.6
Si (At %)		12.5
Phase	MgO	CaMgSiO ₄

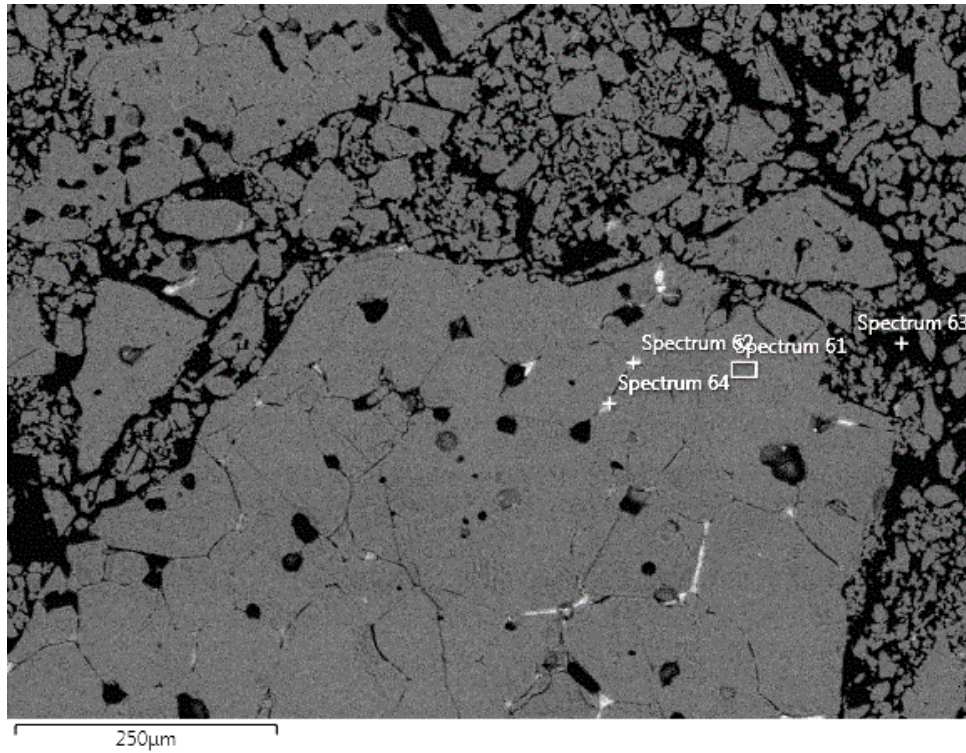


Figure 5: Electron backscatter image of sample 4 situated closer to the hot face than sample 5.

Table 8: SEM-EDS analysis of Figure 5.

	Spectrum 61	Spectrum 62	Spectrum 63	Spectrum 64
Mg (At %)	52.5	1.9	100	3.5
O (At %)	47.5	62.1		64.1
Ca (At %)		24.9		21.2
Si (At %)		11.1		11.2
Phase	MgO	Ca ₃ Mg(SiO ₄) ₂	MgO	Ca ₃ Mg(SiO ₄) ₂

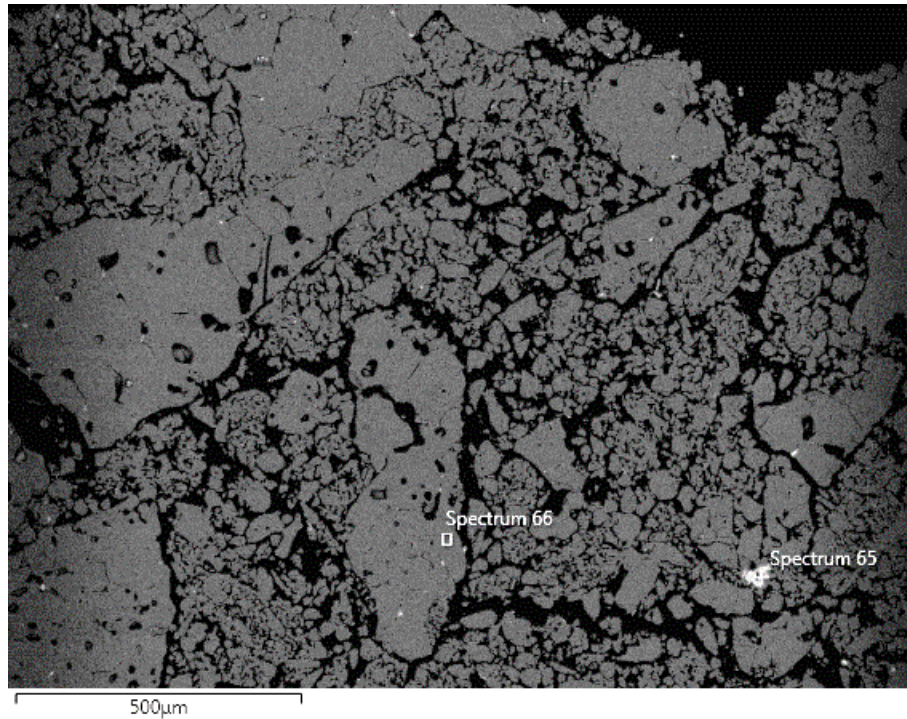


Figure 6: Electron backscatter image of sample 3 situated near the refractory zone that was affected by slag penetration.

Table 9: SEM-EDS analysis of Figure 6.

	Spectrum 65	Spectrum 66
Mg (At %)	4.0	52.5
O (At %)	61.4	47.5
Ca (At %)	23.3	
Si (At %)	11.3	
Phase	Ca₃Mg(SiO₄)₂	MgO

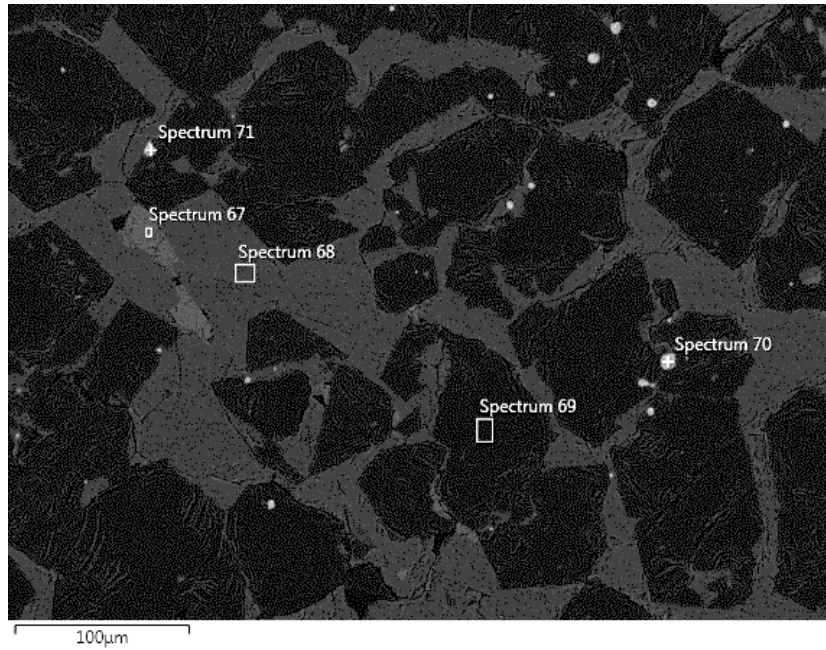


Figure 7: Electron backscatter electron image of the MgO hot face, situated at the slag-refractory interface, containing only slag.

Table 10: SEM-EDS analysis of Figure 7.

	Spectrum 67	Spectrum 68	Spectrum 69	Spectrum 70	Spectrum 71
Mg (At %)			14.6		
Al (At %)	29.2	79	30.7		
O (At %)	55.8		54.6		
Ca (At %)	15	21			
V (At %)				74	75.3
Fe(At %)				26	23.6
Phase	CaAl₂O₄	CaAl₄O₇	MgAl₂O₄	FeV	FeV

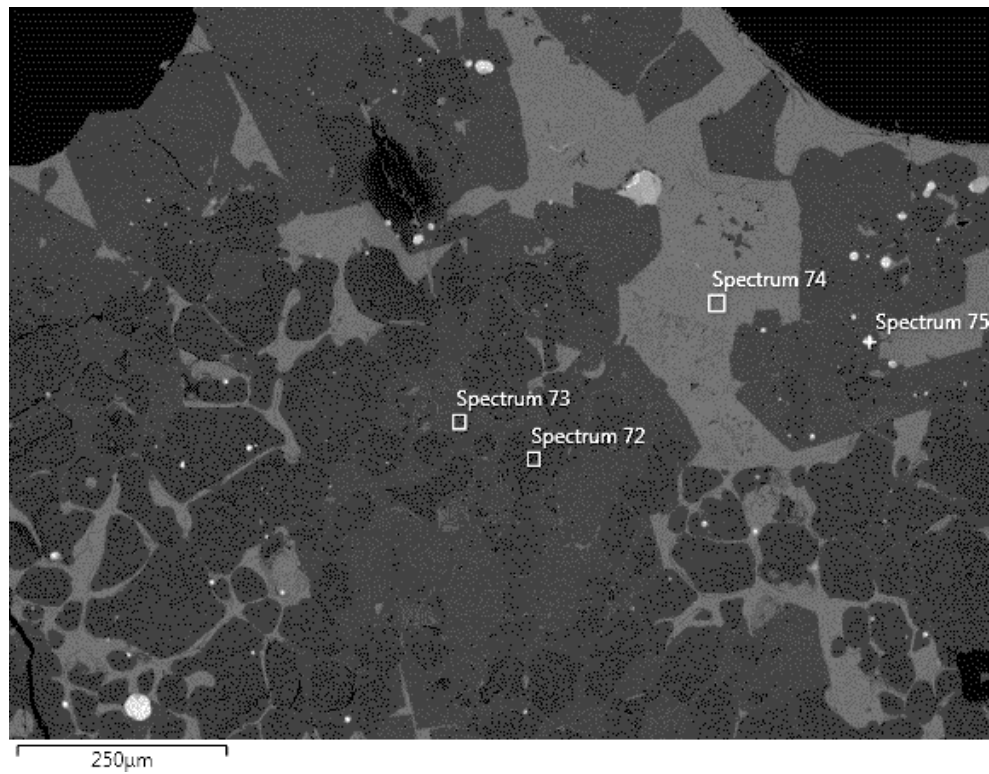


Figure 8: Electron backscatter electron image of the MgO hot face on the same sample as that of Figure 29, but on the refractory side of the slag-refractory interface.

Table 11: SEM-EDS analysis of Figure 8.

	Spectrum 72	Spectrum 73	Spectrum 74	Spectrum 75
Mg (At %)	53.5	14.9		
Al (At %)		30.1	24.1	
O (At %)	46.5	55	55.9	
Ca (At %)			19.9	
V (At %)				70.5
Si (At %)				1.4
Fe (At %)				28.1
Phase	MgO	MgAl₂O₄	Ca₁₂Al₁₄O₃₃	FeV

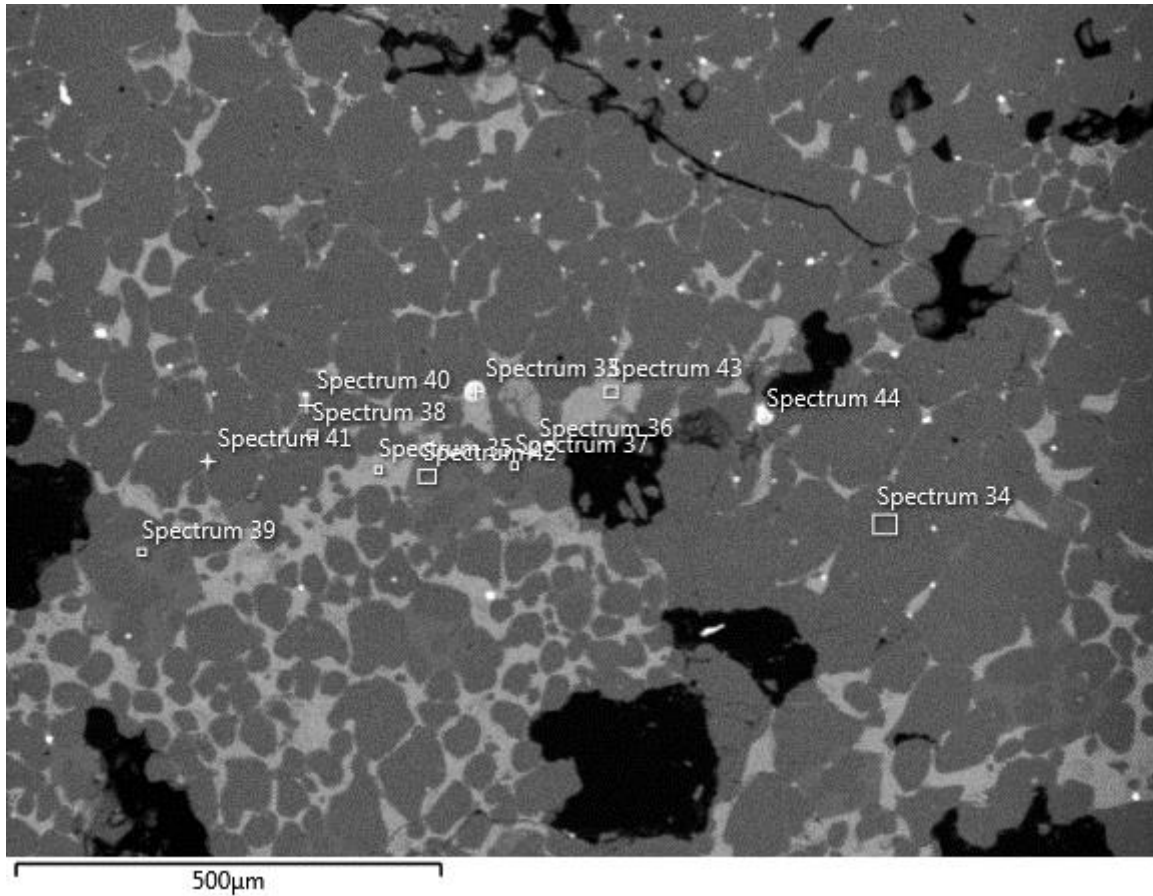


Figure 9: Electron backscatter image of MgO sample near the hot face (sample 1).

Table 12: SEM-EDS analysis of Figure 9.

	Spectrum 33	Spectrum 34	Spectrum 35	Spectrum 36	Spectrum 37	Spectrum 38	Spectrum 39
Mg (At %)		97		29	100	100	14.1
Fe (At %)	100						
Al (At %)		3	53.4	71			27
Ca (At %)			46.6				
O (At %)							59
Phase	Fe	MgO	Ca ₁₂ Al ₁₄ O ₃₃	MgAl ₂ O ₄	MgO	MgO	MgAl ₂ O ₄

Table 13: SEM-EDS analysis of Figure 9.

	Spectrum 40	Spectrum 41	Spectrum 42	Spectrum 43	Spectrum 44
Mg (At %)			14.1		
Fe (At %)		100			100
Al (At %)	22.2		27.7	22	
Ca (At %)	17.5			17.7	
O (At %)	60.3		58.3	60.3	
Phase	Ca ₁₂ Al ₁₄ O ₃₃	Fe	MgAl ₂ O ₄	Ca ₁₂ Al ₁₄ O ₃₃	Fe

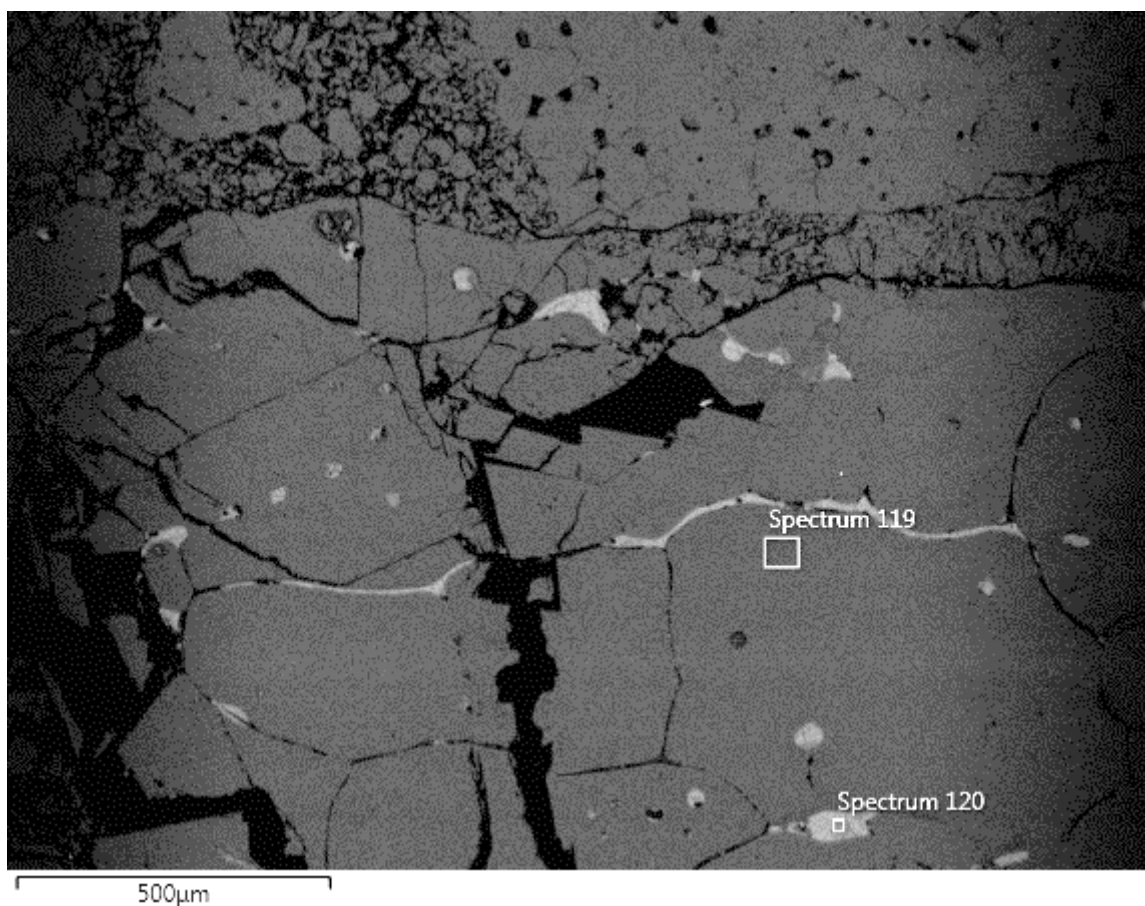


Figure 10: Electron backscatter image of the MgO cold face at the hearth of the furnace.

Table 14: SEM-EDS analysis of Figure 10.

	Spectrum 119	Spectrum 120
Mg (At %)	47.8	4
O (At %)	52.2	65.8
Ca (At %)		20.3
Si (At %)		9.9
Phase	MgO	Ca ₃ Mg(SiO ₄) ₂

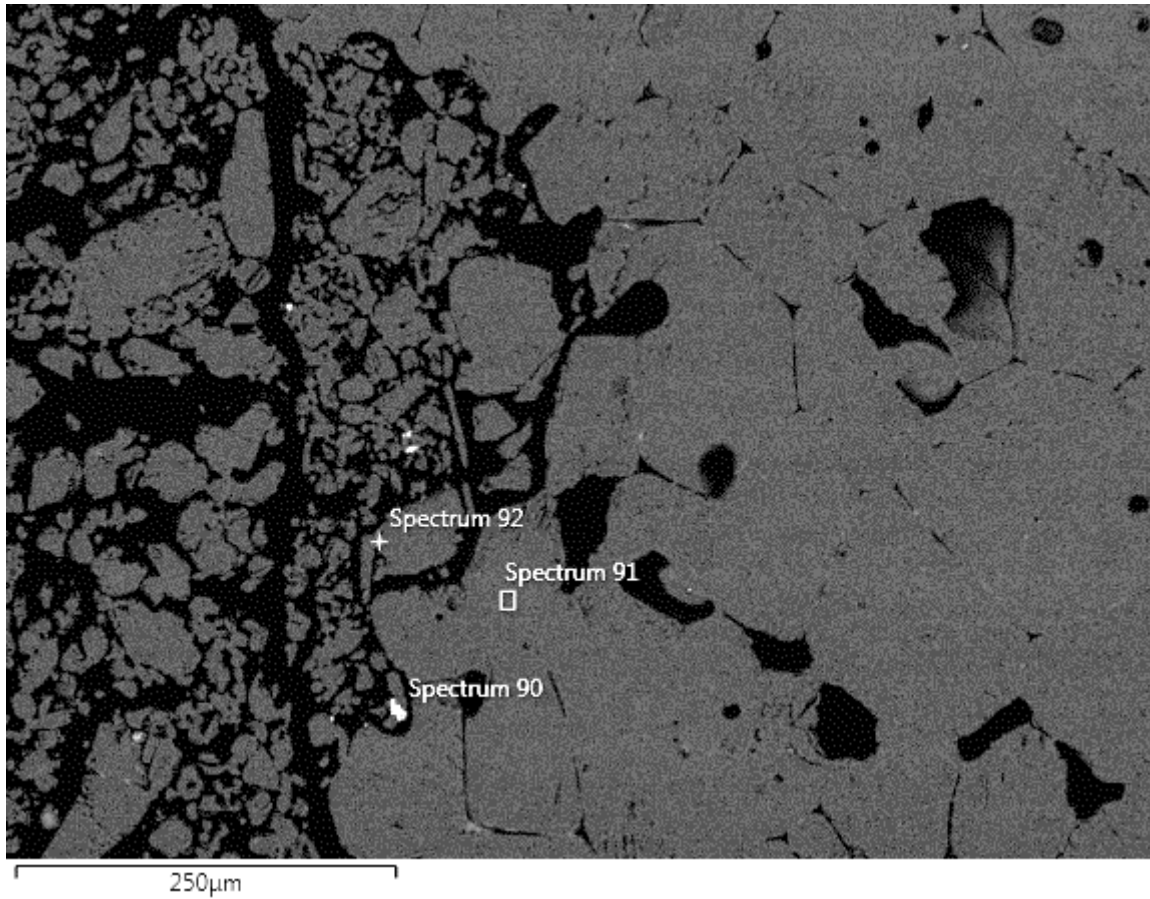


Figure 11: Electron backscatter image of the MgO brick situated at the hearth of the furnace.

Table 15: SEM-EDS analysis of Figure 11.

	Spectrum 90	Spectrum 91	Spectrum 92
Mg (At %)		48	9.9
O (At %)		52	13.1
Zn (At %)	25.4		23.3
S (At %)	21.9		20.2
Phase	ZnS	MgO	ZnS

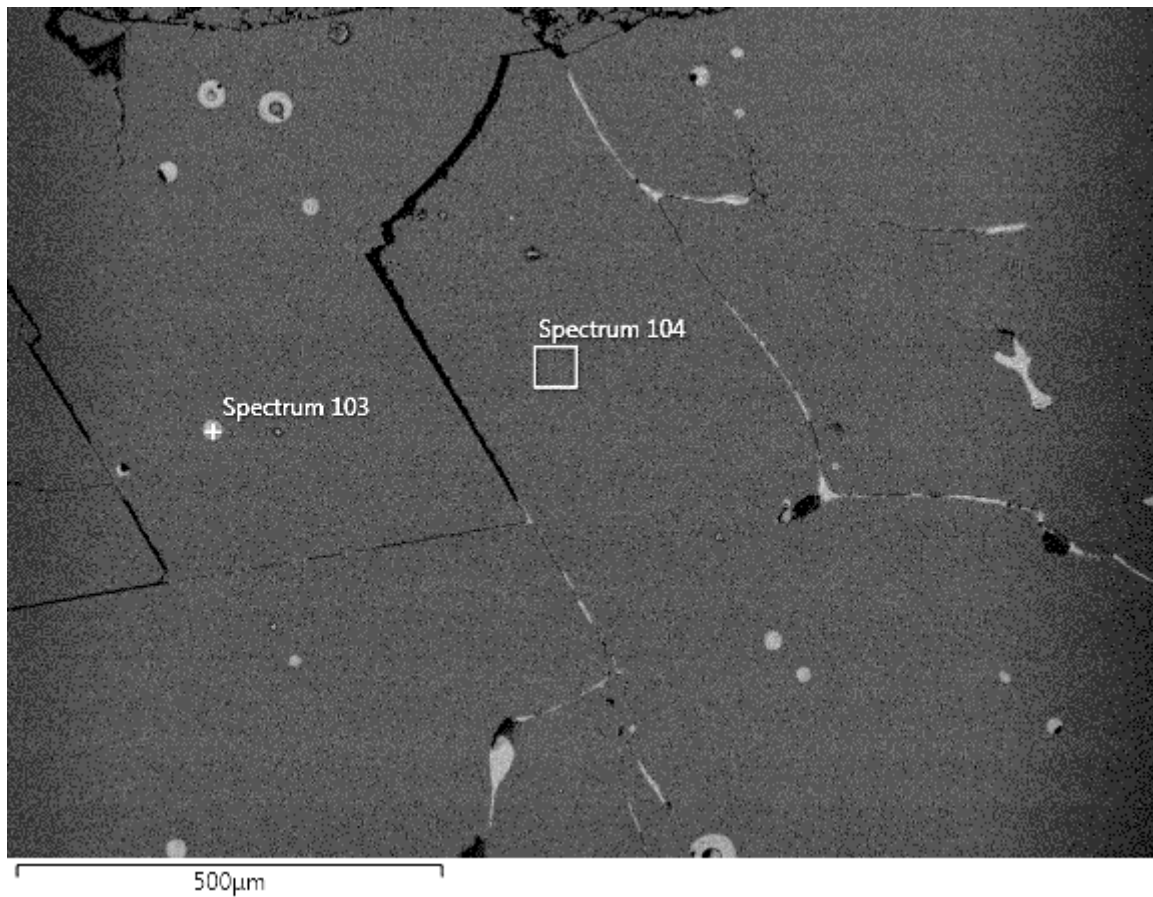


Figure 12: Electron backscatter image of the hot face of the MgO brick at the bottom of the furnace.

Table 16: SEM-EDS analysis of Figure 12.

	Spectrum 103	Spectrum 104
Mg (At %)	7.3	49.5
Al (At %)		
O (At %)	61.5	50.5
Ca (At %)	18.7	
V (At %)		
Si (At %)	12.5	
Phase	Glassy	MgO

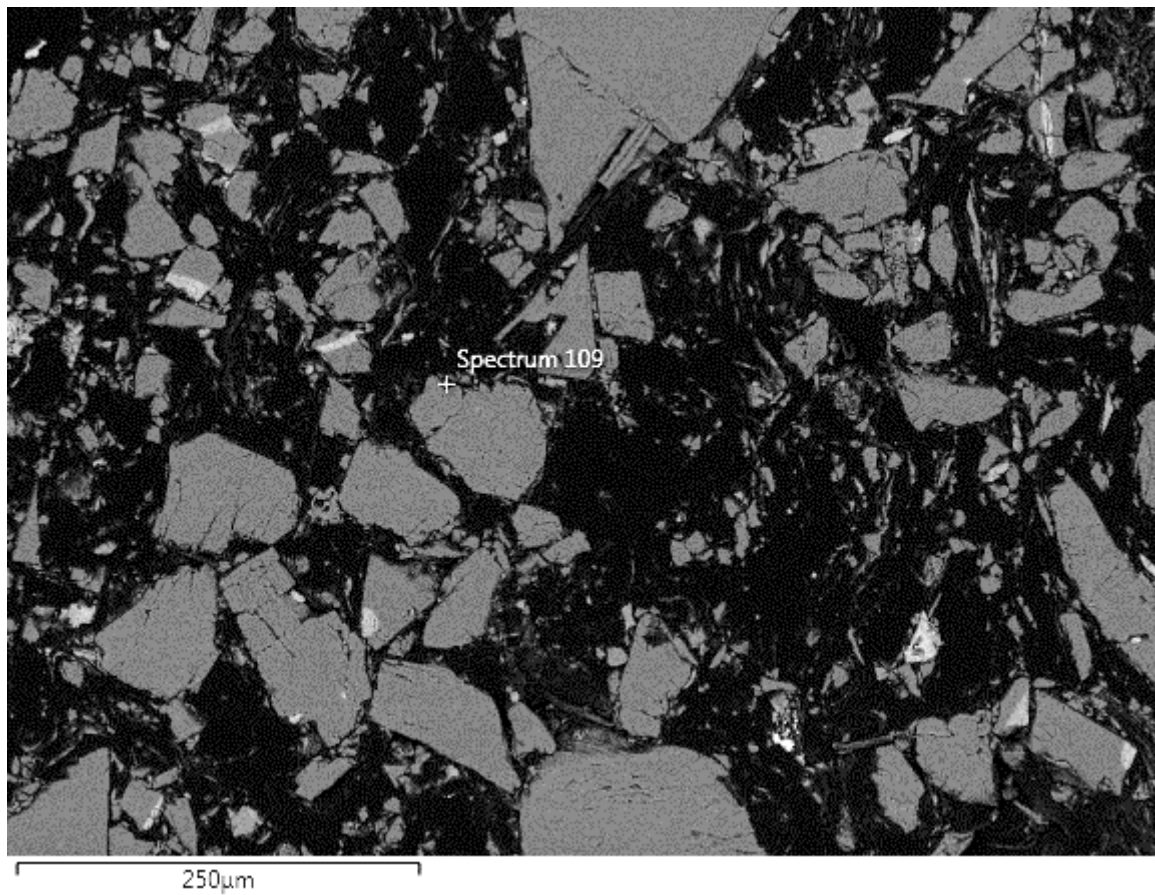


Figure 13: Electron backscatter image of a MgO-C sample at the cold face of the brick.

Table 17: SEM-EDS analysis of Figure 13.

	Spectrum 109
Al (At %)	19.8
Cu (At %)	7.7

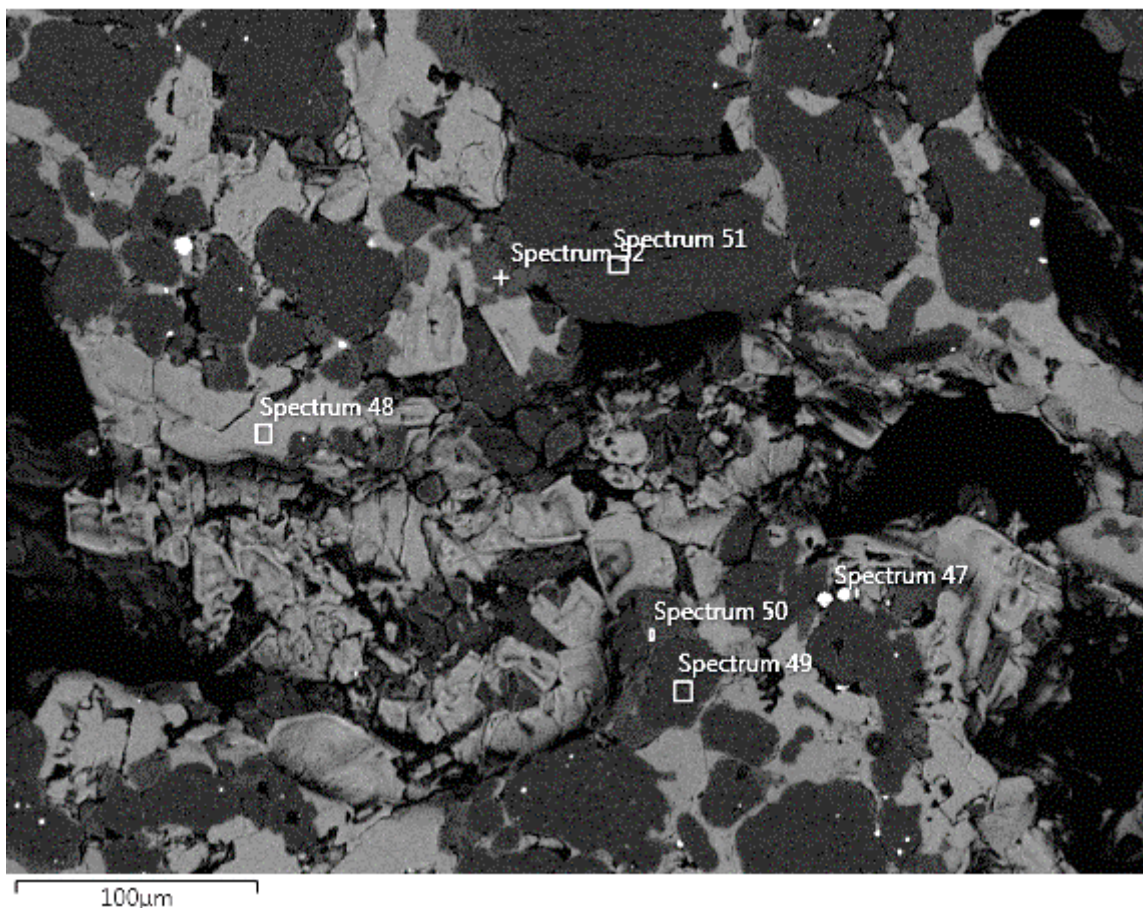


Figure 14: Electron backscatter image of the MgO-C hot-face that contained a precipitate on the surface.

Table 18: SEM-EDS analysis of Figure 14.

	Spectrum 47	Spectrum 48	Spectrum 49	Spectrum 50	Spectrum 51	Spectrum 52
Mg (At %)			52.6	18.3	53.1	19.6
Fe (At %)	93.1					
Al (At %)				40.4		41.4
Ca (At %)		32.9				
O (At %)		52.3	47.4	41.3	46.9	39
Si (At %)		14.7				
Cu (At %)	6.9					
Phase	Metal	Ca ₂ SiO ₄	MgO	Spinel	MgO	Spinel

Figure 15: Backscatter image of the MgO-C hot face that contained a precipitate on the surface.

3. Slag-refractory interaction

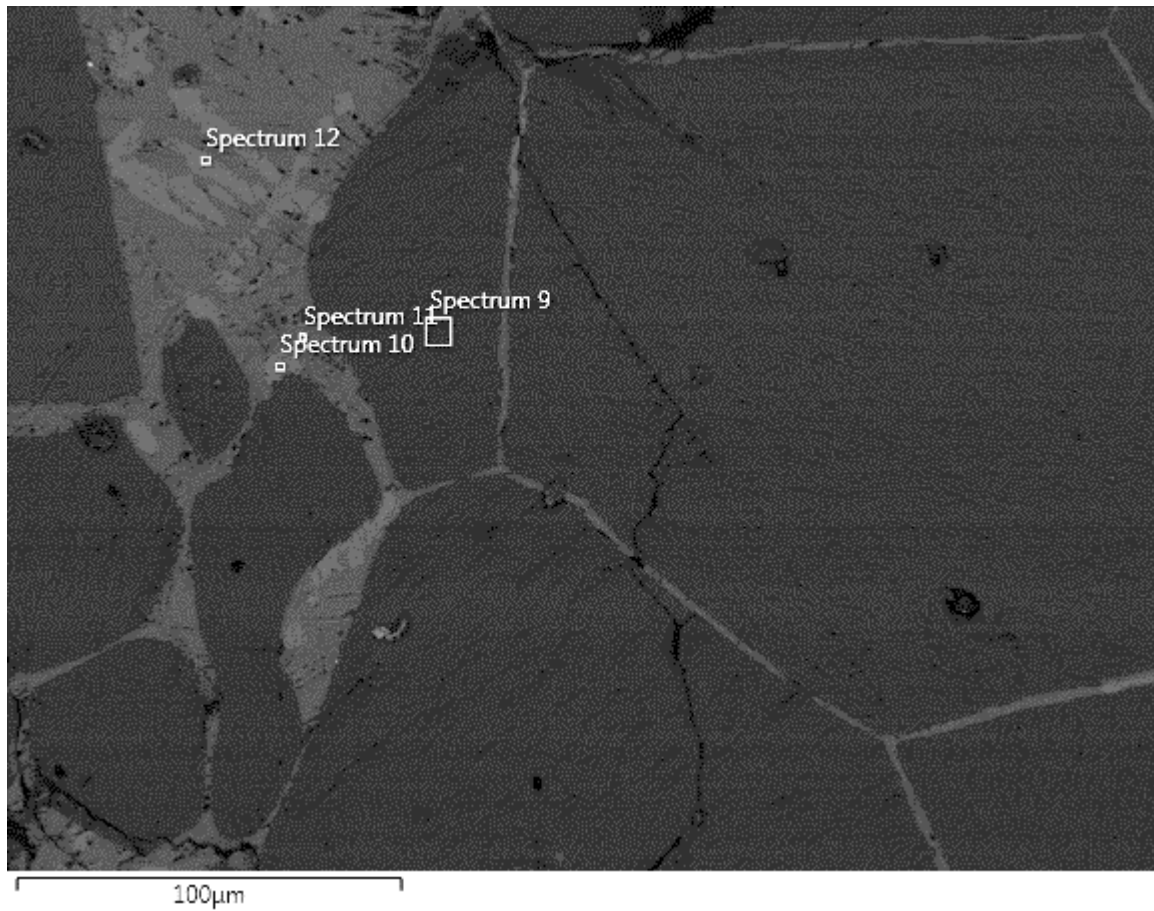


Figure 16: Electron backscatter image of the region analysed at the centre-centre region of the refractory.

Table 19: SEM-EDS analysis of Figure 16.

	Spectrum 9	Spectrum 10	Spectrum 11	Spectrum 12
Mg (At %)	50.0		2.0	
Al (At %)		19.6	23.2	21.3
O (At %)	50.0	65.2	59.4	62.3
Ca (At %)		11.8	15.4	13.2
Mo (At %)		2.9		3.2
Phase	MgO	CaAl ₂ O ₄	Glassy	CaAl ₂ O ₄

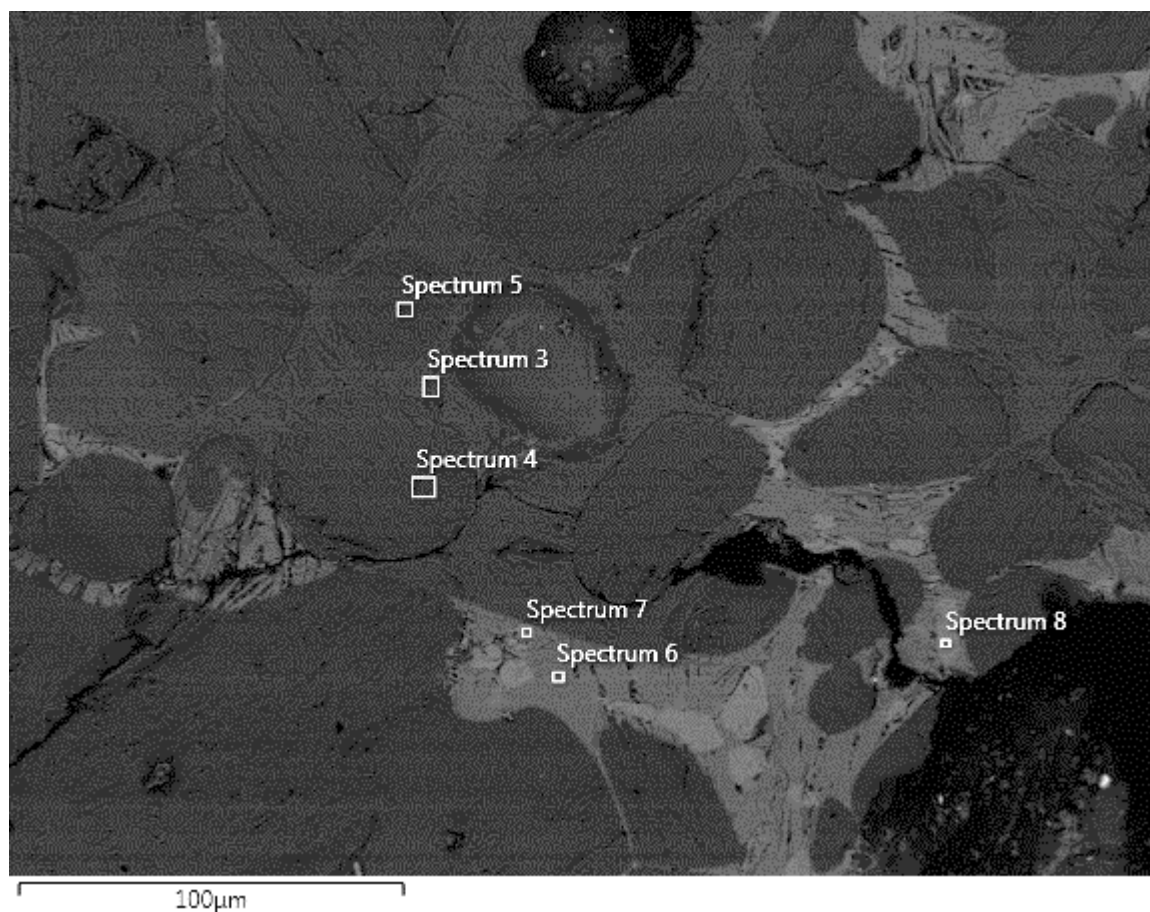


Figure 17: Electron backscatter image of the region analysed at the bottom-centre of the refractory.

Table 20: SEM-EDS analysis of Figure 17.

	Spectrum 3	Spectrum 4	Spectrum 5	Spectrum 6	Spectrum 7	Spectrum 8
Mg (At %)	14.4	51.0	50.5	3.6		
Al (At %)	29.0			21.5	21.3	21.5
O (At %)	56.6	49.0	49.5	60.9	62.3	62.4
Ca (At %)				14.0	13.2	13.1
Mo (At %)					3.2	3.0
Phase	Spinel	MgO	MgO	Glassy	CaAl₂O₄	CaAl₂O₄

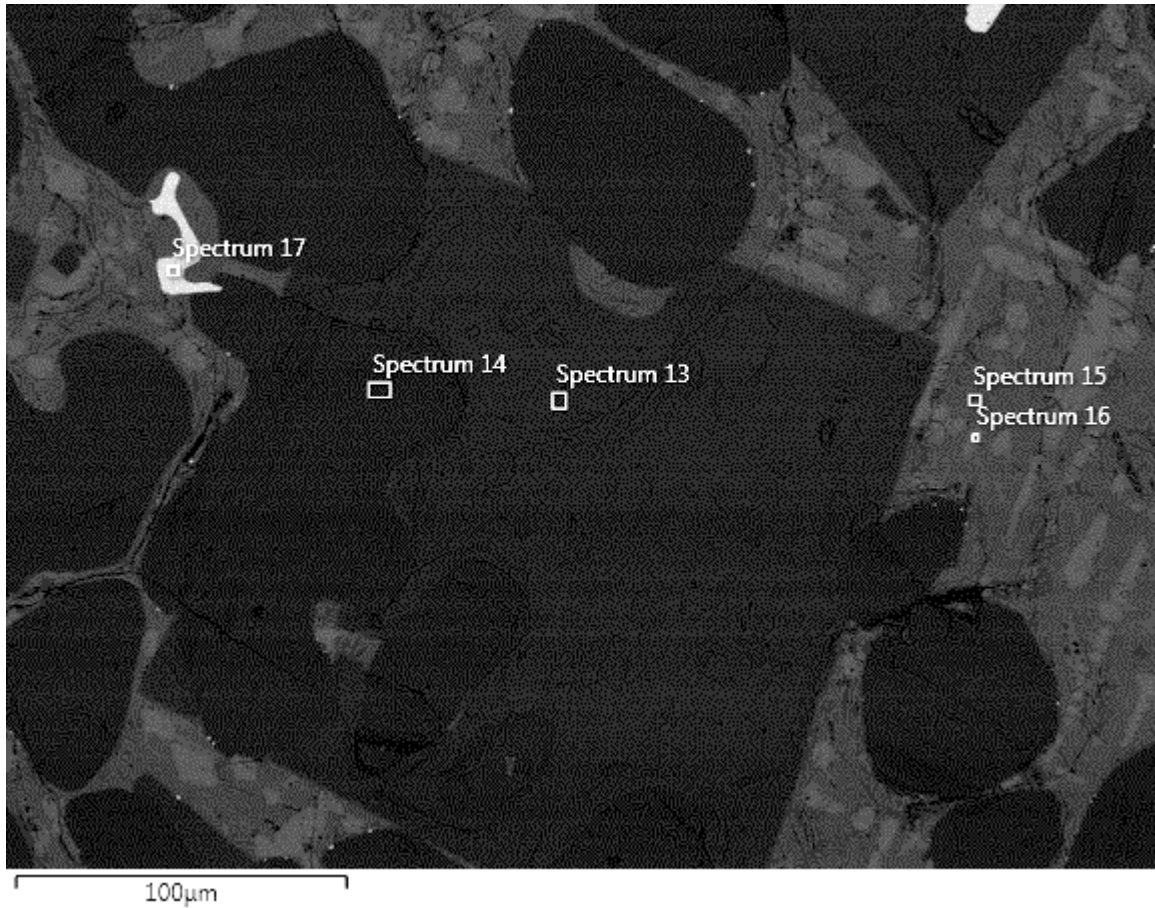


Figure 18: Electron backscatter image of the region analysed at the bottom-edge area of the refractory.

Table 21: SEM-EDS analysis of Figure 18.

	Spectrum 13	Spectrum 14	Spectrum 15	Spectrum 16	Spectrum 17
Mg (At %)	14.4	51.0	3.6		
Al (At %)	29.0		21.5	21.3	
O (At %)	56.6	49.0	60.9	62.3	
Ca (At %)			14.0	13.2	
Mo (At %)				3.2	100.0
Phase	Spinel	MgO	Glassy	CaAl₂O₄	Mo

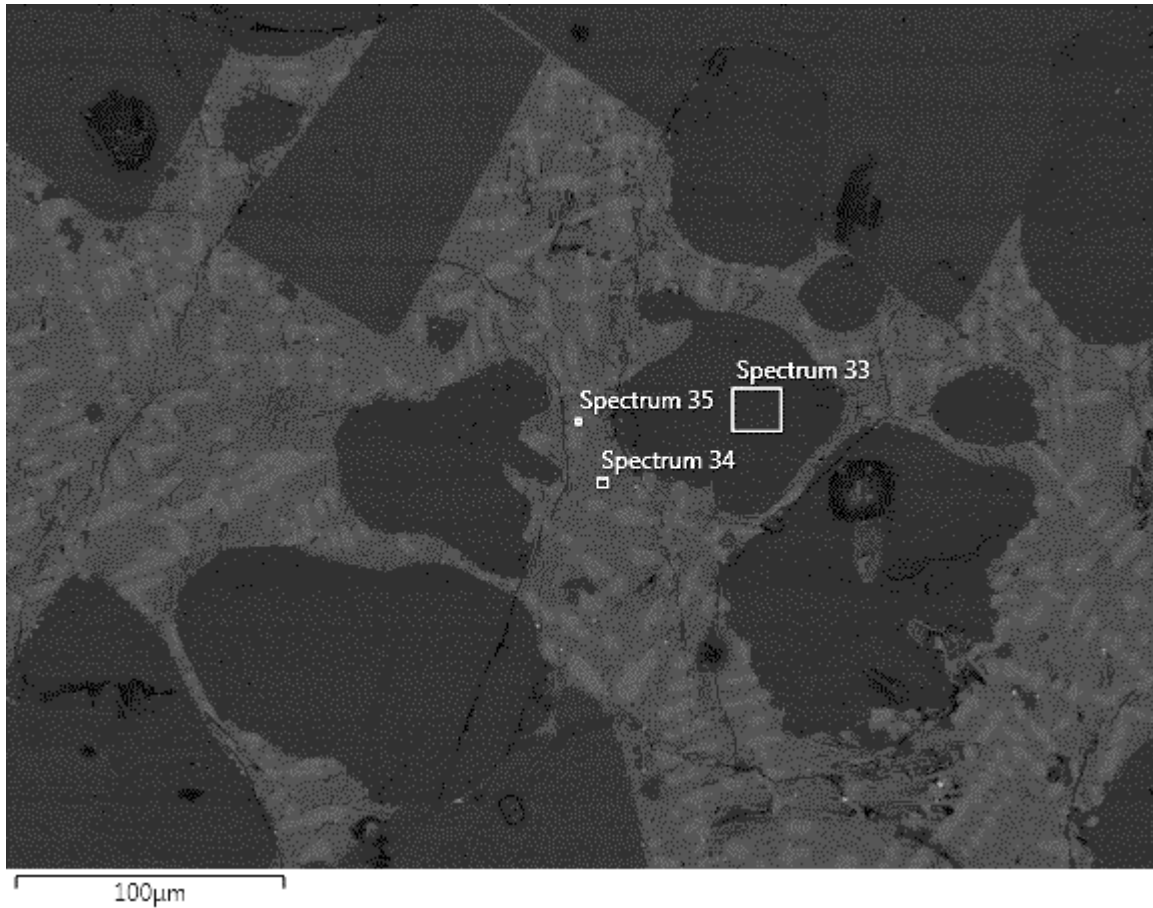


Figure 19: Electron backscatter image of the analysed slag region.

Table 22: SEM-EDS analysis of Figure 19.

	Spectrum 33	Spectrum 34	Spectrum 35
Mg (At %)	49.4	3.6	
Al (At %)	0.7	21.5	21.5
O (At %)	49.9	60.9	62.5
Ca (At %)		14.0	12.5
Mo (At %)			3.5
Phase	MgO	Glassy	CaAl₂O₄

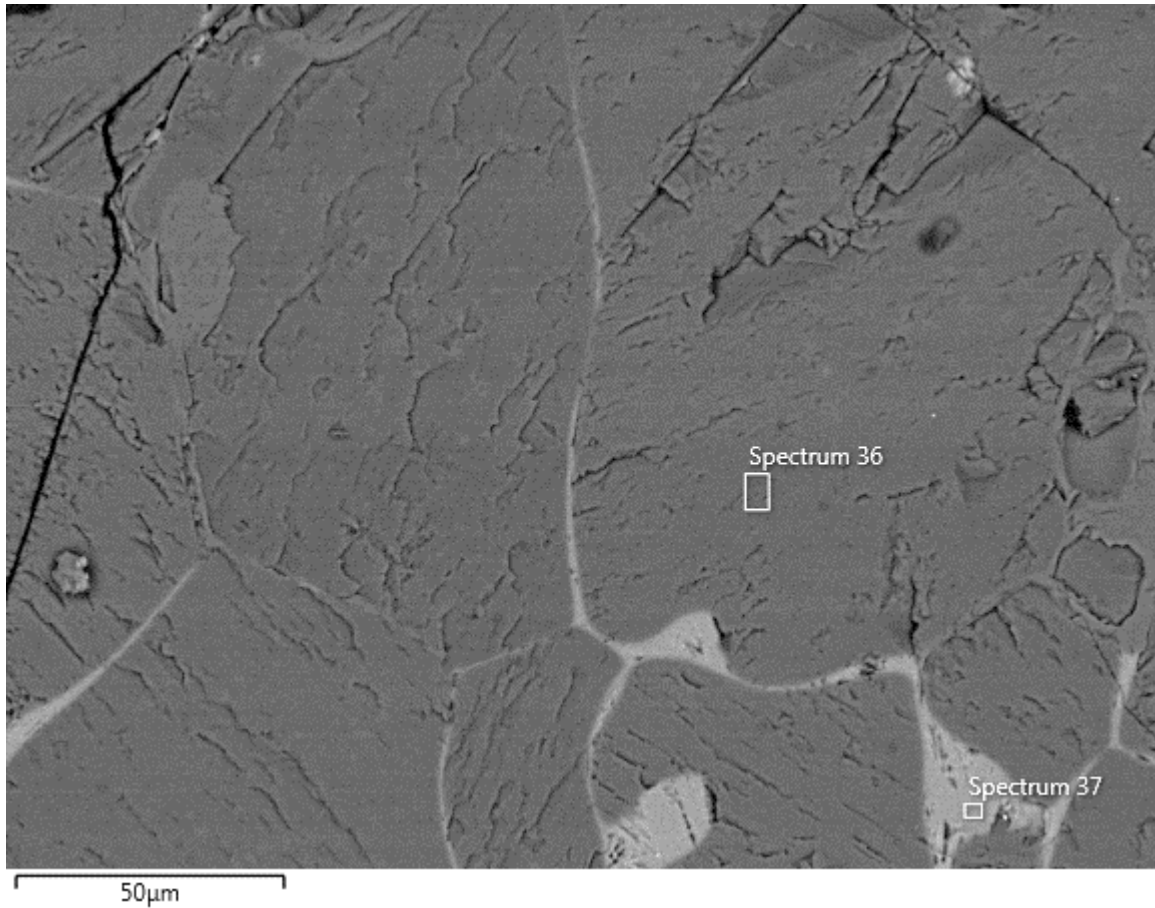


Figure 20: Electron backscatter image of the top-centre of the MgO refractory.

Table 23: SEM-EDS analysis of Figure 20.

	Spectrum 36	Spectrum 37
Mg (At %)	49.5	4.3
Al (At %)	0.6	22.8
O (At %)	49.9	56.6
Ca (At %)		16.3
Mo (At %)		
Phase	MgO	Glassy

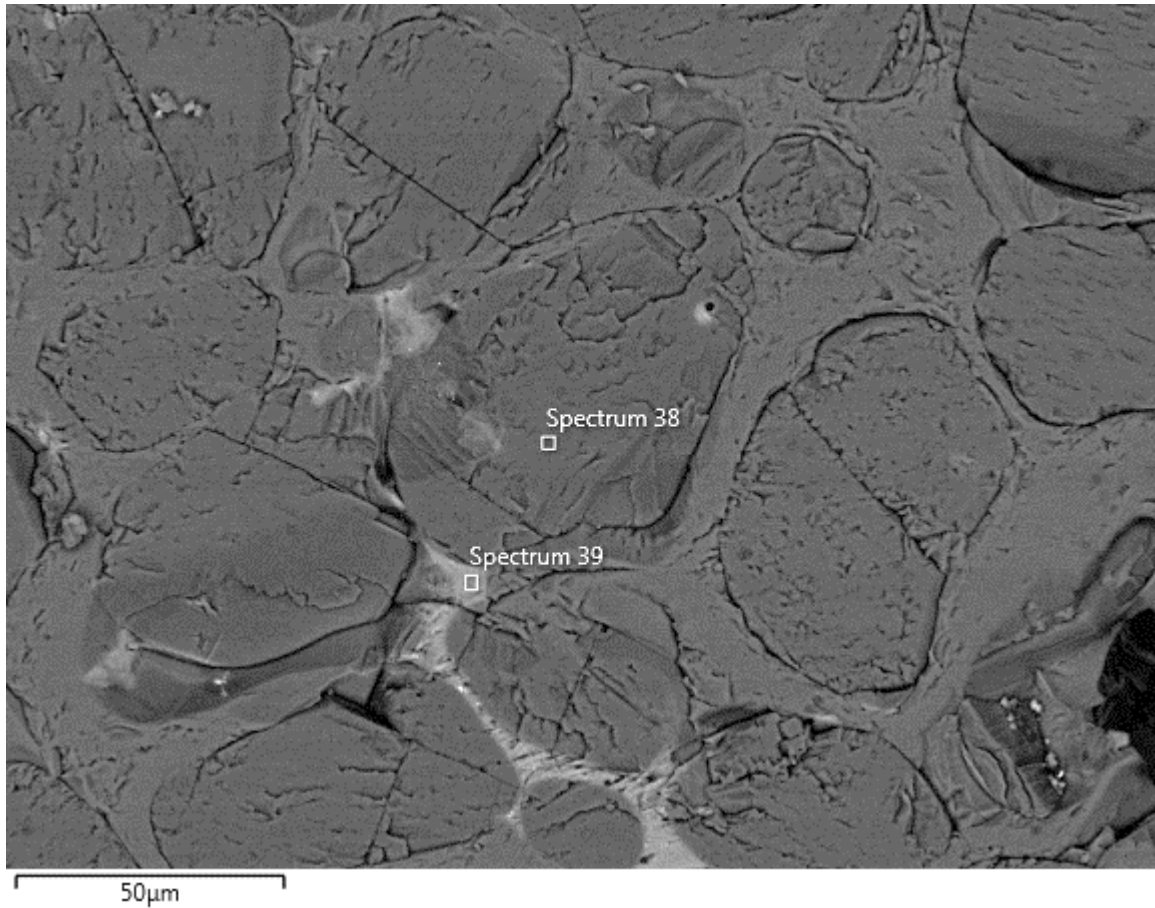


Figure 21: Electron backscatter image of the centre-centre region of the MgO refractory.

Table 24: SEM-EDS analysis of Figure 21.

	Spectrum 38	Spectrum 39
Mg (At %)	51.1	4.6
Al (At %)		21.4
O (At %)	48.9	58.2
Ca (At %)		15.8
Mo (At %)		
Phase	MgO	Glassy

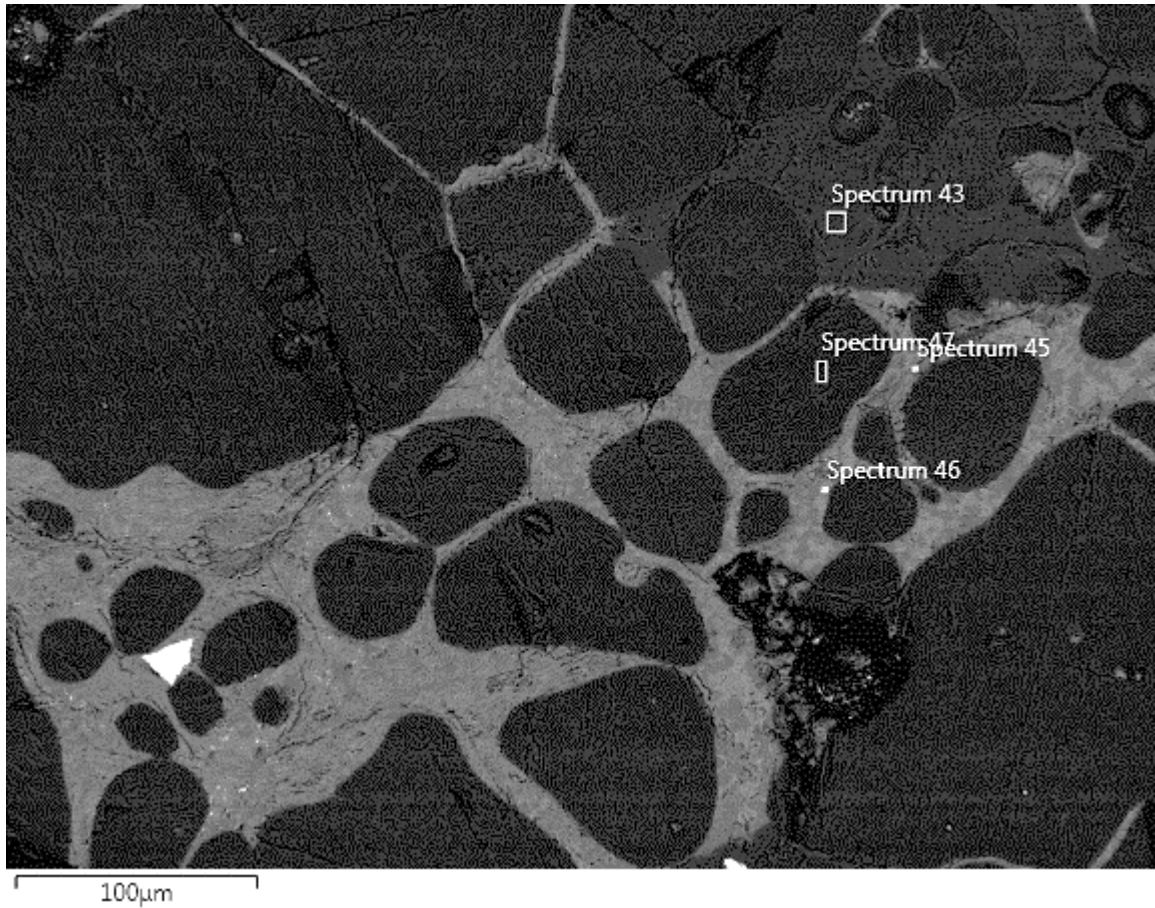


Figure 22: Electron backscatter image of the bottom-centre of the MgO refractory.

Table 25: SEM-EDS analysis of Figure 22.

	Spectrum 43	Spectrum 45	Spectrum 46	Spectrum 47
Mg (At %)	14.4		3.6	51.2
Al (At %)	29.0	27.5	21.5	
O (At %)	56.6	59.2	60.9	48.8
Ca (At %)		13.3	14.0	
Mo (At %)				
Phase	Spinel	CaAl₂O₄	Glassy	MgO

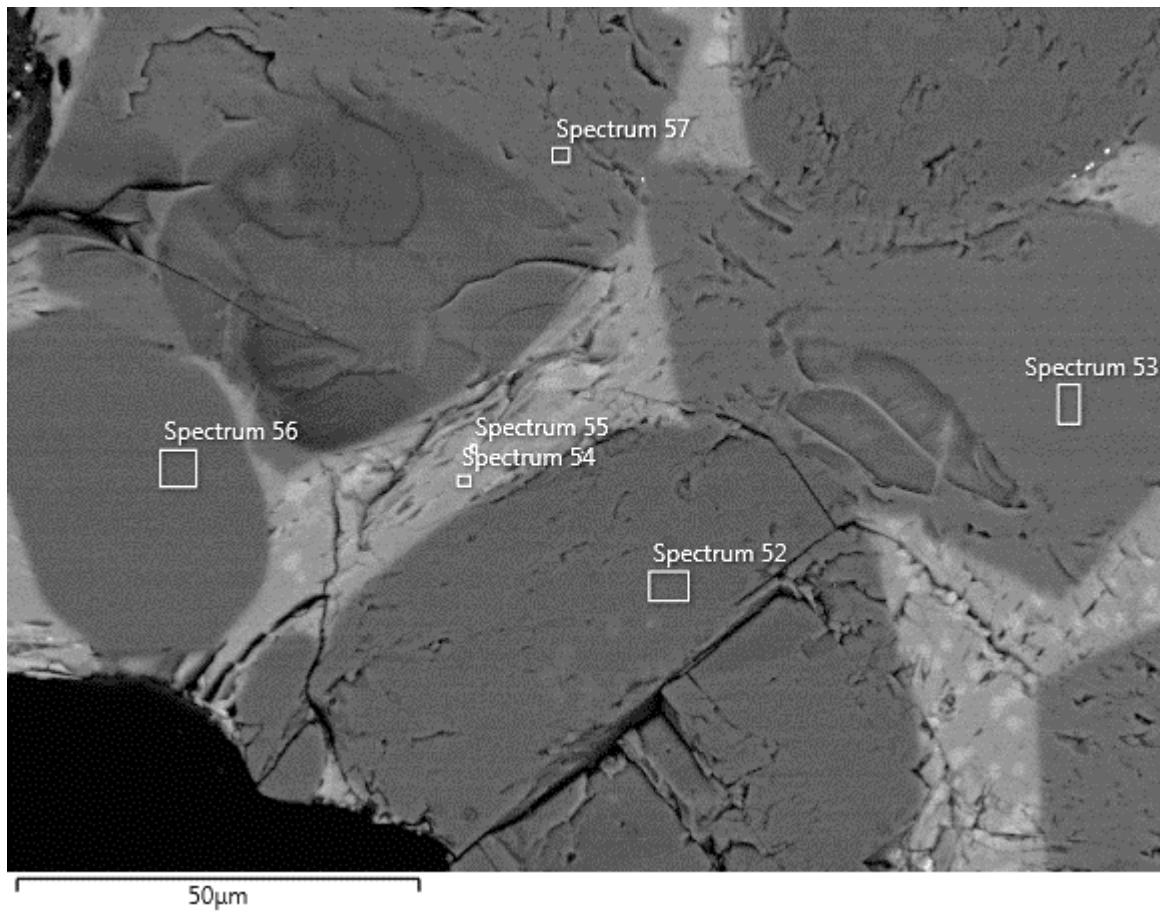


Figure 23: Electron backscatter image of the bottom edge region of the MgO refractory.

Table 26: SEM-EDS analysis of Figure 23.

	Spectrum 52	Spectrum 53	Spectrum 54	Spectrum 55	Spectrum 56	Spectrum 57
Mg (At %)	51.0	14.4	3.6		51.6	14.6
Al (At %)		29.0	21.5	26.5		29.4
O (At %)	49.0	56.6	60.9	59.2	48.4	56.0
Ca (At %)			14.0	12.3		
Mo (At %)				2.0		
Phase	MgO	Spinel	Glassy	CaAl₂O₄	MgO	Spinel

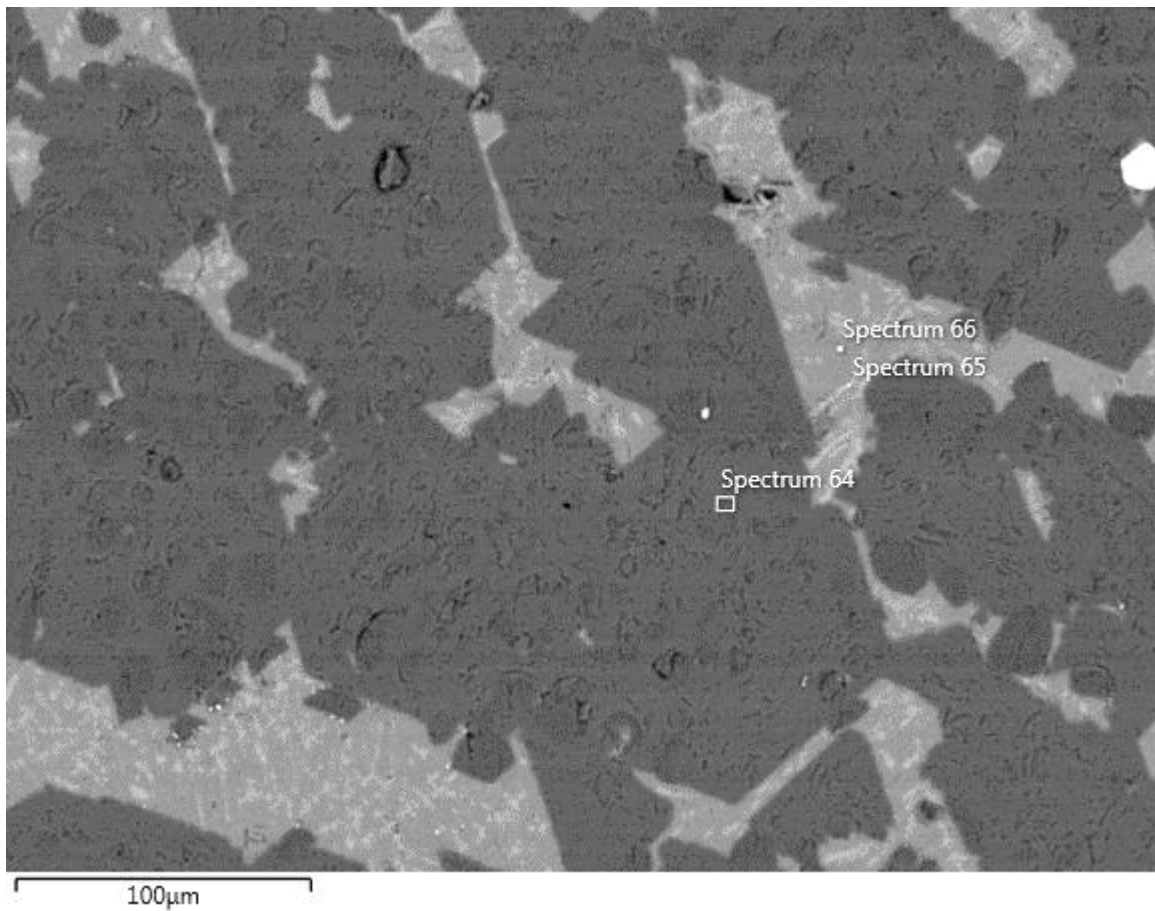


Figure 24: Electron backscatter image of the slag at a magnification of 70x.

Table 27: SEM-EDS analysis of Figure 24.

	Spectrum 64	Spectrum 65	Spectrum 66
Mg (At %)	14.4		3.8
Al (At %)	29.0	26.5	21.4
O (At %)	56.6	59.2	60.8
Ca (At %)		12.3	14.0
Mo (At %)		2.0	
Phase	Spinel	CaAl₂O₄	Glassy

4 Metal-slag interaction

4.1 Vanadium recovery as a function of aluminium content

Table 28: Metal recovery and data used to determine the metal recovery.

Sample	Total Mass (g)	Slag mass (g)	Metal mass (g)	Ideal metal mass (g)	Correction	Metal mass (g)	Metal recovery (%)
C1	5.59	3.7	1.89	2.4	0	1.89	78.75
C2	4.58	2.7	1.88	2.4	0.05	1.9305	80.44
C3	5.11	3.2	1.91	2.4	0.02	1.934	80.58
E	5.86	4.08	1.77	2.4	0	1.77	73.75
F	6.8	5.62	1.27	2.4	0	1.27	52.92
G	6.99	6.37	0.54	2.4	0	0.54	22.5

Table 29: Vanadium recovery and the wt% $\text{Ca}_2\text{Al}_2\text{O}_7$ phase that was present for each test.

Sample	$\text{Ca}_2(\text{Al},\text{V})_2\text{O}_5$	V added	V in metal	V recovery (wt%)
C1	2.7	1.8	1.28	71.4
C2	2.8	1.8	1.33	73.89
C3	1.4	1.8	1.33	74.13
E	3.9	1.8	1.25	69.81
F	9.2	1.8	0.90	50.09
G	26.5	1.8	0.38	21.3

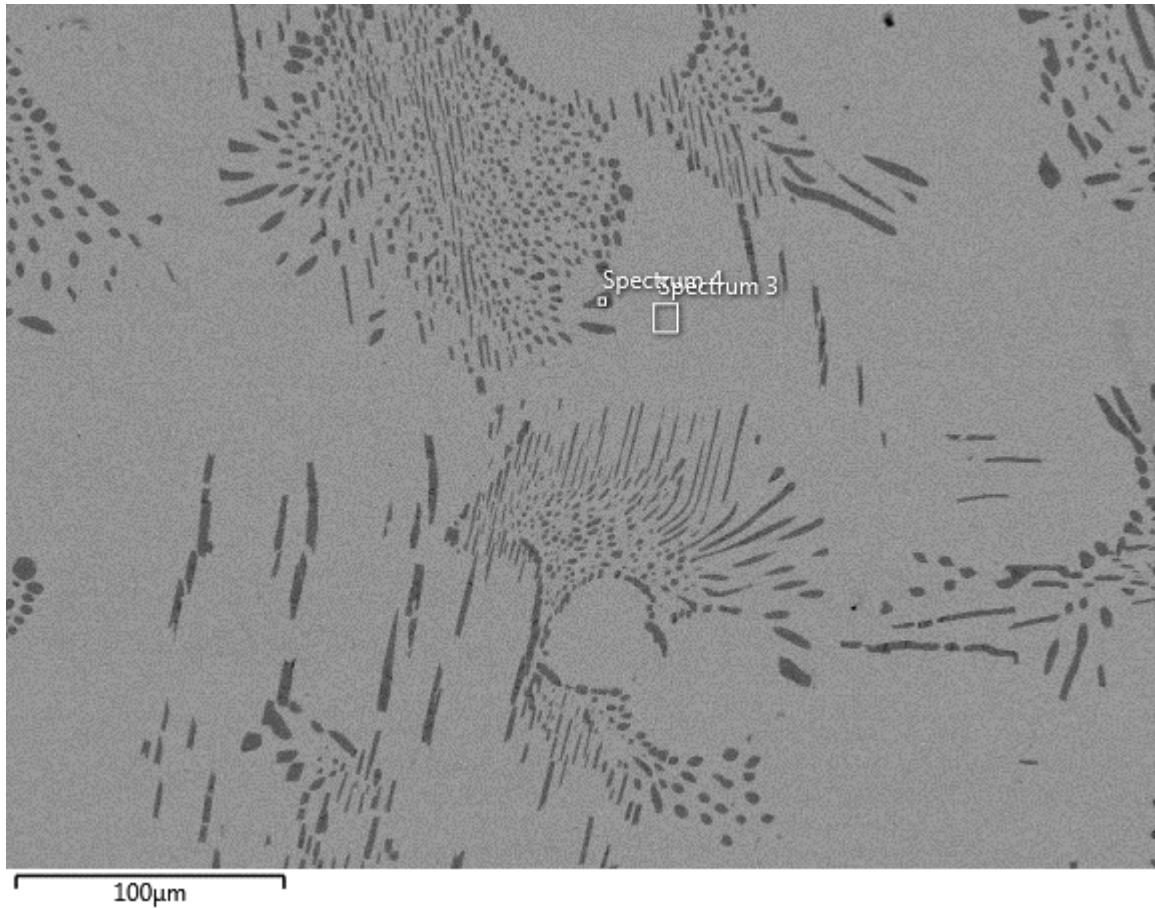


Figure 25: Electron backscatter image of the metal that separated from the slag at a magnification of 300x.

Table 30: SEM-EDS analysis of Figure 25.

	Spectrum 3	Spectrum 4
Fe (At %)	28.7	
V (At %)	71.3	100
Phase	Ferrovandium	Vanadium

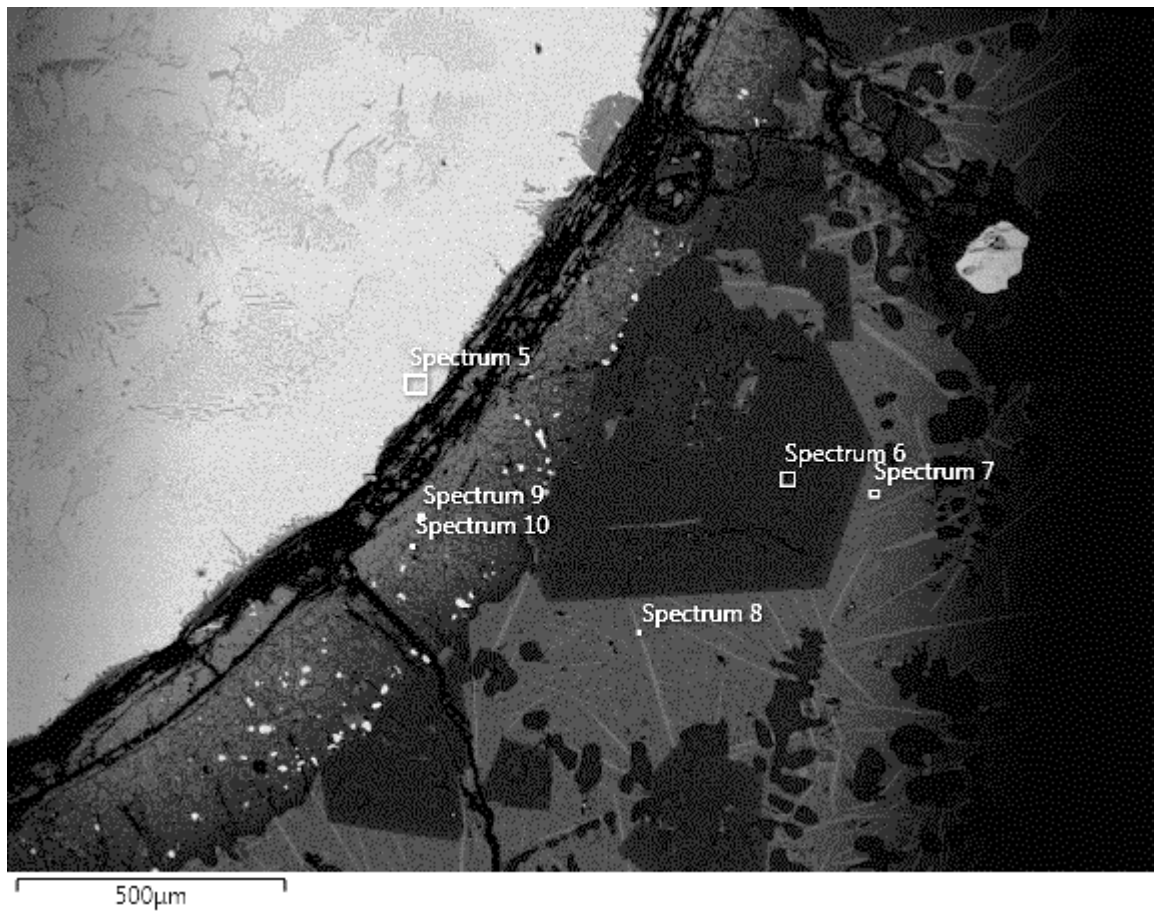


Figure 26: Electron backscatter image of the interface between the slag and the metal of test C1 at a magnification of 60x.

Table 31: SEM-EDS analysis of Figure 26.

	Spectrum 5	Spectrum 6	Spectrum 7	Spectrum 8	Spectrum 9	Spectrum 10
Mg (At %)		16.4	3.0	0.8	17	
Al (At %)		29.7	23.9	18.9	13.8	
O (At %)		49.5	56.6	52.8	45.2	
Ca (At %)			16.5	22.7		
Fe (At %)	28.1					35.5
V (At %)	71.9	4.4		4.7	23.9	64.5
Phase	Ferrovanadium	Spinel	Glassy	Ca₂(Al,V)₂O₅	Spinel	Ferrovanadium

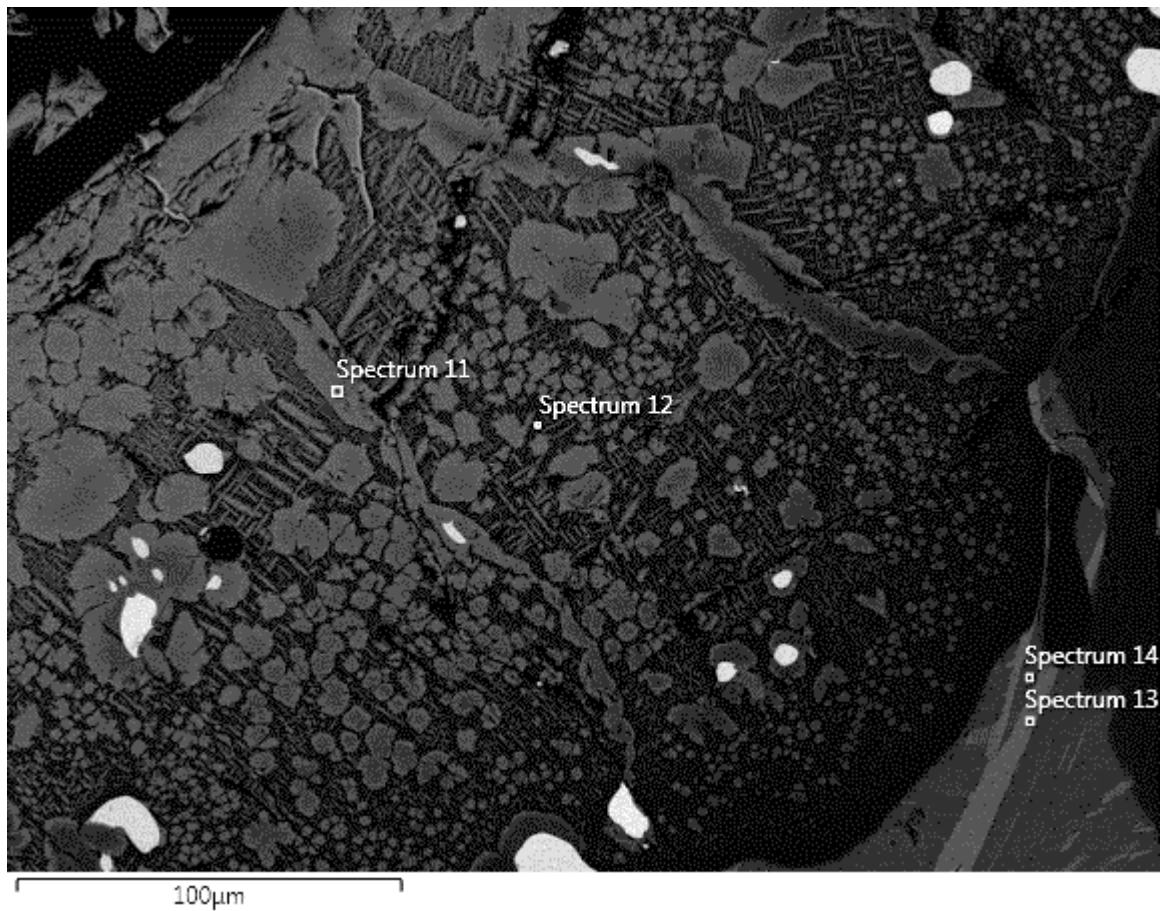


Figure 27: Electron backscatter image of the interface between the slag and the metal at a magnification of 430x.

Table 32: SEM-EDS analysis of Figure 27.

	Spectrum 11	Spectrum 12	Spectrum 13	Spectrum 14
Mg (At %)	17.1	45.8		2.9
Al (At %)	7.7		18.9	24.2
O (At %)	44.7	43.9	51.7	56.6
Ca (At %)			23.1	16.3
Fe (At %)				
V (At %)	30.6	10.3	4.5	
Phase	Spinel	MgO_{ss}	Ca₂(Al,V)₂O₅	Glassy

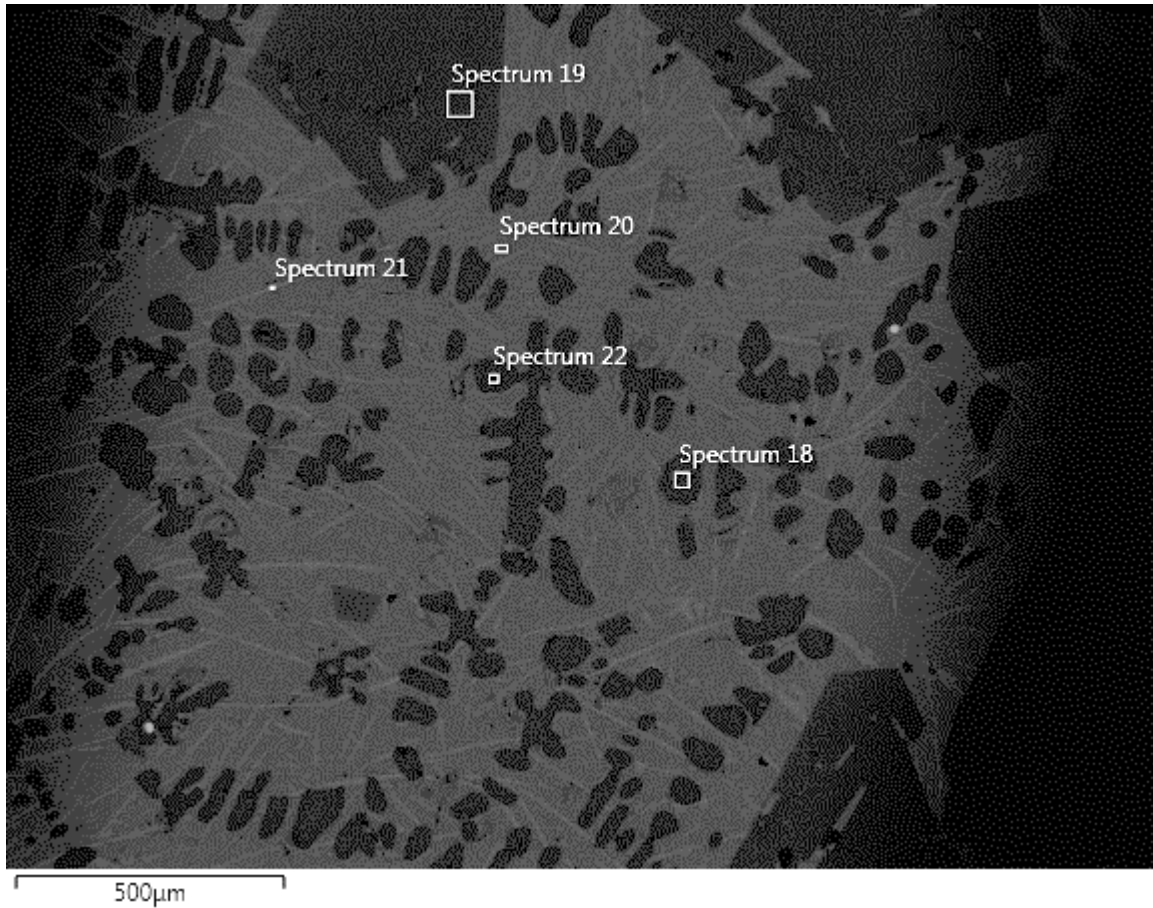


Figure 28: Electron backscatter image of the upper region of the slag metal of test C1 at a magnification of 110x.

Table 33: SEM-EDS analysis of Figure 28.

	Spectrum 18	Spectrum 19	Spectrum 20	Spectrum 21	Spectrum 22
Mg (At %)	44.0	16.5	3.0	1.1	47.2
Al (At %)		29.6	23.9	19.1	
O (At %)	46.5	49.2	56.6	52.8	45.5
Ca (At %)			16.5	22.4	
Fe (At %)					
V (At %)	9.5	4.7		4.6	7.3
Phase	MgO _{ss}	Spinel	Glassy	Ca ₂ (Al,V) ₂ O ₅	MgO _{ss}

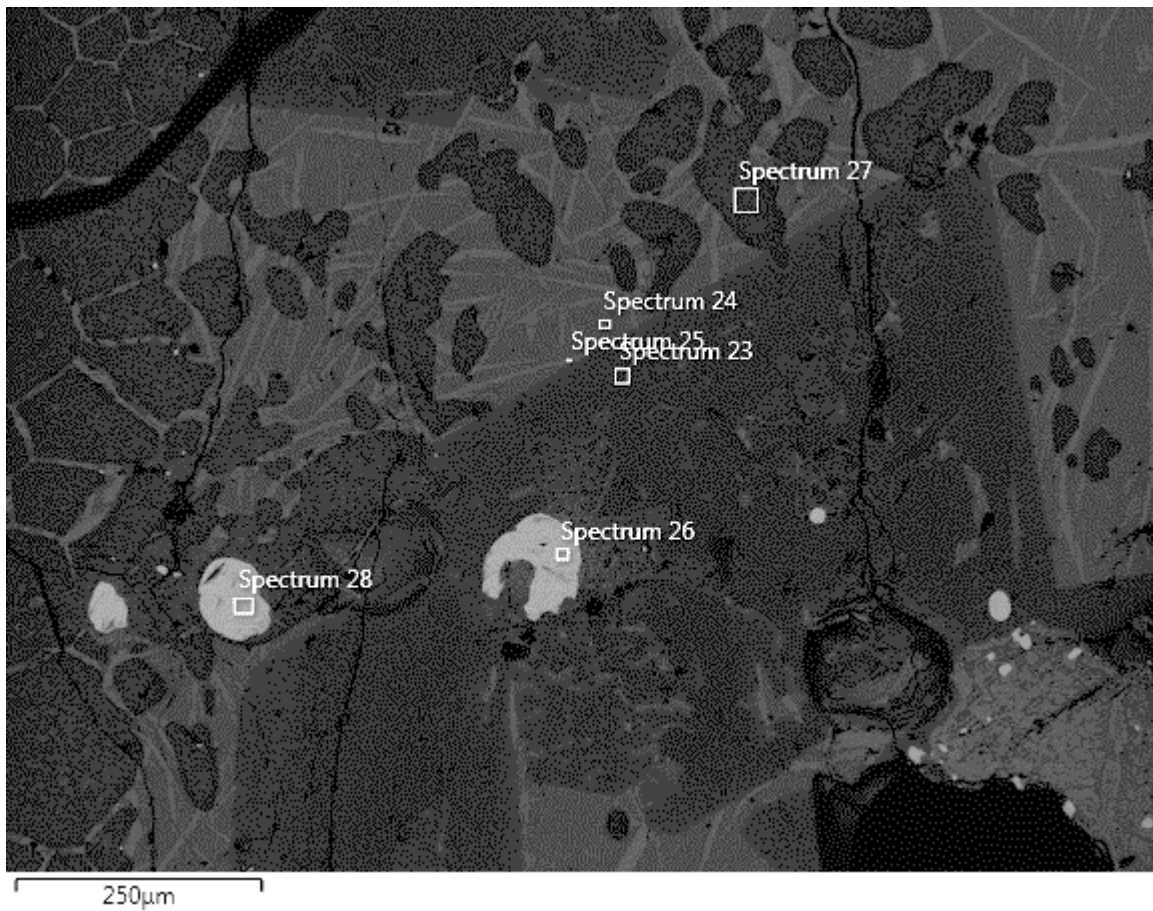


Figure 29: Electron backscatter image of the bottom region of the slag metal of test C1 at a magnification of 110x.

Table 34: SEM-EDS analysis of Figure 29.

	Spectrum 23	Spectrum 24	Spectrum 25	Spectrum 26	Spectrum 27	Spectrum 28
Mg (At %)	16.8	3.0	0.8		47.2	
Al (At %)	27.7	23.9	18.9			
O (At %)	47.6	56.6	52.8		45.5	
Ca (At %)		16.5	22.7			
Fe (At %)				44.5		45.3
V (At %)	7.9		4.7	55.5	7.3	54.7
Phase	Spinel	Glassy	Ca₂(Al,V)₂O₅	Ferrovanadium	MgO_{SS}	Ferrovanadium

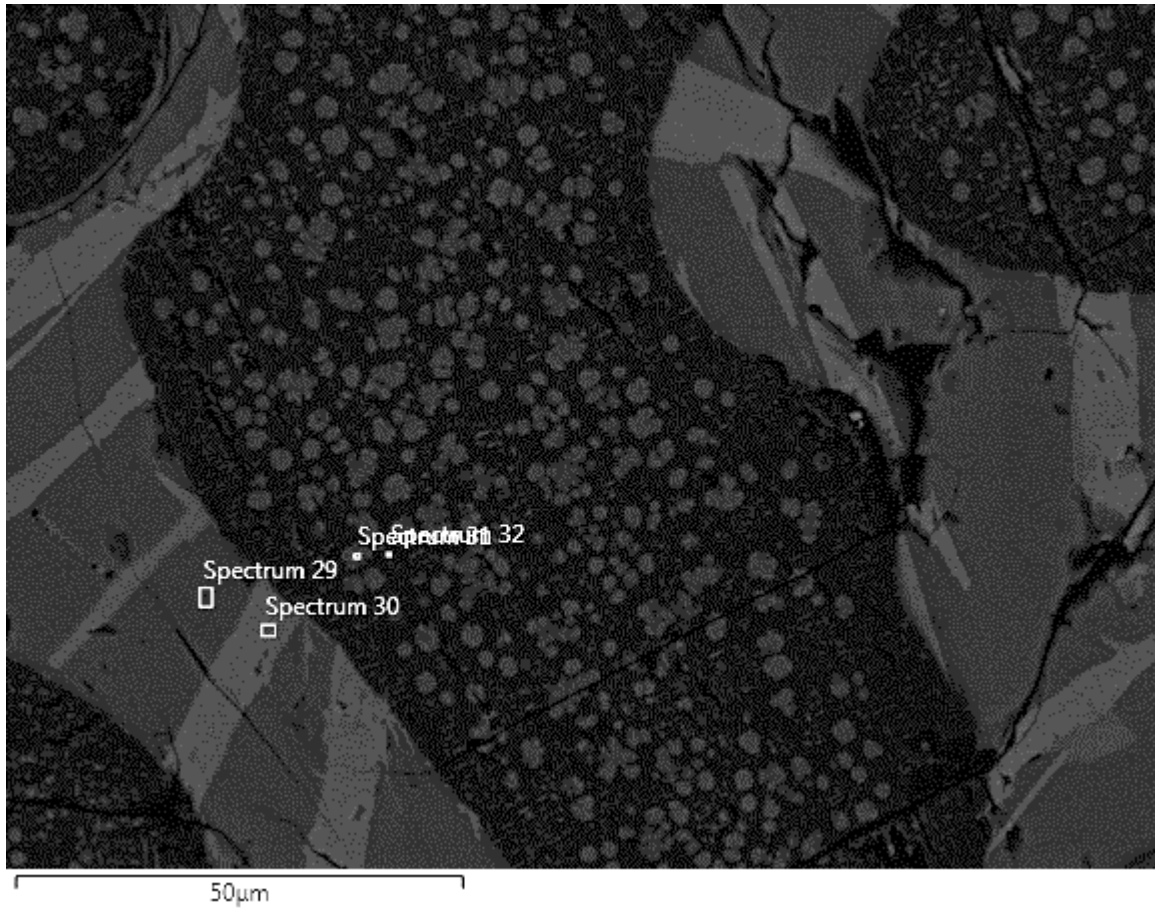


Figure 30: Electron backscatter image metal of test C1 at a higher magnification of the bottom region of the solid solution phase containing a vanadium rich spinel phase.

Table 35: SEM-EDS analysis of Figure 30.

	Spectrum 29	Spectrum 30	Spectrum 31	Spectrum 32
Mg (At %)	3.0	0.8	22.2	48.9
Al (At %)	23.9	19.1	17.5	
O (At %)	56.6	52.8	43.9	45.7
Ca (At %)	16.5	22.4		
Fe (At %)				
V (At %)		4.9	16.4	5.5
Phase	Glassy	$\text{Ca}_2(\text{Al},\text{V})_2\text{O}_5$	Spinel	MgO_{ss}

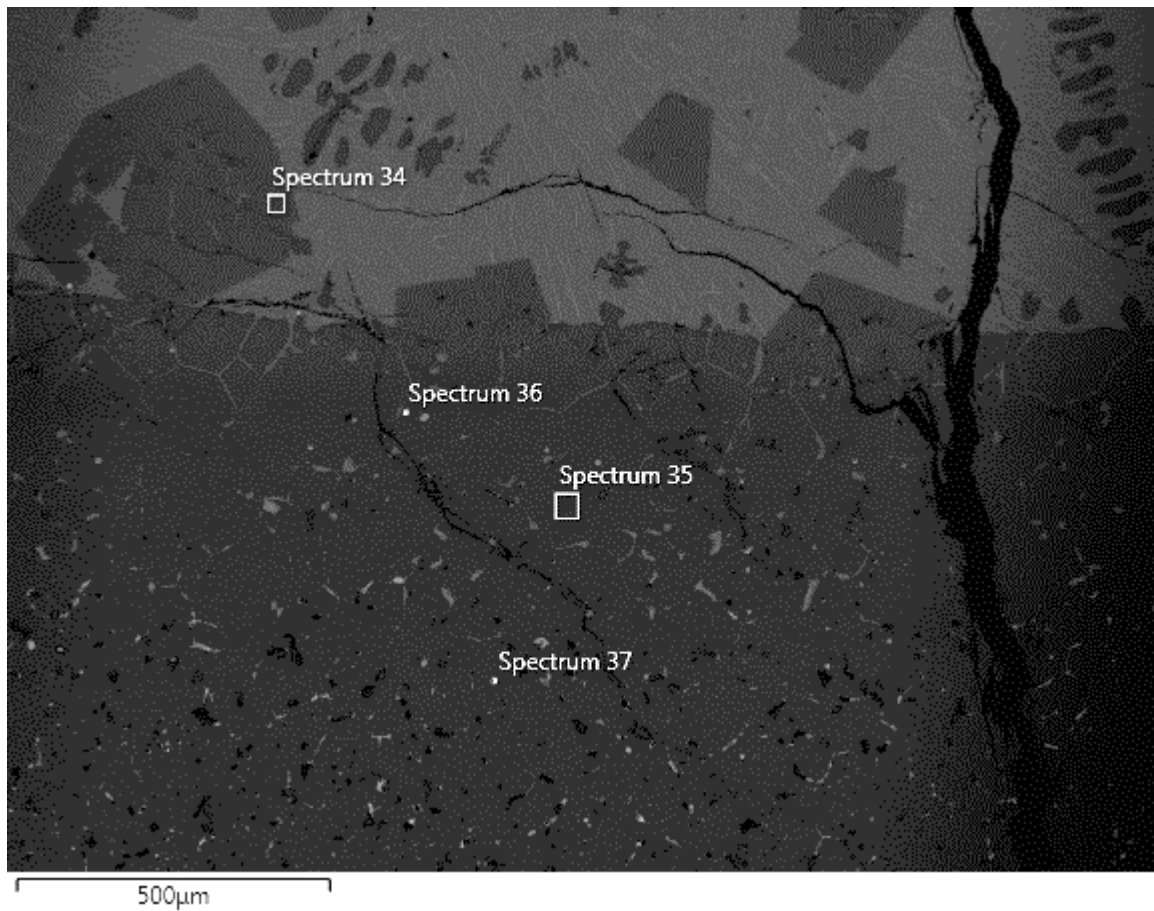


Figure 31: Electron backscatter image of the slag-refractory (MgO crucible) interface metal of test C1.

Table 36: SEM-EDS analysis of Figure 31.

	Spectrum 34	Spectrum 35	Spectrum 36	Spectrum 37
Mg (At %)	16.5	52.2	10.0	5.0
Al (At %)	30.1		17.9	12.6
O (At %)	49.2	47.8	60.3	60.1
Ca (At %)			10.8	11.3
Fe (At %)				
V (At %)	4.2			
Phase	Spinel	MgO	Glassy	Glassy

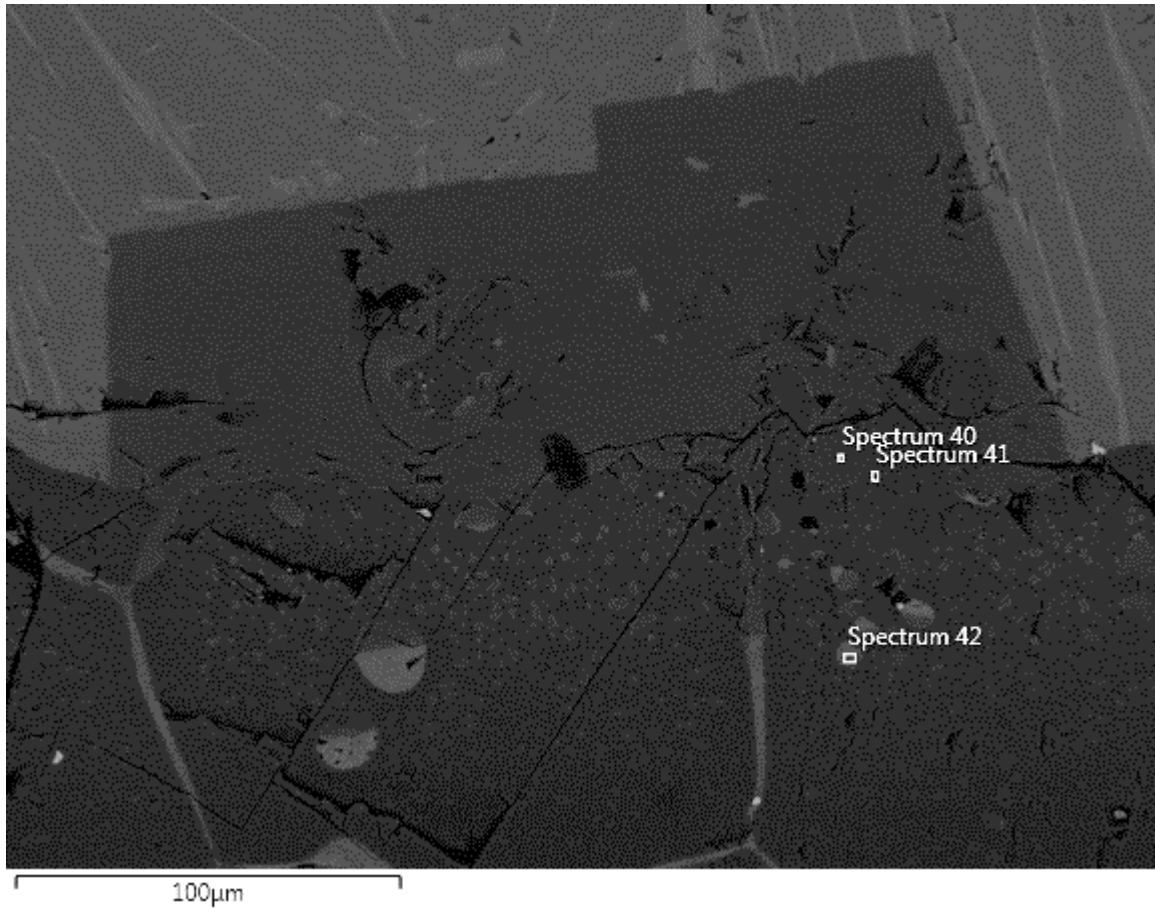


Figure 32: Electron backscatter image of the slag-crucible interface metal of test C1 at a magnification of 430x.

Table 37: SEM-EDS analysis of Figure 32.

	Spectrum 40	Spectrum 41	Spectrum 42
Mg (At %)	16.5	50.6	17.5
Al (At %)	30.1		26.1
O (At %)	49.2	45.0	49.2
Ca (At %)			
Fe (At %)			
V (At %)	4.2	3.7	8.2
Phase	Spinel	MgO	Spinel

4.2 Sample C1

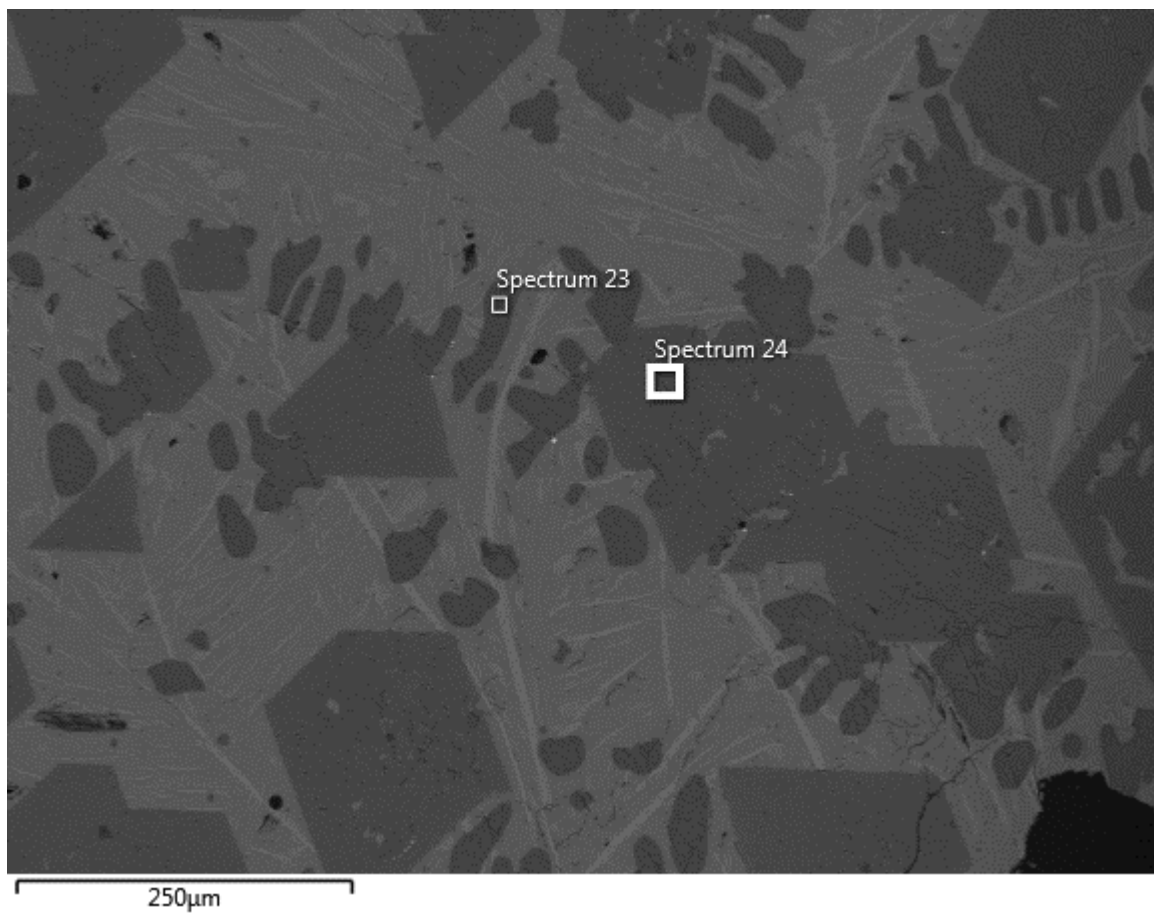


Figure 33: Electron backscatter image of the slag formed metal in test C1 where 1.5wt% excess aluminium was added.

Table 38: SEM-EDS analysis of Figure 33.

	Spectrum 23	Spectrum 24
Mg (At %)	57.7	17.5
Al (At %)		26.1
O (At %)	34.3	49.2
Ca (At %)		
Fe (At %)		
V (At %)	8.0	8.2
Phase	MgO _{ss}	Spinel

4.3 Sample C3

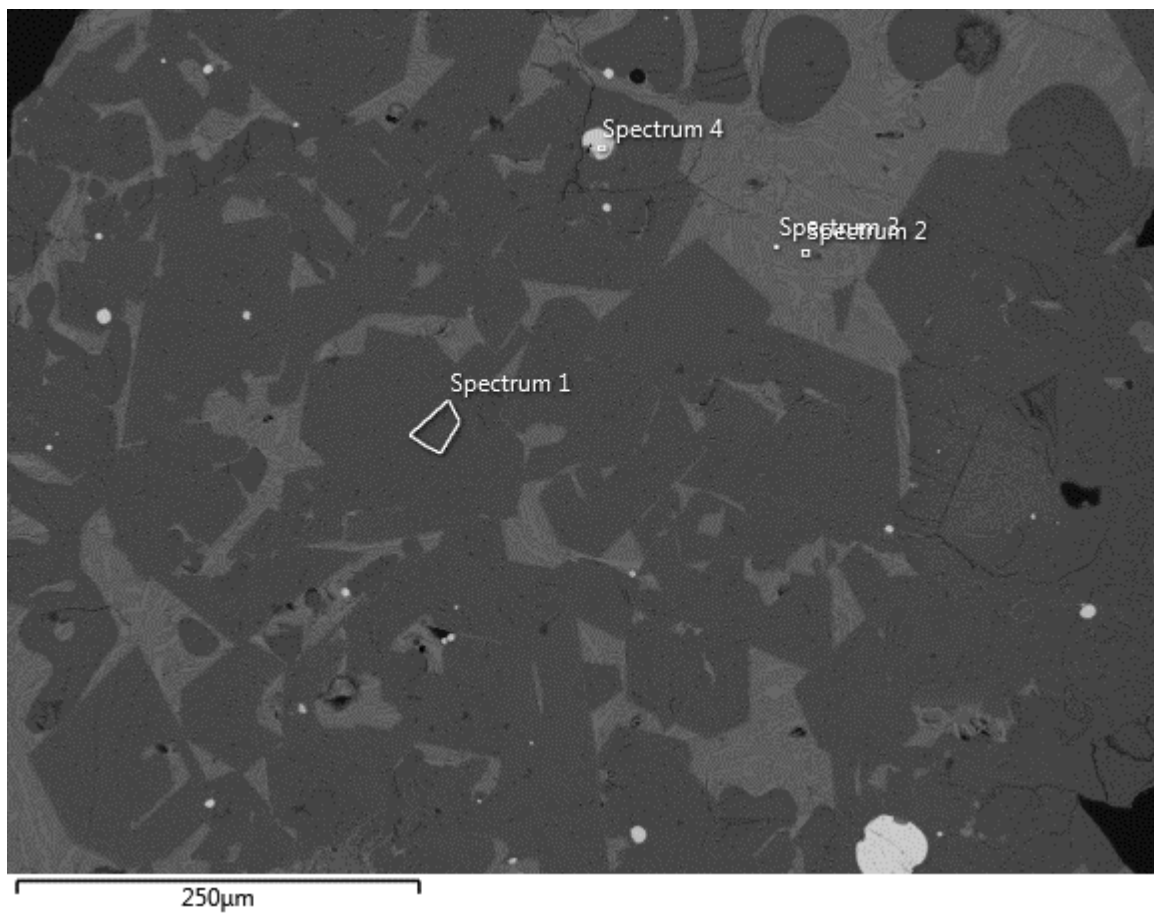


Figure 34: Electron backscatter image of the slag formed in test C3 where 5.5 wt% excess aluminium was added.

Table 39: SEM-EDS analysis of Figure 34.

	Spectrum 1	Spectrum 2	Spectrum 3	Spectrum 4
Mg (At %)	17.5	3.0	0.8	
Al (At %)	26.1	23.9	19.1	
O (At %)	49.2	56.6	52.8	
Ca (At %)		16.5	22.4	
Fe (At %)				69.4
V (At %)	8.2		4.9	30.6
Phase	Spinel	Glassy	$\text{Ca}_2(\text{Al},\text{V})_2\text{O}_5$	Ferrovanadium

5 Vanadium recovery as a function of amount of spinel phases formed

5.1 Sample E

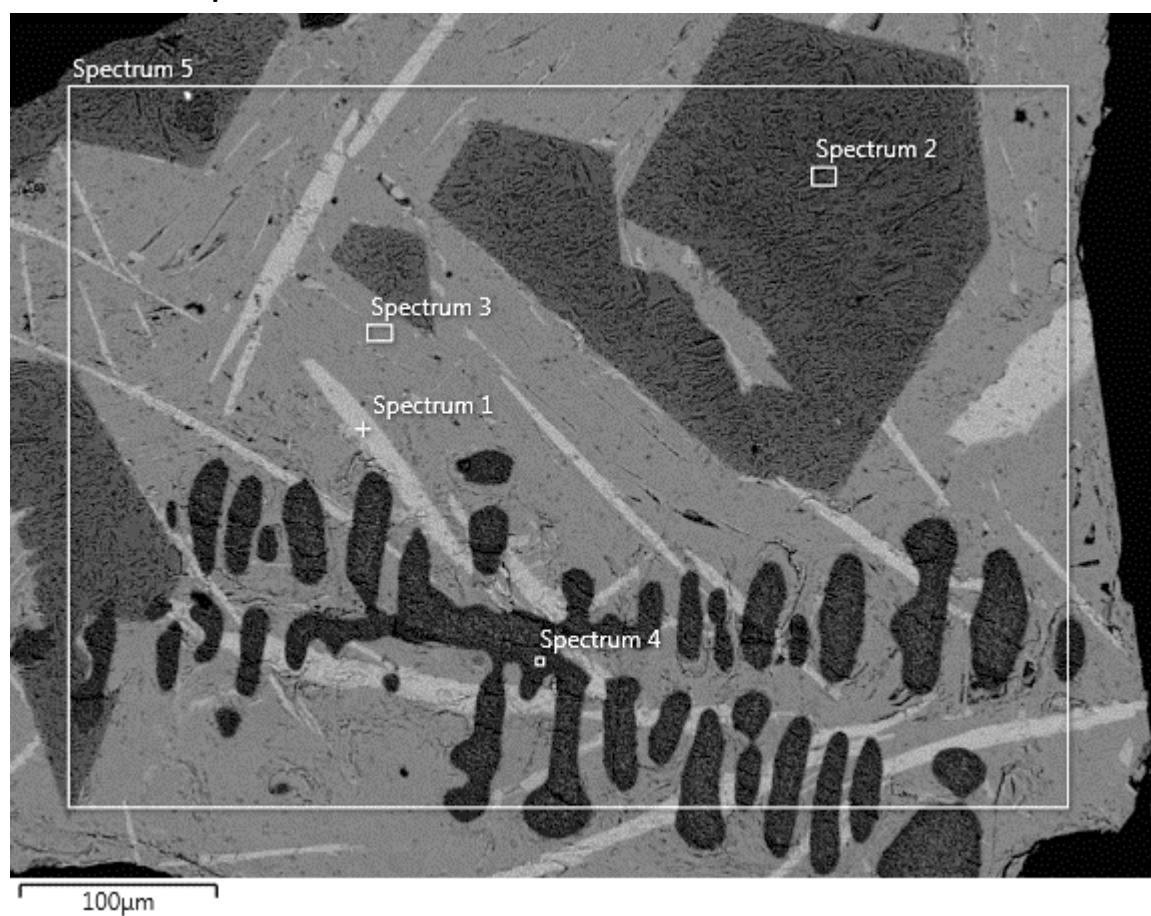


Figure 35: Electron backscatter image of the slag formed in test E.

Table 40: SEM-EDS analysis of Figure 35.

	Spectrum 1	Spectrum 2	Spectrum 3	Spectrum 4	Spectrum 5
Mg (At %)	0.8	17.5	3.0	47.2	12.9
Al (At %)	19.1	26.1	23.9		21.0
O (At %)	52.8	49.2	56.6	46.8	53.3
Ca (At %)	22.4		16.5		10.2
Fe (At %)					
V (At %)	4.9	8.2		6.0	2.6
Phase	$\text{Ca}_2(\text{Al},\text{V})_2\text{O}_5$	Spinel	Glassy	MgO_{ss}	

5.2 Sample F

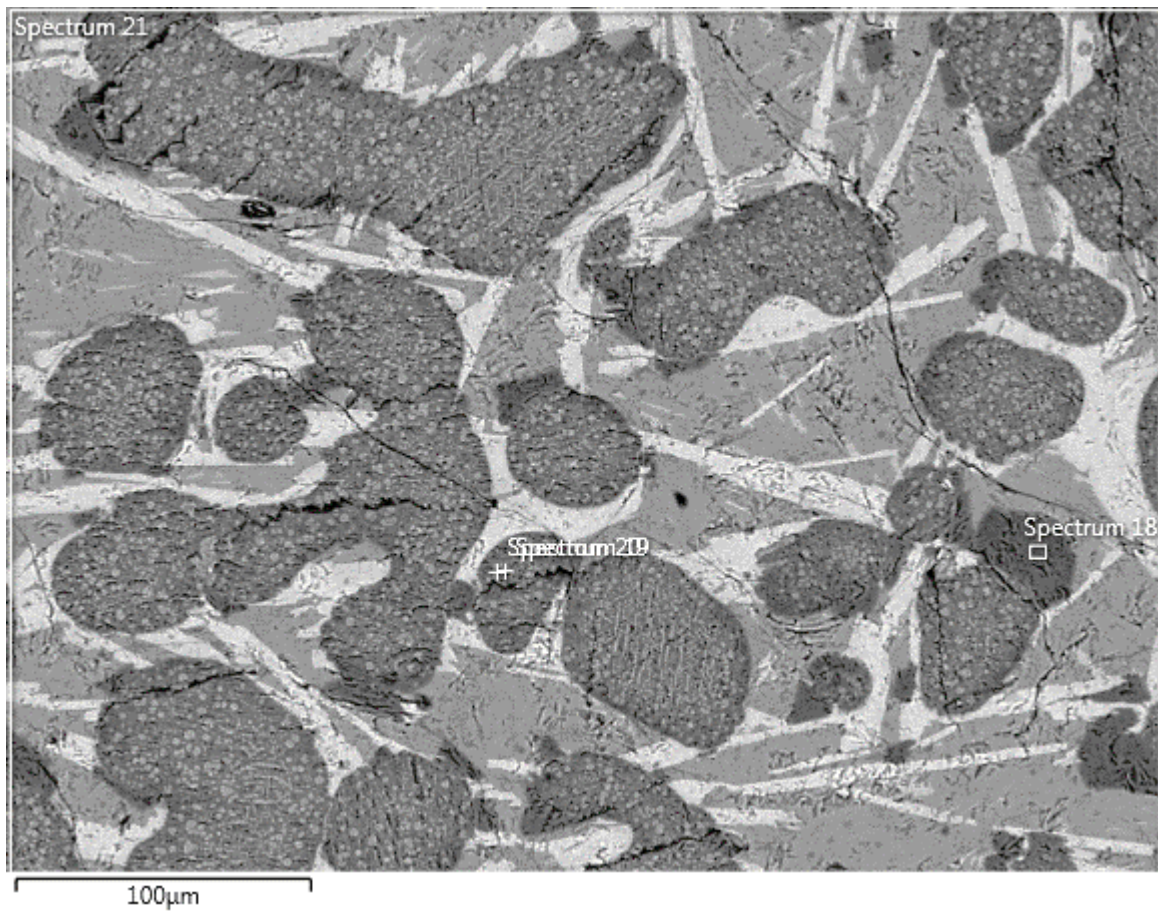


Figure 36: Electron backscatter image of the slag formed in test F.

Table 41: SEM-EDS analysis of Figure 36.

	Spectrum 18	Spectrum 19	Spectrum 20
Mg (At %)	17.5	17.5	45.2
Al (At %)	26.1	17.1	
O (At %)	49.2	49.2	46.8
Ca (At %)			
Fe (At %)			
V (At %)	8.2	17.2	8.0
Phase	Spinel	Spinel	MgO _{ss}

5.3 Sample G

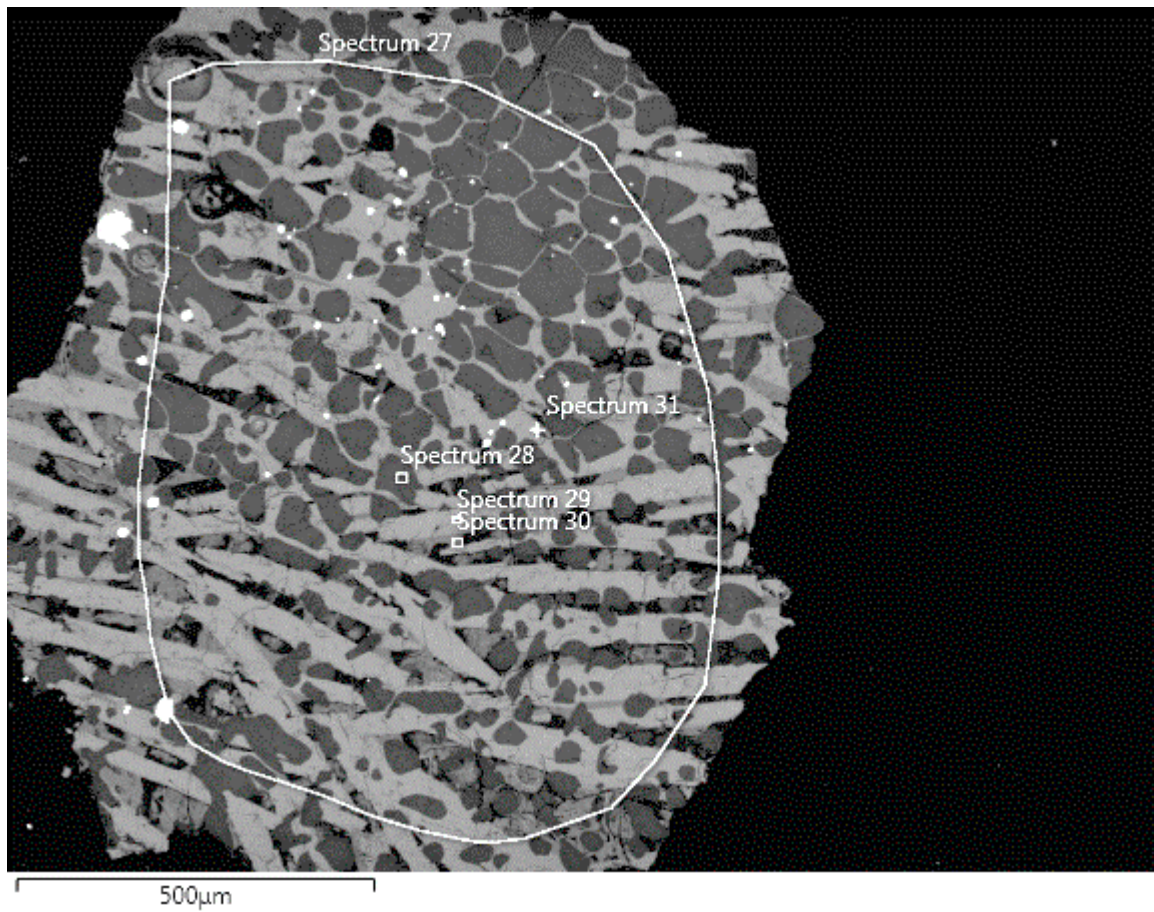


Figure 37: Electron backscatter image of the slag formed in test G.

Table 42: SEM-EDS analysis of Figure 37.

	Spectrum 28	Spectrum 29	Spectrum 30	Spectrum 31
Mg (At %)	47.2	0.8	3.3	
Al (At %)		13.7	20.4	
O (At %)	46.8	51.0	59.1	
Ca (At %)		24.0	16.8	
Fe (At %)				79.0
V (At %)	6.0	10.5	0.4	20.1
Phase	MgO _{ss}	Ca ₂ (Al,V) ₂ O ₅	Glassy	Ferrovanadium

6 Second stage tests

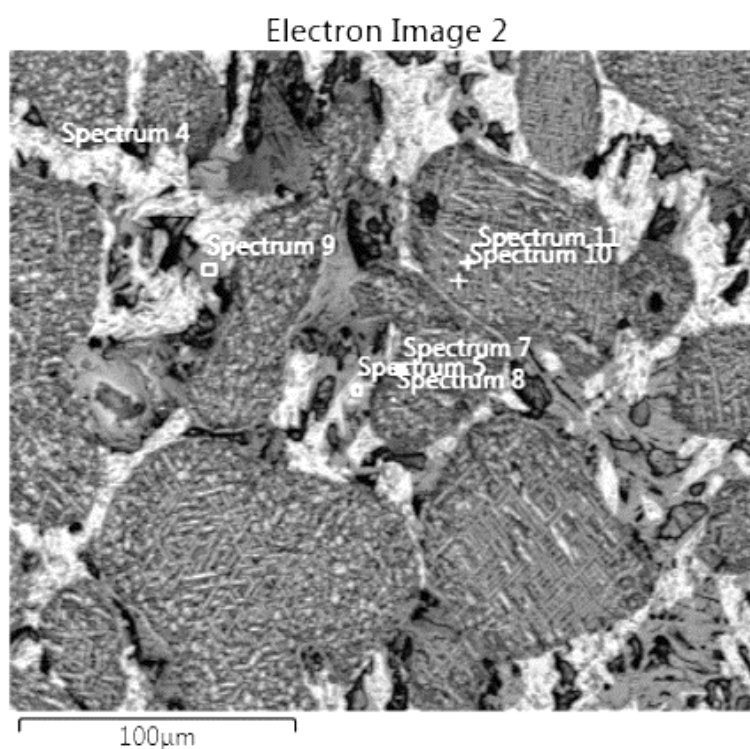


Figure 38: Electron backscatter image of the slag formed in test H1.

Table 43: SEM-EDS analysis of Figure 38.

	Spectrum 4	Spectrum 5	Spectrum 7	Spectrum 8	Spectrum 9	Spectrum 10	Spectrum 11
Mg (At %)	0.8	0.9	30.2	30.2	2.2	17.5	17.2
Al (At %)	13.3	13.5	2.0	1.5	18.9	17.1	15.0
O (At %)	39.6	39.4	46.8	46.8	39.9	49.2	49.5
Ca (At %)	31.4	31.9			30.6		
Fe (At %)							
V (At %)	14.9	14.5	21.0	21.5	8.4	17.2	19.3
Phase	$\text{Ca}_2(\text{Al},\text{V})_2\text{O}_5$	$\text{Ca}_2(\text{Al},\text{V})_2\text{O}_5$	MgO_{ss}	MgO_{ss}	Glassy	Spinel	Spinel

7 Equilibrium tests

7.1 Sample D

Electron Image 3

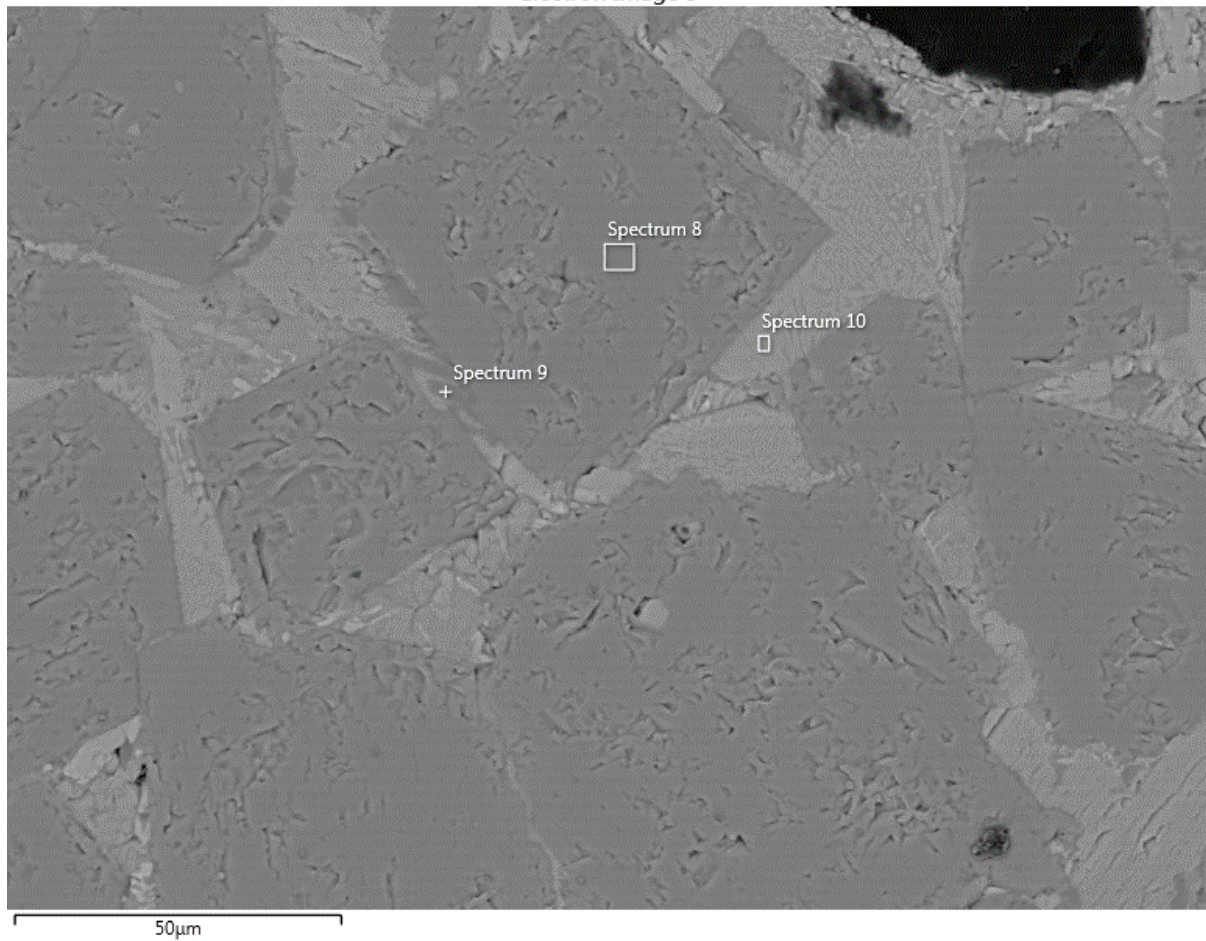


Figure 39: Electron backscatter image of equilibrium test D.

Table 44: SEM-EDS analysis of Figure 39

	Spectrum 8	Spectrum 9	Spectrum 10
Mg (At %)	17.5	3.3	2.0
Al (At %)	26.1	30.4	
O (At %)	49.2	59.1	55.1
Ca (At %)		6.8	22.1
Fe (At %)			0.6
V (At %)	8.2	0.4	20.3
Phase	Spinel	Glassy	Ca₂V₂O₅

7.2 Sample E

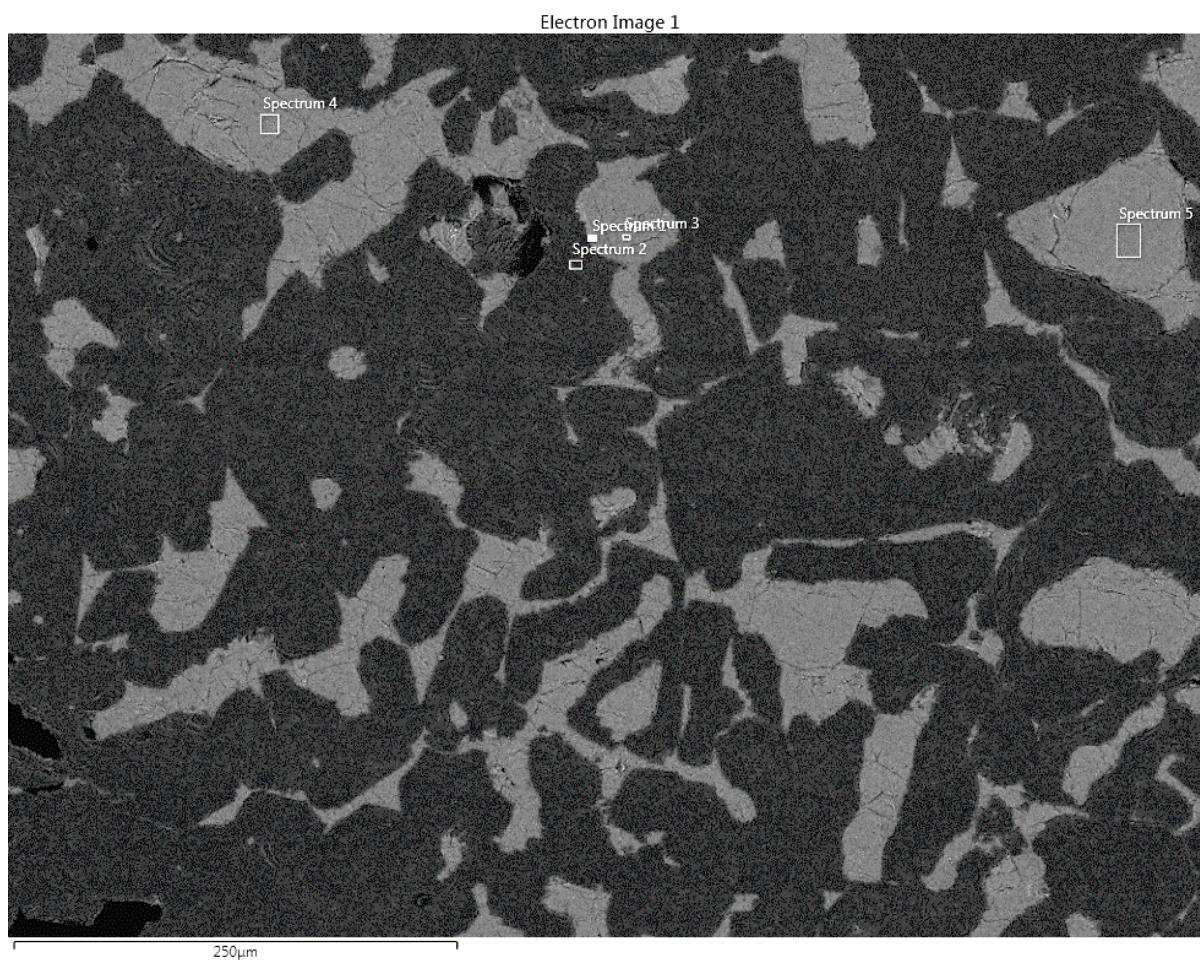


Figure 40: Electron backscatter image of equilibrium test E.

Table 45: SEM-EDS analysis of Figure 40.

	Spectrum 1	Spectrum 2	Spectrum 3	Spectrum 4	Spectrum 5
Mg (At %)	1.4	13.8	1.9	1.4	2.0
Al (At %)		28.3			
O (At %)	56.6	54.5	56.4	56.6	55.4
Ca (At %)	21.7		20.8	21.7	22.0
Fe (At %)		2.4			0.6
V (At %)	20.4	1.0	20.9	20.4	20.0
Phase	Ca ₂ V ₂ O ₅	Spinel	Ca ₂ V ₂ O ₅	Ca ₂ V ₂ O ₅	Ca ₂ V ₂ O ₅

7.3 Sample F

Electron Image 8

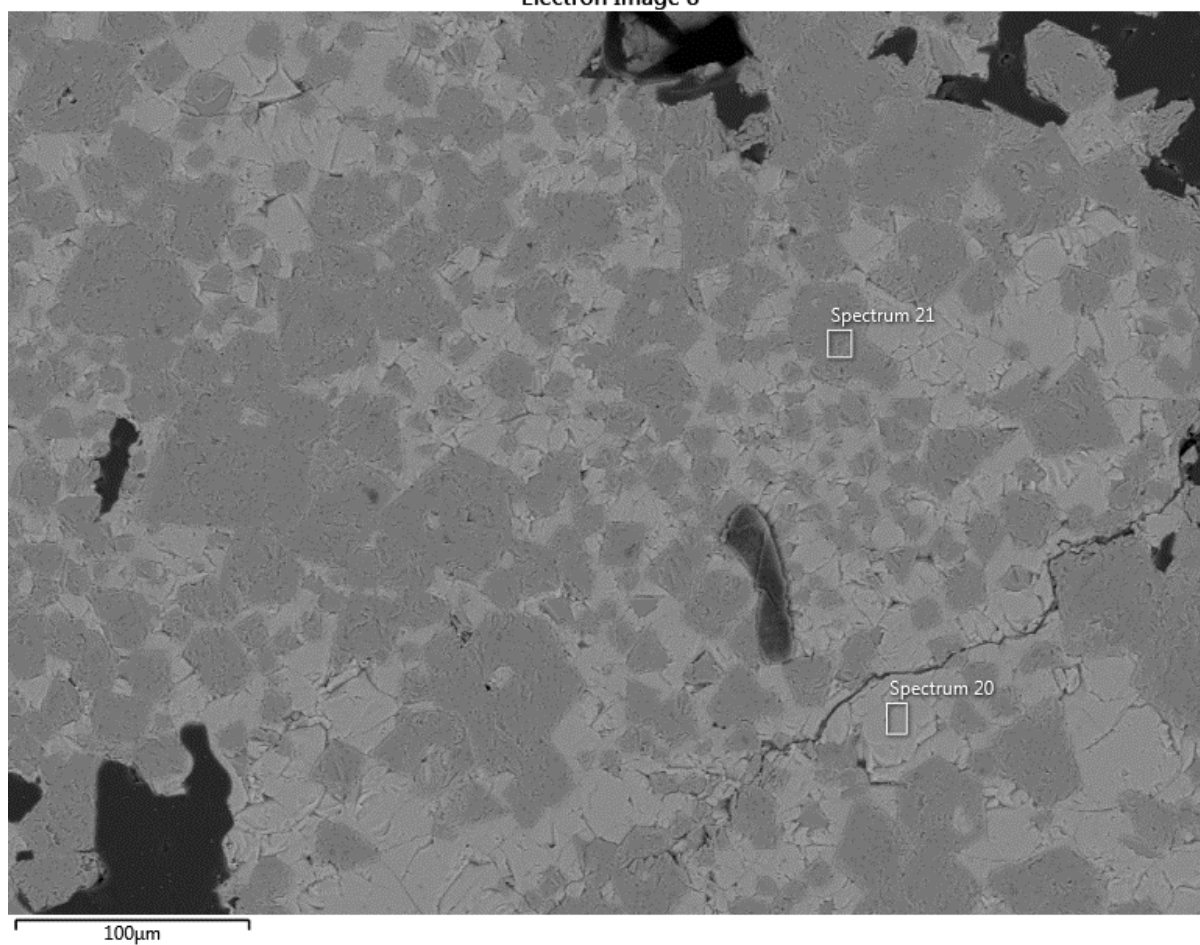


Figure 41: Electron backscatter image of equilibrium test F.

Table 46: SEM-EDS analysis of Figure 41.

	Spectrum 20	Spectrum 21
Mg (At %)	1.5	14.6
Al (At %)		16.1
O (At %)	56.8	54.7
Ca (At %)	21.2	
Fe (At %)	0.7	
V (At %)	19.9	13.6
Phase	Ca₂V₂O₅	Spinel

Electron Image 6

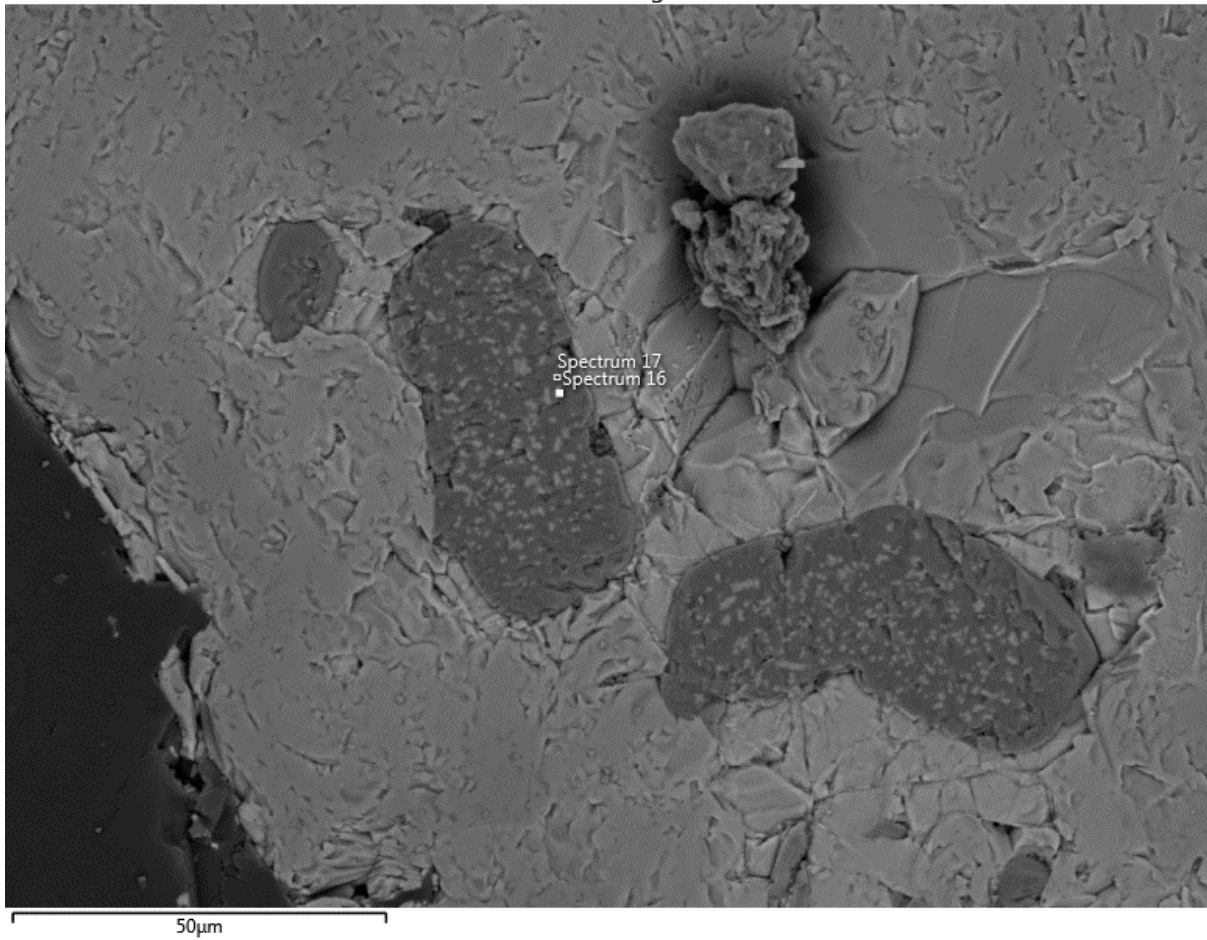


Figure 42: Electron backscatter image of equilibrium test F.

Table 47: SEM-EDS analysis of Figure 42.

	Spectrum 16	Spectrum 21
Mg (At %)	50.6	14.8
Al (At %)	47.8	13.0
O (At %)		54.7
Ca (At %)		
Fe (At %)		
V (At %)	1.6	16.5
Phase	MgO_{ss}	Spinel

7.4 Sample G

Electron Image 7

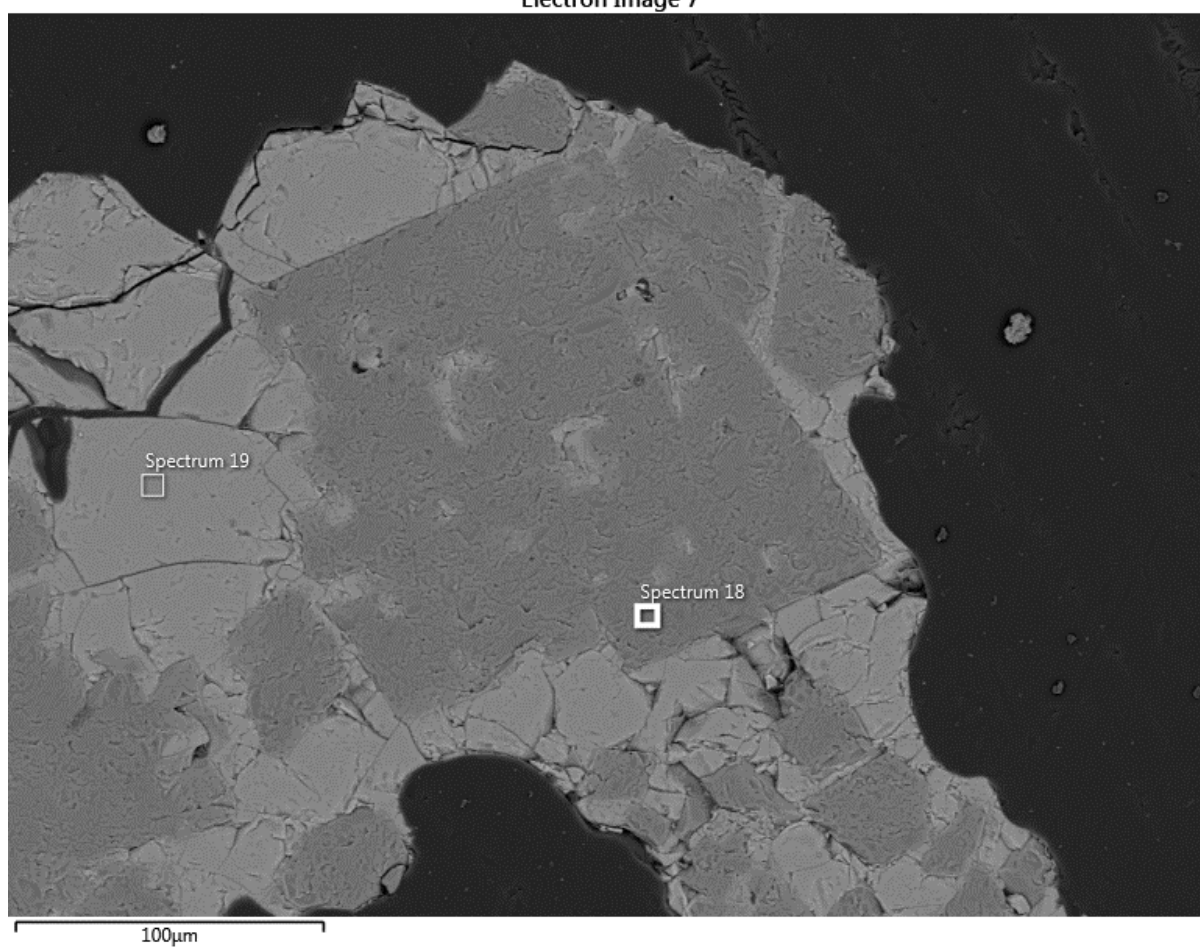


Figure 43: Electron backscatter image of equilibrium test G.

Table 48: SEM-EDS analysis of Figure 43.

	Spectrum 18	Spectrum 21
Mg (At %)	15.8	2.0
Al (At %)	19.8	
O (At %)	53.3	55.1
Ca (At %)		22.1
Fe (At %)		0.6
V (At %)	11.1	20.3
Phase	Spinel	Ca₂V₂O₅